Transverse Steel Confinement Effects on the Structural Behavior of Reinforced Concrete Circular Columns Strengthened with Externally-Bonded Fiber-Reinforced Polymers

By

DIOGO ZIGNAGO VIEIRA

DISSERTATION

Submitted in partial satisfaction of the requirements for the degree of

DOCTOR OF PHILOSOPHY

in

Civil and Environmental Engineering

in the

OFFICE OF GRADUATE STUDIES

of the

UNIVERSITY OF CALIFORNIA

DAVIS

Approved:

_____

Michele Barbato, Chair

_____

John Bolander

_____

Lijuan Cheng

Committee in Charge

2022

Abstract

Application of fiber-reinforced polymer (FRP) composites in strengthening of reinforced concrete (RC) structures has become an increasingly accepted engineering practice. In particular, the use of externally-bonded FRP wraps as a confining material for concrete can enhance both the compressive strength and the ultimate strain of concrete, making it suitable for strengthening and/or seismic retrofit of existing reinforced concrete columns. The confinement effect produced by the externally-bonded FRP acts in addition to the confining mechanism of the existing internal reinforcing steel, thus increasing the load-carrying capacity and ductility of the member. The transverse steel confinement contribution can be significant, although it is generally ignored in existing design guidelines for FRP wrapping, potentially leading to an excessively conservative retrofit design.

This dissertation presents a confined concrete material constitutive model for use in finite element analysis, which is able to accurately model the combined confinement effects of FRP and internal steel reinforcement on the structural monotonic, cyclic, and/or dynamic response of reinforced concrete RC columns confined with externally-wrapped FRP. The proposed material constitutive model for FRP-and-steel confined concrete explicitly models the simultaneous confinement produced by FRP and steel on the core concrete to predict the combined effect on the structural response of circular RC columns. This proposed material model is combined with a force-based frame element to numerically predict the load-carrying capacity of FRP-confined RC columns subjected to different loading conditions. Numerical simulations are compared to experimental test data available in the literature and published by different authors. The numerically simulated responses agree very well with the corresponding experimental results. The proposed model is found to predict the ultimate load for FRP-confined RC circular columns with better accuracy than

models that do not consider the simultaneous confinement effects of FRP and steel.

The proposed FRP-and-steel confined concrete model is employed in a comprehensive parametric study to numerically investigate the steel confinement effects and the relative importance of key modeling and design parameters on the axial strength of FRP-confined RC columns. The results show that the steel confinement effect can significantly increase the axial strength of FRP-confined RC columns, particularly for large cross-sections, low concrete compressive strengths, and low amounts of confining FRP. The steel confinement effects induce two distinct behaviors depending on the ratio between the FRP lateral confinement and the unconfined concrete peak strength. These two behaviors can be described as functions of two different relative confinement coefficients.

The numerical investigation of the effects of the transverse steel confinement on FRP-confined circular RC columns from the case of pure axial loading is also extended to the case of combined axial load and bending moment. A thorough parametric study is conducted to investigate the effects of different design parameters when varied within their range for practical applications. The two synthetic coefficients previously proposed to quantify the effect of transverse steel confinement on concentrically-loaded FRP-confined circular RC columns are modified to incorporate the effects of load eccentricity. The outcome of this research could lead to significant benefits in terms of safer and/or more economic design of FRP-confinement retrofits of RC columns.

Based on the results from the parametric study, a modification is proposed to the ACI 440.2R-17 design equation of FRP-confined RC circular columns subjected to axial loading. The proposed design equation is calibrated through a structural reliability analysis approach, in which the capacity model (corresponding to the probability distribution for the axial load capacity of the columns) is generated via Monte Carlo simulation based on advanced nonlinear finite element

response analyses for multiple realistic combinations of design parameters. Under different design conditions, the newly proposed design equation provides a significantly less variable reliability index than that obtained using the current ACI 440.2R-17 design equation, which produces increasingly excessively conservative retrofit designs for increasing amounts of transverse steel reinforcement. A practical design procedure based on the proposed design equation is also presented.

In order to reduce the associated computational cost of the proposed FRP-and-steel confined concrete model, and to increase the corresponding numerical robustness, this dissertation also proposes a new optimization procedure to obtain an analytical expression for the iteratively-generated monotonic envelope of the original stress-strain model. Several analytical functions are tested and their capability to fit the iteratively-generated uniaxial stress-strain model for the monotonic envelope curve of FRP-and-steel confined concrete is evaluated. The newly-proposed analytical formulation of the uniaxial stress-strain model for FRP-and-steel confined concrete is compared with the original iterative formulation in terms of computational cost for an application example consisting in a nonlinear seismic time-history analysis of a five-span bridge structure with FRP-retrofitted RC piers. It is found that the use of the newly proposed optimization-based analytical monotonic envelope can reduce by more than 30% the computational time associated to the original iteration-based monotonic envelope with negligible changes in the structural response prediction at both global and local levels.

Acknowledgments

I would like to acknowledge and express my deepest gratitude to my advisor Professor Michele Barbato who made this work possible. His guidance and advice carried me through all the stages of this research. I would also like to thank my committee members, Professor John Bolander and Professor Dawn Cheng, for their insightful comments and suggestions.

I would also like to give special thanks to my sister, Danielle Zignago, and my family as a whole for your continuous support and the encouragement I needed throughout this process. Your prayers sustained me this far.

I would also like to thank all my friends form Louisiana and California. This would have been a much more difficult feat without you all. Thank you all for your unwavering support. Also, thanks to my friends in Brazil for being understanding when I have not promptly answered messages and returned phone calls.

And above all, I would like to express my greatest gratitude and honor to God, for His Love and Mercy, especially in the completion of this dissertation; without Him, I would not have been able to finish this work.

Table of Contents

List of Tables

List of Figures

1 Introduction

Aging reinforced concrete (RC) structures, in particular RC columns, can have their functionality affected by environmental deterioration, damage due to extreme events, or increased demands due to adaptive reuse projects. Traditional techniques of repairing and strengthening (e.g., welded steel or concrete jackets) can be expensive, excessively labor-intensive, and vulnerable to future corrosion, and can cause prolonged traffic disruption. The retrofit techniques based on the use of externally-bonded fiber-reinforced polymers (FRP) present several advantages over traditional methods, including high strength-to-weight ratio, excellent corrosion properties, simplified installation, and quick restoration of structural capacity. Externally-bonded FRP can be used to address several potential structural deficiencies in an RC column: (1) increase the axial and bending moment capacities through lateral confinement; (2) improve ductility due to provided confinement; (3) increase shear strength; (4) prevent and/or repair corroded members; (5) enhance seismic performance and resiliency; (6) prevent buckling of longitudinal reinforcing steel; (7) delay concrete spalling; and (8) strengthen lap splices (Parvin and Brighton 2014; ACI 2017). This research focuses on the study of the mechanical behavior of concrete associated with the lateral confinement produced by the internal transverse steel and its implications on the structural capacity of FRP-confined RC columns.

Within the cross-section of these columns, the circumferentially-oriented fibers in the FRP laminates apply a confining pressure onto the concrete that enhances the load capacity and ductility of the structural member by restricting the concrete lateral dilation when subject to compressive loads (Fardis and Khalili 1982). This confinement acts simultaneously with the confining mechanism of the existing internal transverse steel in the concrete core, which can become significant in view of modern seismic design codes that lead to designs with considerable amounts

of both longitudinal and transverse reinforcing steel (Roy et al. 2010; Tatar et al. 2021). Nevertheless, the transverse steel confinement is typically ignored in design codes and guidelines (Kaeseberg et al. 2019), potentially leading to an excessively conservative retrofit design. Only the German DAfStb-Guideline directly addresses the transverse steel reinforcement by including it in the calculation of the confinement pressure, whereas ACI 318-19 and ACI 440.2R-17 qualitatively account for the degree of steel confinement by assigning a different ϕ-factor to the column's axial strength depending on the type of transverse reinforcement (i.e., steel tie or spiral). This issue can be attributed to the fact that the simultaneous confinement phenomenon by FRP laminates and transverse steel is not as well understood and studied as the confinement action of FRP laminates only. In fact, whereas several constitutive models are available in the literature for FRP-confined concrete (Ozbakkaloglu et al. 2013), only a few confined concrete stress-strain models consider the concomitant confining mechanisms from both FRP and steel. Moreover, most of these few available FRP-and-steel confined concrete models are either derived from regression analysis of limited data points (Lee et al. 2010) or rely on the simplifying assumption of linear superposition of the confinement effects (Ilki et al. 2008; Hu and Seracino 2014; Teng et al. 2015). Therefore, the accuracy of these models is compromised.

1.1 Objectives and Motivation

The first objective of this work is to develop an accurate yet computationally inexpensive analysis-oriented stress-strain model for confined concrete that accurately accounts for the complex nonlinear phenomenon associated with the simultaneous confining mechanisms produced by FRP laminates and transverse steel (Chapter 2). The specific outcomes of this study are: (1) development of a stress-strain model for the monotonic envelope of FRP-and-steel confined concrete; (2) development of hysteretic laws for the concrete model based on previously conducted

experimental tests to enable nonlinear finite element (FE) analysis involving cyclic and/or dynamic loading; (3) validation of the model against experimental data available in the literature corresponding to FRP-confined columns subject to different loading schemes (i.e., concentric compression, eccentric compression, and cyclic lateral load).

The second objective is to better understand the structural behavior of FRP-strengthened RC columns and to quantify the effects of transverse steel confinement on the structural capacity of such columns. To this end, the proposed FRP-and-steel confined concrete model is employed in the numerical simulations of FRP-confined RC columns through extensive parametric studies, in which several key parameters are varied. This objective is accomplished in two phases, each corresponding to different chapters of this dissertation: (1) investigating columns subjected only to concentric axial loads (Chapter 3); and (2) investigating columns subjected to the combined action of axial compression and bending moment (Chapter 4). These two chapters provide an in depth understanding of the structural behavior of RC columns subject to the simultaneous confinement of transverse steel and FRP wraps, and propose relative confinement coefficients that can represent transverse steel confinement effects in a concise and effective manner.

Based on the results of the parametric investigation carried out for concentrically-loaded columns, the third objective is to propose a design procedure for FRP-confined RC columns subject to pure compression that includes the transverse steel confinement effects and, therefore, reduce the conservativeness associated with existing design guidelines (Chapter 5). The specific outcomes of this study are: (1) to propose a design equation that incorporates the contribution of the internal steel confinement to the axial strength of FRP-confined RC columns; (2) to calibrate the design equation by means of robust structural reliability principles; (3) to develop the statistical distributions for variables involved in the structural reliability calibration for which these

distributions are not available in the literature; and (4) to quantify the savings on FRP material associated with the proposed design equation in the strengthening of RC columns through a case study.

Finally, the fourth objective is to reduce the associated computational cost and increase the corresponding numerical robustness of the proposed iteratively-generated FRP-and-steel confined concrete model (Chapter 6). The outcome of this study is a new optimization procedure to obtain an analytical expression for the monotonic envelope of the proposed confinement model while keeping the accuracy as close as possible to that of the original model.

1.2 Scope

The scope of this research work is limited to FRP-confined RC columns with circular cross-sections with preserved structural integrity. Further research is needed to investigate its application to other shapes (e.g., rectangular cross-sections) or pre-damaged RC columns.

1.3 Organization of the Dissertation

In Chapter 2 of this dissertation, an analysis-oriented constitutive model for confined concrete simultaneously confined with FRP and steel is proposed. The complex nonlinear phenomenon of double confinement is handled at the material level by considering a superposition of confining pressures from both materials. It adopts an incremental-iterative approach to solve equilibrium and compatibility relationships involving the laterally-expanding concrete whose radial deformation is restricted by the confining devices. A hysteresis model is also proposed to enable use in cyclic and/or dynamic analysis. The FRP-and-steel confined concrete stress-train model is validated against experimental data in the literature for concentric compression, eccentric compression, and cyclic lateral loading conditions.

In Chapter 3, the proposed FRP-and-steel-confined concrete model is employed to simulate the mechanical behavior of confined concrete in the finite element modeling of FRP-strengthened RC columns. An extensive parametric analysis is carried out to investigate the structural behavior of these columns and to quantify the transverse steel confinement's contribution to the axial load bearing capacity. Relative confinement coefficients are proposed in order to synthetically quantify the effects of the transverse steel confinement on the peak axial strength of FRP-strengthened RC columns.

In Chapter 4, the parametric analysis conducted in Chapter 3 is extended to columns subjected to combined axial load and bending moment. It is noteworthy that FRP-and-steel confined concrete models have been rarely employed in the literature in the computation of axial load-bending moment interaction diagrams of FRP-confined RC columns. Only a very recent study by Yuan et al. (2022) was found to investigate the effects of internal steel hoops on the interaction diagram of such columns. The topic remains understudied, and the present research helps to systematically investigate these effects.

In Chapter 5, in order to produce more efficient retrofit while keeping acceptable reliability levels, a new design equation is proposed for FRP-confined RC circular columns subject to pure compression, which accounts for the simultaneous confinement effects of transverse steel and FRP. The new equation is calibrated via structural reliability analysis methods, which account for the uncertainties associated with material, dimension, modeling, and loading variables. A new iterative design procedure is also proposed and demonstrated via a realistic application example. The savings on FRP material used in retrofit design associated with the new design equation are investigated and quantified.

In Chapter 6, several analytical functions are tested and their capability to fit the original

iteratively-generated uniaxial stress-strain curve for the monotonic envelope of FRP-and-steel-confined concrete is evaluated. A new optimization procedure to obtain an analytical expression for the corresponding monotonic envelope is developed. The computational costs associated with both the original iterative model and the analytical model are compared via the nonlinear seismic time-history analyses of: (1) a two-column bridge pier; and (2) a five-span bridge structure with FRP-retrofitted RC piers.

Finally, Chapter 7 presents a summary of the conducted research, points out the conclusions derived from this study, and suggests future research directions.

1.4 Journal publications derived from this Dissertation

Journal article based on Chapter 2 (published):

- Zignago, D.[1], Barbato, M.[2], and Hu, D.[3] (2018). "Constitutive model of concrete simultaneously confined by FRP and steel for finite-element analysis of FRP-confined RC columns." *J. Compos.* Constr., 22(6): 04018064.

Journal article based on Chapter 3 (published):

- Zignago, D., and Barbato, M. (2021). "Effects of transverse steel on the axial-compression strength of FRP-confined reinforced concrete columns based on a numerical parametric study." *J. Compos. Constr.*, 25(4): 04021024.

[1] Ph.D. candidate, Department of Civil & Environmental Engineering, University of California, Davis, One Shields Avenue, 2209 Academic Surge, Davis, California 95616, USA; Email: zignago@ucdavis.edu

[2] Professor, Department of Civil & Environmental Engineering, University of California, Davis, One Shields Avenue, 3149 Ghausi Hall, Davis, California 95616, USA; E-mail: mbarbato@ucdavis.edu

[3] Project Engineer, ATI Architects and Engineers; Email: lsu.hudan@gmail.com

Journal article based on Chapter 4 (submitted):

- Zignago, D., and Barbato, M. “Numerical investigation of axial force-bending moment interaction for FRP-confined reinforced concrete columns with internal steel transverse reinforcement.”

Journal article based on Chapter 5 (published):

- Zignago, D., and Barbato, M. (2022). “Reliability-based calibration of a new design procedure for axially-loaded reinforced concrete circular columns accounting for simultaneous confinement by fiber reinforced polymers and steel.” *J. Compos. Constr.*, 26(3): 04022017.

Journal article based on Chapter 6 (submitted):

- Zignago, D., and Barbato, M. “New analytical analysis-oriented stress-strain model for FRP-and-steel confined concrete.”

2 Constitutive model of concrete simultaneously confined by FRP and steel for finite element analysis of FRP-confined reinforced concrete columns

This chapter presents a confined concrete material constitutive model that is able to accurately model the combined confinement effects of FRP and internal steel reinforcement on the structural response of reinforced concrete columns confined with externally-wrapped FRP. The complex nonlinear phenomenon of simultaneous confinement is handled at the material level through an iterative-incremental approach, in which force equilibrium and strain compatibility relationships involving the radial deformation of concrete and the confining devices (FRP and steel) are enforced when their respective lateral confining pressures exerted to concrete are superimposed. This proposed material model is combined with a force-based frame element to numerically predict the load-carrying capacity of FRP-confined RC columns subjected to different loading conditions. Numerical simulations are compared to experimental test data available in the literature and published by different authors. The relative confinement coefficient c_f is introduced for the first time to help quantify the importance of the transverse steel confinement to the structural response of FRP-confined RC columns.

2.1 Introduction

Existing reinforced concrete (RC) structures often need rehabilitation or strengthening due to inappropriate design or construction, modification of the use and of the corresponding design loads, and damage caused by environmental factors and/or extraordinary loading events. Retrofitting and repairing of damaged and/or inappropriately designed concrete structures using externally-bonded fiber reinforced polymers (FRP) has proved to be an effective alternative to other types of strengthening techniques (e.g., steel jackets), presenting some advantages like

excellent corrosion resistance, fire resistance, ease of transportation and installation, high strength-to-weight ratio of FRP sheets, which leads to a minimum increase of the structure's weight and dimensions (Bakis et al. 2002; Cheng and Karbhari 2006; Basalo et al. 2012). This retrofit method has become more common during the last few decades, being widely applied specially to columns of bridges and buildings (Seible et al. 1997; Flaga 2000; Pantelides et al. 2000; Mertz 2003; Motavalli and Czaderski 2007).

The amount of longitudinal and transverse reinforcement in RC columns must satisfy minimum design codes' requirements in terms of flexural and shear strength. As a result, RC columns that need to be retrofitted with FRP laminates also contain longitudinal and transverse steel reinforcement. Thus, in these retrofitted RC columns, a significant portion of the concrete is subjected to two simultaneous confinement actions: the confinement due to FRP plates/sheets and the confinement due to internal (longitudinal and transverse) steel reinforcement. FRP jacketing of RC columns exerts a linearly increasing confining pressure up to rupture on the concrete due to its lateral dilation when loaded, while the internal reinforcing steel is responsible for a constant confining pressure after yielding (Spoelstra and Monti 1999). Both types of confinement enhance the seismic performance of the RC column, improving the concrete compressive strength and thus the ductility of the member, and making FRP-wrapped RC columns more suitable, e.g., to undergo large lateral displacements imposed by severe earthquakes.

The majority of the stress-strain models available in the literature to model FRP-confined concrete do not account for the influence of the existing internal steel reinforcement on the mechanical behavior of concrete confined through externally-bonded FRP laminates (Fardis and Khalili 1982; Mirmiran and Shahawy 1996; Karbhari and Gao 1997; Samaan et al. 1998; Spoelstra and Monti 1999; Toutanji 1999; Xiao and Wu 2000; Fam and Rizkalla 2001; Shao et al. 2006). Kawashima

et al. (2000) proposed two different confined concrete stress-strain models: one for concrete confined with carbon FRP only, and one for concrete confined simultaneously by carbon FRP and transverse steel ties. A regression analysis, based on the experimental results obtained through two-phase loading tests on RC specimens with circular and rectangular sections, was used to calibrate the parameters needed to define these two stress-strain confined concrete models. The model was validated by comparing the envelope curves of the lateral force versus lateral displacement response of six specimens with the corresponding curves analytically obtained through a fiber analysis based on the developed equations. Li et al. (2003) developed a constitutive model for carbon FRP-confined concrete. The peak strength of the confined concrete was derived from the Mohr-Coulomb failure criterion, whereas the strain at the peak strength was obtained from a regression analysis based on experimental compression tests. This material constitutive model was modified to model concrete confined by both steel reinforcement and carbon FRP. In the modified model, the strength of the confined concrete was obtained as the sum of the unconfined concrete strength and the increments of strength due to the confinement of carbon FRP and steel reinforcement considered independently. This modified confined concrete model was also verified by comparisons with experimental tests. Using a similar approach to that employed in Li et al. (2003), Ilki et al. (2008) derived a set of empirical equations to describe the stress-strain response of concrete confined simultaneously by steel and FRP and used this new model to successfully predict the compressive strength and corresponding axial deformation of FRP jacketed columns. Pellegrino and Modena (2010) investigated the interaction mechanisms between internal steel reinforcement and external FRP confinement. An analytical model was proposed to describe the stress-strain monotonic envelope response of FRP confined elements with circular and rectangular cross-sections with or without internal steel reinforcement. The model was found to agree well

with experimental results available in the literature. Hu and Seracino (2014) developed an analysis-oriented FRP-confined model that also accounts for the confinement produced by internal steel reinforcement. This model uses a stress-strain curve proposed by Popovics (1973), in which the peak strength of the confined material is obtained as the summation of the peak strength of the unconfined material and the strength contributions due to steel and FRP confinement considered as independent. These contributions are based on the models proposed by Mander et al. (1988) for the steel confinement and Teng et al. (2007) for the FRP confinement. Shirmohammadi et al. (2015) also developed a model that predicts the monotonic stress-strain relationship of confined concrete, considering the double confinement. The model was implemented in a fiber-based moment-curvature analysis, showing a better agreement with experimental results than other tested models. Ismail et al. (2017) modified a design-oriented model for FRP-confined concrete by adding the effect of steel confinement through a shift in the stress-strain curve without any modification of the stiffness.

This paper extends an analysis-oriented material constitutive model of FRP-confined concrete, originally developed by Spoelstra and Monti (1999) and applied to FE analysis of FRP-retrofitted columns by Hu and Barbato (2014). This modified model accounts for the simultaneous confinement effects of internal steel reinforcement and externally-bonded FRP laminates on the structural monotonic, cyclic, and/or dynamic response of FRP-retrofitted RC columns. The proposed material constitutive model is validated against experimental data available in the literature for the structural response of FRP-retrofitted RC columns with circular cross-section and subjected to different loading conditions. The structural response of these columns was numerically predicted using the proposed material model in conjunction with a force-based frame FE with fiber-discretized sections (Spacone et al. 1996; Neuenhofer and Filippou 1997; Scott and

Fenves 2006; Hu and Barbato 2014).

2.2 Research relevance

The proposed material constitutive model enables a computationally efficient approach to model the simultaneous confinement mechanisms of reinforcing steel and FRP within the cross-section of a RC column. In conjunction with the fiber-section force-based frame element used in this research, it can provide structural analysts with a practical tool for performance assessment and design of FRP retrofit of deficient RC columns. The proposed model is particularly suitable for accurate and computationally efficient modeling of large-scale structures (e.g., building and bridges) subject to static and dynamic loadings, as well as for reliability assessment of real-world structures. Moreover, the accurate modeling of the simultaneous steel-FRP confinement effects of concrete could improve the efficiency of columns' FRP retrofit by reducing the conservativeness of models that neglect the steel's confining effect and by providing better estimates of the structural component ductility after retrofit, which is a crucial ingredient, e.g., for performance-based design of RC bridges.

2.3 Material constitutive model for concrete confined with steel and FRP

The material constitutive model proposed by Spoelstra and Monti (1999) (referred to as SM model hereinafter) provides an axial stress-axial strain curve based on an iterative numerical procedure that enforces equilibrium and compatibility between the radial stress and deformation for the confined concrete and the axial stress and hoop deformation for the confinement devices. The SM model is suitable to predict the structural behavior of concrete confined with externally-bonded FRP, steel jackets, or internal steel reinforcement. However, this model does not consider the interaction effects due to simultaneous confinement actions of steel and FRP and is valid only for

monotonic loading of the confined concrete.

This study proposes a modified SM (mSM) confined concrete model that: (1) can account for simultaneous confinement by steel and FRP in determining the monotonic envelope of the confined concrete, and (2) possesses simple unloading and reloading rules that allow the use of the material constitutive model under general loading conditions. The mSM model is based on the same iterative procedure used by the SM model, but it differs from it for the calculation of the total confinement pressure. This new model is described in the following subsections. It is also noted here that both SM and mSM models assume that the confined concrete has zero stress and zero stiffness in tension, i.e., they neglect tension stiffening because the focus of this study is on the ultimate behavior of columns. However, tension stiffening (Lin 2010) can be easily integrated into the proposed material constitutive model.

2.3.1 Monotonic envelope of the stress-strain curve

The mSM model evaluates the lateral confinement pressure as the sum of the confinement pressure due to the externally-bonded FRP and internal transverse steel reinforcement. This approach differs from that used in most of the previous studies (Li et al. 2003; Ilki et al. 2008; Pellegrino and Modena 2010; Hu and Seracino 2014), which considers independently the sum of the strength increments due to the confinement action of each material (steel and FRP).

The total confinement pressure, $f_l^{'}$, for the mSM model is calculated as follows:

$$f_l^{'} = f_{l,\text{steel}} + f_{l,\text{FRP}} = \frac{1}{2} \cdot k_s \cdot \rho_s \cdot \sigma_s + \frac{1}{2} \cdot k_f \cdot \rho_f \cdot \sigma_f \tag{2-1}$$

The term $f_{l,\text{steel}}$ in Eq. (2-1) represents the confinement action due to the transverse reinforcement steel, where k_s = steel confinement effectiveness coefficient (Mander et al. 1988), ρ_s = transverse steel reinforcement ratio defined as

$$\rho_s = \frac{4 \cdot A_{st}}{s \cdot d_c} \tag{2-2}$$

with A_{st} = cross-sectional area of a transverse reinforcing stirrup/spiral, s = clear distance between adjacent hoops or spiral turns, and d_c = diameter of the confined concrete core, and σ_s = stress of the transverse reinforcing steel. The stress of the transverse reinforcing steel is given by

$$\sigma_s = \begin{cases} E_s \cdot \varepsilon_l & \text{for} \quad \max(\varepsilon_l) < \varepsilon_y \\ f_{yt} & \text{for} \quad \varepsilon_y \le \max(\varepsilon_l) < \varepsilon_{su} \\ 0 & \text{for} \max(\varepsilon_l) \ge \varepsilon_{su} \text{ or } \varepsilon_l < 0 \end{cases} \tag{2-3}$$

where E_s = elastic modulus of the transverse reinforcing steel, f_{yt} = yield strength of the transverse reinforcing steel, ε_y = yield strain of the transverse reinforcing steel, ε_{su} = rupture strain of the transverse reinforcing steel, and ε_l = lateral strain.

The term $f_{l,\text{FRP}}$ in Eq. (2-1) represents the confinement action due to the externally-bonded FRP, where k_f = FRP confinement effectiveness coefficient (Saadatmanesh et al. 1994), ρ_f = FRP volume ratio defined as

$$\rho_f = \frac{4 \cdot t_f}{D} \tag{2-4}$$

with t_f = thickness of the jacket, D = diameter of the FRP jacket/sheet; and

$$\sigma_f = \begin{cases} E_f \cdot \varepsilon_l & \text{for} \quad \max(\varepsilon_l) < \varepsilon_{f,\text{rup}} \\ 0 & \text{for} \quad \max(\varepsilon_l) \ge \varepsilon_{f,\text{rup}} \text{ or } \varepsilon_l < 0 \end{cases} \tag{2-5}$$

where $\varepsilon_{f,\text{rup}} = \xi_f \cdot \varepsilon_{fu} = \xi_f \cdot f_{fu} / E_f$ = rupture strain of FRP, ξ_f = efficiency factor, ε_{fu} = ultimate strain from coupons tests, f_{fu} = ultimate strength of the FRP material from coupons tests, and E_f = elastic modulus of the FRP.

The axial stress-axial strain relation is calculated incrementally through the iterative procedure described in Spoelstra and Monti (1999), in which the calculation of $f_l^{'}$ is performed according to Eq. (2-1). The confining pressure for concrete confined simultaneously by steel and FRP is shown in Figure 2-1 as a function of the radial strain. Typical monotonic axial stress-strain response curves for the SM model and the mSM model are compared in Figure 2-2. As expected, the stress achieved in the mSM model for a given strain is higher than that in the SM model and depends on the amount and configuration of confining steel. It is also noted that the peak strength (corresponding to the FRP failure) occurs at different levels of strains, with the mSM model achieving at higher strain its peak strength.

Figure 2-2 also plots the stress-strain curves corresponding to the steel-confined concrete model proposed by Mander et al. (1988) and the Popovics-Saenz model for unconfined concrete (Popovics 1973; Balan et al. 1997) with the same underlying properties. It is observed that, after the FRP failure (i.e., when only the confinement from the transverse steel reinforcement is active), the mSM model reduces to the Mander's model, until the concrete lateral strain ε_l reaches the rupture strain of the transverse reinforcing steel ε_{su}, after which the mSM model reduces to residual stress of the unconfined curve. On the other hand, the SM model reduces directly to the unconfined curve as soon as the confining FRP reaches its ultimate strain.

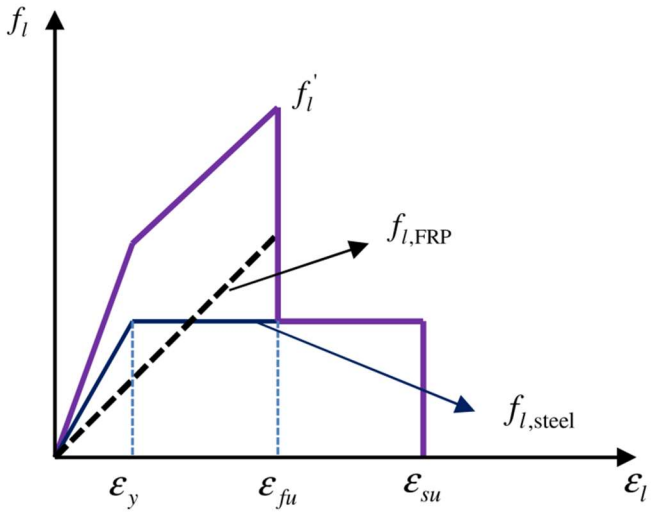

Figure 2-1. Confinement pressure acting on concrete that is simultaneously confined by steel and FRP.

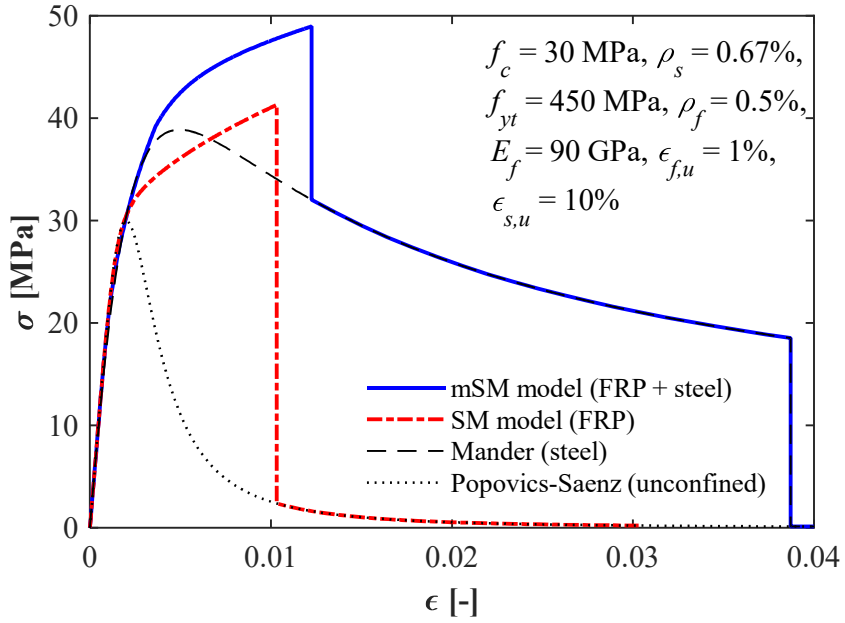

Figure 2-2. Monotonic envelopes for the stress-strain relations obtained using different models

The description provided here implies that the FRP confining material reaches failure before the confining steel, which is the most common case in practice. However, it is noteworthy that the proposed model accounts also for the less likely cases in which the confining steel reaches its

ultimate strain before the confining FRP. In these cases, the mSM model first reduces to the SM model when the steel fails, and then to the Popovics-Saenz model when also the FRP fails.

2.3.2 Hysteretic behavior of the stress-strain curve

The hysteretic behavior of the mSM model is described by linear hysteretic unloading/reloading branches that are defined based on a set of experimental tests conducted by Barbato et al. (2003). The proposed model does not model strength deterioration due to the cumulative damage produced by repeated hysteresis loops, the effect of which was found to be very small in the experimental results. However, this effect could be added by introducing a cumulative damage parameter (e.g., see Fardis et al. (1983)). The stiffness degradation due to the propagation of internal cracks for increasing plastic strain is considered in the calculation of the reloading stiffness, E_{rel}, and is based on the model developed by Imran and Pantazopoulou (1996). It is noted here that the original SM model consisted only of a monotonic envelope, i.e., it did not consider the hysteretic response of FRP-confined concrete. The hysteretic behavior developed in this study for the mSM model is adopted also for the SM model, which is thus extended to allow the numerical analysis of the cyclic behavior of FRP-confined concrete.

Figure 2-3 illustrates the unloading/reloading rules of the proposed hysteretic model by representing compression stress and strain as positive quantities for clarity's sake. Starting from a virgin material condition with zero stress and strain (point (0) on Figure 2-3), the constitutive model follows the monotonic envelope for increasing compression strain up to point (1) defined by axial stress σ_{unl} and axial strain ε_{unl} where the unloading (i.e., decreasing compression strain) starts by following a straight line with a slope equal to the initial stiffness of concrete, $E_{\text{rel}} = E_c$, until zero stress is reached at a residual strain, $\varepsilon_{r,\text{unl}}$, corresponding to point (2) in Figure 2-3. When the unloading initiates from the monotonic envelope, history variables representing the

unrecoverable plastic strain, $\varepsilon_{r,\mathrm{rel}}$ (corresponding to the axial strain at point (5) in Figure 2-3), and the corresponding reloading stiffness, E_{rel} are evaluated as:

$$\varepsilon_{r,\mathrm{rel}} = \varepsilon_{\mathrm{unl}} - \frac{\sigma_{\mathrm{unl}}}{E_{\mathrm{rel}}} \tag{2-6}$$

$$E_{\mathrm{rel}} = \frac{E_c}{\left(1 + 2 \cdot \alpha \cdot \varepsilon_{l,\mathrm{unl}}\right)} \tag{2-7}$$

where $\alpha = 20$ (Imran and Pantazopoulou 1996) and $\varepsilon_{l,\mathrm{unl}} =$ lateral strain coordinate of unloading point on the envelope (point (1)). Unless the axial strain reduces to values smaller than $\varepsilon_{r,\mathrm{unl}}$, any reloading/unloading with strain values between $\varepsilon_{r,\mathrm{unl}}$ and $\varepsilon_{\mathrm{unl}}$ happens along the straight line contained between points (1) and (2). For strain values smaller than $\varepsilon_{r,\mathrm{unl}}$, the unloading follows a zero stress line. If a reloading occurs and the inversion point corresponds to an axial strain contained between $\varepsilon_{r,\mathrm{rel}}$ and $\varepsilon_{r,\mathrm{unl}}$ (i.e., point (3) in Figure 2-3), the stress-strain relation follows a straight line pointing to the inversion point on the monotonic envelope (i.e., point (1)), which is defined by a slope $E_{\mathrm{unl},2}$ given by:

$$E_{\mathrm{unl},2} = \frac{\sigma_{\mathrm{unl}}}{\varepsilon_{\mathrm{unl}} - \varepsilon_{\mathrm{unl},2}} \tag{2-8}$$

in which $\varepsilon_{\mathrm{unl},2}$ denotes the new inversion point from negative strain increment to positive strain increment, the value of which is used to update history variable $\varepsilon_{r,\mathrm{unl}}$ (with the line between points (1) and (3) effectively replacing the line between points (1) and (2) as the unloading/reloading path). If the strain increment changes again direction (e.g., at point (4)), the hysteretic behavior follows the unloading/reloading rules previously described until the strain becomes smaller than

$\varepsilon_{r,\mathrm{rel}}$, after which no further degradation of the plastic strain recovery is allowed. This assumption implies that any reloading/unloading cycle occurring afterward (e.g., at point (6)) follows a zero stress line for any strain value smaller than $\varepsilon_{r,\mathrm{rel}}$ (including negative values corresponding to tension strains), or the straight line between points (1) and (5) for strain values contained between $\varepsilon_{r,\mathrm{rel}}$ and $\varepsilon_{\mathrm{unl}}$. Finally, if during a reloading phase the strain becomes larger than $\varepsilon_{\mathrm{unl}}$ (e.g., point (7) in Figure 2-3), the stress-strain relation follows again the monotonic envelope and all history variables governing the unloading/reloading behavior are reset to their initial zero values.

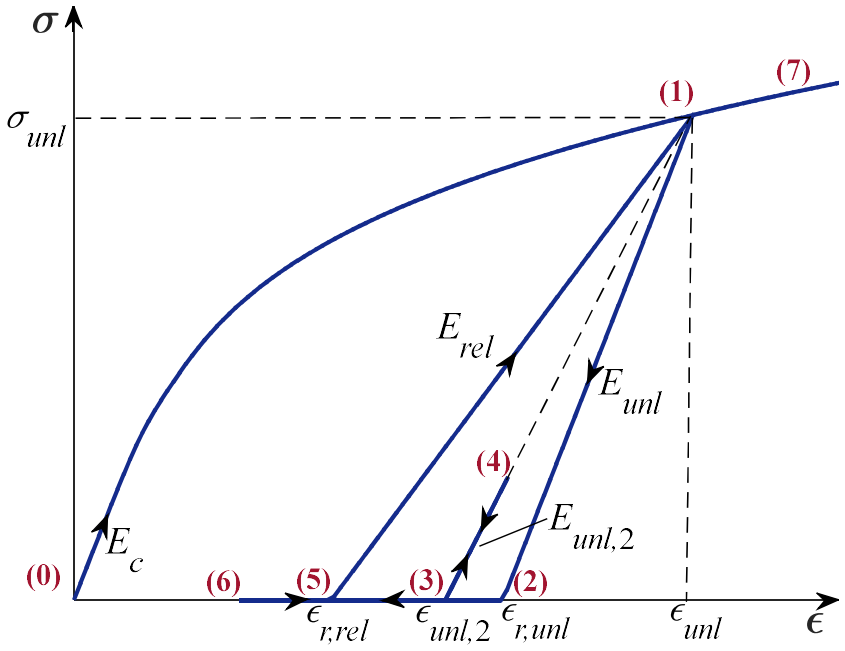

Figure 2-3. Hysteretic behavior proposed for the mSM model

It is noted here that this proposed hysteretic behavior is identical for any portion of the monotonic envelope, including early stages during which both FRP and steel confinements are active, the phases during which only FRP or only steel confinement is active (because one of the two has failed), and the phase in which the concrete is unconfined (i.e., when both FRP and steel have failed).

2.4 Computer implementation and finite element formulation

The proposed material constitutive model was implemented in FEDEASLab (Filippou and Constantinides 2004), a Matlab-based (MathWorks 1997) program appropriate for linear and nonlinear, static and dynamic structural analysis. The mSM constitutive model was used to describe the stress-strain response of confined concrete fibers in a two-node one-dimensional force-based frame FE with fiber sections (Spacone et al. 1996; Hu and Barbato 2014). In particular, each section is discretized into concrete core fibers (simultaneously confined by steel and FRP and modeled using the newly developed mSM model), concrete cover fibers (confined only by FRP, for which the mSM model reduces to the SM model), and steel bar fibers, which are modeled using the model by Menegotto and Pinto (1973) as extended in Filippou et al. (1983) to include isotropic hardening effects. Figure 2-4 shows a representation of the cross-section fiber discretization of the FE model. The frame FE is based on the Euler-Bernoulli beam theory with small deformations and its element state determination employs the non-iterative algorithm (Neuenhofer and Filippou 1997).

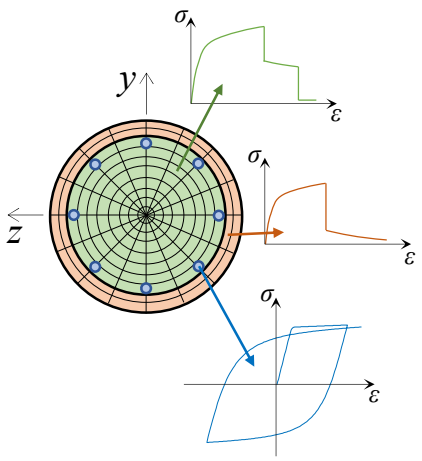

Figure 2-4. Cross-section fiber discretization of the FE model

It is pointed out here that any selection of finite element formulation (e.g., ordinary displacement-

based frame elements or a single force-based frame element), numerical integration of section response (e.g., Gauss-Legendre or Gauss-Lobatto integration), and material constitutive models for steel fibers can be used in conjunction with the material constitutive model presented in this paper, as long as a fiber-section approach is employed. Based on the authors' experience, the numerical integration scheme using five Gauss-Lobatto integration points in conjunction with force-based elements provides the best compromise between computational cost and accuracy for the majority of the cases. However, when there is a formation of a plastic hinge in the member (e.g., in correspondence of large lateral tip displacements of cantilever beams), the strain-softening behavior of the concrete can cause a localization issue and loss of objectivity in force-based elements, making their post-peak responses dependent on the number of integration points considered in the integration scheme (Coleman and Spacone 2001). This loss of response objectivity is controlled by the integration weight of the integration point closest to the plastic hinge formation, which corresponds to the strain-softening region assumed by the FE model and not necessarily to the actual plastic hinge length of the physical member. It is worth noting that this localization issue occurs also when displacement-based elements are used to model structural members with softening behavior, in which case it is controlled by the length of the FE that is closest to the plastic hinge formation (Coleman and Spacone 2001). In order to solve this issue, several regularization techniques were suggested in the literature (Coleman and Spacone 2001; Scott and Fenves 2006). In this study, for columns subjected to a combination of axial and lateral loads, for which plastic hinge formation was expected in correspondence of large lateral loads, the force-based beam-column element developed by Scott and Fenves (2006) was adopted. This element's formulation employs a plastic hinge integration method to overcome the non-objectivity problem of force-based elements' response due to localization for softening structures. This

element considers a plastic hinge with nonlinear behavior at each end of the element, whereas the remaining portion of the element has a linear elastic behavior. The length of the plastic hinge was assumed equal to the experimentally observed plastic hinge length (when this information was available in the literature) or estimated based on Paulay and Priestley (1992) (when this information was not reported in the literature).

2.5 Model validation through comparison of numerical estimates and experimental results

The proposed material constitutive model was validated through a comparison between an extensive experimental database obtained from existing literature and numerical simulation of the FE response of circular RC columns retrofitted with FRP laminates. Different loading conditions, typically adopted in the existing literature, were considered separately, namely: (a) quasi-static compressive axial load only, (b) quasi-static eccentric axial load, and (c) constant axial load and quasi-static lateral load (Figure 2-5). For each quasi-static analysis, the columns were modeled as cantilever beams with the coarsest mesh possible (i.e., with a single frame FE unless differently required by the presence of cross-sectional changes in the physical specimen). These analyses were performed based on the Newton-Raphson iterative procedure (Bathe 1996) and incremental displacement control, in order to investigate also the post-peak behavior of the models.

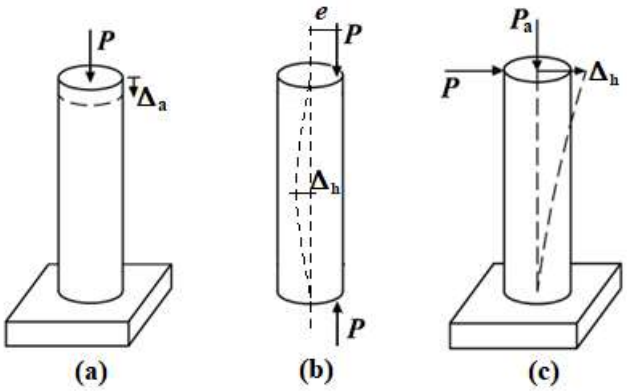

Figure 2-5. Loading configurations considered in validation

The experimental database for this study was collected from the literature in order to emphasize the contribution of internal steel on the confining pressure imposed to the core concrete. This contribution was measured by considering the ratio c_f between the steel and FRP confinement forces, defined as:

$$c_f = \frac{f_{l,\text{steel}} \cdot A_{c,\text{core}}}{f_{l,\text{FRP}} \cdot A_g} \tag{2-9}$$

in which $A_{c,\text{core}}$ denotes the area of the concrete core (i.e., confined by the steel reinforcement) and A_g denotes the gross area of the member cross-section. The experimental results were selected so that the minimum value of c_f for all cases was larger than or equal to 5%, below which the effects of simultaneous confinement by steel and FRP was considered to be negligible (i.e., the mSM model effectively reduces to the SM model).

2.5.1 Columns subject to compressive axial load only

A set of 46 RC columns confined with FRP and subjected to a monotonically increasing and concentrically applied axial load was identified from nine different authors. The description of the

select column specimens' geometry and material properties, as well as the references from which the data were taken are provided in Table 2-1. The selected database contains specimens with a wide range of cross-section diameters (from 150 mm to 400 mm), lengths (from 300 mm to 2000 mm), concrete peak strength (from 23.9 MPa to 50.8 MPa), transverse steel reinforcement ratio (from 0.39% to 3.02%) and FRP volume ratio (from 0.22% to 2.01%). The ratio between steel and FRP confinement forces, c_f, varies between 8.3% and 193.6%, with an average value of 40.7%.

Table 2-1. Experimental test database for FPR-confined RC column subjected to concentric axial loading: specimens' identification, geometry, and material properties

Ref.	ID	d (mm)	L (mm)	f_c (MPa)	f_{yt} (MPa)	f_y (MPa)	ρ_s (%)	ρ_f (%)	E_f (GPa)	σ_f (MPa)	ξ_f	c_f (%)
Parretti and Nanni (2002)	DB450-C	200	914	25.5	517	393	1.42	0.54	126	1689	0.45	45.7
Matthys et al. (2006)	K2	400	2000	32	560	620	0.39	0.59	198	2600	0.61	8.3
	K3	400	2000	32	560	620	0.39	0.94	480	1100	1.14	12.3
	K4	400	2000	32	560	620	0.39	1.8	60	780	0.58	9.0
	K5	400	2000	32	560	620	0.39	0.6	60	780	0.62	27.1
	K8	400	2000	32	560	620	0.39	0.49	120	1100	0.55	23.5
Eid et al. (2009)	A1NP2C	303	1200	31.7	602	486	2.49	1.01	78	1050	0.67	87.7
	A3NP2C	303	1200	31.7	602	550	1.6	1.01	78	1050	0.60	50.5
	A5NP2C	303	1200	29.4	602	423	0.75	1.01	78	1050	0.33	15.9
	C4NP2C	303	1200	31.7	456	423	1.59	1.01	78	1050	0.46	40.3
	C4NP4C	303	1200	31.7	456	423	1.59	2.01	78	1050	0.89	20.2
	B4NP2C	303	1200	31.7	456	550	1.59	1.01	78	1050	0.78	33.3
	C4MP2C	303	1200	50.8	456	423	1.59	1.01	78	1050	0.56	40.3
	C2NP2C	303	1200	31.7	456	423	2.44	1.01	78	1050	0.43	67.3
	C2N1P2C	303	1200	36	456	423	2.44	1.01	78	1050	0.49	67.3
	C2N1P4C	303	1200	36	456	423	2.44	2.01	78	1050	0.63	33.6
	C2MP2C	303	1200	50.8	456	423	2.44	1.01	78	1050	0.64	67.3
	C2MP4C	303	1200	50.8	456	423	2.44	2.01	78	1050	0.80	33.6
Lee et al. (2010)	S2F1	150	300	36.2	1200	-	3.02	0.29	250	4510	0.42	193.6
	S2F2	150	300	36.2	1200	-	3.02	0.59	250	4510	0.42	96.8
	S2F3	150	300	36.2	1200	-	3.02	0.88	250	4510	0.36	64.5
	S2F4	150	300	36.2	1200	-	3.02	1.17	250	4510	0.36	48.4
	S2F5	150	300	36.2	1200	-	3.02	1.47	250	4510	0.33	38.7

	S4F1	150	300	36.2	1200	-	1.51	0.29	250	4510	0.31	88.9
	S4F2	150	300	36.2	1200	-	1.51	0.59	250	4510	0.33	44.4
	S4F3	150	300	36.2	1200	-	1.51	0.88	250	4510	0.31	29.6
	S4F4	150	300	36.2	1200	-	1.51	1.17	250	4510	0.35	22.2
	S4F5	150	300	36.2	1200	-	1.51	1.47	250	4510	0.35	17.8
	S6F1	150	300	36.2	1200	-	1.01	0.29	250	4510	0.22	54.0
	S6F2	150	300	36.2	1200	-	1.01	0.59	250	4510	0.38	27.0
	S6F4	150	300	36.2	1200	-	1.01	1.17	250	4510	0.31	13.5
	S6F5	150	300	36.2	1200	-	1.01	1.47	250	4510	0.27	10.8
Demers and Neale (1999)	U25-2	300	1200	23.9	400	400	1.07	1.2	84	1270	0.38	10.4
	U40-4	300	1200	43.7	400	400	1.07	1.2	84	1270	0.22	10.7
Wang et al. (2012)	C1H2L1M	305	915	47	397	340	1.05	0.22	244	4340	0.79	30.5
	C1H2L2M	305	915	24.5	397	340	1.05	0.44	244	4340	0.89	15.2
	C1H1L1M	305	915	24.5	397	340	0.53	0.22	244	4340	0.81	12.9
	C1H1L1C	305	915	24.5	397	340	0.53	0.22	244	4340	0.81	12.9
	C2H2L1M	204	612	24.5	397	312	1.05	0.33	244	4340	0.73	16.8
	C2H2L1C	204	612	24.5	397	312	1.05	0.33	244	4340	0.85	16.8
Cairns (2001)	#28	356	1524	29.8	510	402	0.56	1.12	82.3	1770	0.41	10.4
Jaffry (2001)	#16	356	1524	29.8	510	402	0.56	1.12	45.2	1070	0.48	17.2
Carrazedo and Hanai (2006)	C2S25	190	570	28.9	756	554.8	1.96	0.55	219	2801	0.85	65.2
	C2S50	190	570	26.2	756	554.8	0.98	0.55	219	2801	0.70	29.9
	C1S25	190	570	28.9	756	554.8	1.96	0.27	219	2801	0.85	130.5
	C1S50	190	570	26.2	756	554.8	0.98	0.27	219	2801	0.88	59.8

Table 2-2 reports the experimental values and numerical estimates for both the load-carrying capacity and the strain at peak strength for the different FRP-confined RC columns. The numerical estimates obtained by employing the mSM model to describe the mechanical behavior of the core concrete fibers (i.e., those confined by both lateral steel and FRP) are also compared to those obtained by using the SM model for the entire cross-section (i.e., neglecting the reinforcing steel's confinement effects) and to those (identified in Table 2-2 as "SM + ΔP_{steel}") obtained by superposing the contributions to the load-carrying capacity due to the FRP confinement (estimated using the SM model) and the steel confinement contribution (ΔP_{steel}), which is estimated based on the relation suggested by Nilson et al. (2010) as:

$$\Delta P_{\text{steel}} = 2k_s \rho_s f_{yt} A_{c,\text{core}} \tag{2-10}$$

in which the k_s coefficient is taken from Mander et al. (1988). The constitutive material model parameters were taken from the data reported in the reference for each set of experiments, whenever the information was available. When some of the information needed to define the model was missing, typical values were used (e.g., the unconfined concrete strain at peak stress ε_{co} was assumed equal to 0.0020, 0.0022, or 0.0024 when the concrete strength was less than 28 MPa, between 28 and 40 MPa, and greater than 40 MPa, respectively, and the parameter β was estimated according to Spoelstra and Monti (1999). Table 2-2 reports also the ratio between the numerical results and the experimental estimates for both maximum axial load and strain at peak strength for all specimens, as well as the global statistics of these ratios in terms of sample means (μ), coefficients of variations (COV), minima, and maxima for both models considered in this study. The same global statistics were also reported for the estimates of the maximum axial loads obtained by superposing the FRP and steel confinement effects.

Table 2-2. Comparison between experimental results and numerical simulation with both models of load-carrying capacity of RC column specimens subjected to concentric axial loading

ID	Maximum axial load (kN)							Axial strain at peak strength (mm/m)				
	Exp.	mSM model	Ratio	SM model	Ratio	SM + ΔP_{steel}	Ratio	Exp.	mSM model	Ratio	SM model	Ratio
DB450-C	1715	1692	0.99	1502	0.88	1834	1.07	14.9	14.6	0.98	14.6	0.98
K2	7460	7969	1.07	7744	1.04	8091	1.08	11.1	10.4	0.94	10.4	0.94
K3	7490	7542	1.01	7455	1.00	7802	1.04	4.3	4.8	1.12	4.8	1.12
K4	7580	7723	1.02	7458	0.98	7805	1.03	6.9	9.6	1.39	9.5	1.38
K5	7580	7723	1.02	7458	0.98	7805	1.03	6.9	9.6	1.39	9.5	1.38
K8	6230	6263	1.01	5930	0.95	6277	1.01	5.9	5.8	0.98	5.8	0.98
A1NP2C	4571	5120	1.12	4106	0.90	5717	1.25	15	12.3	0.82	12.3	0.82
A3NP2C	4331	4744	1.10	4095	0.95	5023	1.16	12.5	11	0.88	11	0.88
A5NP2C	3326	3558	1.07	3333	1.00	3626	1.09	6.3	6.3	1.00	6.3	1.00

C4NP2C	3704	4164	1.12	3731	1.01	4474	1.21	7.7	8.3	1.08	8.3	1.08
C4NP4C	5468	5765	1.05	5515	1.01	6258	1.14	20.8	22.7	1.09	22.7	1.09
B4NP2C	4182	4776	1.14	4404	1.05	5017	1.20	13.6	11.5	0.85	11.5	0.85
C4MP2C	5434	5869	1.08	5364	0.99	6107	1.12	8.8	8.8	1.00	8.8	1.00
C2NP2C	4034	4278	1.06	3663	0.91	4899	1.21	8.1	6.5	0.80	6.5	0.80
C2N1P2C	4502	4816	1.07	4080	0.91	5316	1.18	11	7.8	0.71	7.8	0.71
C2N1P4C	5459	5856	1.07	5310	0.97	6546	1.20	17.5	13	0.74	13	0.74
C2MP2C	5689	6308	1.11	5496	0.97	6732	1.18	10.4	8.5	0.82	8.5	0.82
C2MP4C	7062	7770	1.10	7208	1.02	8444	1.20	15.9	13.8	0.87	13.8	0.87
S2F1	1255	1354	1.08	767.9	0.61	1819	1.45	39	33.3	0.85	33.3	0.85
S2F2	1590	1558	0.98	1045	0.66	2096	1.32	36	45.3	1.26	45.3	1.26
S2F3	1873	1627	0.87	1194	0.64	2245	1.20	34	44.6	1.31	44.6	1.31
S2F4	2015	1741	0.86	1351	0.67	2402	1.19	38	50.6	1.33	50.6	1.33
S2F5	2651	1793	0.68	1446	0.55	2497	0.94	43	50	1.16	50	1.16
S4F1	1025	1053	1.03	718.9	0.70	1201	1.17	19	23.3	1.23	23.3	1.23
S4F2	1343	1265	0.94	979.5	0.73	1462	1.09	23	34	1.48	34	1.48
S4F3	1572	1384	0.88	1144	0.73	1627	1.03	29	37.3	1.29	37.3	1.29
S4F4	1820	1561	0.86	1342	0.74	1825	1.00	30	49	1.63	49	1.63
S4F5	2209	1661	0.75	1473	0.67	1956	0.89	36	54	1.50	54	1.50
S6F1	901.2	887.7	0.99	678.6	0.75	973	1.08	17	16	0.94	16	0.94
S6F2	1202	1216	1.01	1016	0.85	1310	1.09	25	40	1.60	40	1.60
S6F4	1696	1432	0.84	1292	0.76	1586	0.94	34	42	1.24	42	1.24
S6F5	1767	1483	0.84	1364	0.77	1658	0.94	36	39.3	1.09	39.3	1.09
U25-2	2950	3340	1.15	3180	1.08	3451	1.17	10	9	0.90	9	0.90
U40-4	4650	4950	1.08	4783	1.03	5063	1.09	5.9	5	0.85	5	0.85
C1H2L1M	3726	3666	0.98	3329	0.89	3810	1.02	23.1	19.5	0.84	19.5	0.84
C1H2L2M	4807	4663	0.97	4457	0.93	4938	1.03	32.9	29.8	0.91	29.8	0.91
C1H1L1M	3338	3497	1.05	3348	1.00	3554	1.06	18.3	20	1.09	20	1.09
C1H1L1C	3445	3503	1.02	3358	0.97	3558	1.03	19.6	20.3	1.04	20.3	1.04
C2H2L1M	1837	1810	0.99	1705	0.93	1883	1.02	25.3	21.2	0.84	21.2	0.84
C2H2L1C	1992	1873	0.94	1775	0.89	1953	0.98	28	25.2	0.90	25.2	0.90
#28	7329	6736	0.92	6070	0.83	6532	0.89	18.8	15.5	0.82	15.5	0.82
#15	6020	6238	1.04	5276	0.88	5738	0.95	16.7	15	0.90	15	0.90
C2S25	2097	2102	1.00	1795	0.86	2473	1.18	19.2	21.1	1.10	21.1	1.10
C2S50	1855	1873	1.01	1693	0.91	2004	1.08	15.8	16.5	1.04	16.5	1.04
C1S25	1692	1836	1.09	1409	0.83	2087	1.23	16.5	15.6	0.95	15.6	0.95
C1S50	1482	1531	1.03	1344	0.91	1655	1.12	11.6	18.9	1.63	18.9	1.63
		Mean	1.00	**Mean**	0.88	**Mean**	1.10		**Mean**	1.07	**Mean**	1.07
		COV	0.10	**COV**	0.15	**COV**	0.10		**COV**	0.23	**COV**	0.23
		Min	0.68	**Min**	0.55	**Min**	0.89		**Min**	0.71	**Min**	0.71
		Max	1.15	**Max**	1.08	**Max**	1.45		**Max**	1.63	**Max**	1.63

It is observed that, in average, the mSM model provides excellent estimates of the columns'

maximum axial load capacity, with $\mu = 1.00$ and (i.e., in average the model predicts exactly the columns' axial strength) and $\text{COV} = 0.10$, which indicates a small dispersion of the results. The minimum and maximum values of the numerical to experimental axial strength are 0.68 and 1.15, respectively, which indicate that the mSM model can sometimes significantly underestimate the axial strength of the FRP-confined columns. The SM model produces less accurate and slightly more disperse results than the mSM model, with $\mu = 0.88$ and $\text{COV} = 0.15$. In particular, the SM model tends to underestimate the axial load capacity of the specimens, which is consistent with the fact that it neglects the effects of steel confinement. This result is also confirmed by the minimum and maximum values of the numerical to experimental axial strength obtained using the SM model, which are 0.55 and 1.08, respectively. Conversely, both models provide practically identical estimates of the strain at peak strength, which slightly overestimate the experimental results ($\mu = 1.07$ for both models) and present a significantly larger dispersion of the results when compared to the axial strength estimates ($\text{COV} = 0.23$). This result was also expected, because the numerical prediction of the strain at peak strength is inherently more complex and more affected by uncertainties than the numerical prediction of the peak axial strength (e.g., due to uncertainties/potential inaccuracies in the experimental measurements and the lack of accurate measurements of modeling parameters that affect the numerical prediction of the strains). The results obtained considering a linear superposition of the effects of FRP and steel confinement tend to overestimate the columns' axial load capacity by approximately 10% in average ($\mu = 1.10$), with a dispersion that is similar to that observed for the mSM results (COV = 0.10). This observation implies that using Eq. (2-10) to estimate the steel confinement effect of FRP-confined RC columns subject to concentric axial loads overestimates this effect by a factor approximately equal to 2. The reasons for this overestimation are that: (1) the maximum capacity corresponding to each confining

mechanism is achieved at different levels of strains, and (2) the linear combination of the FRP and steel confinement effects does not provide a realistic description of the highly nonlinear behavior of the confined RC columns, particularly near the peak strength region.

Figure 2-5 plots the experimental and numerical axial force-axial strain responses for two select columns, i.e., specimens DB450-C (Parretti and Nanni 2002) and S2F1 (Lee et al. 2010), for which the coefficients c_f assume the values 45.7% (i.e., close to the average value for the specimens considered here) and 193.6% (i.e., the largest value in the considered database), respectively. In both cases, it is observed that the mSM model, which explicitly accounts for the simultaneous confinement of steel and FRP on the core concrete, shows a better agreement with the experimental results than the SM model not only in terms of the peak strength of the column, but also for the entire axial force-axial strain response curve up to and beyond the failure of the FRP confinement. As expected, the improvement in the experimental results' prediction from the SM to the mSM model is more evident for increasing values of c_f.

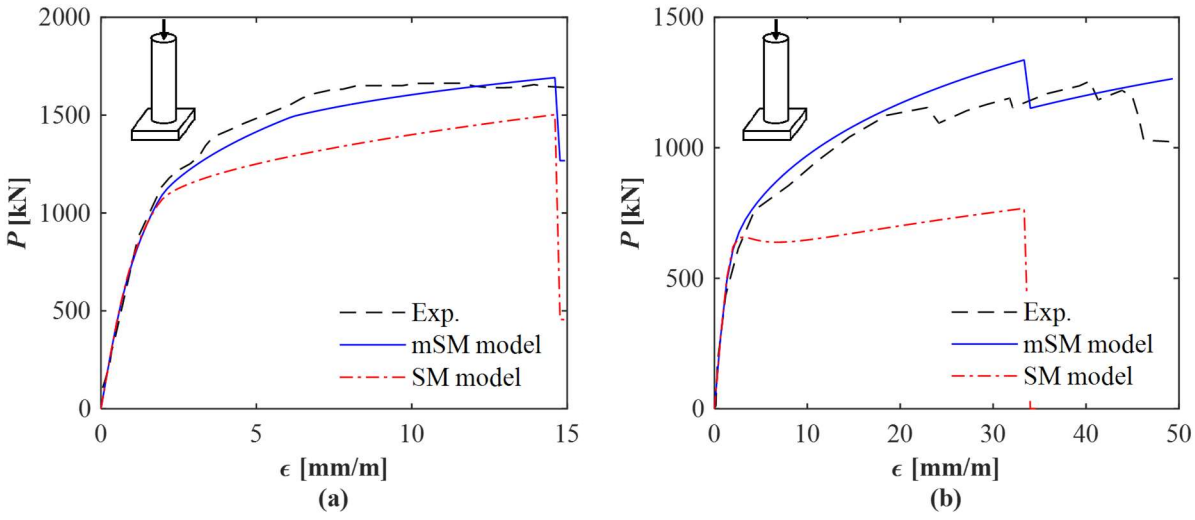

Figure 2-6. Comparison between the analytical concrete models and test results for specimens subject to concentric axial load: (a) DB450-C (Parretti and Nanni 2002), and (b) S2F1 (Lee et al. 2010)

2.5.2 Columns subject to eccentric axial load

A set of 22 specimens of RC columns subjected to monotonically increasing eccentric axial loads was collected from five different authors. In order to accurately account for second order effects produced by the eccentricity of the load, the FE analysis was performed considering the nonlinear geometry conditions based on a *P-Δ* formulation (Fenves and Filippou 2004). The description of these specimens is given in Table 2-3, whereas

Table 2-4 provides the comparison between experimental results and numerical estimates obtained using both SM and mSM models, including the means, COVs, minima, and maxima for each model. The experimental specimens include circular columns with cross-section diameters ranging between 150 mm and 205 mm; length between 500 mm and 1200 mm; concrete peak strength between 28 MPa and 75 MPa; transverse steel reinforcement ratio between 1.26% and 4.76%; and FRP volume ratio between 0.45% and 3.08%. The ratio between steel and FRP confinement forces, c_f, varies between 9.8% and 55.7%, with an average value of 15.3%. The last three listed specimens from Fitzwilliam and Bisby (2010) presented longitudinal FRP reinforcement in addition to FRP confinement and were modeled using the FE proposed in Barbato (2009). The specimens from Mostofinejad and Moshiri (2014) were wrapped with discontinuous rings of FRP sheets. The results presented in

Table 2-4 show that both SM and mSM models are able to predict accurately the load-carrying capacity of FRP-confined columns under a combination of a compressive axial load and the bending moment induced by load eccentricity, with a small improvement from a mean ratio of numerical to experimental strength equal to 0.97 for the mSM model and to 0.94 for the SM model. In addition, the COVs of the numerical to experimental strength ratio are also almost the same for the two models, i.e., 0.08 and 0.09 for the mSM and SM models, respectively. Thus, the differences

between the two models for this loading case are significantly smaller than the differences observed for the concentric axial load case. This results can be explained as follows: (1) the experimental database of specimens subject to eccentric axial loads contains specimens with significantly smaller amounts of transverse steel than the database available for specimens subject to concentric axial loads, as demonstrated by the smaller average value of c_f (i.e., 15.3% for the case of eccentric axial loads, compared to 42.2% for the case of concentric axial loads); (2) the presence of a bending moment induced by the eccentricity of the load produces a non-uniform compression or even some tension within the specimen's cross-section, which reduces the effectiveness of the passive confining mechanism of both steel and FRP.

Table 2-3. Experimental test database for FPR-confined RC column subjected to eccentric axial loading: specimens' identification, geometry, and material properties

Ref.	ID	d (mm)	L (mm)	f_c (MPa)	f_{yt} (MPa)	f_y (MPa)	ρ_s (%)	ρ_f (%)	E_f (GPa)	σ_f (MPa)	c_f (%)
Hadi (2006)	C2	150	620	32	500	500	4.76	2.67	25	700	55.7
Hadi (2009)	CF-25	205	925	49.9	437	640	3.17	3.08	45.8	884.6	28.9
	CF-50	205	925	49.9	437	640	3.17	3.08	45.8	884.6	28.9
Bisby and Ranger (2010)	C-5	152	608	33.2	710	710	1.26	1.00	90	894	13.2
	C-10	152	608	33.2	710	710	1.26	1.00	90	894	13.2
	C-20	152	608	33.2	710	710	1.26	1.00	90	894	13.2
	C-30	152	608	33.2	710	710	1.26	1.00	90	894	13.2
	C-40	152	608	33.2	710	710	1.26	1.00	90	894	13.2
Fitzwilliam and Bisby (2010)	300C10A	152	300	30.5	693	710	1.26	1.00	88.2	1014	11.5
	300C10B	152	300	30.5	693	710	1.26	1.00	88.2	1014	11.5
	300C20B	152	300	30.5	693	710	1.26	1.00	88.2	1014	11.5
	600C10A	152	600	30.5	693	710	1.26	1.00	88.2	1014	11.5
	900C10A	152	900	30.5	693	710	1.26	1.00	88.2	1014	11.5
	1200C10A	152	1200	30.5	693	710	1.26	1.00	88.2	1014	11.5
	1200C10B	152	1200	30.5	693	710	1.26	1.00	88.2	1014	11.5
	1200C20A	152	1200	30.5	693	710	1.26	1.00	88.2	1014	11.5
	300C12A	152	300	30.5	693	710	1.26	1.00	88.2	1014	11.5
	1200C12A	152	1200	30.5	693	710	1.26	1.00	88.2	1014	11.5
	1200C14A	152	1200	30.5	693	710	1.26	1.00	88.2	1014	11.5
	IW-30	150	500	28	502	502	2.15	0.45	230	3900	9.8
	IW-60	150	500	28	502	502	2.15	0.45	230	3900	9.8

Mostofinejad and Moshiri (2014)	IW-90	150	500	28	502	502	2.15	0.45	230	3900	9.8

Table 2-4. Comparison between experimental results and numerical simulation with both models of load-carrying capacity of RC column specimens subjected to eccentric axial loading

ID	Maximum axial load (kN)				
	Exp.	mSM model	Ratio	SM model	Ratio
C2	409	404	0.99	373	0.91
CF-25	2345	2377	1.01	2215	0.94
CF-50	1372	1438	1.05	1387	1.01
C-5	770	828	1.08	795	1.03
C-10	664	708	1.07	691	1.04
C-20	579	575	0.99	557	0.96
C-30	337	361	1.07	360	1.07
C-40	264	246	0.93	246	0.93
300C10A	672	604	0.90	587	0.87
300C10B	683	640	0.94	620	0.91
300C20B	911	912	1.00	902	0.99
600C10A	561	498	0.89	490	0.87
900C10A	549	522	0.95	507	0.92
1200C10A	449	455	1.01	447	1.00
1200C10B	480	449	0.94	444	0.93
1200C20A	537	494	0.92	482	0.90
300C12A	681	622	0.91	604	0.89
1200C12A	582	501	0.86	481	0.83
1200C14A	671	529	0.79	479	0.71
IW-30	544	602	1.11	592	1.09
IW-60	279	269	0.96	265	0.95
IW-90	168	154	0.92	152	0.91
		Mean	0.97	**Mean**	0.94
		COV	0.08	**COV**	0.09
		Min	0.79	**Min**	0.71
		Max	1.11	**Max**	1.09

Figure 2-6 compares the experimental and numerical response (i.e., axial force versus displacement at mid-height) using both mSM and SM concrete constitutive models for specimens 900C10A (Fitzwilliam and Bisby 2010) and C2 (Hadi 2006), for which the coefficients c_f assume

the values 11.5% (i.e., close to the average value for the specimens considered here) and 55.7% (i.e., the largest value in the considered database), respectively. It is observed that: (1) for specimen 900C10A (c_f = 11.5%), the two concrete constitutive models provide almost the same results in terms of peak axial strength and ultimate displacement at mid-height; (2) for specimen C2 (c_f = 55.7%), the mSM model provides significantly improved estimates of the peak strength and of the displacement at failure when compared to the corresponding results obtained using the SM model. This result indicates that the internal steel's confinement can significantly affect the response of FRP-confined columns subject to eccentric axial loads when the amount of transverse steel reinforcement is sufficiently large relatively to the amount of FRP, as measured by the coefficient c_f. It is also observed that, for both specimens, the axial load-mid-height displacement responses obtained using the FE models present non-negligible differences with the experimental results. These differences may be due to: (1) the complexity of the experimental set-up for these eccentric axial load tests, which may affect the accuracy of the experimental displacement results; (2) the approximations of the *P-Δ* formulation, which considers only some of the nonlinear geometry effects that are affecting the response of these specimens; and (3) the presence of complex three-dimensional nonlinear behavior in the concrete, e.g., triaxial stress conditions and concrete dilation (Kabir and Shafei 2012; Cao et al. 2018), that cannot be accurately represented by a simplified fiber-section frame model.

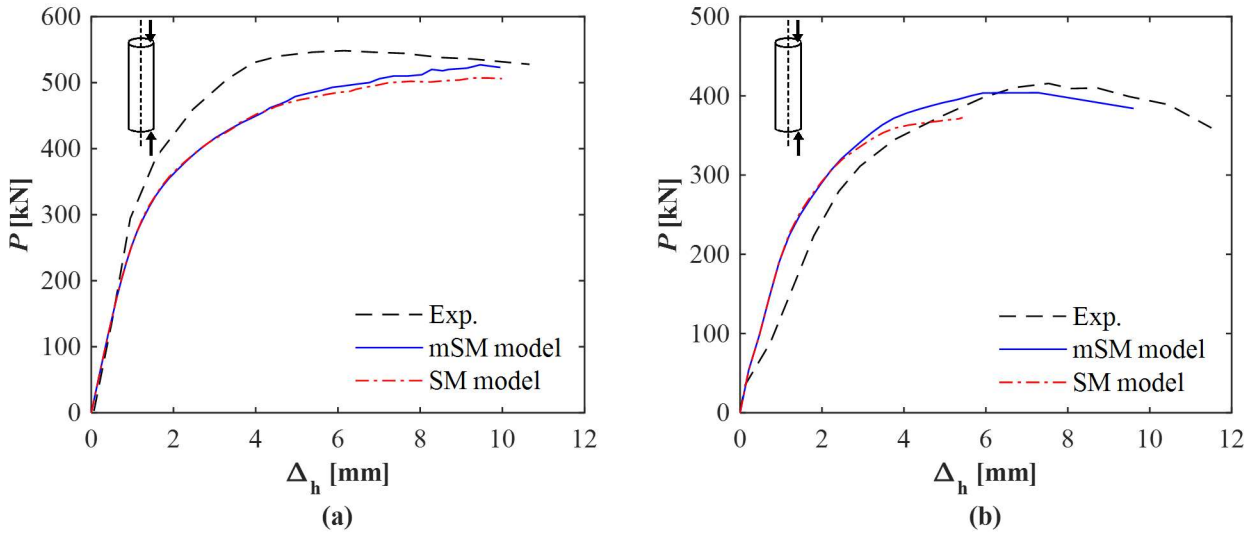

Figure 2-7. Comparison between the analytical concrete models and test results for specimens subject to eccentric axial load: (a) 900C10A (Fitzwilliam and Bisby 2010), and (b) C2 (Hadi 2006)

2.5.3 Columns subject to axial and lateral loads

A set of 18 FRP-confined RC columns subjected to a constant axial load, P_a, and a cyclic lateral displacement was selected from seven different published works. These specimens are described in Table 2-5. The considered specimens consist of columns with cross-section diameters varying between 300 mm and 760 mm, lengths between 850 mm and 2000 mm, concrete peak strength between 18.6 MPa and 40.8 MPa, transverse steel reinforcement ratio between 0.13% and 2.22%, FRP volume ratio between 0.11% and 4.06%, and ratio between axial load and cross-section capacity (i.e., P_a/P_o, where P_o corresponds to the concrete strength f_c times the gross area A_g) between 5% and 64%. The coefficient c_f varies between 5.7% and 47.3%, with an average value of 13.2%. The efficiency factors for the FRP rupture strain were taken from the experimental data (when available) or estimated according to Lam and Teng (2004) (when not reported in the experimental investigations).

Table 2-6 reports the comparison of the experimental results with the numerical estimates of the maximum lateral load-carrying capacity and of the ductility obtained using both mSM and SM models. The ductility is measured here by the ductility parameter $\mu_{\Delta} = \Delta_2 / \Delta_{yI}$ (displacement ductility) or $\mu_{\varphi} = \varphi_2 / \varphi_{yI}$ (curvature ductility) (Paultre et al. 2015), which are obtained using an idealized bilinear load-displacement diagram (Sheikh and Khoury 1993). In this study, Δ_2 and φ_2 are conventionally defined as the displacement and curvature, respectively, where the specimens reach the 80% of the maximum lateral capacity in the post-peak response; and Δ_{yI} and φ_{yI} denote the conventional yield displacement and curvature, respectively, corresponding to the intersection between the peak strength's horizontal line and the secant line of the lateral load-lateral displacement/curvature curve passing through the origin and 75% of the peak strength. The usage of the displacement or curvature ductility for different specimens was dictated by the manner in which the experimental data were presented in each publication considered in the experimental database.

Table 2-5. Experimental test database for FPR-confined RC column subjected to axial and lateral loads: specimens' identification, geometry, and material properties

Ref.	ID	d (mm)	L (mm)	f_c (MPa)	P_a/P_o	f_{yt} (MPa)	f_y (MPa)	d_b (mm)	ρ_s (%)	ρ_f (%)	E_f (GPa)	σ_f (MPa)	ξ_f	c_f (%)
Kawashima et al. (2000)	A2	400	1350	30	0.05	296	296	16	0.23	0.11	243	4277	0.64*	6.1
Li and Sung (2004)	FCS-2	760	1750	18.6	0.11	426	426	19.6	0.13	0.14	232	4170	0.64*	6.7
Paultre et al. (2015)	S75P10C1	305	2000	36	0.09	470	415	19.6	2.13	1.32	70.6	849	0.91	47.3
	S150P10C1	305	2000	33.6	0.35	470	415	19.6	1.07	1.32	70.6	849	0.64	16.2
	S75P35C1	305	2000	33.6	0.1	470	415	19.6	2.13	1.32	70.6	849	0.91	47.3
	S150P35C1	305	2000	34.6	0.32	470	415	19.6	1.07	1.32	70.6	849	0.76	16.2
Desprez et al. (2013)	P1C	300	2000	35.8	0.1	470	415	19.5	2.22	4.06	70.6	849	0.61	16.6
	P2C	300	2000	34.9	0.35	470	415	19.5	2.22	4.06	70.6	849	0.61	16.6
	P3C	300	2000	34.4	0.1	470	415	19.5	1.11	4.06	70.6	849	0.61	5.7
	P4C	300	2000	34.3	0.35	470	415	19.5	1.11	4.06	70.6	849	0.61	5.7
Gu et al. (2010)	J1	300	850	28	0.05	350	400	19	0.33	0.34	60	1832	0.52	6.6
	J2	300	850	28	0.05	350	400	19	0.33	0.15	230	4232	0.43	6.6
Sheikh and Yau (2002)	ST-2NT	356	1473	40.4	0.64	450	450	25	0.3	1.4	20	400	0.74*	5.8
	ST-4NT	356	1473	44.8	0.32	450	450	25	0.3	0.56	75	900	0.64*	6.4
	ST-5NT	356	1473	40.8	0.32	450	450	25	0.3	1.4	20	400	0.74*	5.8
Liu and Sheikh (2013)	P271CF3	356	1473	40	0.32	490	496	25	0.3	1.12	76.4	939	0.83	6.2
	P401CF8	356	1473	40	0.47	490	496	25	0.3	1.12	76.4	939	0.91	6.2
	P401GF9	356	1473	40	0.47	490	496	25	0.3	1.4	25.5	518	0.82	9.0

Note: * efficiency factor estimated based on Lam and Teng (2004)

Table 2-6. Comparison between experimental results and numerical simulation with both models of load-carrying capacity of RC column specimens subjected to axial and lateral loads

ID	Maximum lateral load (kN)					Ductility (-)				
	Exp.	mSM model	Ratio	SM model	Ratio	Exp.	mSM model	Ratio	SM model	Ratio
A2	108.5	110.8	1.02	110.0	0.99	10.8*	13.3	1.05	12.4	0.99
FCS-2	878.5	835.7	0.95	828.9	0.94	8.8*	8.8	1.00	8.8	1.00
S75P10C1	64.0	59.8	0.93	57.0	0.89	14.4*	14.4	1.00	12.4	0.86
S150P10C1	65.8	55.9	0.85	55.5	0.84	10.9*	10.9	1.00	10.9	1.00
S75P35C1	91.5	76.9	0.84	74.9	0.82	9.5*	11.3	1.19	5.1	0.54
S150P35C1	86.0	76.2	0.89	75.3	0.88	8.5*	10.7	1.12	6.6	0.69
P1C	65.0	61.9	0.95	60.1	0.92	12.2*	12.2	1.00	7.4	0.61
P2C	90.9	83.8	0.92	82.7	0.91	8.3*	10.6	1.08	3.4	0.35
P3C	66.2	62.3	0.94	62.0	0.94	10.6*	10.6	1.00	7.2	0.68
P4C	85.5	80.4	0.94	79.5	0.93	10.1*	8.2	0.81	4.4	0.43
J1	179.2	177.1	0.99	175.4	0.98	9.7*	11.2	1.16	11.2	1.16
J2	192.3	172.2	0.90	171.5	0.89	7.5*	9.5	1.15	9.5	1.15
ST-2NT	131.0	142.3	1.09	139.0	0.98	12.7**	13.9	1.09	12.9	1.01
ST-4NT	131.6	143.9	1.09	142.1	0.99	13.3**	10.4	0.78	9.5	0.71
ST-5NT	124.8	144.3	1.16	141.3	0.98	16.2**	14.3	0.88	13.3	0.82
P271CF3	118.6	125.7	1.06	125.1	1.05	14.6**	12.8	0.88	12.1	0.83
P401CF8	98.7	108.6	1.10	107.6	1.09	17.3**	15.5	0.90	14.9	0.86
P401GF9	115.5	97.3	0.84	94.0	0.81	12.3**	13.7	1.11	12.7	1.03
		Mean	0.97	**Mean**	0.95		**Mean**	1.01	**Mean**	0.82
		COV	0.10	**COV**	0.10		**COV**	0.12	**COV**	0.29
		Min	0.84	**Min**	0.81		**Min**	0.78	**Min**	0.35
		Max	1.16	**Max**	1.13		**Max**	1.19	**Max**	1.16

Note: * displacement ductility; ** curvature ductility

It is observed that, also for this load case, both mSM and SM models provide very good estimates of the peak lateral load, with a mean equal to 0.97 for the mSM model and to 0.95 for the SM model. The corresponding dispersions are also very similar, i.e., COV = 0.10 for both mSM and SM models. This result is consistent with that obtained for the eccentric axial load case and can be explained in the same way (i.e., small values of c_f and smaller effectiveness of the confinement effect when the columns' cross-sections are not subjected to uniform compression). Due to the

limited experimental database available, further investigations will be needed to determine the actual significance of the simultaneous confinement by steel and FRP on the lateral capacity of FRP-confined RC columns.

With respect to the ductility predictions, the mSM model provides results that are in excellent agreement with the experimental results (with $\mu = 1.01$ and COV = 0.12), whereas the SM model tends to underestimate the experimental results and produce a greater dispersion of the ductility estimates (with $\mu = 0.82$ and COV = 0.29). This result seems to indicate that considering the simultaneous confinement of steel and FRP on the core fibers of FRP-confined RC columns could be important for the prediction of their ductility capacity, even if this simultaneous confinement has small or negligible effects on the lateral load capacity. However, additional studies and experimental data are necessary to confirm this preliminary observation, because it is based on a very limited experimental database.

Figure 2-7 and Figure 2-8 compare the experimental and numerical cyclic lateral load-lateral displacement response for two select columns, i.e., specimens P1C (Desprez et al. 2013) and S75P10C1 (Paultre et al. 2015), respectively, for which the coefficients c_f assume the values 16.6% (i.e., close to the average value for the specimens considered here) and 47.3% (i.e., the largest value in the considered database). The results for both specimens indicate that both the mSM and SM models are able to predict the overall cyclic behavior and the lateral load capacity of the specimens; however, the mSM model is also capable to simulate with accuracy the columns' ductile behavior after peak strength, whereas the SM model predicts a strength degradation that is faster than that observed in the experimental results. This result suggests that, for the range of c_f values in the available experimental database, the internal steel's confinement has only a negligible effect on the lateral load capacity, but a larger effect on the lateral ductility capacity of FRP-

confined RC columns subjected to a combined loading due to axial and lateral loads. It is pointed out that the columns were modeled considering a fixed base. The inclusion of a bond-slip model based on experimental data could improve the performance of the simulated results with respect to the pinching behavior of the hysteresis loops.

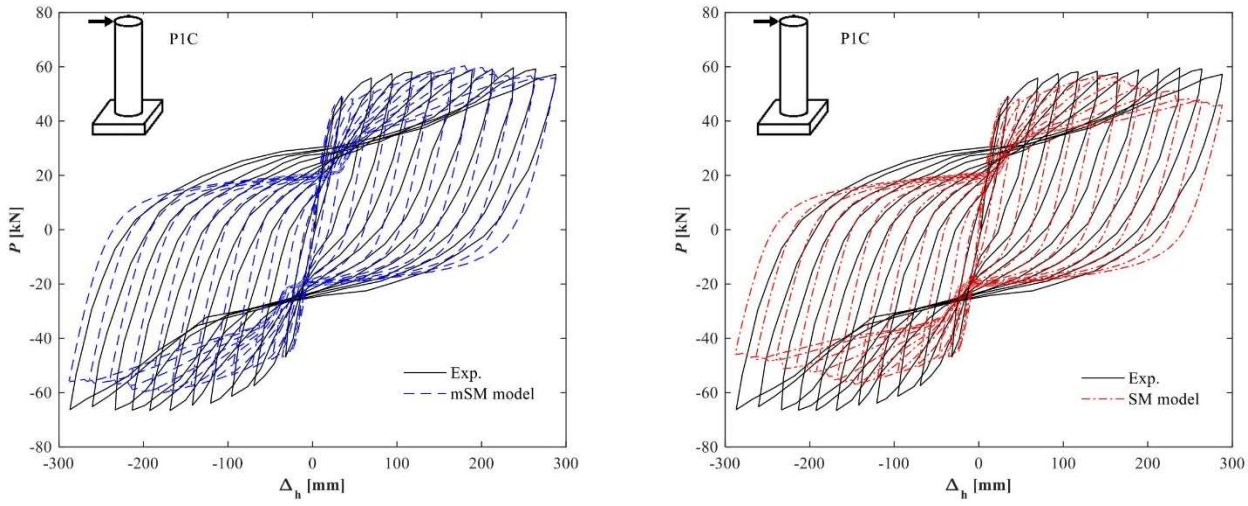

Figure 2-8. Comparison between the analytical concrete models and test results for specimen P1C subject to axial and cyclic lateral loads (Data from Desprez et al. 2013)

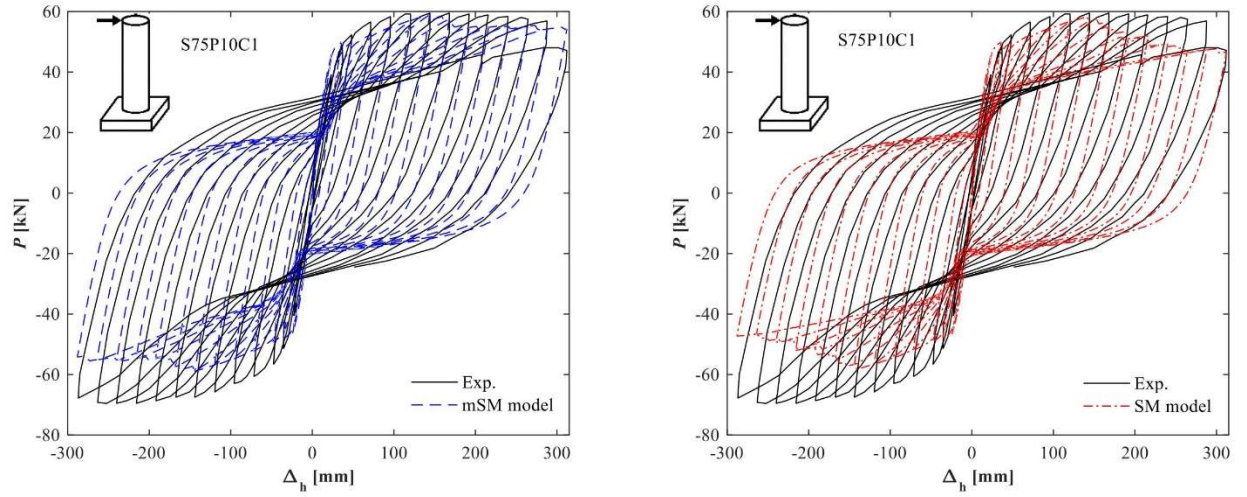

Figure 2-9. Comparison between the analytical concrete models and test results for specimen S75P10C1 subject to axial and cyclic lateral loads (Data from Paultre et al. 2015)

2.6 Conclusions

This paper proposes a new confined concrete material constitutive model that accounts for simultaneous confinement of steel and fiber reinforced polymers (FRP). The monotonic envelope of the newly proposed model, referred to as modified Spoelstra-Monti (mSM) model, is a modification of the monotonic envelope of the Spoelstra-Monti (SM) model for FRP-confined concrete. Simple hysteresis rules are also proposed to allow the use of the mSM model for cyclic and dynamic loading conditions. This new model is implemented into a research-oriented general-purpose finite element (FE) program and used in conjunction with a fiber-section force-based frame FE to analyze FRP-confined reinforced concrete columns for which experimental test results are available in the literature. The additional confining effect due to internal reinforcing steel is modeled through the use of the mSM model to characterize the stress-strain behavior of the core concrete's fibers. A new relative confinement coefficient c_f, defined as the ratio of the ultimate reinforcing steel's and FRP's confinement forces in a given cross-section, is proposed as a measure of the internal steel's confinement effects on the response behavior of the FRP-confined columns. Three loading conditions are considered: (1) concentric axial load, (2) eccentric axial load, and (3) a combination of axial load and applied lateral displacement. It is found that the use of the mSM model provides very good agreement with the experimental results, with estimates of the peak strength and axial/lateral deformations that are always more accurate than those obtained using the SM model (i.e., by neglecting the internal reinforcing steel's confinement effect). The internal steel's confinement effect on the peak strength of FRP-confined columns subject to concentric axial loads is significant, whereas the same effect is found to be negligible on the value of the strain at peak strength. The internal steel's confinement effect is found to be small but not negligible for the peak strength of FRP-confined columns subject to eccentric axial load. The same

effect appears to be even smaller for the lateral load capacity of FRP-confined columns subject to a combination of axial and lateral loads. However, this effect is larger and could be significant for the lateral ductility capacity of columns under axial and lateral loads. It is noted here that the observations made regarding columns subject to eccentric axial loads and to a combination of axial and lateral loads may require additional investigation to be fully confirmed, due to the limited size of the experimental database.

The steel-and-FRP confined concrete model developed in this paper is suitable for use in FE models in conjunction with fiber-section force-based frame FE and can be used for accurate and computationally-efficient FE analysis of real-world large-scale structures (e.g., buildings and bridges) with FRP-confined RC columns, for which more accurate three-dimensional FE models could be computationally prohibitive.

3 Investigation of the transverse steel effects on the axial compression strength of FRP-confined reinforced concrete columns based on a numerical parametric study

The proposed FRP-and-steel confined concrete model is employed in an extensive parametric study to quantify the contribution of the often-ignored steel confinement on the axial load-bearing capacity of FRP-strengthened RC columns. The impact of design limits on concrete deformation by design guidelines is also investigated. A new relative confinement coefficient C_s is proposed to describe the steel confinement effects in the structural behavior of FRP-confined RC columns considering design limitations on concrete deformation.

3.1 Introduction

Use of fiber-reinforced polymer (FRP) composites for retrofitting reinforced concrete (RC) structures has been extensively investigated throughout the last four decades (Fardis and Khalili 1982; Lam and Teng 2003a; Raza et al. 2019). The utilization of FRP has gained particular attention in recent years as a repair technology to aging RC structures that have their functionality affected by environmental deterioration, damage due to extreme events, or increased demands produced by unplanned loads (Parvin and Brighton 2014). In many cases, the retrofit of RC columns using external FRP jackets or wraps represents a reasonable and cost-effective alternative to steel jackets or enlarged RC cross-sections (Fardis and Khalili 1982; Rocca 2007; Roy et al. 2010). Among the possible applications, FRP wraps can be used to increase the axial compression strength of RC members by producing a confinement effect (Nanni and Bradford 1995; Toutanji 1999; ACI 2017). Whereas RC members that are subject to axial compression only are quite rare in buildings and other structures, axial compression strength of FRP-confined columns has been widely investigated (Spoelstra and Monti 1999; Matthys et al. 2006; Rocca et al. 2006; Hu and Barbato 2014; Piscesa et al. 2018), is explicitly addressed in modern design codes and guidelines

(e.g., ACI 2017), and needs to be evaluated when constructing the axial force-bending moment interaction diagram for an RC column (Bank 2006). Axial rehabilitation of RC columns using FRP confinement is also common in practical applications (Parvin and Brighton 2014).

The design of RC columns using modern design standards generally requires a ductile behavior, which leads to relatively higher volumetric ratios of transverse steel reinforcement when compared to columns designed using older standards (Roy et al. 2010). However, the presence of transverse steel reinforcement is generally neglected in the retrofit and rehabilitation of RC columns using FRP wraps, e.g., when using the ACI 440.2R-17 (ACI 2017) guidelines. This situation is probably due to the fact that, whereas the behavior of concrete confined by FRP only is extensively studied and documented in the literature (Fardis and Khalili 1982; Mirmiran and Shahawy 1996; Karbhari and Gao 1997; Samaan et al. 1998; Spoelstra and Monti 1999; Toutanji 1999; Xiao and Wu 2000; Fam and Rizkalla 2001; Lam and Teng 2003a; b; Shao et al. 2006), only a few studies have investigated the simultaneous confining mechanisms of FRP and steel (Demers and Neale 1999; Eid et al. 2009; Wang et al. 2012). Moreover, most of the existing stress-strain models of FRP-and-steel confined concrete use a linear superposition of the confining effects of each material (Li et al. 2003; Ilki et al. 2008; Hu and Seracino 2014), and/or are based on regression analyses of limited data points (Lee et al. 2010), which may lead to inaccurate estimates of the axial strength of FRP-confined RC columns with parameters laying outside the models' calibration ranges. Teng et al. (2015) proposed a model that considers the peak strength of simultaneously confined concrete as a linear superposition of the global contributions from the unconfined concrete strength, FRP, and steel, with the latter being a nonlinear function of the FRP reinforcement ratio.

An FRP-and-steel confined concrete constitutive model based on an incremental procedure that efficiently accounts for the nonlinear interaction of FRP and steel confinement was recently

developed to model the stress-strain behavior of confined concrete within the cross-section of FRP-confined circular RC columns (Zignago et al. 2018). This model, used in conjunction with a force-based frame finite element (FE) with fiber-based cross-sections (Hu and Barbato 2014), was thoroughly validated and shown to produce accurate estimates of the structural response of FRP-confined circular RC columns subject to different loading conditions for any realistic combination of design parameters and material properties.

This paper investigates the effects of transverse steel confinement on the axial strength of FRP-confined circular RC columns through an extensive parametric study by using these efficient and accurate nonlinear FE and FRP-and-steel confined concrete models (Hu and Barbato 2014; Zignago et al. 2018). The paper considers wide but realistic ranges of the different design parameters to quantify their relative importance and suggest possible improvements of existing design guidelines. To the authors' knowledge, this is the first study to investigate systematically the issue of simultaneous confinement of RC columns by FRP and steel to understand its effects on the structural behavior of RC members retrofitted using FRP wrapping. This study also identifies easy-to-compute parameters that can synthetically describe the effects of transverse steel on the design strength of the structural members under consideration. The characterization of these parameters represents a preliminary but necessary step towards the improvement of existing design equations for FRP-confined RC columns subject to axial compression.

3.2 FE modeling of FRP-confined RC columns

This study estimates the axial strength of FRP-confined columns by using nonlinear FE analysis performed via the general-purpose software framework Open System for Earthquake Engineering Simulation (OpenSees) (Mazzoni et al. 2006). By assuming a concentric axial load condition applied to a short column, the axial strength of the column is calculated as the column sectional

capacity using a zero-length fiber-section element (Mazzoni et al. 2006). The material nonlinearity is modeled by associating to the different fibers in the cross-section the appropriate uniaxial stress-strain constitutive models for the corresponding material. Both concrete cover and core fibers within the cross-section are modeled using the FRP-and-steel confined concrete model developed by Zignago et al. (2018), which reduces to the Spoelstra-Monti model (Spoelstra and Monti 1999) for concrete fibers confined by FRP only (i.e., concrete cover confined by FRP), to the Mander model (Mander et al. 1988) for concrete fibers confined by steel only (i.e., core concrete when no FRP is applied), and to the Popovics-Saenz model (Popovics 1973; Balan et al. 1997) for unconfined concrete fibers (i.e., concrete cover when no FRP is applied). A clear concrete cover thickness t_c = 25 mm is assumed for all column models. The unconfined concrete initial tangent modulus, E_c, is calculated as a function of the unconfined concrete compressive peak strength, f_c', as (Mander 1983):

$$E_c = 5000\sqrt{f_c'} \text{ (MPa)} \tag{3-1}$$

The unconfined concrete strain at peak strength, ε_c', is calculated using the equation proposed by De Nicolo et al. (1994), which was obtained through regression analysis of experimental results from compressive tests of concrete cylinders collected from several different authors, as:

$$\varepsilon_c' = 0.00076 + \left[\left(0.626 f_c' - 4.33\right)\cdot 10^{-7}\right]^{0.5} \text{ (MPa)} \tag{3-2}$$

The maximum allowable strain of the concrete, $\varepsilon_{c,\max}$, is assumed equal to the value specified by ACI 440.2R-17 (ACI 2017) as:

$$\varepsilon_{c,\max} = \varepsilon_c' \cdot \left[1.5 + 12\kappa_b \cdot \frac{f_{lf}}{f_c'} \cdot \left(\frac{\varepsilon_{fe}}{\varepsilon_c'}\right)^{0.45}\right] \le 0.01 \tag{3-3}$$

where κ_b is the geometry efficiency factor and is equal to 1 for circular cross-sections; $\varepsilon_{fe} = \kappa_\varepsilon \varepsilon_{fu}$ denotes the effective strain of the FRP at failure, in which κ_ε is the FRP strain efficiency factor determined by using the model proposed by Realfonzo and Napoli (2011) as a function of concrete strength and FRP confining stiffness $K_f = 0.5\rho_f E_f$ (with ρ_f = FRP volumetric reinforcement ratio and E_f = FRP elastic modulus), and ε_{fu} denotes the ultimate strain of the FRP obtained from flat coupon tensile tests; and $f_{lf} = \kappa_\varepsilon f_{lfu}$ is the maximum confinement pressure exerted by the FRP, where f_{lfu} is the ultimate FRP lateral confining pressure. It is observed here that the FRP strain efficiency factor model proposed by Realfonzo and Napoli (2011) decreases linearly for increasing FRP confining stiffness K_f, which also implies that κ_ε increases for increasing column diameter, when everything else is being kept the same. The Menegotto-Pinto plasticity model (Menegotto and Pinto 1973), as modified by Filippou et al. (1983) to include isotropic hardening effects, is used to model the longitudinal steel rebars. The sectional analyses are performed by applying quasi-static, monotonically increasing, and concentric axial loads.

3.3 Parametric study

The parameters considered in this study are: (1) fiber type, i.e., carbon FRP (CFRP) or glass FRP (GFRP); (2) FRP volumetric reinforcement ratio, with six different levels for each type of fiber, i.e., ρ_f = 0%, 0.25%, 0.5%, 1%, 2%, and 3% for CFRP, and ρ_f = 0%, 0.5%, 1%, 2%, 4%, and 6% for GFRP; (3) column diameter, with four different diameters, i.e., D = 150 mm, 300 mm, 600 mm, and 1,200 mm; (4) concrete compressive strength, with four different strength levels, i.e., f'_c = 20 MPa, 30 MPa, 50 MPa, and 70 MPa; and (5) transverse steel volumetric reinforcement ratio, with six different levels, i.e., ρ_{st} = 0%, 0.5%, 1%, 2%, 3%, and 4%. The combination of the different values for all the parameters results in a total of 1,152 nonlinear FE analyses. Table 3-1

summarizes the parameters considered and their values, whereas Table 3-2 shows the material properties considered as constants and their values used in the FE simulations.

Table 3-1. Design parameters considered in the parametric study

Parameter	Values
Fiber type	Carbon (CFRP), Glass (GFRP)
CFRP ratio, ρ_f (%)	0, 0.25, 0.5, 1, 2, 3
GFRP ratio, ρ_f (%)	0, 0.5, 1, 2, 4, 6
Column diameter, D (mm)	150, 300, 600, 1200
Concrete strength, f_c' (MPa)	20, 30, 50, 70
Transverse steel ratio, ρ_{st} (%)	0, 0.5, 1, 2, 3, 4

Table 3-2. Material properties used in the FE simulations

Material	Properties	Value
Transverse steel	Yield strength, f_{yt} (MPa)	450
	Young's modulus, E_{st} (GPa)	200
Longitudinal steel	Strain hardening ratio, b (-)	0.005
	Yield strength, f_{yl} (MPa)	450
	Young's modulus, E_{sl} (GPa)	200
	Longitudinal steel ratio, ρ_{sl} (%)	1.0
CFRP	Tensile strength, f_{fu} (MPa)	1200
	Young's modulus, E_f (GPa)	100
GFRP	Tensile strength, f_{fu} (MPa)	600
	Young's modulus, E_f (GPa)	25

The ultimate tensile strength, f_{fu}, and modulus of elasticity, E_f, of the CFRP material are two and four times larger than those of the GFRP material, respectively, leading to an ultimate strain for the GFRP sheets twice as large as that for the CFRP sheets. The GFRP reinforcement ratios are selected to be twice those for CFRP to allow for an easier comparison of both FRP ultimate lateral confining pressure, f_{lfu}, and FRP confining stiffness, K_f, for the different fiber types. The

range of the transverse steel reinforcement ratio, ρ_{st}, is selected to be between 0%, i.e., no stirrups or ties, and 4%, which represents a practical upper limit for real-world applications, as it is a slightly higher value than that obtained from the shear strength caps given in Provision 11.4.3 of ACI 440.2R-17 (ACI 2017).

3.4 Parametric study results

The parametric study results are expressed here in terms of the peak axial strength, $\overline{P}_{\max}$ or $P_{\max}$, for the different columns. Hereinafter, quantities with a superposed bar represent strengths obtained by imposing the design limitation on concrete deformation given by Eq. (3-3); whereas the same symbol without the superposed bar indicates strengths obtained without imposing any limitation on the concrete deformation. In particular, the quantity $\overline{P}_{\max}$ is relevant when making design considerations, for which imposing a limitation on concrete crushing is a desirable feature; whereas the quantity $P_{\max}$ can better describe experimental testing results when specimens are loaded up to their complete failure. In order to separate the confinement effects due to steel only from the FRP confinement effects, two reference axial strengths are considered for each given column: (1) the peak axial strength of the reference unconfined column, P_0 (i.e., a column with the same properties as the given column but with $\rho_f = 0\%$ and $\rho_{st} = 0\%$); and (2) the peak axial strength of the reference FRP-only-confined column without transverse steel, $\overline{P}_{f0}$ and P_{f0} (i.e., i.e., a column with the same properties as the given column but with $\rho_{st} = 0\%$). It is noteworthy that, for the reference unconfined column, the peak axial strengths obtained by imposing or not imposing the concrete deformation limit given by Eq. (3-3) coincide (i.e., $P_0 = \overline{P}_0$), as the columns reach their peak axial strengths at a concrete strain $\varepsilon_c = \varepsilon'_c < \varepsilon_{c,\max}$. For easy comparison, all

strength results are presented hereinafter in non-dimensional form, as relative strength increments normalized by P_0.

3.4.1 Increment in peak axial strength due to simultaneous steel and FRP confinement

Figure 3-1(a) through (d) summarize the effects of FRP confining stiffness, column diameter, concrete compressive strength, and transverse steel ratio, respectively, on the peak axial strength's normalized total increment $\left(\overline{P}_{\max} - P_0\right)/P_0$. The results are presented in the form of box-and-whisker plots (Cleveland 1985) and exclude the data points for which $\rho_f = 0\%$ or $\rho_{st} = 0\%$. The central horizontal line of each plot represents the median value, with the bottom and top edges of the boxed area indicating the first and third quartile of the data, respectively. The whiskers identify the complete range of the data. The notches in the boxed area display the confidence interval around the median.

Figure 3-1(a) shows that $\left(\overline{P}_{\max} - P_0\right)/P_0$ significantly increases for increasing FRP confining stiffness, even though not monotonically. The median value of $\left(\overline{P}_{\max} - P_0\right)/P_0$ increases from approximately 29% for $K_f =$ 62.5 MPa to approximately 97% for $K_f =$ 1.5 GPa. More dispersion in the results is found for low FRP reinforcement ratios. This result was expected, as the beneficial effect of FRP-confinement on the concrete compressive strength is well-known (Fardis and Khalili 1982; Karbhari and Gao 1997). Figure 3-2 plots $\left(\overline{P}_{\max} - P_0\right)/P_0$ as a function of the ratio between the FRP confining pressure and the unconfined concrete strength, f_{lf} / f_c' (referred to as FRP confinement ratio hereinafter), which is known to be strongly positively correlated with the FRP-confined concrete peak strength, f_{cc}' (Fardis and Khalili 1982; Spoelstra and Monti 1999; Lam and Teng 2003a).

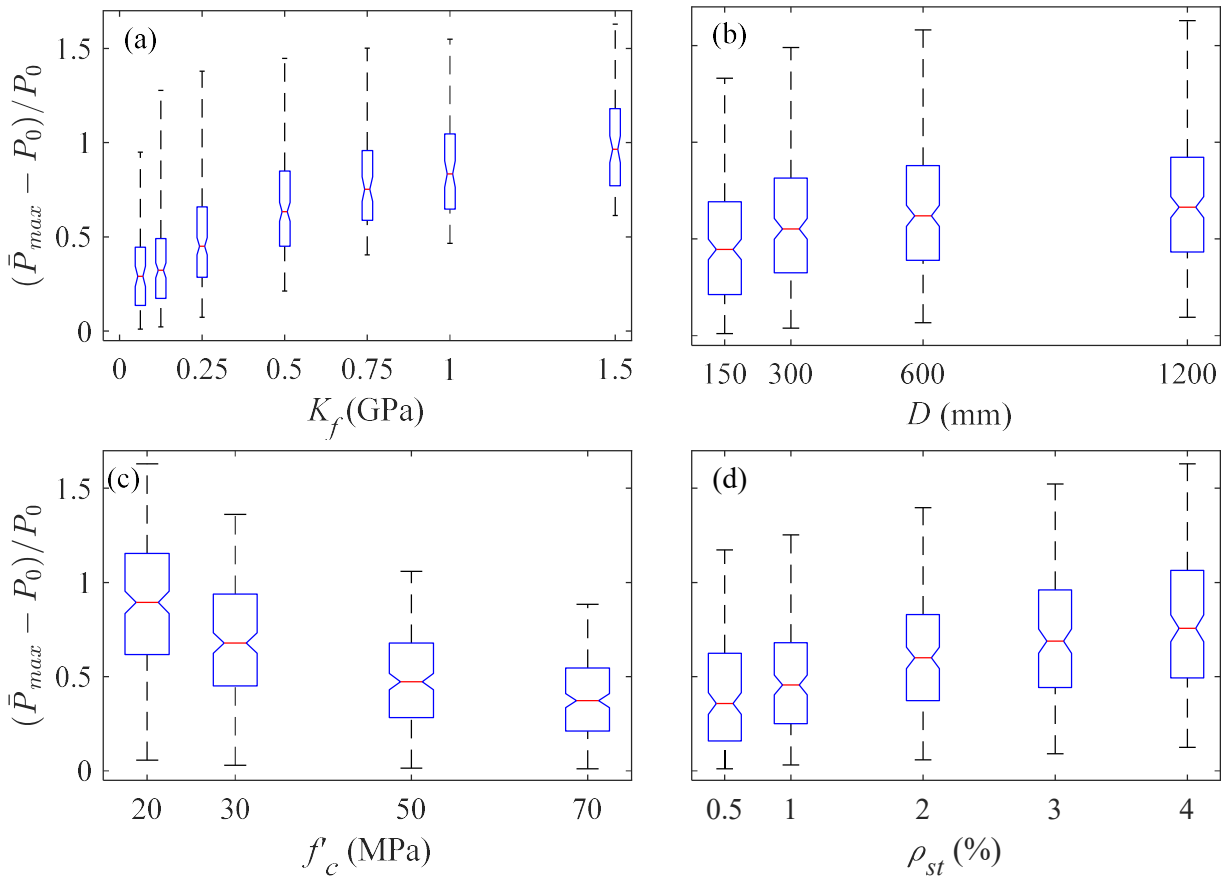

Figure 3-1. Box-and-whisker plots of the normalized total increment in peak axial strength, $\left(\bar{P}_{\max} - P_0\right)/P_0$, for variations of: (a) FRP confining stiffness; (b) diameter; (c) concrete strength; and (d) transverse steel ratio

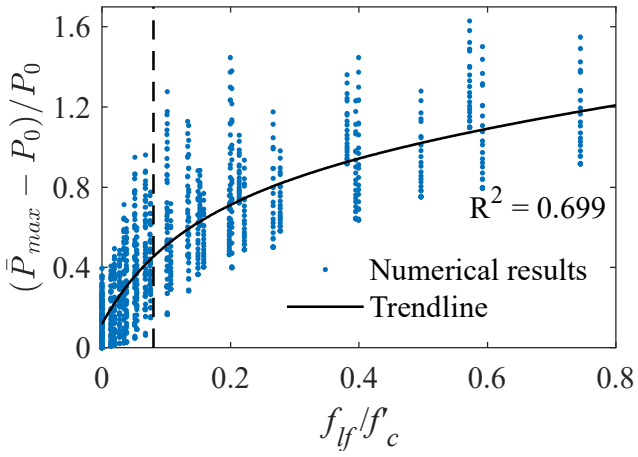

Figure 3-2. Effect of FRP confinement ratio on the normalized total increment in peak axial strength, $\left(\bar{P}_{\max} - P_0\right)/P_0$

Figure 3-2 also reports the trendline of the numerical simulation results in conjunction with its coefficient of determination, R^2 = 0.699. This trendline is computed based on a quadratic/linear rational function (i.e., a rational function in which numerator and denominator are polynomials of order 2 and 1, respectively). The vertical dashed line represents the value $f_{lf} / f_c' = 0.08$, which is the lower limit for FRP confinement recommended in ACI 440.2R-17 (ACI 2017). The relatively low value of the coefficient of determination indicates a large dispersion of the data points. Based on the trendline, it is observed that, for the lower values of the FRP confinement ratio (i.e., $f_{lf} / f_c' < 0.05$), $\left(\overline{P}_{\max} - P_0\right)/P_0$ increases almost proportionally with f_{lf} / f_c', whereas for the higher values of the FRP confinement ratio (i.e., $f_{lf} / f_c' > 0.10$), the increase of $\left(\overline{P}_{\max} - P_0\right)/P_0$ rapidly slows down, until only small increases are observed when $f_{lf} / f_c' > 0.30$. It is concluded that, for small amounts of FRP, $\overline{P}_{\max}$ is mainly controlled by the FRP confinement ratio; whereas, for large amounts of FRP (and in particular for $f_{lf} / f_c' \geq 0.08$), $\overline{P}_{\max}$ is mainly controlled by the FRP confining stiffness. It is also observed that the value of the trendline for $f_{lf} / f_c' = 0$ (i.e., no FRP confinement) is approximately equal to 12%, which provides an approximate measure of the average effect of the transverse steel confinement on the core concrete for the range of geometries and material parameters considered in this study.

Figure 3-1(b) shows that $\left(\overline{P}_{\max} - P_0\right)/P_0$ slightly increases as the column diameter increases. This effect is less significant than that of the FRP confining stiffness, but it is not negligible. In fact, the median value of $\left(\overline{P}_{\max} - P_0\right)/P_0$ increases from approximately 45% when D = 150 mm to approximately 66% for columns with D = 1200 mm. By contrast, the interquartile range is found to be almost independent of the diameter. The observed influence of the diameter on $\left(\overline{P}_{\max} - P_0\right)/P_0$

is attributed to the increase in the cross-sectional core to gross area ratio, A_c / A_g, for increasing column diameter, which is produced by the modeling choice of keeping the concrete cover's thickness as constant and equal to 25 mm for all column diameters. Because the concrete core is subjected to the combined confinement of both FRP and steel, whereas the concrete cover is subjected to the confinement of the FRP only, an increase of A_c / A_g is likely to produce an increase in the peak axial strength. To test this hypothesis, four additional numerical simulations were performed by setting $A_c / A_g = 0.840$ (i.e., the ratio corresponding to a column with D = 600 mm and t_c = 25 mm), considering the same four column diameters used in the parametric study (i.e., D = 150 mm with t_c = 6.25 mm, D = 300 mm with t_c = 12.5 mm, D = 600 mm with t_c = 25 mm, and D = 1200 mm with t_c = 50 mm), and assuming the following constant values for the other variables: concrete strength f'_c = 30 MPa, CFRP reinforcement ratio $\rho_f = 1\%$, and steel reinforcement ratio $\rho_{st} = 4\%$. The steel confinement effectiveness coefficient was also kept constant and equal to $k_s = 0.99$ (Mander et al. 1988). The four additional FE analyses produced the same value of $(\overline{P}_{\max} - P_0) / P_0 = 106.8\%$, which confirms that the gain in strength observed in Figure 3-1(b) is due to the increase of A_c / A_g.

Figure 3-1(c) shows that $\left(\overline{P}_{\max} - P_0\right)/P_0$ drastically decreases for increasing values of f'_c. This result is consistent with existing confined concrete models that describe the relative gain in strength of confined concrete, i.e., $(f'_{cc} - f'_c) / f'_c$, as inversely proportional (Richart et al. 1929; Lam and Teng 2003a) or approximately inversely proportional (Mander et al. 1988) to the unconfined concrete strength f'_c. Figure 3-1(c) also shows a larger scatter of the results for lower strength concretes, which present a larger interquartile range than higher strength concretes.

Figure 3-1(d) shows an approximately linear increase in the median of $\left(\overline{P}_{\max} - P_0\right)/P_0$ for increasing values of ρ_{st}. The interquartile range of these results is almost independent of the reinforcement level. This result was also expected, as the additional confinement effect due to the transverse steel generally increases the confined concrete's peak strength, f'_{cc} (Zignago et al. 2018).

The results presented in Figure 3-1, albeit expected, lead to the conclusion that both the transverse steel volumetric ratio, ρ_{st}, and the column diameter, *D*, have significant beneficial effects on the peak axial strength of FRP-confined columns. This conclusion is important because current design codes and guidelines generally neglect the effects of these two parameters on the prediction of the load-carrying capacity of FRP-confined RC columns (ACI 2017).

In order to investigate more in detail the effects of transverse steel confinement on the peak axial strength of FRP-confined columns, as well as the interaction among different parameters, Figure 3-3(a) plots $\left(\overline{P}_{\max} - P_0\right)/P_0$ versus ρ_{st} for columns strengthened with CFRP wraps and with f'_c = 30 MPa, when the amount of FRP and the column diameter are varied. The observed interaction among the different parameters is quite complex. FRP confinement contributes significantly to $\left(\overline{P}_{\max} - P_0\right)/P_0$, e.g., with a value of 91.7% for a CFRP ratio of ρ_f = 3.0% when ρ_{st} = 0, which increases to 134.4% when ρ_{st} = 4% and D = 1200 mm. This increment is independent of the column diameter when no transverse steel is present. The value of $\left(\overline{P}_{\max} - P_0\right)/P_0$ increases rapidly for lower values of ρ_f, up to ρ_f = 1%, whereas it increases in a decreasing fashion for higher values of ρ_f, indicating a diminishing effectiveness of the FRP confinement.

These results also confirm that steel confinement effect can be significant and that the increase in axial strength of the FRP-confined columns strongly depends on both the column diameter, *D*, and

the transverse steel reinforcement ratio, ρ_{st}. The increase in axial strength due to the steel confinement effect becomes more pronounced going from $\rho_f = 0\%$ with $\max\left[\left(\bar{P}_{\max} - P_0\right)/P_0\right] =$ 34.4%, to $\rho_f =$ 1.0% with $\max\left[\left(\bar{P}_{\max} - P_0\right)/P_0\right] =$ 68.3%, and then gradually decreases from $\rho_f =$ 1.0% to $\rho_f =$ 3.0% with $\max\left[\left(\bar{P}_{\max} - P_0\right)/P_0\right] =$ 44.4%. This result confirms the strong nonlinearity of the combination of FRP and steel confinement effects. It is noted here that similar behaviors were observed also for the other combinations of concrete strength and FRP materials considered in this study.

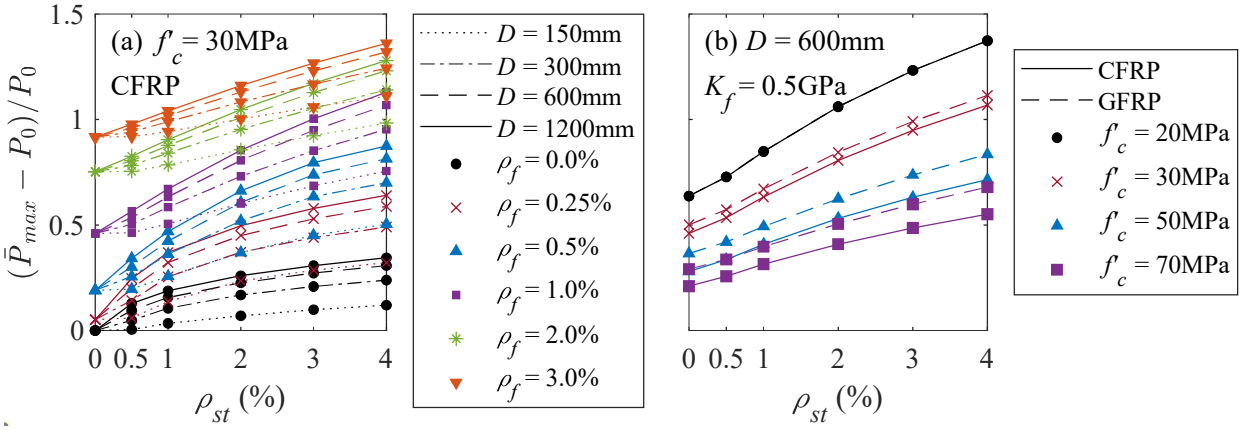

Figure 3-3. Transverse steel confinement effect on the normalized total increment in peak axial strength, $\left(\bar{P}_{\max} - P_0\right)/P_0$, for FRP-confined columns with: (a) f'_c = 30 MPa for varying amount of CFRP and column diameter, and (b) D = 600 mm and K_f = 0.5 GPa for varying FRP type and concrete strength

Figure 3-3(b) plots $\left(\bar{P}_{\max} - P_0\right)/P_0$ versus ρ_{st} for columns with diameter D = 600 mm and confining stiffness K_f = 0.5 GPa (which corresponds to ρ_f = 1% for CFRP or ρ_f = 4% for GFRP), when the FRP material and the concrete compressive strength are varied. The quantity $\left(\bar{P}_{\max} - P_0\right)/P_0$ always increases for increasing transverse steel ratio, and this increase is more pronounced as the concrete compressive strength decreases. In general, for a fixed value of FRP confining stiffness,

$\left(\overline{P}_{\max} - P_0\right)/P_0$ for a column strengthened with GFRP wraps is greater than or equal to that of a column with CFRP sheets. This difference is larger for higher concrete compressive strengths, and it gradually decreases with f_c', until no differences are observed between columns strengthened with GFRP and CFRP for f_c' = 20 MPa.

These results can be explained by considering the combination of two phenomena affecting the peak axial strength, $\overline{P}_{\max}$: (1) the limitation on the maximum concrete strain imposed by Eq. (3-3), which depends on f_{lf} / f_c' until $\varepsilon_{c,\max}$ reaches the value 0.01; and (2) the effects of the FRP and steel confinement, which depend on K_f/E_c and f_{ls} / f_c', respectively. To investigate more in depth these two phenomena, the FRP-and-steel confined concrete axial stress-strain behavior obtained using the model developed by Zignago et al. (2018) is plotted in Figure 3-4 for a concrete with f_c' = 30 MPa with four levels of FRP confining stiffness to concrete elastic modulus ratio (i.e., K_f/E_c = 0.0023, 0.0046, 0.0092, and 0.0274), and four levels of steel confinement ratio (i.e., f_{ls} / f_c' = 0, 0.05, 0.15, 0.25), for a total of 16 different FRP and transverse steel confinement configurations. These K_f/E_c levels correspond to GFRP reinforcement ratios ρ_f = 0.5%, 1%, 2%, and 6%, respectively, and to CFRP reinforcement ratios ρ_f = 0.125%, 0.25%, 0.5%, and 1.5%, respectively; whereas the considered f_{ls} / f_c' levels correspond to transverse steel ratios ρ_{st} = 0% (identified by thicker lines), 0.67%, 2.0%, and 3.33%, respectively, and a constant steel confinement effectiveness coefficient k_s = 1.00 (Mander et al. 1988). Figure 3-4 also provides: the axial strains at which the GFRP and CFRP wraps fail, $\varepsilon_{c,fu}$ (identified by filled markers); the maximum allowable concrete compressive strain based on Eq. (3-3), $\varepsilon_{c,\max}$, for each fiber type

(identified by unfilled markers); and the axial strains at which the transverse steel yields, $\varepsilon_{c,sy}$ (identified by crosses). It is important to note that, for given properties of the unconfined concrete and confining steel, the confined concrete axial stress-axial strain curve is fully determined by the values of K_f/E_c and f_{ls}/f_c', and that the only difference among various fiber materials is the axial strain at which the fibers fail, which is determined by their effective strain at failure, ε_{fe}.

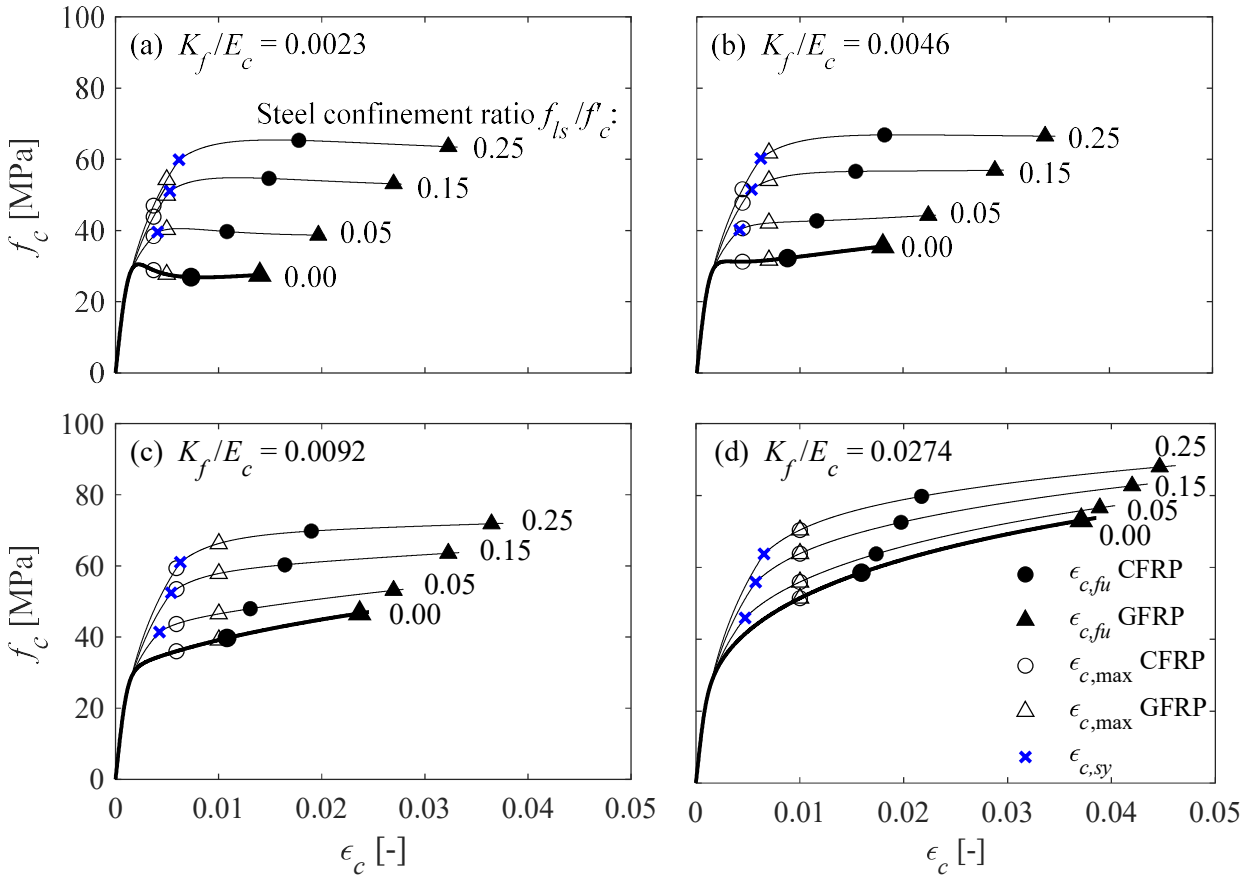

Figure 3-4. Stress-strain responses of confined concrete with f_c' = 30 MPa for different FRP and transverse steel confinement configurations

The FRP-confined concrete stress-strain curves in Figure 3-4 can be classified into three categories (Lam and Teng 2003a): type I curves, which correspond to low confinement levels and have post-peak decreasing branches with a concrete ultimate stress $f_{cu} < f_c'$, e.g., the thick curve reported in

Figure 3-4(a); type II curves, which correspond to moderate confinement levels and have post-peak branches with a softening or flat portion followed by a hardening portion with $f_{cu} > f_c'$, e.g., the thick curve reported in Figure 3-4(b); and type III curves, which correspond to high confinement levels and are monotonically increasing everywhere, e.g., the thick curves reported in Figure 3-4(c) and (d). The stress-strain behavior of concrete confined simultaneously by steel and FRP generally have the same characteristics of the stress-strain behavior of FRP-confined concrete. Therefore, it is concluded that the compressive strain at which an FRP-confined RC column reaches its peak strength corresponds to the maximum allowable compressive strain of the concrete, $\varepsilon_{c,\max}$, when the confinement effect is sufficient to achieve a type III curve; whereas it is contained between ε_c' and $\varepsilon_{c,\max}$ when the confinement effect is limited and the concrete stress-strain behavior correspond to a type I or type II curve.

From Figure 3-4, it is also observed that, as K_f/E_c increases, the $\varepsilon_{c,\max}$ increases faster for GFRP than for CFRP, until the $\varepsilon_{c,\max}$ for GFRP reaches the upper limit of 0.01, at which point only the $\varepsilon_{c,\max}$ for the CFRP keeps increasing until it also reaches the value of 0.01. This phenomenon contributes to the faster increase followed by a slower increase of $\left(\overline{P}_{\max} - P_0\right)/P_0$ for increasing ρ_f, which is observed in Figure 3-3(a). It also explains why, for a given f_c' and any level of ρ_{st}, the value of $\left(\overline{P}_{\max} - P_0\right)/P_0$ for GFRP confinement is higher than or equal to that for CFRP confinement, as observed in Figure 3-3(b). In particular, the equal peak axial strength of RC columns confined with GFRP and CFRP for f_c' = 20 MPa is due to the fact that, for the given level of FRP confining stiffness, the value of $\varepsilon_{c,\max}$ has already reached the upper limit of 0.01 for both fiber types, similar to the case shown in Figure 3-4(d). The differences in $\left(\overline{P}_{\max} - P_0\right)/P_0$ for the two types of fiber at

any given value of K_f is amplified for increasing values of f_c' because the FRP-confining stiffness ratio, K_f/E_c, decreases due to the proportionality between E_c and $\sqrt{f_c'}$ given by Eq. (3-1).

Figure 3-4 also shows that, for low levels of K_f/E_c (i.e., low values of $\varepsilon_{c,\max}$) and (in minor measure) of f_{ls}/f_c' (i.e., high values of $\varepsilon_{c,sy}$), yielding of the transverse steel can take place at strains larger than $\varepsilon_{c,\max}$ (i.e., $\varepsilon_{c,sy} > \varepsilon_{c,\max}$), thus preventing the transverse steel confining mechanism from being fully utilized. By contrast, when $\varepsilon_{c,sy} < \varepsilon_{c,\max}$, the transverse steel confining mechanism can fully develop. This phenomenon is the major contributor to the rapid increase in $\left(\overline{P}_{\max} - P_0\right)/P_0$ observed in Figure 3-3(a) for low values of ρ_f going from 0% to 1.0%, as the corresponding increase in K_f/E_c gradually allows full development of the transverse steel confining mechanism.

3.4.2 Effects of concrete strain design limit on column peak axial strength

Figure 3-5 shows the relative peak axial strength increment $\left(P_{\max} - \overline{P}_{\max}\right)/P_0$ obtained by removing the design limitation on concrete axial strain given by Eq. (3-3). In particular, Figure 3-5(a) plots $\left(P_{\max} - \overline{P}_{\max}\right)/P_0$ versus ρ_{st} for columns strengthened with CFRP wraps and with f_c' = 30 MPa, when the amount of FRP and the column diameter are varied; whereas Figure 3-5(b) plots $\left(P_{\max} - \overline{P}_{\max}\right)/P_0$ versus ρ_{st} for columns with diameter D = 600 mm and confining stiffness K_f = 0.5 GPa, when the FRP material and the concrete compressive strength are varied.

The results in Figure 3-5(a) show that the columns most impacted by the concrete strain limitation are those with low amounts or no FRP, large amounts of transverse steel, and large diameters. As the transverse steel ratio increases, the concrete core's peak strength increases; however, $\varepsilon_{c,\max}$ is

not affected by ρ_{st}, and the peak strength for steel-confined concrete and for concrete confined with large amounts of steel and small amounts of FRP is achieved only at axial strains that are often significantly larger than $\varepsilon_{c,\max}$. The quantity $\left(P_{\max}-\bar{P}_{\max}\right)/P_0$ can reach values as high as approximately 66% for columns with $D=1200$ mm and $\rho_{st}=4.0\%$ when no limitation is considered. It is observed that, for $\rho_f=0\%$ and 0.25%, the column diameter has a major effect on $\left(P_{\max}-\bar{P}_{\max}\right)/P_0$, with larger diameters corresponding to large values of $\left(P_{\max}-\bar{P}_{\max}\right)/P_0$ and smaller diameters corresponding to small values of $\left(P_{\max}-\bar{P}_{\max}\right)/P_0$ (almost negligible for $D=150$ mm). This phenomenon results from two effects: (1) the steel confinement effectiveness, k_s, decreases rapidly for decreasing column diameters and constant ρ_{st}; (2) the transverse steel confinement effect increases for increasing column diameters, as the ratio A_c/A_g also increases.

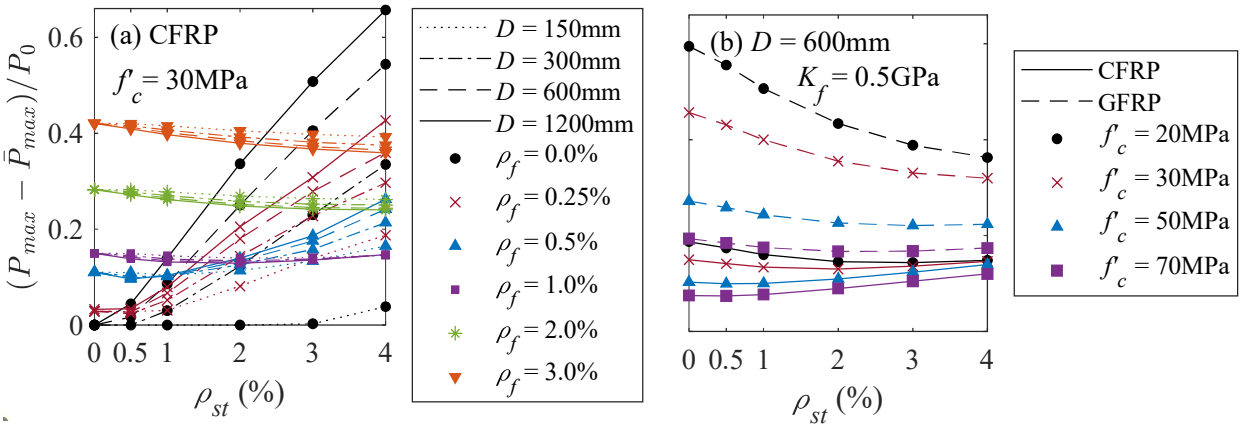

Figure 3-5. Effect of concrete strain design limitation provision on columns' peak axial strength: (a) for varying amount of FRP and column diameter, and (b) for varying FRP material and concrete compressive strength

$\left(P_{\max}-\bar{P}_{\max}\right)/P_0$ increases for increasing values of ρ_{st} and D for all columns with $\rho_f=0.0\%$ and 0.25%, and for columns with $\rho_f=0.5\%$ and $\rho_{st}\geq 2\%$. These cases correspond to columns in

which the transverse steel reaches yielding at strains larger than $\varepsilon_{c,\max}$, as shown in Figure 3-4(a) through (c). For $\rho_f = 0.5\%$, there is a change of behavior between the cases with $\rho_{st} < 2\%$ and $\rho_{st} \geq 2\%$: $\left(P_{\max} - \bar{P}_{\max}\right)/P_0$ decreases for ρ_{st} increasing from 0% to 1.0% and increasing column diameter, before increasing again for $\rho_{st} \geq 2\%$. For larger amounts of CFRP (i.e., $\rho_f \geq 1.0\%$), $\left(P_{\max} - \bar{P}_{\max}\right)/P_0$ always slightly decreases for increasing ρ_{st} and *D*. This phenomenon is the result of two contrasting effects: (1) $P_{\max}$ increases more than $\bar{P}_{\max}$ for increasing values of ρ_f as the confined concrete stress-strain curve moves from a type I or type II curve to a type III curve, and the axial strain corresponding to FRP failure, $\varepsilon_{c,fu}$, is significantly larger than $\varepsilon_{c,\max}$ (see Figure 3-4); and (2) as ρ_f increases, a larger portion of the transverse steel contribution to the peak axial strength takes place before the axial strain reaches $\varepsilon_{c,\max}$ (i.e., the transverse steel contribution to $\bar{P}_{\max}$ increases more than its contribution to $P_{\max}$).

The results in Figure 3-5(b) show that, for any value of f_c' and ρ_{st}, $\left(P_{\max} - \bar{P}_{\max}\right)/P_0$ is always higher for GFRP-confined columns than for CFRP-confined columns. This results is due to two superposing effects: (1) for a given K_f/E_c, $P_{\max}$ is higher for RC columns confined with GFRP than for those confined with CFRP because of the higher values of ε_{fe} and, thus, of $\varepsilon_{c,fu}$ for GFRP than for CFRP; and (2) the GFRP-confined concrete reaches the upper limit $\varepsilon_{c,\max} = 0.01$ at a lower value of f_{lf} / f_c' than CFRP-confined concrete, thus reaching a cap for $\bar{P}_{\max}$ at lower values of K_f/E_c. For example, assuming the average value $\kappa_\varepsilon = 0.65$ suggested by Realfonzo and Napoli (2011), $\varepsilon_{c,\max} = 0.01$ is reached at $f_{lf} / f_c' = 0.158$ for CFRP and at $f_{lf} / f_c' = 0.116$ for GFRP. It is also observed that, for GFRP, $\left(P_{\max} - \bar{P}_{\max}\right)/P_0$ decreases for increasing f_c' and ρ_{st}, with values

as high as approximately 60% for $f_c' = 20$ MPa and $\rho_{st} = 0\%$, and as low as 17% for $f_c' = 70$ MPa and $\rho_{st} = 4\%$; whereas for CFRP, the value of $\left(P_{\max} - \overline{P}_{\max}\right)/P_0$ presents only a small variability between 8% and 19% for all considered values of f_c' and ρ_{st}, without a monotonic trend with respect of these two variables.

3.4.3 Effects of transverse steel confinement on peak axial strength of FRP-confined columns

Figure 3-6(a) through (d) summarize the effects of FRP confining stiffness, column diameter, concrete compressive strength, and transverse steel ratio, respectively, on $\left(\overline{P}_{\max} - \overline{P}_{f0}\right)/P_0$. These results separate the transverse steel confinement effects on the peak axial strength of FRP-confined RC columns from the global effects due to the simultaneous FRP and steel confinement. Similar to Figure 3-1, these results are presented in the form of box-and-whisker plots (Cleveland 1985) and exclude the data points for which $\rho_f = 0\%$ or $\rho_{st} = 0\%$.

Figure 3-6(a) shows that $\left(\overline{P}_{\max} - \overline{P}_{f0}\right)/P_0$ decreases significantly for increasing values of K_f, with the median value going from approximately 27% for $K_f =$ 62.5 MPa to approximately 13% for $K_f =$ 1.5 GPa. This trend is the opposite of that observed in Figure 3-1(a) and indicates that the transverse steel confinement effects become less important for increasing amounts of FRP confinement, confirming the strongly nonlinear global behavior associated with the interaction between the FRP and steel confining mechanisms. The variability of the results, as indicated by both the interquartile ranges and the entire data ranges, is drastically reduced as K_f increases.

Figure 3-7 plots $\left(\overline{P}_{\max} - \overline{P}_{f0}\right)/P_0$ versus f_{lf} / f_c'. It also provides the trendline (based on a quadratic/linear rational function) of the numerical simulation results, which has a coefficient of

determination $R^2 = 0.031$, and indicates the value $f_{lf} / f_c' = 0.08$ with a vertical dashed line. This trendline suggests that $\left(\overline{P}_{\max} - \overline{P}_{f0}\right)/P_0$ increases with f_{lf} / f_c' for low values of the FRP confinement ratio (i.e., $f_{lf} / f_c' < 0.05$), whereas it slightly decreases with f_{lf}/f_c' for high values of the FRP confinement ratio (i.e., $f_{lf} / f_c' > 0.10$). These results seem to confirm that the behavior of FRP-confined RC columns changes for FRP confinement ratios that are lower or higher than the lower bound $f_{lf} / f_c' = 0.08$ recommended in ACI 440.2R-17 (ACI 2017). However, the very low value of the coefficient of determination for this trendline indicates that the dispersion of the results is very high and that the dependence of $(\overline{P}_{\max} - \overline{P}_{f0}) / \overline{P}_{f0}$ on f_{lf}/f_c' is most likely not meaningful.

The results in Figure 3-6(b) show that $\left(\overline{P}_{\max} - \overline{P}_{f0}\right)/P_0$ increases for increasing column diameters, with the median values going from 10.6% for D = 150 mm to 32.2% for D = 1200 mm. This positive correlation is stronger than that observed in Figure 3-1(b) between $\left(\overline{P}_{\max} - P_0\right)/P_0$ and D. In fact, the increases in the median values of $\left(\overline{P}_{\max} - \overline{P}_{f0}\right)/P_0$ and $\left(\overline{P}_{\max} - P_0\right)/P_0$ from D = 150 mm to D = 1200 mm are both equal to approximately 21%, indicating that this increase is due exclusively to the steel confinement effect. This result is also confirmed by the four additional numerical simulations performed by setting $A_c / A_g = 0.840$, which yield the same value $\left(\overline{P}_{\max} - \overline{P}_{f0}\right)/P_0 = 60.7\%$.

Figure 3-6(c) shows that both the median and the interquartile range of $\left(\overline{P}_{\max} - \overline{P}_{f0}\right)/P_0$ slightly decreases as f_c' goes from 20 MPa to 70 MPa. As expected, Figure 3-6(d) shows a drastic increase of both the median and the interquartile range of $\left(\overline{P}_{\max} - \overline{P}_{f0}\right)/P_0$ for increasing values of ρ_{st}.

Again, these results are consistent with the steel confinement mechanism and its effects on the axial stress-axial strain behavior observed in Figure 3-4.

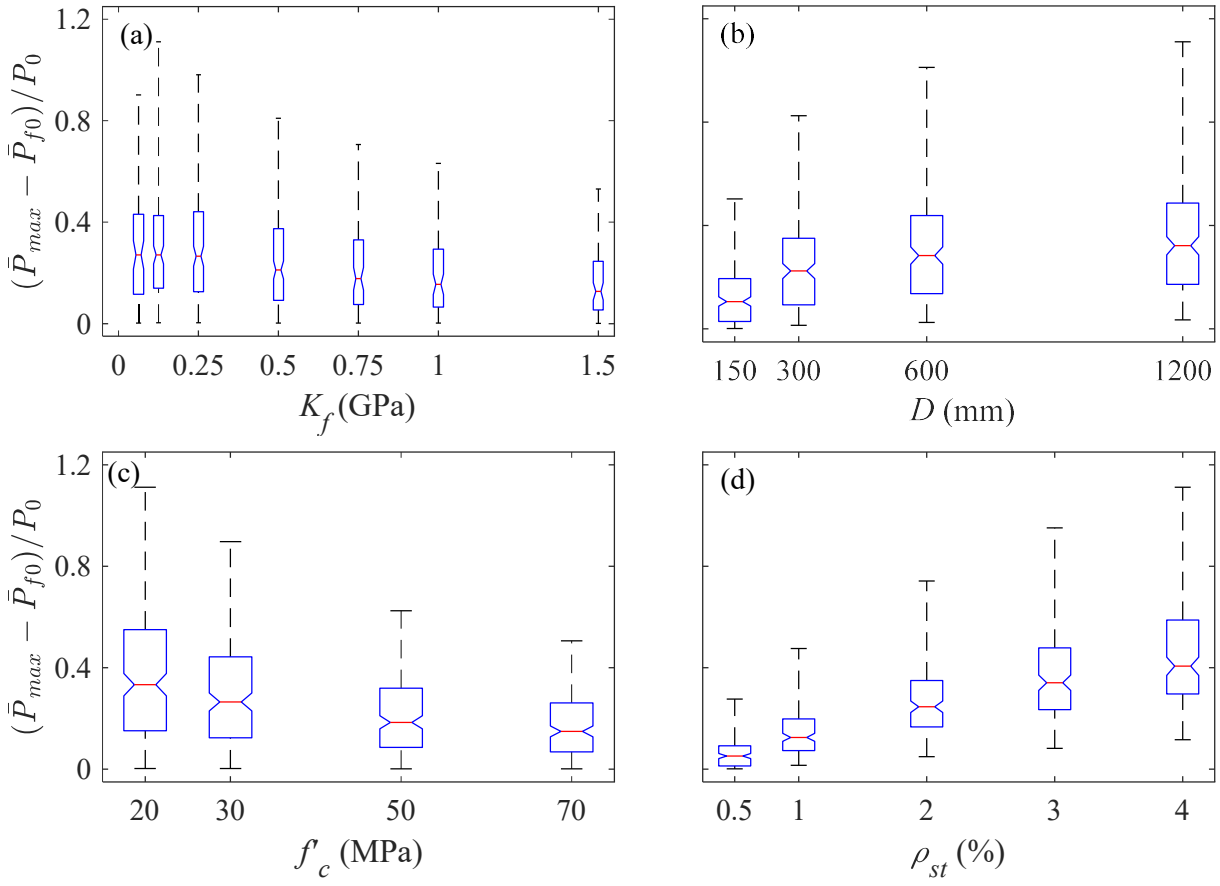

Figure 3-6. Box-and-whisker plots of the normalized increment to axial strength due to steel confinement, $\left(\bar{P}_{\max} - \bar{P}_{f0}\right)/P_0$, for variations of: (a) FRP confining stiffness; (b) diameter; (c) concrete strength; and (d) transverse steel ratio

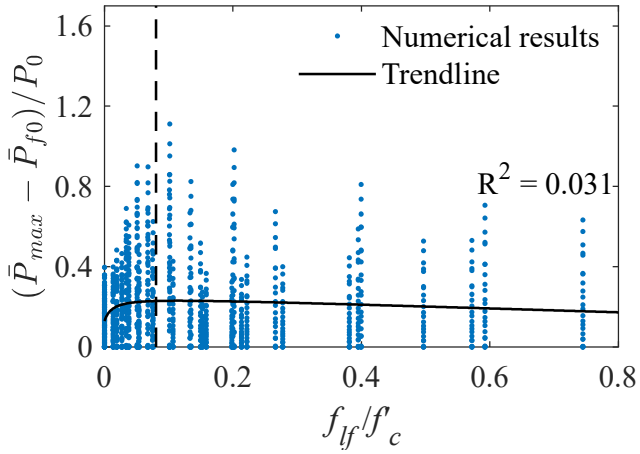

Figure 3-7. Effect of FRP confinement ratio on relative peak axial strength increment with respect to the reference FRP-only-confined columns

3.4.4 Selection of synthetic parameters to describe the transverse steel confinement effects

The results of the parametric study presented in this paper suggest that the transverse steel confinement effects on the peak axial strength of an FRP-confined RC columns depend on: (1) the ratio of the confinement separately exerted by the steel and the FRP, and (2) the ratio between the core area (confined by both steel and FRP) and the gross area of the columns. Therefore, the following two relative confinement effect coefficients are proposed to synthetically describe the effects of transverse steel confinement on the columns' peak axial strength:

$$c_f = \frac{f_{ls} \cdot A_c}{f_{lf} \cdot A_g} \tag{3-4}$$

$$C_s = \frac{100 f_{ls} \cdot A_c}{K_f \cdot A_g} \tag{3-5}$$

It is noteworthy that c_f was originally introduced in Zignago et al. (2018) and used in Zignago and Barbato (2019), where only $P_{\max}$ values were considered; whereas C_s is proposed here for the first time. These two nondimensional coefficients differ in the way they account for the magnitude of FRP confinement. In particular, c_f is a function of the maximum FRP confining pressure f_{lf},

which depends on the effective strain of the FRP at failure, ε_{fe}. Thus, the use of c_f is more appropriate for applications in which failure of the confining FRP is expected, e.g., in the prediction of the ultimate strength of experimental specimens loaded to failure. By contrast, C_s is a function of the FRP confining stiffness K_f, and its use is more appropriate for applications in which failure of the confining FRP should be avoided, e.g., in developing design equations.

Figure 3-8(a) plots $\left(\overline{P}_{\max} - \overline{P}_{f0}\right) / \overline{P}_{f0}$ versus c_f for $f_{lf} / f_c' \geq 0.08$; Figure 3-8(b) plots $\left(\overline{P}_{\max} - \overline{P}_{f0}\right) / \overline{P}_{f0}$ versus c_f for $f_{lf} / f_c' < 0.08$; Figure 3-8(c) plots $\left(P_{\max} - P_{f0}\right) / P_{f0}$ versus c_f for $f_{lf} / f_c' \geq 0.08$; and Figure 3-8(d) plots $\left(P_{\max} - P_{f0}\right) / P_{f0}$ versus c_f for $f_{lf} / f_c' < 0.08$. The different plots also report a bilinear fit with the corresponding coefficient of determination, R^2. It is observed that, for $f_{lf} / f_c' \geq 0.08$, $\left(P_{\max} - P_{f0}\right) / P_{f0}$ is described very well by the bilinear fit (R^2 = 0.982), whereas $\left(\overline{P}_{\max} - \overline{P}_{f0}\right) / \overline{P}_{f0}$ presents a higher dispersion (R^2 = 0.880). This result was expected, as c_f is directly related to the FRP confinement pressure achieved at the FRP failure, which is the predominant mechanism in determining the values of $P_{\max}$ and P_{f0}. This general behavior of higher dispersion for $\left(\overline{P}_{\max} - \overline{P}_{f0}\right) / \overline{P}_{f0}$ than for $\left(P_{\max} - P_{f0}\right) / P_{f0}$ is observed also for FRP-confined columns with $f_{lf} / f_c' < 0.08$; however, the dispersion is significantly higher than for the cases for which $f_{lf} / f_c' \geq 0.08$.

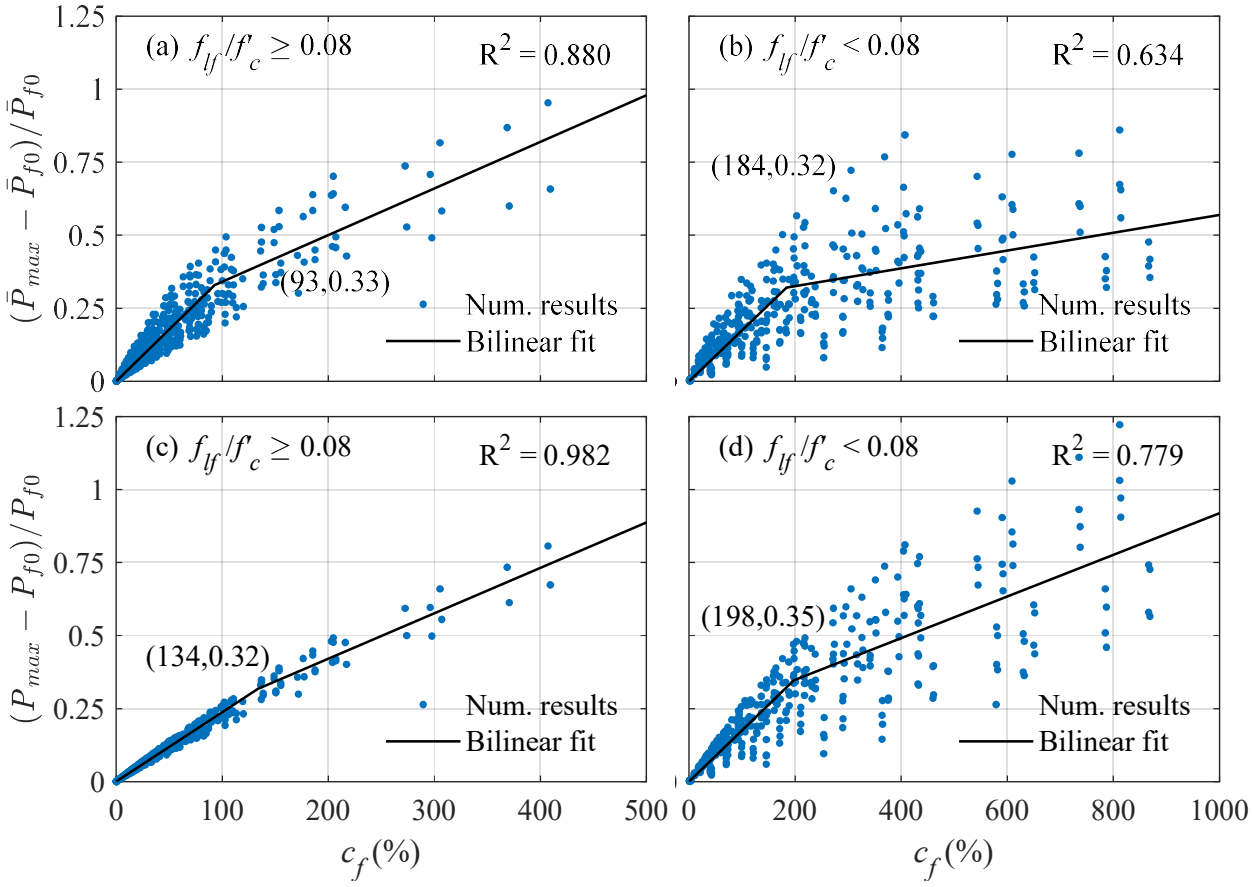

Figure 3-8. Steel confinement contribution to normalized peak axial strength increment versus relative confinement effect coefficient c_f: (a) $\left(\bar{P}_{\max} - \bar{P}_{f0}\right)/\bar{P}_{f0}$ for $f_{lf}/f'_c \geq 0.08$; (b) $\left(\bar{P}_{\max} - \bar{P}_{f0}\right)/\bar{P}_{f0}$ for $f_{lf}/f'_c < 0.08$; (c) $\left(P_{\max} - P_{f0}\right)/P_{f0}$ for $f_{lf}/f'_c \geq 0.08$; and (d) $\left(P_{\max} - P_{f0}\right)/P_{f0}$ for $f_{lf}/f'_c < 0.08$.

Similar to Figure 3-8, Figure 3-9(a) plots $\left(\bar{P}_{\max} - \bar{P}_{f0}\right)/\bar{P}_{f0}$ versus C_s for $f_{lf}/f'_c \geq 0.08$; Figure 3-9(b) plots $\left(\bar{P}_{\max} - \bar{P}_{f0}\right)/\bar{P}_{f0}$ versus C_s for $f_{lf}/f'_c < 0.08$; Figure 3-9(c) plots $\left(P_{\max} - P_{f0}\right)/P_{f0}$ versus C_s for $f_{lf}/f'_c \geq 0.08$; and Figure 3-9(d) plots $\left(P_{\max} - P_{f0}\right)/P_{f0}$ versus C_s for $f_{lf}/f'_c < 0.08$. Also in this case, the different plots report a bilinear fit with the corresponding R^2. For $f_{lf}/f'_c \geq 0.08$, the bilinear fit is a good representation of both $\left(\bar{P}_{\max} - \bar{P}_{f0}\right)/\bar{P}_{f0}$ and

$\left(P_{\max}-P_{f0}\right)/P_{f0}$ as functions of C_s. However, the dispersion is lower for $\left(\bar{P}_{\max}-\bar{P}_{f0}\right)/\bar{P}_{f0}$ ($R^2=0.957$) than for $\left(P_{\max}-P_{f0}\right)/P_{f0}$ ($R^2=0.921$), because C_s is directly related to the FRP confinement stiffness achieved when the axial strain in the concrete reaches $\varepsilon_{c,\max}$, which is the predominant mechanism in determining the values of $\bar{P}_{\max}$ and $\bar{P}_{f0}$. Also in this case, the dispersion observed for $f_{lf}/f_c'<0.08$ is significantly higher than that for $f_{lf}/f_c'\geq 0.08$.

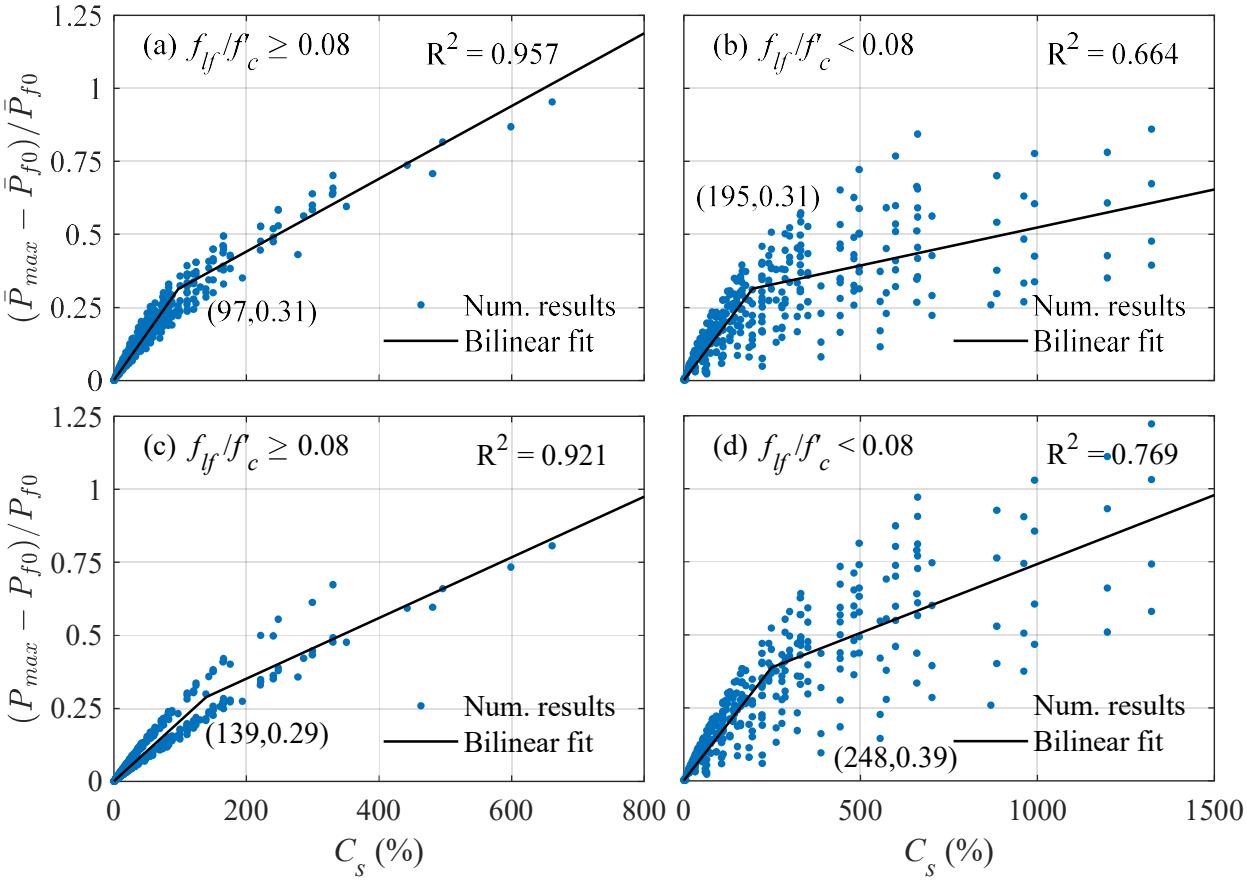

Figure 3-9. Steel confinement contribution to normalized peak axial strength increment versus relative confinement effect coefficient C_s: (a) $\left(\bar{P}_{\max}-\bar{P}_{f0}\right)/\bar{P}_{f0}$ for $f_{lf}/f_c'\geq 0.08$; (b) $\left(\bar{P}_{\max}-\bar{P}_{f0}\right)/\bar{P}_{f0}$ for $f_{lf}/f_c'<0.08$; (c) $\left(P_{\max}-P_{f0}\right)/P_{f0}$ for $f_{lf}/f_c'\geq 0.08$; and (d) $\left(P_{\max}-P_{f0}\right)/P_{f0}$ for $f_{lf}/f_c'<0.08$.

These results indicate that the effect of transverse steel confinement on the peak axial strength of FRP-confined RC columns is captured well by the two proposed coefficients c_f and C_s when $f_{lf} / f_c' \geq 0.08$. The use of coefficient c_f should be preferred when investigating the behavior of columns loaded up to their physical collapse (usually by fracture of the FRP confinement), whereas the coefficient C_s is better suited to describe the behavior of column designed to satisfy the deformation requirement imposed by Eq. (3-3). From the bilinear models in Figure 3-8 and Figure 3-9, it is observed that $(P_{\max} - P_{f0}) / P_{f0} = 0.05$ corresponds in average to a value of $c_f \approx 20\%$ for $f_{lf} / f_c' \geq 0.08$ and to $c_f \approx 28\%$ for $f_{lf} / f_c' < 0.08$; whereas $(\overline{P}_{\max} - \overline{P}_{f0}) / \overline{P}_{f0} = 0.05$ corresponds to a value of $C_s \approx 15\%$ for $f_{lf} / f_c' \geq 0.08$ and to $C_s \approx 31\%$ for $f_{lf} / f_c' < 0.08$. Thus, it is recommended that the effect of simultaneous confinement by FRP and steel is considered whenever $c_f \geq 20\%$ and/or $C_s \geq 15\%$. It is also observed that, for typical values of $c_f \leq 100\%$ and $C_s \leq 200\%$, the effect of transverse steel confinement can be very significant, with increases of the peak axial strength up to 30%-40% of the peak axial strength obtained by neglecting the transverse steel confinement effect. It is noted here that larger values of c_f and C_s than these typical values are still possible (as shown in Figure 3-8 and Figure 3-9), albeit they are expected to be uncommon in practical applications, as they generally correspond to a combination of high transverse steel reinforcement and low FRP volumetric reinforcement ratios.

3.5 Conclusions

This paper investigates the effects of internal transverse steel confinement on the axial load-carrying capacity of FRP-confined reinforced concrete (RC) columns through a numerical parametric study. This parametric study is based on 1,152 nonlinear finite element (FE) analyses

of FRP-confined RC columns considering a wide but realistic range of key parameters (i.e., type of FRP, volumetric FRP ratio, volumetric transverse steel ratio, concrete compressive strength, and column diameter). The nonlinear FE analyses are performed using a recently-developed confined concrete constitutive model able to accurately describe the simultaneous confinement effects of transverse steel reinforcement and FRP external wraps. The peak axial strengths of FRP-confined RC columns are estimated both considering the design limitation on maximum allowable concrete strain recommended by ACI 440.2R-17 (ACI 2017), $\overline{P}_{\max}$, and without imposing any strain limitation on the concrete, $P_{\max}$. For any given column, a reference unconfined column with strength P_0, and a reference FRP-only-confined column without transverse steel with strengths $\overline{P}_{f0}$ (with imposed strain design limitation) and P_{f0} (without imposed strain design limitation), are also considered. It is noteworthy that $\overline{P}_{\max}$ is a better representation of the columns' behavior for design purposes, whereas $P_{\max}$ provides a better estimate of the behavior of columns loaded up to physical collapse, as often done in experimental tests available in the literature.

It is observed that the normalized peak axial strength increment, $\left(\overline{P}_{\max} - P_0\right)/P_0$, of FRP-confined RC columns increases for increasing amounts of FRP and transverse steel, whereas it decreases for increasing unconfined concrete compressive strength. A small positive correlation is also found between $\left(\overline{P}_{\max} - P_0\right)/P_0$ and the ratio between concrete core and gross area, A_c / A_g. The FRP confinement alone can increase the column's peak axial strength by as much as approximately 90%. The interaction between FRP confinement and transverse steel confinement is highly nonlinear. In fact, the transverse steel confinement contribution to the peak axial strength of the columns increases with the amount of FRP for smaller FRP reinforcement ratios, and then decreases for increasing amounts of FRP for larger FRP reinforcement ratios. The threshold

between smaller and larger FRP reinforcement ratios depends on the FRP material properties and the unconfined concrete compressive strength.

It is found that the design limitation on maximum allowable concrete strain recommended by ACI 440.2R-17 (ACI 2017) can have a significant impact (up to approximately 66% of the strength of the reference unconfined RC column) on the estimate of a column's peak axial strength, particularly for columns with high amounts of transverse steel and low amounts of FRP, and for columns with high amounts of FRP. For a given FRP confining stiffness, the effects of the strain design limitation are more pronounced for FRP materials with lower stiffness and higher ultimate strain, i.e., they are higher for GFRP than for CFRP confinement.

The contribution of the transverse steel confinement to the columns' peak axial strength can be very significant, with normalized peak axial strength increments $\left(\overline{P}_{\max}-\overline{P}_{f0}\right)/P_0$ as high as 111%. This relative contribution increases significantly with the transverse steel ratio and the A_c/A_g ratio, whereas it decreases for increasing FRP confining stiffness and unconfined concrete compressive strength. It is found that $\left(\overline{P}_{\max}-\overline{P}_{f0}\right)/P_0$ is almost independent of the FRP confining ratio f_{lf}/f_c' for $f_{lf}/f_c' \geq 0.08$.

In order to synthetically quantify the effects of the transverse steel confinement on the peak axial strength, two confinement pressure ratio coefficients are proposed in this study: $c_f=\left(f_{ls}\cdot A_c\right)/\left(f_{lf}\cdot A_g\right)$ and $C_s=\left(100 f_{ls}\cdot A_c\right)/\left(K_f\cdot A_g\right)$. It is found that, for $f_{lf}/f_c' \geq 0.08$, the relationships between $\left(\overline{P}_{\max}-\overline{P}_{f0}\right)/\overline{P}_{f0}$ and C_s, and between $\left(P_{\max}-P_{f0}\right)/P_{f0}$ and c_f are very well described by a bilinear fit. For typical values of $c_f \leq 100\%$ and $C_s \leq 200\%$, the transverse steel confinement effect can increase the peak axial strength up to 30%-40% of the peak axial

strength estimated by neglecting this effect. It is concluded that, for values of $c_f \geq 20\%$ and $C_s \geq 15\%$, the effect of the transverse steel confinement should be considered in order to obtain accurate estimates of the peak axial strength of FRP-confined RC columns.

The synthetic parameters, c_f and C_s, identified in this study to describe the effects of transverse steel confinement in experimental and design applications, respectively, represent a preliminary but necessary step towards the development of improved predictive strength and design equations for FRP-confined RC columns subject to axial compression. Current research is ongoing to develop a design procedure for axially loaded FRP-confined RC columns based on rigorous structural reliability analysis procedures. Additional research is also needed to investigate and understand the effects of transverse steel confinement on the axial force-bending moment interaction behavior of FRP-confined RC columns.

4 Numerical investigation of axial force-bending moment interaction for FRP-confined reinforced concrete columns with internal steel transverse reinforcement

The parametric analysis conducted in Chapter 3 is extended to columns subjected to combined axial load and bending moment. The development of interaction diagrams of FRP-confined RC columns that take into account the effects of internal steel confinement is an understudied topic, and the present research helps to systematically investigate these effects.

4.1 Introduction

Reinforced concrete (RC) structures often require to be repaired and/or strengthened when damaged (e.g., due to environmental degradation or extreme events) or when use changes cause increased demand. In particular, RC columns can be retrofitted through a confinement mechanism produced by externally-bonded fiber-reinforced polymer (FRP) wraps, a retrofit technique thoroughly studied throughout the last four decades (Fardis and Khalili 1982; Raza et al. 2019). This technique has been efficiently employed in the strengthening of real-world structures, particularly for improving the load-bearing capacity and seismic resilience of structurally-deficient RC columns (Parvin and Brighton 2014; Tatar et al. 2021).

In FRP-confined RC columns, the concrete confinement produced by the externally-bonded FRP wraps acts in addition to the confining action exerted by the internal transverse steel reinforcement (i.e., steel ties and spirals), although the transverse steel confinement contribution is typically ignored in current design codes and guidelines for strengthening of RC structures by use of FRP wrappings (Kaeseberg et al. 2019). This disregard of the internal steel confinement effects reflects the extensive availability in the literature of constitutive models for FRP-only confined concrete (Ozbakkaloglu et al. 2013), whereas the simultaneous confinement of concrete by FRP and steel has been investigated in a smaller number of studies (Wang and Restrepo 2001; Lee et al. 2010;

Teng et al. 2015; Zignago et al. 2018). Furthermore, the majority of current FRP-and-steel-confined concrete stress-strain models: (1) assume a linear superposition of the global confinement effects from each confining material (Ilki et al. 2008; Hu and Seracino 2014; Teng et al. 2015); (2) are fitted to a limited number of data points that constrain their range of validity (Lee et al. 2010); or (3) are based on an oversimplified lateral-to-axial deformation relationship for confined concrete (Wang and Restrepo 2001).

A new analysis-oriented material constitutive model for FRP-and-steel confined concrete was recently developed to describe the complex phenomenon of concurrent confinement by FRP laminates and transverse steel by superimposing the confining pressures exerted by each confining material at the material level (Zignago et al. 2018). This new stress-strain model was validated against experimental data available in the literature of FRP-confined RC columns subject to pure compression, eccentric compression, and cyclic lateral loading with constant axial load. The use of this material constitutive model, associated with fiber-discretized force-based frame finite element (FE) cross-sections (Hu and Barbato 2014), was found to produce accurate numerical estimations of the experimental structural response of FRP-confined columns. The effect of transverse steel confinement can be significant (Zignago and Barbato 2021, 2022), especially in light of modern design codes with higher ductility requirements, which leads to RC column designs with considerable amounts of longitudinal and transverse steel (Roy et al. 2010; Tatar et al. 2021). Columns are generally loaded through a combination of axial forces and bending moments. In fact, even columns nominally subjected to pure axial compression are expected to behave under the combined effects of axial and flexural loads (Nilson et al. 2010). The bending action on the columns can result from different causes, including accidental load eccentricities, vertical misalignment, and lateral forces such as earthquakes or wind. For this reason, design codes and

standards typically present design procedures that account for eccentric loading for columns subject to a nominally concentric loading condition (ACI 2017, 2019).

This paper extends the numerical investigation of the effects of the transverse steel confinement on FRP-confined circular RC columns from the case of pure axial loading (Zignago and Barbato 2021) to the case of combined axial load and bending moment. A thorough parametric study is conducted to investigate the effects of different design parameters when varied within their range for practical applications. Based on previous work for concentrically-loaded columns, two new synthetic coefficients are proposed to quantify the effect of transverse steel confinement on eccentrically-loaded FRP-confined circular RC columns.

4.2 Novelty and relevance

This study represents the first investigation of axial force-bending moment (*P-M*) interaction for FRP-confined RC circular columns accounting for simultaneous confinement of FRP and steel at the material level using frame FEs. To the authors' knowledge, only another very recent study has investigated the effects of internal steel hoops on *P-M* interaction diagrams by employing an FRP-and-steel confined concrete model (Yuan et al. 2022); however, this previous study used a significantly more computationally-expensive 3-dimensional FE model based on solid elements. The topic remains understudied and the present paper further advances the mechanical understanding of the concurrent confinement by FRP wrappings and internal reinforcing steel in FRP-wrapped RC columns subject to combined axial force and bending moments.

The new knowledge gained in this study on the *P-M* interaction of FRP-confined RC columns, as well as the development of synthetic parameters to describe the confinement effect of internal steel reinforcement, represent essential steps toward the development of new and improved design equations for this type of structural components. Thus, this research could lead to significant

benefits in terms of safer and/or more economic design of FRP-confinement retrofits of RC columns.

4.3 FE modeling and development of *P-M* interaction diagrams

This study employs nonlinear FE analysis to develop *P-M* interaction diagrams of FRP-confined RC columns. In particular, each point of interest in a *P-M* interaction diagrams is obtained through a monotonic incremental analysis in which axial force and bending moment are proportionally increased to represent the behavior of the RC column for a given load eccentricity. The generated data points correspond to different values of assumed load eccentricity and are connected by straight lines. A sufficiently large number of points is computed to produce smooth interaction diagrams. The FE analyses are performed using the general purpose FE software framework OpenSees (Mazzoni et al. 2006), using a force-based frame or a zero-length FE with fiber-discretized cross-sections (Spacone et al. 1996; Barbato 2009; Hu and Barbato 2014; Zignago et al. 2018; Zignago and Barbato 2021), in which the concrete behavior is modeled using the Zignago-Barbato-Hu (ZBH) model (Zignago et al. 2018) and the longitudinal steel fibers are modeled using the extended Menegotto-Pinto model (Menegotto and Pinto 1973; Filippou et al. 1983). In particular, the FE models are based on a force-based frame element when, in addition to forces and moments, displacements and deflections are needed and/or slender columns are considered, for which nonlinear geometry effects may be significant; whereas the use of a zero-length element is preferred when the focus is on strength, strains, and curvatures and/or on computational efficiency. Additional modeling details can be found elsewhere (Zignago et al. 2018; Zignago and Barbato 2021, 2022).

Figure 4-1(a) compares the experimentally-measured and numerically-estimated axial force versus mid-height lateral deflection response for two eccentrically-loaded FRP-confined RC columns for

which experimental results are documented in the literature (Hadi 2009). Figure 4-1(b) compares the experimental and numerical peak axial strength for both concentrically- and eccentrically-loaded FRP-confined RC column specimens with a steel-to-FRP confinement ratio $c_f \geq 0.05$, as reported elsewhere (Zignago et al. 2018). The experimental results reported in Figure 4-1 are obtained by using a 2-node force-based frame FE with spread plasticity, which is able to provide information on both strength and displacement response. It is shown that the adopted model provides numerical results that are in excellent agreement with the experimental measurements. The full experimental validation of the FE modeling approach used to obtain these results is available elsewhere (Zignago et al. 2018).

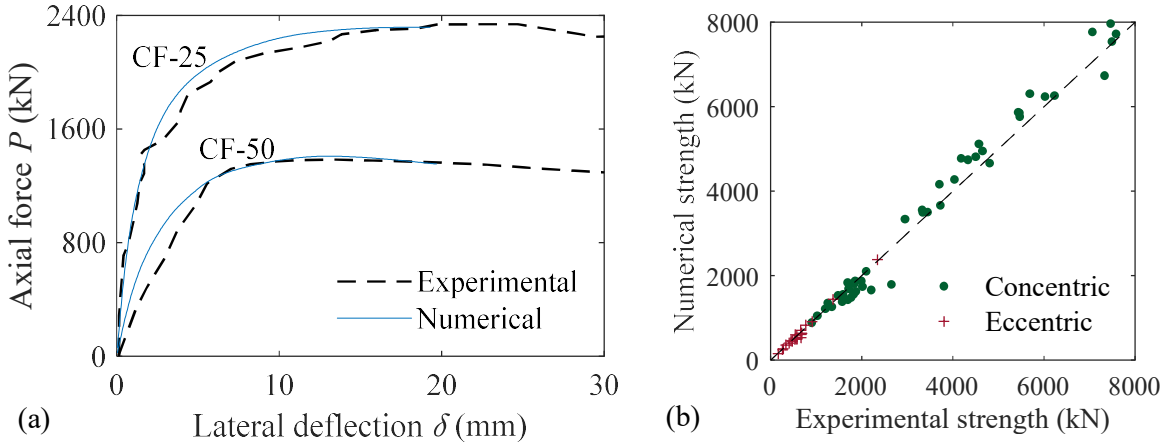

Figure 4-1. Comparison between experimental and numerical responses of FRP-confined RC columns: (a) axial force versus mid-height deflection (experimental data from Hadi 2009), and (b) axial strength of concentrically- and eccentrically-loaded columns.

It is noted here that *P-M* interaction diagrams for FRP-confined RC columns are often obtained via conventional sectional analyses based on strain compatibility and force equilibrium, with the assumption of a linear strain profile along the cross-section for a given sectional rotation (Bank 2006; Wight and MacGregor 2009). This approach is computationally very efficient, as it does not require a nonlinear FE analysis to obtain the *P-M* interaction diagram. However, this approach can

provide the load eccentricity only as a post-processed result, and thus it does not allow the investigation of the column behavior for a given eccentricity value or for a given load path.

4.4 Validation of *P-M* interaction diagrams

Figure 4-2 compares the normalized *P-M* interaction diagrams obtained by using the ZBH FRP-and-steel confined concrete model (Zignago et al. 2018) and the Lam and Teng (LT) FRP-only confined concrete model (Lam and Teng 2003a) with experimental results for FRP-confined RC columns documented in the literature (Hadi 2009; Bisby and Ranger 2010; Mostofinejad and Torabian 2016; Xing et al. 2020). In this diagrams, the axial strength P is normalized by the nominal axial strength P_n calculated according to ACI 318-19 (ACI 2019) for the unconfined (no transverse steel and no FRP) member (i.e., as per equation 22.4.2.2 of ACI 318-19, excluding accidental eccentricity reduction factors); whereas the bending moment strength M is normalized by the nominal bending moment M_n according to ACI 318-19 (ACI 2019) (i.e. calculated in accordance with assumptions in Section 22.2 of ACI 318-19). The bending moment strengths from the experimental data are obtained as the sum of the applied moments and the second-order moments produced by the mid-height lateral deflection δ measured during the test, i.e., $M = P \cdot (e_i + \delta) = P \cdot e,$ in which e_i denotes the initial load eccentricity imposed in the experimental test, and e is the total load eccentricity.

The development of the numerical *P-M* interaction diagrams is performed through a careful examination of the experimental data and testing procedures, with three parameters requiring particular attention: (1) the value of f_c', (2) the value ε_{fe}, and (3) the precision of the testing equipment. Regarding f_c', all specimens in Figure 4-2(a)-(b) were built using the same batch of concrete, with a single value of f_c' used for all points of the numerical *P-M* interaction diagrams.

The numerical value of f_c' used for the specimens in Figure 4-2(b) (Hadi 2009) was obtained as the average of the compression strength from the two stronger concrete cylinders out of the three specimens tested in the reference work, as the third cylinder presented a significantly (26.3%) lower strength than the average of the other two and, thus, was considered as an outlier. The specimens in Figure 4-2(c) (Mostofinejad and Torabian 2016) and Figure 4-2(d) (Xing et al. 2020) were fabricated from different concrete batches; thus, the average f_c' is used here to construct the theoretical *P-M* interaction diagram. Regarding ε_{fe}, the authors of the experimental studies reported in Figure 4-2(a) and Figure 4-2(d) (Bisby and Ranger 2010; Xing et al. 2020), reported the FRP hoop strain at ultimate axial load for each eccentricity, from which the effective FRP rupture strain ε_{fe} is directly calculated and used for the points corresponding to the experimentally-tested eccentricities. The ε_{fe} values for the other points of the corresponding *P-M* interaction diagrams are obtained through linear interpolation the experimental ε_{fe} as a function of the eccentricity. For the other two studies for which the experimental values of the effective FRP rupture strain ε_{fe} were not reported, a single value of the FRP efficiency factor κ_ε is estimated based on a well-established model (Realfonzo and Napoli 2011) and used for all points of the *P-M* interaction diagrams. Regarding the precision of the testing equipment, for the specimens reported in Figure 4-2(a) (Bisby and Ranger 2010), the authors reported a testing machine precision of approximately 2 mm for the load eccentricity. Therefore, the final eccentricity considered for each data point on the experimental *P-M* interaction diagram is increased by 1 mm to account in an approximate averaged manner for the equipment precision.

In general, the *P-M* interaction diagrams constructed by employing the FRP-and-steel confined concrete model show better agreement with the experimental data than the diagrams obtained by

using the FRP-only confined concrete model for all analyzed studies. In order to quantify the accuracy of the different models, the following relative error measure is introduced:

$$\varepsilon_R = \frac{R_{\max,FE} - R_{\max,\exp}}{R_{\max,\exp}} \tag{4-1}$$

in which

$$R_{\max} = \sqrt{\left(\frac{P}{P_n}\right)^2 + \left(\frac{M}{M_n}\right)^2} \tag{4-2}$$

represents a synthetic normalized measure of the combined axial and bending moment strength (referred to as combined strength hereinafter), and the subscripts "*FE*" and "exp" denote the numerical and experimental values of $R_{\max}$, respectively.

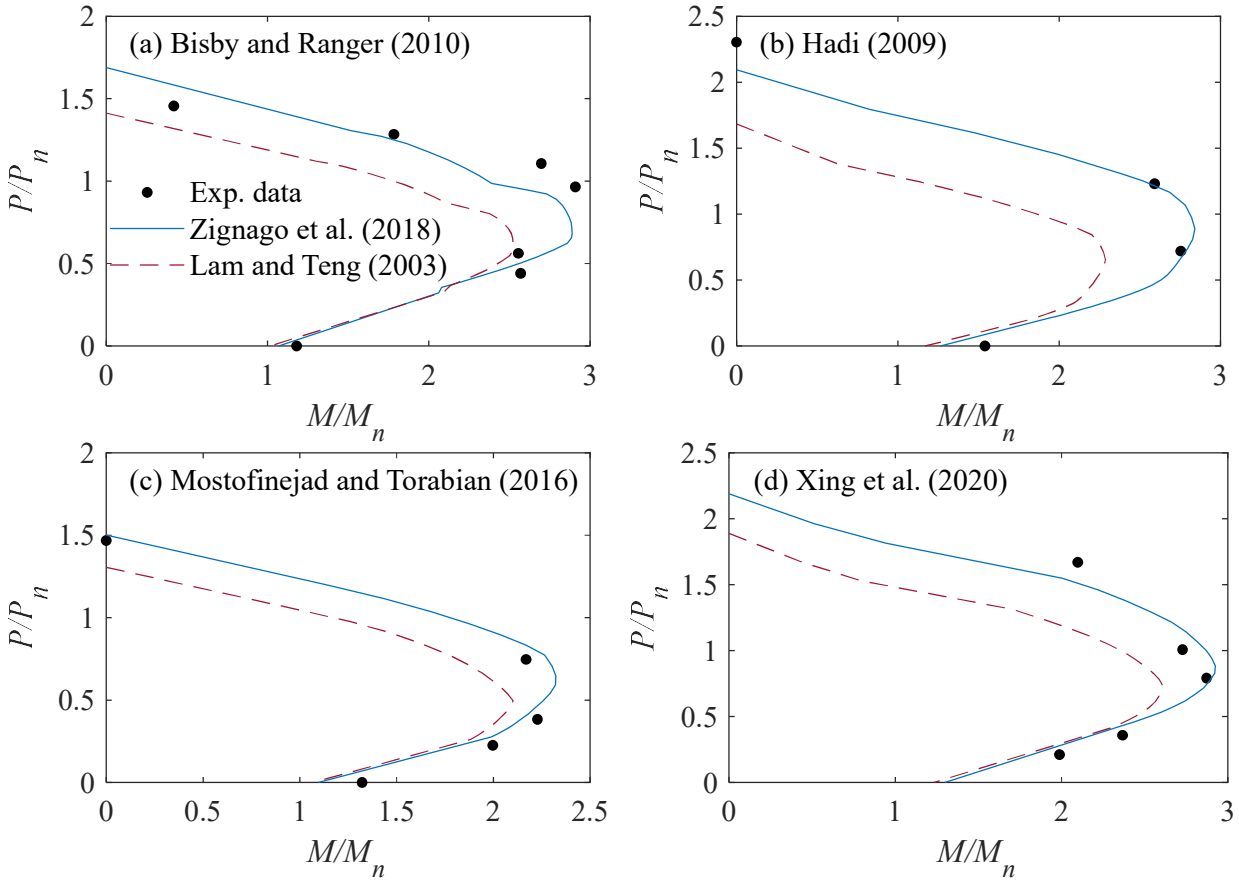

Figure 4-2. Comparison of theoretical and experimental normalized *P*-*M* interaction diagrams: (a) single-layer carbon FRP hoop wrap specimens (Bisby and Ranger 2010); (b) three-layer

carbon FRP wrap (CF) specimens (Hadi 2009); (c) FRP-wrapped (IW) specimens (Mostofinejad and Torabian 2016); and (d) four-layer carbon FRP wrap with length-to-diameter ratio equal to 6 (Xing et al. 2020).

Table 4-1 reports the relative error means, standard deviations, maxima, and minima for the two models (i.e., with and without accounting for the internal steel confinement effects) for all four sets of experimental data considered in this study. The errors are reported for all available experimental data points and for the points corresponding to axial loads higher than those of the balanced points, P_B (i.e., the points of attainment of both steel yielding and concrete crushing limit states). It is observed that, on average, the ZBH model provides excellent estimates of the columns' combined strength, with the relative error mean and standard deviation calculated over all specimens equal to -0.039 and 0.070, respectively. The LT model produces less accurate although slightly less disperse results than the ZBH model, with an average relative error of -0.146 and standard deviation equal to 0.060. The LT model generally underestimates the combined strength $R_{\max}$ of the specimens because it neglects the confinement effects of transverse steel. The results in terms of maximum and minimum error values also confirm the better performance of the ZBH over the LT model, with the ZBH model providing a maximum and minimum error of 0.112 and -0.028, respectively, whereas the LT model yields errors of -0.163 and -0.270, respectively.

Table 4-1. Comparison of relative errors in combined strength obtained using the ZBH and LT models for the FRPP-confined RC column specimens in Figure 4-2

Error (%)		Bisby and Ranger (2010)		Hadi (2009)		Mostofinejad and Torabian (2016)		Xing et al. (2020)		All data	
		ZBH	LT	ZBH	LT	ZBH	LT	ZBH	LT	ZBH	LT
All points	Mean	-2.0	-13.7	-6.2	-22.5	-4.7	-12.1	-4.3	-12.2	-3.9	-14.6
	St. Dev.	8.5	6.3	8.0	3.9	7.8	1.9	3.3	5.2	7.0	6.0
	Maximum	11.2	-2.8	0.9	-17.6	3.7	-10.0	0.8	-8.2	11.2	-2.8
	Minimum	-10.7	-21.4	-16.3	-27.0	-13.8	-15.0	-6.7	-21.0	-16.3	-27.0
$P \geq P_B$	Mean	-2.4	-16.3	-2.9	-22.6	2.9	-11.3	-1.8	-14.7	-1.4	-16.6
	St. Dev.	7.9	5.1	5.4	4.7	1.1	0.5	4.3	5.6	6.1	5.7
	Maximum	8.1	-9.5	0.9	-17.6	3.7	-10.9	0.8	-10.1	8.1	-9.5
	Minimum	-10.7	-21.4	-9.0	-27.0	2.1	-11.7	-6.7	-21.0	-10.7	-27.0

The discrepancy between experimental results and numerical estimates based on the LT model is more pronounced in the compression-controlled region of the interaction diagram (i.e., for $P \geq P_B$), with an average relative error of -0.166. By contrast, the ZBH model becomes slightly more accurate, with an average relative error of -0.014. In the tension-controlled region of the diagram (i.e., for $P < P_B$), both confinement models were found to generally underestimate the experimental combined strength and to produce very similar numerical predictions of the structural behavior of FRP-wrapped RC columns. This result was expected because the confinement effect is small in this region of the diagram, where only a small portion of the cross-section is subject to compression and, thus, the confining mechanism from FRP and transverse steel is not fully activated. In fact, it is observed that the ACI 440.2R-17 guidelines do not admit any strength enhancement in FRP-confined RC columns for axial loads smaller than those corresponding to the balanced point (ACI 2017). Based on *P-M* interaction diagrams constructed with the ZBH concrete model, the balanced point for each of the diagrams in Figure 4-2(a)-(d) is achieved at e/D = 0.232, 0.256, 0.249, and 0.213, respectively. When the diagrams are constructed with the LT model, their corresponding balanced points are obtained at slightly higher eccentricity ratios, i.e., at e/D = 0.239, 0.280, 0.295, and 0.227, respectively.

4.5 Parametric analysis of *P-M* interaction

A parametric study is performed to numerically investigate the effects of relevant design variables on the structural capacity of FRP-confined RC columns subjected to the combined action of axial load and bending moment. In addition to the load eccentricity ratio e / D, this study considers the same design parameters considered in a previous study for FRP-confined RC columns subjected to axial load only (Zignago and Barbato 2021), i.e.: (1) fiber type (carbon or glass FRP); (2) FRP

volumetric reinforcement ratio, ρ_f; (3) column diameter, D; (4) concrete compressive strength, f'_c; and (5) transverse steel volumetric reinforcement ratio, ρ_{st}. Three different levels are considered for the load eccentricity ratio, i.e., $e/D = 0.05$, 0.15, and 0.25. These values are selected to focus the investigation on the compression-controlled region of the *P-M* interaction diagram. The results for concentric axial loads (i.e., with $e/D = 0$) were already presented elsewhere (Zignago and Barbato 2021). It is noteworthy that the balanced point for ordinary RC columns can be achieved for load eccentricity ratios as high as 1.0 (Wight and MacGregor 2009), whereas the balanced point of FRP-confined compression members is generally reached at lower values of the load eccentricity ratio, often in the range $e/D = 0.20 \sim 0.25$, as previously observed for the results reported in Figure 4-2. Table 4-2 summarizes the parameters considered and their corresponding values, and Table 4-3 shows the material properties considered as constants and their values used in the FE simulations. The combination of the different parameter values results in a total of 3,456 nonlinear FE analyses considered in this parametric study. Additional details on the selection of parameters and their respective considered range can be found elsewhere (Zignago and Barbato 2021).

Table 4-2 – Design parameter values considered in the FE-based parametric study

Parameter	**Values**
Fiber type	Carbon (CFRP), Glass (GFRP)
CFRP ratio, ρ_f (%)	0, 0.25, 0.5, 1, 2, 3
GFRP ratio, ρ_f (%)	0, 0.5, 1, 2, 4, 6
Column diameter, D (mm)	150, 300, 600, 1200
Concrete strength, f'_c (MPa)	20, 30, 50, 70
Transverse steel ratio, ρ_{st} (%)	0, 0.5, 1, 2, 3, 4
Eccentricity ratio, e/D	0.05, 0.15, 0.25

Table 4-3 - Material properties modeled as constants in the FE-based parametric study

Material	Properties	Value
Transverse steel	Yield strength, f_{yt} (MPa)	450
	Young's modulus, E_{st} (GPa)	200
Longitudinal steel	Strain hardening ratio, b (-)	0.005
	Yield strength, f_{yl} (MPa)	450
	Young's modulus, E_{sl} (GPa)	200
	Longitudinal steel ratio, ρ_{sl} (%)	1.0
CFRP	Tensile strength, f_{fu} (MPa)	1200
	Young's modulus, E_f (GPa)	100
GFRP	Tensile strength, f_{fu} (MPa)	600
	Young's modulus, E_f (GPa)	25

4.5.1 Results obtained from the parametric study

The parametric study results are reported here in terms of the combined strengths for any given eccentricity ratio e/D, as defined in Eq. (4-2). In particular, the following quantities are considered: (1) the combined strength accounting for both FRP and steel confinement effects, $R_{\max}$ and $\overline{R}_{\max}$; (2) the combined strength accounting only for the FRP confinement (i.e., with $\rho_{st} = 0\%$), R_{f0} and $\overline{R}_{f0}$; and (3) the combined strength of the unconfined column (i.e., with $\rho_f = 0\%$ and $\rho_{st} = 0\%$), $R_0 = \overline{R}_0$, which also represents the reference conditions for all other columns with the same properties and same eccentricity ratio, but different values of ρ_f and ρ_{st}. All quantities without a superposed bar correspond to the maximum combined strength obtained by subjecting the corresponding column to a monotonically increasing displacement-controlled loading with a constant eccentricity ratio up to failure (i.e., up to rupture of the external FRP wraps for columns with $\rho_f > 0\%$); these quantities can be used to predict the experimental structural behavior of specimens loaded up to failure (Zignago and Barbato 2021). By contrast, all quantities with a

superposed bar are obtained using the same loading procedure but ending the analysis when the design strain limitations recommended by the ACI 440.2R-17 guidelines (ACI 2017) are applied. In particular, unconfined columns are assumed to reach their ultimate axial and flexural capacities when the maximum strain at the extreme concrete compression fiber is equal to 0.003 as per ACI 318-19 (ACI 2019); whereas FRP-confined columns are subject to two strain design limitations (ACI 2017): (1) the maximum compressive strain of concrete to avoid concrete crushing, which is given by:

$$\varepsilon_{c,\max} \le \varepsilon_c' \cdot \left[1.5 + 12\kappa_b \cdot \frac{f_{lf}}{f_c'} \cdot \left(\frac{\varepsilon_{fe}}{\varepsilon_c'} \right)^{0.45} \right] \le 0.01 \tag{4-3}$$

where ε_c' is the unconfined concrete strain at peak stress; f_{lf} denotes the maximum confinement pressure exerted by the FRP; and κ_b is the geometry efficiency factor, which is equal to 1.0 for circular cross-sections; and (2) the maximum effective hoop strain of FRP wraps ε_{fe}, which is given by:

$$\varepsilon_{fe} = \kappa_\varepsilon \cdot \varepsilon_{fu} \le 0.004 \tag{4-4}$$

in which ε_{fu} is the ultimate strain of the FRP ply obtained from flat coupon tensile tests.

4.5.2 Combined strength increment due to simultaneous steel and FRP confinement

Figure 4-3 reports the relative combined strength increment $(\overline{R}_{\max} - R_0)/R_0$ versus the transverse steel reinforcement ratio ρ_{st} for columns with $f_c' = 30$ MPa retrofitted with CFRP jackets for different eccentricity ratios, FRP reinforcement ratios, and diameters. It is observed that this relative combined strength increment has a similar pattern for all the studied eccentricity ratios, indicating that $(\overline{R}_{\max} - R_0)/R_0$ is only slightly influenced by the eccentricity ratios for $e/D \le 0.25$.

FRP confinement alone can significantly enhance the combined strength, with an increase of approximately 70% for a CFRP reinforcement ratio ρ_f = 3% and ρ_{st} = 0%, independently of the eccentricity level. This strength enhancement can reach 111%, 107%, and 99% for $e/D = 0.05$, 0.15, and 0.25, respectively, when FRP and steel reinforcement ratios are at their maximum considered levels (i.e., ρ_f = 3% and ρ_{st} = 4%) and D = 1200 mm. For comparison, the improvement reported in Zignago and Barbato (2021) for pure compression (i.e., $e/D = 0$) was of 134%.

The contribution of transverse steel confinement to $(\bar{R}_{\max} - R_0)/R_0$ is highly dependent on and monotonically increases with the transverse steel reinforcement, ρ_{st}, and the cross-section diameter, D. The relative combined strength increments also monotonically increase for increasing FRP reinforcement ratios, ρ_f, albeit less significantly than the other two parameters; this increase is more pronounced for lower levels of ρ_f.

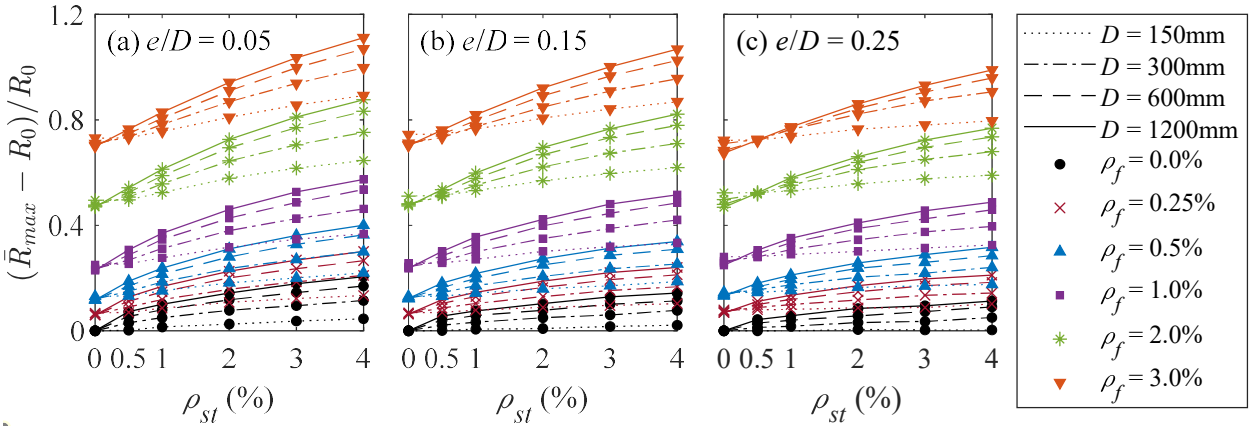

Figure 4-3. Effect of transverse steel confinement on the relative combined strength increment due to simultaneous steel and FRP confinement for FRP-confined RC columns with f_c' = 30 MPa for varying CFRP reinforcement ratio, column diameter, and eccentricity ratio: (a) e/D = 0.05; (b) e/D = 0.15; and (c) e/D = 0.25.

The maximum relative combined strength increment between columns with $\rho_{st} = 0\%$ and $\rho_{st} = 4\%$ is reached always for $\rho_f = 3\%$ and D = 1200 mm, and is equal to 41.2%, 36.5%, and 31.6% for $e / D = 0.05$, 0.15, and 0.25, respectively. This behavior is different from that observed for pure compression cases, for which the maximum relative combined strength increment was equal to 68.3% and was reached for $\rho_f = 1\%$, whereas it decreased for larger values of ρ_f (Zignago and Barbato 2021). This difference is explained by the additional limit imposed by ACI 440.2R-17 on the effective hoop strain of FRP wraps on FRP-confined RC columns, which affects the compressive concrete strain limit: because the compressive concrete strain is further restricted in the case of eccentric loads, the lateral dilation of concrete is significantly limited, preventing the transverse steel confinement from fully developing, or even keeping the transverse steel ties and/or hoops from yielding. This phenomenon is accentuated by the rotation of the cross-section, which makes the outermost fiber in the concrete core subject to compressive strains always smaller than that of the outermost concrete fiber in the cover (assuming a linear strain profile within the cross-section), hence delaying the transverse steel yielding even further.

Figure 4-4 plots $(\overline{R}_{\max} - R_0) / R_0$ versus ρ_{st} for 600-mm diameter RC columns strengthened with FRP wraps with a confining stiffness K_f = 0.5 GPa (corresponding to CFRP reinforcement ratio $\rho_f = 1\%$ or GFRP reinforcement ratio $\rho_f = 4\%$), for different FRP material types, concrete compressive strengths, and eccentricity ratios.

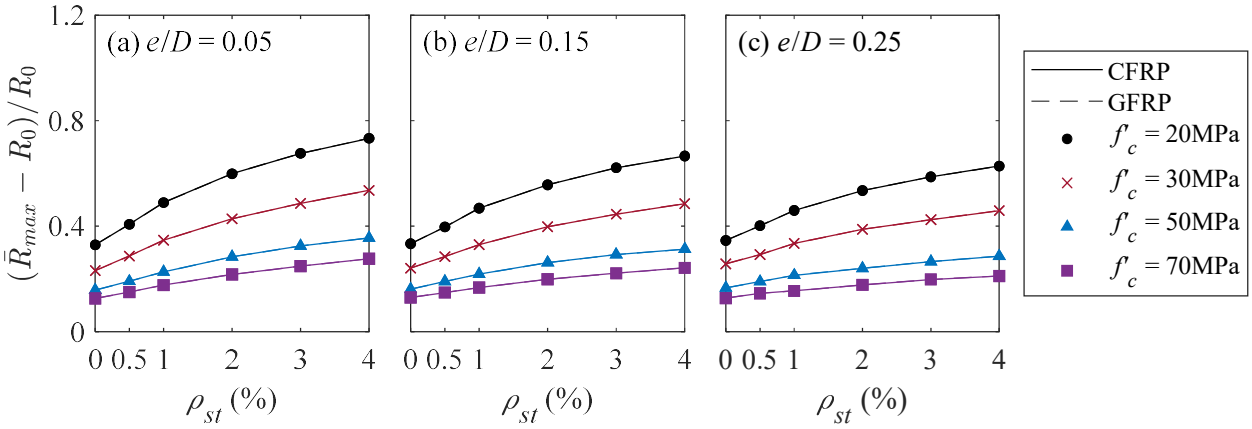

Figure 4-4. Effect of transverse steel confinement on the relative combined strength increment due to simultaneous steel and FRP confinement for FRP-confined RC columns with D = 600 mm and K_f = 0.5 GPa for varying FRP type, concrete strength, and eccentricity ratio: (a) e/D = 0.05; (b) e/D = 0.15; and (c) e/D = 0.25.

The relative combined strength increment is highly dependent on the concrete compressive strength, f'_c, and increases for decreasing concrete compressive strengths. The eccentricity ratio has a small influence on $(\bar{R}_{\max} - R_0)/R_0$ values, which slightly decrease for increasing eccentricity ratios. The material type has no influence on $(\bar{R}_{\max} - R_0)/R_0$ for a similar confining stiffness, because the FRP effective hoop strain is limited to the same value ε_{fe} = 0.004. The relative combined strength increments between columns with $\rho_{st} = 0\%$ and $\rho_{st} = 4\%$ are more pronounced for lower concrete strengths, and reach their maximum values for $f'_c = 20$ MPa, which are equal to 40.4%, 33.3%, and 28.2% for $e/D = 0.05$, 0.15, and 0.25, respectively.

4.5.3 Effects of strain design limits on combined strength

This study investigates the effects of design limits on the concrete compressive strain $\varepsilon_{c,\max}$ in Eq. (4-3), and on the FRP hoop strain ε_{fe} in Eq. (4-4) on the combined strength of FRP-confined RC columns. Figure 4-5 reports the relative combined strength increment $(R_{\max} - \bar{R}_{\max})/R_0$ versus the

transverse steel reinforcement ratio ρ_{st} for columns with $f'_c = 30$ MPa retrofitted with CFRP jackets for different eccentricity ratios, FRP reinforcement ratios, and diameters.

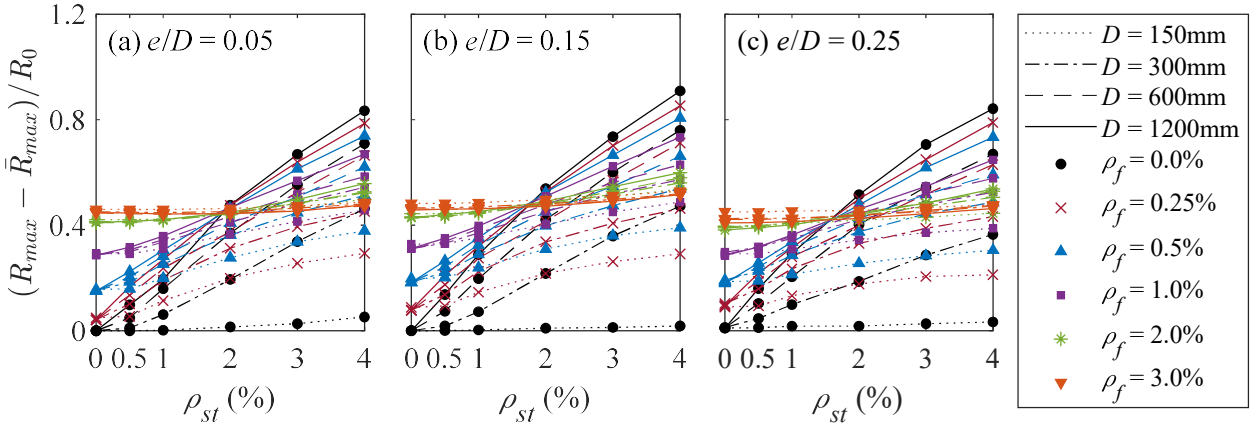

Figure 4-5. Effect of ACI 440.2R-17 strain design limits on the combined strength of FRP-confined RC columns with $f'_c = 30$ MPa for varying CFRP reinforcement ratio, column diameter and eccentricity ratio: (a) $e/D = 0.05$; (b) $e/D = 0.10$; and (c) $e/D = 0.15$.

As shown in Figure 4-5, the effects of the design strain limits are quite complex, but they follow similar patterns for all eccentricity ratios considered in this study. RC columns with small FRP ratios, large transverse steel reinforcement ratios, and large diameters are most affected by the imposed limits. The maximum normalized reduction in combined strength occurs for columns with $\rho_f = 0\%$, $\rho_{st} = 4\%$, and $D = 1{,}200$ mm, and is equal to 83.4%, 90.9%, and 84.2% for $e/D = 0.05$, 0.15, and 0.25, respectively. This result is because $\varepsilon_{c,\max}$ is not affected by ρ_{st} and corresponds to a stricter deformation limit on columns strengthened with low amounts of FRP. For these columns, the steel confinement mechanism cannot be fully activated. This reduction is found to be more pronounced than the 66% strength reduction observed for FRP-confined RC columns subject to pure axial loads (Zignago and Barbato 2021). Conversely, columns with high amounts of FRP (i.e., $\rho_f \geq 2.0\%$) are the most affected by the design strain limits when lightly reinforced with transverse steel (i.e., $\rho_{st} < 2\%$), and this effect is almost independent on ρ_{st} and D, and only

weakly dependent on the eccentricity ratio. In fact, the $(R_{\max} - \bar{R}_{\max})/R_0$ values for columns with $\rho_f = 3\%$ are contained between 41% and 51% among all combinations of parameters considered in Figure 4-5.

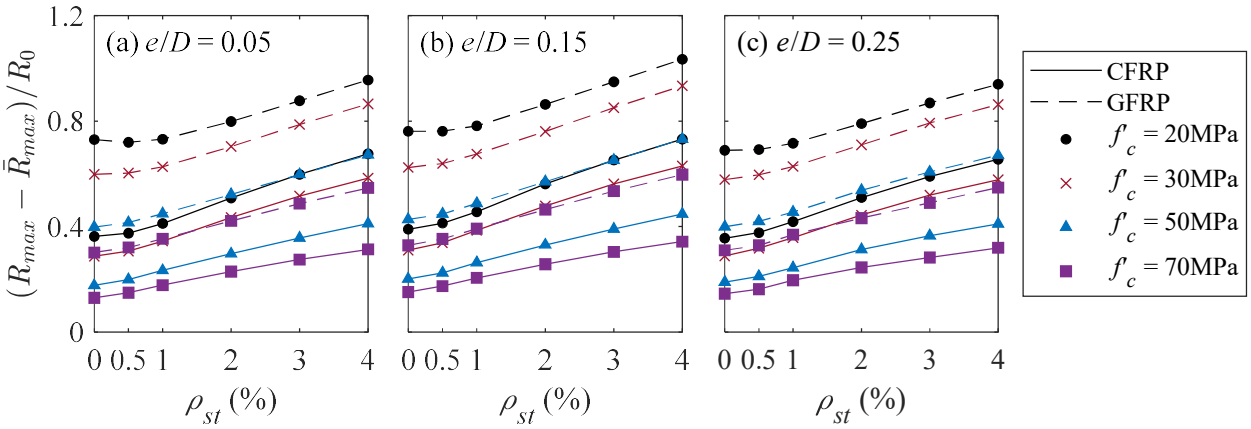

Figure 4-6. Effect of ACI 440.2R-17 strain design limits on the combined strength of FRP-confined RC columns with D = 600 mm and K_f = 0.5 GPa for varying FRP type, concrete strength, and eccentricity ratio: (a) e/D = 0.05; (b) e/D = 0.10; and (c) e/D = 0.15.

Figure 4-6 plots $(R_{\max} - \bar{R}_{\max})/R_0$ versus ρ_{st} for 600-mm diameter columns strengthened with an FRP confining stiffness $K_f = 0.5$ GPa, and varying eccentricity ratio, fiber type, and concrete compressive strength. Also in this case, the effects of the load eccentricity ratio are small. The $(R_{\max} - \bar{R}_{\max})/R_0$ increase for decreasing concrete compressive strength. When everything else is equal, the combined strength of columns confined using GFRP is significantly more affected by the design strain limits than that of CFRP-confined columns (with a difference contained between 16.5% and 37.1%). This phenomenon is consistent with results available in the literature for FRP-confined RC columns subjected to concentric axial load, although the $(R_{\max} - \bar{R}_{\max})/R_0$ values for eccentrically-loaded columns are significantly higher than those corresponding to pure axial loads (Zignago and Barbato 2021), because of the absence of the design strain limit on ε_{fe}. For example, $(R_{\max} - \bar{R}_{\max})/R_0$ is equal to 95.6%, 103.4%, and 94.0% for a column retrofitted with GRFP wraps

with $f_c' = 20$ MPa, $\rho_{st} = 0\%$, and $e/D = 0.05$, 0.15, and 0.25, respectively, whereas $(R_{\max} - \overline{R}_{\max})/R_0 = 60\%$ for the same column and $e/D = 0$ (pure axial load).

4.5.4 Effects of transverse steel confinement on combined strength

Figure 4-7 plots $(\overline{R}_{\max} - \overline{R}_{f0})/R_0$ versus ρ_{st} for CFRP-confined columns with $f_c' = 30$ MPa and varying levels of ρ_f, D, and e/D. Figure 4-8 plots $(\overline{R}_{\max} - \overline{R}_{f0})/R_0$ versus ρ_{st} for FRP-confined columns with $D = 600$ mm and $K_f = 0.5$ GPa and varying FRP type, f_c', and e/D. These results quantify the confinement effects on the combined strength due only to the internal steel reinforcement of FRP-strengthened RC columns.

In Figure 4-7, it is observed that $(\overline{R}_{\max} - \overline{R}_{f0})/R_0$ increases for increasing values of (in decreasing order of importance) ρ_{st}, D, and ρ_f, and decreases for increasing e/D. The maximum increments occur for columns with $\rho_f = 3\%$, $\rho_{st} = 4\%$, and $D = 1{,}200$ mm, and are equal to 41.2%, 36.5%, and 31.6% for $e/D = 0.05$, 0.15, and 0.25, respectively. It is observed that the $(\overline{R}_{\max} - \overline{R}_{f0})/R_0$ values for $\rho_f = 2\%$ are very close to those for $\rho_f = 3\%$. Figure 4-8 shows that the $(\overline{R}_{\max} - \overline{R}_{f0})/R_0$ significantly decreases for decreasing f_c' and e/D, whereas it is insensitive to the FRP type because of the FRP hoop strain limitation. For $f_c' = 20$ MPa, $(\overline{R}_{\max} - \overline{R}_{f0})/R_0$ is equal to 40.4%, 33.3%, and 28.2% for $e/D = 0.05$, 0.15, and 0.25, respectively.

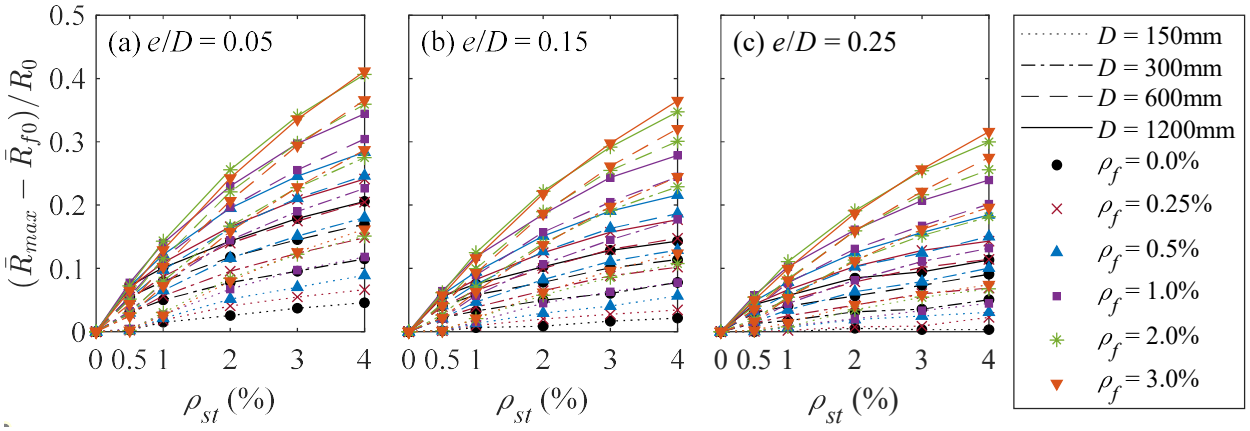

Figure 4-7. Transverse steel confinement contribution to the combined strength, $(\bar{R}_{\max} - \bar{R}_{f0})/R_0$, of FRP-confined columns with $f_c' = 30$ MPa for varying levels CFRP reinforcement ratio, column diameter, and eccentricity ratio: (a) $e/D = 0.05$; (b) $e/D = 0.15$; and (c) $e/D = 0.25$.

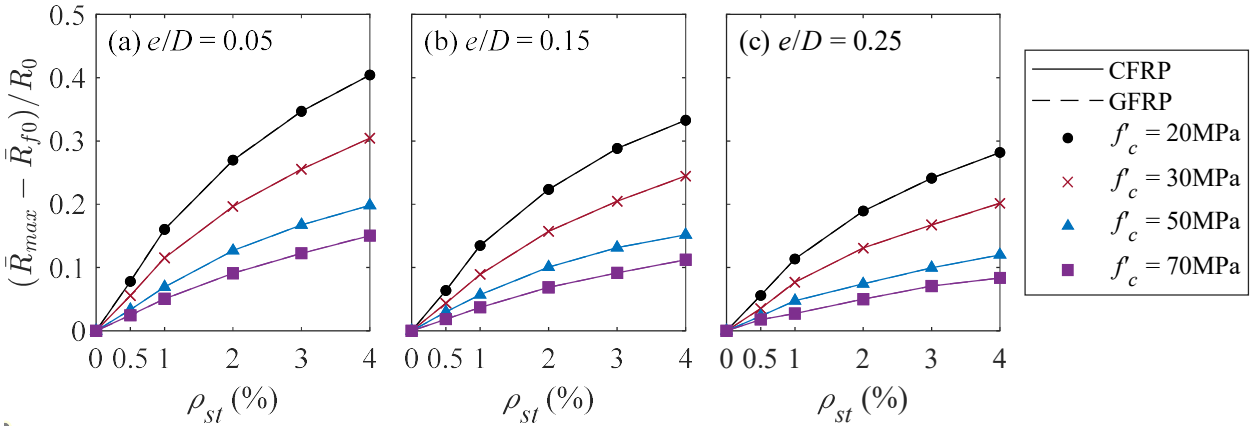

Figure 4-8. Transverse steel confinement contribution to the combined strength, $(\bar{R}_{\max} - \bar{R}_{f0})/R_0$, of FRP-confined columns with $D = 600$ mm and $K_f = 0.5$ GPa for varying FRP type, concrete strength, and eccentricity ratio: (a) $e/D = 0.05$; (b) $e/D = 0.15$; and (c) $e/D = 0.25$.

4.6 Modified synthetic parameters describing the transverse steel confinement effects

Previous studies have proposed two synthetic parameters to describe the effects of transverse steel confinement on the peak axial strength of axially-loaded FRP-confined RC columns: c_f and C_s (Zignago et al. 2018; Zignago and Barbato 2019, 2021). Coefficient c_f represents the steel-to-FRP confinement pressure ratio at rupture of the FRP, and is highly correlated with the axial

strength increment produced by the internal steel confinement of FRP-confined RC columns at failure conditions, thus being useful in simulating experimental results (Zignago et al. 2018; Zignago and Barbato 2021). Coefficient C_s represents a scaled ratio the steel confinement pressure and the FRP confinement stiffness (Zignago and Barbato 2021), and is highly correlated with the axial strength increment produced by the internal steel confinement of FRP-confined RC columns subjected to the design strain limits given in Eq. (4-1) (ACI 2017), thus being useful in design-oriented applications (Zignago and Barbato 2022). Both parameters have been shown to perform better for $f_{lf} / f_c' \geq 0.08$, i.e., when the FRP confinement ratio is sufficient to prevent a softening behavior in the confined concrete (Spoelstra and Monti 1999; Lam and Teng 2003a).

Figure 4-9(a) plots $(R_{\max} - R_{f0}) / R_{f0}$ versus c_f for $f_{lf} / f_c' \geq 0.08$ when the design strain limits are not considered. The data presented in Figure 4-9(a) includes both the cases with $e/D > 0$ (obtained in the present study) and those for columns subjected to pure axial load (i.e., with $e/D = 0$), which were presented in Zignago and Barbato (2021). Bilinear fit models for the concentrically-loaded and eccentrically-loaded columns are also shown. The two bilinear fits are almost coincident. The coefficients of determination, R^2, for these bilinear fits are $R^2 = 0.924$ for $e/D > 0$ and $R^2 = 0.982$ for $e/D = 0$, suggesting a slightly higher scatter for the columns subjected to a combination of axial load and bending moment.

Figure 4-9(b) plots $(\overline{R}_{\max} - \overline{R}_{f0}) / \overline{R}_{f0}$ versus C_s for $f_{lf} / f_c' \geq 0.08$ when the design strain limits are imposed in the FE analysis. Also this data set includes the FE analysis results from the present study for eccentrically-loaded columns (i.e., with $e/D > 0$) and the results for concentrically-loaded columns (i.e., $e/D = 0$) reported in Zignago and Barbato (2021), which are plotted in conjunction with their respective bilinear fits. It is observed that the additional limitation on the FRP hoop strain (i.e., $\varepsilon_{fe} \leq 0.004$) for columns subject to combined axial compression and bending moment,

in conjunction with the $f_{lf} / f_c' \geq 0.08$ requirements, drastically limits the possible values of the relative confinement coefficient C_s. In fact, C_s is always less than 165% for eccentrically-loaded columns, with a maximum increment in combined strength due to the internal steel confinement only $\max[(\bar{R}_{\max} - \bar{R}_{f0}) / \bar{R}_{f0}] = 34.6\%$; whereas C_s can reach values as high as 661% for columns subjected to pure axial loads, with $\max[(\bar{R}_{\max} - \bar{R}_{f0}) / \bar{R}_{f0}] = 95\%$. The two branches of the bilinear fits have similar slopes; however, as another effect of the FRP hoop strain limitation, the slope change of the bilinear fit for $e/D > 0$ takes place at a lower value of C_s (i.e., $C_s = 51\%$), when compared to the bilinear fit for $e/D = 0$ (i.e., $C_s = 97\%$). Also in this case, the coefficients of determination are high (i.e., $R^2 = 0.957$ for $e/D = 0$ and $R^2 = 0.861$ for $e/D > 0$), with a higher dispersion for the columns subjected to combined axial forces and bending moments.

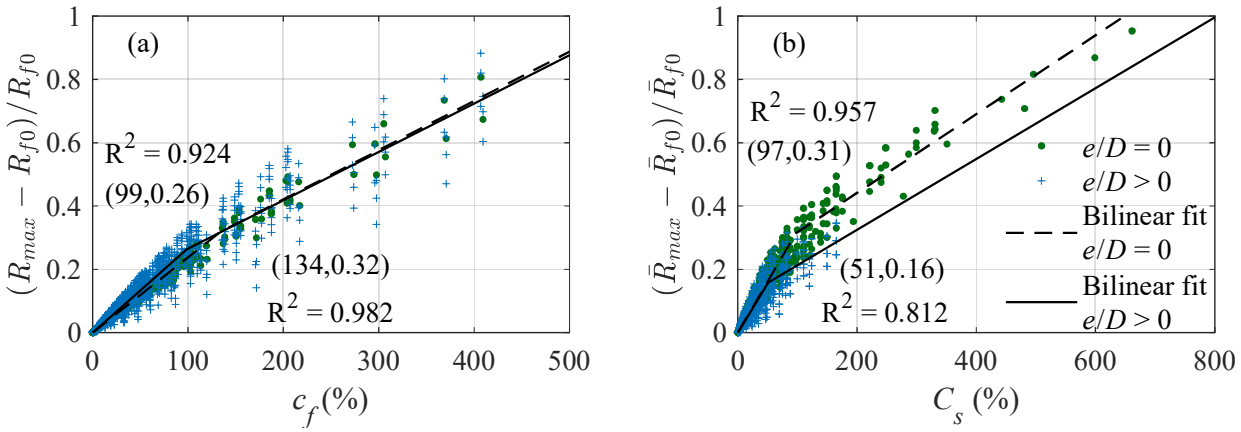

Figure 4-9. Relative contribution of transverse steel confinement to combined strength increment $(R_{\max} - R_{f0}) / R_{f0}$ as a function of relative confinement coefficient: (a) c_f; and (b) C_s.

The increased dispersion in the bilinear fit models for $e/D > 0$ suggests that eccentricity-independent confinement coefficients might not be ideal to describe the normalized resultant strength increment due to transverse steel confinement for varying eccentricity levels. For this

reason, a modification to the relative confinement coefficients c_f and C_s is proposed here to account for the effects of the eccentricity ratio *e*/*D*. The newly proposed coefficients are given by:

$$c_{fm} = \left(\frac{f_{ls}}{f_{lf}}\right)^{1-0.6(e/D)} \cdot \left(\frac{A_c}{A_g}\right)^{1+2.2(e/D)} \tag{4-5}$$

$$C_{sm} = \left(\frac{100 f_{ls}}{K_f}\right)^{1-1.2(e/D)} \cdot \left(\frac{A_c}{A_g}\right)^{1+8.6(e/D)} \tag{4-6}$$

These functional forms were selected so to provide the best bilinear fit to all data (i.e., for both $e/D > 0$ and $e/D = 0$) while converging to the corresponding original relative confinement coefficient when $e/D = 0$.

Figure 4-10(a) plots the $(R_{\max} - R_{f0}) / R_{f0}$ values versus c_{fm} in conjunction with the corresponding bilinear fit, which achieves a very good coefficient of determination ($R^2 = 0.953$). Based on the bilinear model, a small change in slope takes place at $c_{fm} = 130\%$ and $(R_{\max} - R_{f0}) / R_{f0} = 35\%$, suggesting only a minor reduction of the steel confinement effect for large values of c_{fm}. Figure 4-10(b) plots $(\overline{R}_{\max} - \overline{R}_{f0}) / \overline{R}_{f0}$ versus C_{sm} with the corresponding bilinear fit. Also in this case, the coefficient of determination is high (i.e., $R^2 = 0.942$). The change of slope is more pronounced than for the previous case and takes place at $C_{sm} = 63\%$ and $(\overline{R}_{\max} - \overline{R}_{f0}) / \overline{R}_{f0} = 22\%$, suggesting a more significant reduction of the steel confinement effect for large values of C_{sm}. The high values of the coefficients of determination of the bilinear fits presented in Figure 4-10 indicates that the newly proposed modified relative confinement coefficients, c_{fm} and C_{sm}, can be reliably used to predict the internal steel confinement contribution to the combined strengths $R_{\max}$ and $\overline{R}_{\max}$, respectively.

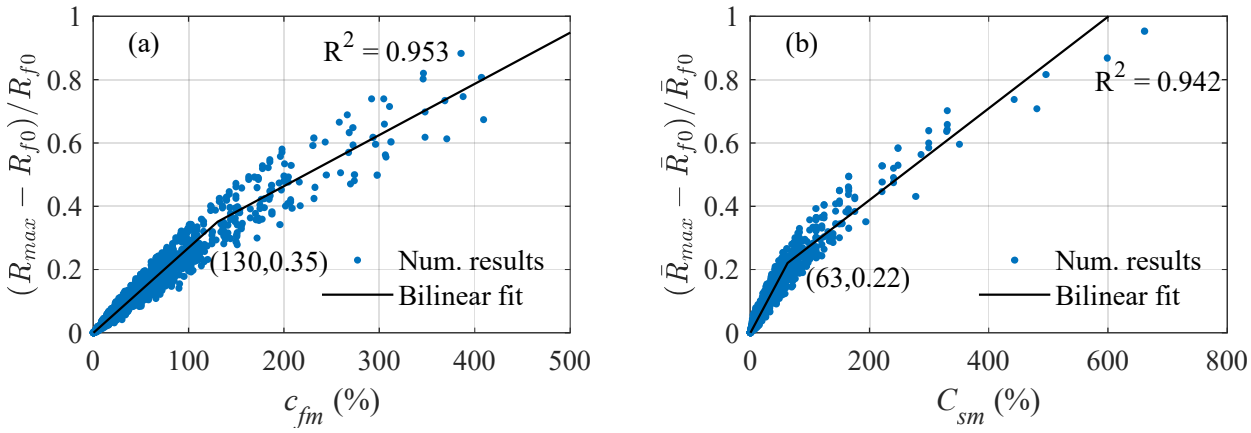

Figure 4-10. Relative contribution of transverse steel confinement to combined strength increment as a function of modified relative confinement coefficient: (a) $(R_{\max} - R_{f0}) / R_{f0}$ versus c_{fm}, and (b) $(\overline{R}_{\max} - \overline{R}_{f0}) / \overline{R}_{f0}$ versus C_{sm}.

4.7 Conclusions

This study numerically investigates the effects of the confinement produced by internal steel reinforcement on the strength of FRP-wrapped circular RC columns subject to a combination of axial compression and bending moment. First, the accuracy of a recently-developed FRP-and-steel confined concrete uniaxial model (Zignago et al. 2018) is validated against experimental data available in the literature. The FRP-and-steel confined concrete model is employed to generate axial force-bending moment (*P-M*) interaction diagrams of FRP-confined RC columns experimentally tested for different eccentricities. It is shown that this model is significantly more accurate in predicting the combined axial force-bending moment strength than a confined concrete model that considers only the effects of the FRP confinement.

Second, an extensive numerical parametric analysis based on this FRP-and-steel confined concrete model is performed considering several key design parameters, i.e., fiber type, FRP volumetric ratio, transverse steel volumetric ratio, column diameter, unconfined concrete strength, and eccentricity ratio. This parametric study involves a total of 3,456 nonlinear FE analyses performed

by monotonically and proportionally increasing axial forces and bending moments. The combined strength of FRP-confined RC columns is defined as the distance between the origin and the point on the normalized *P-M* interaction diagram corresponding to the maximum load achieved for a given eccentricity. The following quantities are considered: (1) combined strength considering both FRP and steel confinement, $R_{\max}$ and $\overline{R}_{\max}$; (2) combined strength considering only FRP confinement, R_{f0} and $\overline{R}_{f0}$; and (3) combined strength of the reference columns without any confinement, R_0. In this study, the overbar notation indicates FE analysis results that are obtained by imposing the concrete and FRP hoop strain limits recommended by the ACI 440.2R-17 design provisions. The parametric study results show that the normalized combined strength increment $(\overline{R}_{\max} - R_0)/R_0$ due to simultaneous FRP and steel confinement can be as high as 111%, and this increment slightly decreases as the eccentricity increases. The quantity $(\overline{R}_{\max} - R_0)/R_0$ is positively correlated with FRP ratio, transverse steel reinforcement ratio, and column diameter, and negatively correlated with the unconfined concrete strength. Because of the FRP effective hoop strain design limit provision, the fiber type is found to have no influence on the column's normalized combined strength increment when the FRP confining stiffness is kept constant. The design limitation on the FRP hoop strain was found to severely impact the column strength, with the normalized reduction in combined strength, $(R_{\max} - \overline{R}_{\max})/R_0$, being as high as 90.9%.

Finally, two new modified relative confinement coefficients, c_{fm} and C_{sm}, are proposed to quantify the effects of internal steel confinement by taking into account the effects of load eccentricity. It is shown that contribution of the internal steel confinement to the combined strength, $(R_{\max} - R_{f0})/R_{f0}$ and $(\overline{R}_{\max} - \overline{R}_{f0})/\overline{R}_{f0}$, can be accurately described by a bilinear fit as a function of the corresponding modified relative confinement coefficient, c_{fm} and C_{sm},

respectively. It is concluded that c_{fm} can be used to estimate the internal steel confinement contribution to the combined strength of FRP-confined RC columns at ultimate conditions; whereas C_{sm} can be used to estimate the internal steel confinement contribution to the design strength of FRP-confined RC columns.

Further investigations are needed to develop a reliability-based design procedure that is able to account for the internal steel confinement effects in FRP-confined RC columns subject to combined axial loads and bending moments. The results presented in this study are valid for columns with circular cross-section, and additional studies are necessary to extend these results to FRP-confined RC columns with different cross-section geometry.

5 Reliability-based calibration of new design procedure for reinforced concrete columns under simultaneous confinement by fiber-reinforced polymers and steel

The results from the parametric study in Chapter 3 are used to propose a modification to the design equation for FRP-confined RC circular columns subject to pure compression with the objective to produce a more efficient retrofit while keeping acceptable reliability levels. This design equation accounts for the simultaneous confinement effects of internal transverse steel and externally-wrapped FRP and is calibrated via structural reliability analysis methods. A new iterative design procedure is also proposed and demonstrated via a realistic application example.

5.1 Introduction

Externally-bonded fiber-reinforced polymer (FRP) systems have been adopted as an alternative to traditional materials and techniques for the retrofit of existing reinforced concrete (RC) structures, as they have been shown to be efficient and effective in strengthening and repairing aging RC structures, such as building columns and bridge piers (Rocca 2007; Roy et al. 2010; Parvin and Brighton 2014). In particular, FRP jacketing of columns can be used to: (1) increase the axial strength through a confinement effect; (2) provide confinement to improve ductility requirements; (3) improve corrosion resistance and/or repair corroded members; (4) improve seismic behavior; (5) prevent longitudinal rebar buckling; and (6) strengthen lap splices (Parvin and Brighton 2014; ACI 2017). This paper focuses on the design of FRP confinement to increase the axial strength of the compression members. In this case, the surface bonded FRP improves the columns' strength and ductility through a confinement effect, in which the lateral dilation of concrete is restricted due to the confining action of the FRP sheets (Fardis and Khalili 1982). In the concrete core of an RC member, the lateral confining pressure exerted by the externally-bonded FRP sheets acts in addition to that produced by the existing internal transverse steel (e.g., steel ties and spirals),

although most of the stress-strain models for FRP-confined concrete found in the literature ignore the confining contribution from the existing transverse steel (Fardis and Khalili 1982; Spoelstra and Monti 1999; Lam and Teng 2003a), and only very few concrete constitutive models that account for the simultaneous confining mechanisms of FRP and steel are available (Wang and Restrepo 2001; Eid and Paultre 2008; Teng et al. 2015; Zignago et al. 2018).

A number of international design standards and guidelines address the FRP confinement phenomenon in RC columns (GB50608 2010; DAfStb 2012; CNR-DT-200-R1 2013; ACI 2017; CSA 2017), differing in several aspects that include adopted predictive models, covered loading conditions and limits states, and limitations on cross-section dimensions and FRP wrapping schemes (Kaeseberg et al. 2019). Only ACI 440.2R-17 (ACI 2017) and the Italian CNR-DT-200-R1 (2013) guidelines address explicitly the design for pure compression as an independent loading condition, whereas the other guidelines focus on the more common loading condition of combined axial load and bending moment in which the pure compression condition is considered only to build the axial force-bending moment interaction diagram for a given column. In addition, only the German guidelines (DAfStb 2012) adopt a predictive model that considers the interaction of transverse steel and FRP confining actions by including the lateral confining pressure from transverse steel into the equation for the confined concrete strength. A detailed comparison of design approaches for FRP confinement of RC structures used in different international design codes and guidelines can be found in Kaeseberg et al. (2019). A few studies (Val 2003; Zou and Hong 2011; Casas and Chambi 2014; Wang and Ellingwood 2015; Baji et al. 2016; Baji 2017) have conducted reliability assessments of FRP-wrapped RC columns. These studies were based on confinement models for FRP-only confined concrete, mainly to calibrate partial safety factors and resistance reduction factors for confined concrete and FRP materials.

This paper proposes a new design equation, based on an existing equation in ACI 440.2R-17 (ACI 2017), for the axial capacity of FRP-confined RC circular columns. This new design equation accounts for the effects of the transverse steel confinement based on rigorous structural reliability procedures. In this study, the statistical distribution of the axial capacity of FRP-wrapped RC columns is estimated via Monte Carlo simulation based on advanced nonlinear finite element (FE) response analysis. The FE analyses employ a zero-length element with fiber-discretized cross-sections (Barbato 2009; Hu and Barbato 2014) and a material constitutive model for FRP-and-steel confined concrete (Zignago et al. 2018), which provide a computationally inexpensive and accurate tool to model the highly nonlinear behavior of FRP-confined RC columns under a wide range of parameters. This modeling tool is particularly suited for structural reliability analysis applications, which generally require considerable numbers of FE analyses.

This paper focuses on axially-loaded RC circular columns with preserved structural integrity (i.e., undamaged columns), which are retrofitted using externally-bonded FRP confinement. This study does not consider the effect of aggressive environment exposure on the durability of FRP-confined RC columns. A detailed review on the long-term safety of FRP-confined RC columns exposed to harsh environment can be found in Micelli et al. (2015).

The paper is organized as follows: the analysis-oriented model used to estimate the axial strength of FRP-confined RC columns is established and validated; the parameters involved in the analysis are identified and reduced through a dimensional analysis; the parametric design space is defined based on the realistic ranges of the different design parameters; the capacity and demand statistical models are developed; the proposed design equation is presented, calibrated, compared with admissible alternative forms, and validated in terms of reliability index values; and an iterative

design procedure is proposed and presented through a case study. Finally, the conclusions are presented, summarizing the main findings of this paper.

5.2 Novelty and relevance

Existing design equations for the axial capacity of FRP-confined RC columns do not account for the combined confinement effect due to internal steel reinforcement. The present manuscript proposes for the first time a simple modification of the design equation to take into account this effect based on reliability analysis principles. The development of a probabilistic model for the structural capacity employing nonlinear FE-based Monte Carlo simulation, is also new when applied to calibration of a design equation for FRP-confined RC columns. In fact, this study decouples the capacity term used in the structural reliability calculations, which is obtained here from nonlinear FE analyses based on an accurate analysis-oriented model for FRP-and-steel confined concrete, from the design strength obtained using a closed-form design equation. This methodology is different from those used, e.g., in Zou and Hong (2011), Casas and Chambi (2014), Wang and Ellingwood (2015), Baji et al. (2016), and Baji (2017), where an approximate closed-form equation was used to estimate the capacity term in the stuctural reliability calculations. In particular, the approach used in the present study provides more accurate and less disperse estimates of the structural reliability indices when compared to investigations using the same closed-form equation for both structural reliability and design calculations. This manuscript is also the first structural reliability analysis study of FRP-wrapped RC columns based on an FRP-and-steel confined concrete model.

In terms of relevance, the design equation for FRP-confined RC columns loaded in pure compression is rarely used, as RC columns that can be considered nominally loaded only in compression are rare. Notwithstanding this consideration, the newly proposed design equation

represents an improvement with respect to the existing one for this loading condition. More importantly, the calculation of the design strength for this loading case is essential to build the axial force-bending moment interaction diagram that is needed for the very common design case of columns loaded through a combination of axial compression and bending moment.

5.3 Adopted model for simultaneous FRP-and-steel confined concrete: description and validation

To estimate the axial strength of an FRP-confined RC column, this investigation adopts the analysis-oriented material constitutive model for concrete simultaneously confined with FRP and steel developed by Zignago et al. (2018). This constitutive model rigorously accounts for the complex nonlinear phenomenon associated with the concurrent confinement of concrete by FRP and steel at the local level through a superposition of the confining pressures produced by the two confining mechanisms. It is based on an incremental-iterative approach that enforces equilibrium and compatibility of the radial deformation of concrete and the confining device (FRP and steel) at the interface of these materials. It has been shown that the superposition of confining pressure at the material level provides a significantly improved estimate of the ultimate strength of an FRP-confined column when compared to the direct superposition of the independent confining effects (Zignago et al. 2018). This model can be used to predict the compressive strength of FRP-confined columns through nonlinear FE analysis, thus providing strength estimates that are generally more accurate than those obtained from simplified closed-form mathematical expressions, as typically done with design-oriented models of FRP-confined concrete.

The Zignago et al. (2018) model was validated against the experimental load-carrying capacity of 46 axially-loaded FRP-confined RC specimens available in the literature and reported by nine different authors. These experimental results were purposely selected among those available in the

literature to represent columns with significant amounts of transverse steel (i.e., significant steel confinement), as the focus was to quantify the effects of simultaneous concrete confinement by steel and FRP. The model was found to be accurate in numerically predicting the axial strength of the FRP-confined columns, with an average absolute normalized error between the experimental and numerical results equal to 7.6%, and a maximum absolute normalized error equal to 32.4%. Figure 5-1(a) reports the comparison of the experimentally measured axial strengths $\left(P_{\max,\exp}\right)$ with those obtained from numerical simulation $\left(P_{\max,\text{num}}\right)$. In addition to the results based on the Zignago et al. (2018) model, Figure 5-1(a) also reports the estimations provided by the design-oriented model by Lam and Teng (2003a), which is the basis of the current design equation in ACI 440.2R-17 (ACI 2017), and the design-oriented model by Wang and Restrepo (2001), which includes the effects of the simultaneous confinement produced by the internal steel reinforcement and the externally-bonded FRP. The mean and coefficient of variation of the ratio between the numerical and the experimental estimates ($\xi = P_{\max,\exp}/P_{\max,\text{num}}$) of the columns' peak strength are equal to 1.01 and 0.12, respectively, for the analysis-oriented model by Zignago et al. (2018); to 1.35 and 0.16, respectively, for the Lam and Teng (2003a) design-oriented model; and to 1.19 and 0.12, respectively, for the Wang and Restrepo (2001) design-oriented model. The large bias of the Lam and Teng (2003a) design-oriented model is due to the fact that this model neglects the effects of the confinement produced by the internal steel reinforcement on the concrete core. The improved accuracy of the results for the Zignago et al. (2018) model when compared to those of the Wang and Restrepo (2001) model is mainly because the Zignago et al. (2018) model does not introduce any additional approximations needed to derive a design-oriented model.

Figure 5-1(b) reports the strength ratio $\xi = P_{\max,\exp}/P_{\max,\text{num}}$ for the same three confinement models as a function of the relative steel confinement coefficient C_s proposed in Zignago and Barbato

(2021) to describe the effects of transverse steel confinement in design applications. This coefficient is defined as:

$$C_s = \frac{100 f_{ls} \cdot A_c}{K_f \cdot A_g} \tag{5-1}$$

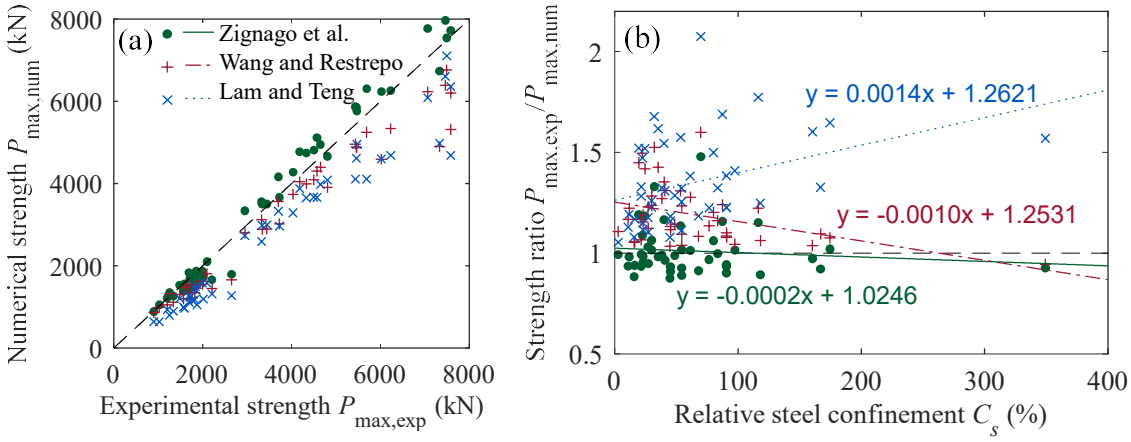

Figure 5-1. Experimental validation and comparison with other models of the proposed FRP-and-steel confined concrete: (a) comparison of numerically estimated and experimentally measured strength of FRP-confined RC columns, and (b) ratio of experimental to numerical strength as a function of C_s

in which f_{ls} represents the confining pressure exerted by internal steel; A_c is the area of core concrete; $K_f = 0.5\rho_f \cdot E_f$, with ρ_f = FRP volumetric reinforcement ratio, and E_f = FRP elastic modulus; and A_g is the gross cross sectional area. Figure 5-1(b) also includes the trend lines (and their respective equations) of the experimental to numerical strength ratios associated with the three considered models. It is observed that the strength ratio estimated with the Zignago et al. (2018) model assumes values close to 1.0 for any values of C_s, as indicated by the corresponding trend line having an intercept equal to 1.0246 and a slope equal to -0.0002, which demonstrates that the bias of this model is almost independent of C_s. The design-oriented Wang and Restrepo (2001) model presents estimates that are overall less accurate when compared to those obtained by using the analysis-oriented model by Zignago et al. (2018). Its trend line shows a non-negligible

negative slope (equal to -0.0010), which indicates that the model tends to underestimate the column's strength for lower values of C_s. Finally, the strength ratio estimated with the Lam and Teng (2003a) model, which considers only the effect of FRP confinement, significantly deviates from the ideal ratio of 1.0, with differences that increase as the coefficient C_s increases, i.e., it increasingly underestimates the column's strength for increasing values of C_s, as indicated by its trend line with a relatively large positive slope equal to 0.0014. It is concluded that the strength estimates obtained using the Zignago et al. (2018) model are the most accurate among the models considered in this study, and represent a significant improvement when compared to those obtained using the Lam and Teng (2003a) model and, thus, the current design equation in ACI 440.2R-17 (ACI 2017).

5.4 Dimensional analysis

A dimensional analysis is performed to identify the relevant parameters and the minimum number of parameter groups that can be used to describe the design of an FRP-confined RC column. The design equation for axial compression strength in ACI 440.2R-17 (ACI 2017) can be expressed as:

$$\phi \cdot P_n = \phi \cdot \alpha \cdot \left[0.85 f'_{cc} \cdot (A_g - A_{sl}) + f_{yl} \cdot A_{sl} \right] \geq \sum_i (\gamma_i \cdot Q_i) \tag{5-2}$$

in which ϕ is the strength reduction factor as per ACI 318-19 (ACI 2019); P_n denotes the nominal axial strength of the member; α is an nondimensional coefficient that assumes a value of 0.80 or 0.85, depending on the internal transverse steel type (ties or spirals, respectively); f'_{cc} is the confined concrete peak strength; A_{sl} is the total area of longitudinal reinforcing steel; f_{yl} is the yielding strength of longitudinal reinforcing steel; and γ_i and Q_i denote the partial load factors and the axial loads, respectively, corresponding to load case i in a given load combination considered for the design of the RC member. Based on Zignago et al. (2018), the best estimate of

the confined concrete peak strength f'_{cc} can be expressed as an implicit function of eight mechanical and geometric parameters as follows:

$$f'_{cc} = f'_{cc}\left(f'_c, E_c, \varepsilon'_c, f_{ls}, f_{lf}, \varepsilon_{fe}, A_c, A_g\right) \tag{5-3}$$

in which f'_c denotes the unconfined concrete strength; E_c denotes the initial (tangent) concrete stiffness; ε'_c denotes the unconfined concrete strain at peak strength; f_{lf} denotes the effective confining pressure applied by FRP wraps; and $\varepsilon_{fe} = \kappa_\varepsilon \cdot \varepsilon_{fu}$ denotes the effective strain of FRP at failure, in which κ_ε = FRP strain efficiency factor and ε_{fu} = ultimate strain of the FRP obtained from flat coupon tensile tests.

The load effects acting on a column derive from different load combinations of several load cases including, e.g., dead loads, live loads, wind loads, and seismic loads. This study considers the ultimate load combination due to dead and lives loads only, as specified by the ACI 318-19 standard (ACI 2019), which constitutes the most common governing load combination for axial compression of short columns in most practical cases (Israel et al. 1987), i.e.,

$$\sum_i \left(\gamma_i \cdot Q_i\right) = 1.2DL_n + 1.6LL_n \tag{5-4}$$

where DL_n and LL_n represent the nominal values of dead and live loads, respectively.

Considering that E_c and ε'_c can be approximately described as functions of f'_c, $n_v = 11$ variables are needed to describe Eq. (5-2), i.e., $V_V = \left\{P_n, f'_c, f_{ls}, f_{lf}, \varepsilon_{fu}, A_c, A_g, A_{sl}, f_{yl}, DL_n, LL_n\right\}$. By using the modified Buckingham's Π-theorem (Butterfield 1999), $m_v = 3$ independent primary dimensions can be selected (e.g., one quantity with dimension of stress, one with dimension of length, and one with dimension of force), and an acceptable set of repeating variables is $Q_v = \left\{f'_c, A_g, DL_n\right\}$. Thus, the minimum number of dimensionless groups is $N = n_v - m_v = 11 - 3 = 8$,

and a valid set of dimensionless groups is given by: $\pi_1 = P_n / f_c' A_g$, $\pi_2 = f_{yl} / f_c'$, $\pi_3 = f_{lf} / f_c'$, $\pi_4 = \varepsilon_{fu}$, $\pi_5 = A_c / A_g$, $\pi_6 = A_{sl} / A_g$, $\pi_7 = f_{ls} / f_c'$, and $\pi_8 = LL_n / DL_n$. In this study, the nondimensional parameter describing the effects of the lateral steel confinement pressure (i.e., π_7) is substituted by the dimensionless coefficient C_s defined by Eq. (5-1) and proposed in Zignago and Barbato (2021) to describe the effects of transverse steel confinement in design applications. Differently from the model proposed by Zignago et al. (2018) and described by Eq. (5-3), the value of f_{cc}' recommended by ACI 440.2R-17 (ACI 2017) for design purposes assumes a simple closed-form expression given by:

$$f_{cc}' = f_c' + \psi_f \cdot 3.3 \kappa_a \cdot f_{lf} \tag{5-5}$$

where $\psi_f = 0.95$ is a reduction factor, and κ_a is a shape factor equal to 1.0 for circular cross-sections. The corresponding maximum compressive strain in the FRP-confined concrete, ε_{ccu}, is given by:

$$\varepsilon_{ccu} = \varepsilon_c' \cdot \left[1.5 + 12 \kappa_b \cdot \frac{f_{lf}}{f_c'} \cdot \left(\frac{\varepsilon_{fe}}{\varepsilon_c'} \right)^{0.45} \right] \tag{5-6}$$

where κ_b is the geometry efficiency factor and is equal to 1.0 for circular cross-sections. This value should be limited to a maximum allowable strain $\varepsilon_{c,\max} = \varepsilon_{ccu} \leq 0.01$ to prevent excessive cracking and, in this case, f_{cc}' needs to be recalculated using the stress-strain model proposed in ACI 440.2R-17 (ACI 2017). Therefore, the physical similarity of the normalized axial strength (i.e., π_1) based on Eq. (5-2) is valid as long as the calculated value of ε_{ccu} is less than 0.01. This physical similarity is only approximately valid when the axial strength of a column is estimated using FE simulations, in which material nonlinearity and several other parameters are also needed to fully

describe the structural response (e.g., stress-strain model of concrete, steel strain hardening, load eccentricity). Thus, the presented dimensional analysis results are used in this study to allow a more compact representation of the structural reliability analysis results.

5.5 Parametric design space

Based on the dimensional analysis results, the design parameters considered in this study are: (1) ratio of longitudinal steel yield strength and concrete compressive strength, with four different levels, i.e., $f_{yl} / f_c' = 5.9,\ 8.3,\ 13.8,\ 20.7$ (corresponding to Grade 60 longitudinal rebars with $f_{yl} = 414$ MPa and concrete with $f_c' = 20$ MPa, 30 MPa, 50 MPa, and 70 MPa, respectively); (2) FRP confining ratio, with five different levels, i.e., $f_{lf} / f_c' = 0.08,\ 0.12,\ 0.2,\ 0.3,$ and 0.4; (3) ultimate FRP strain, with four different levels, i.e., $\varepsilon_{fu} = 0.01,\ 0.012,\ 0.018,\ 0.024$; (4) core to gross area ratio, with four different levels, i.e., $A_c / A_g = 0.6,\ 0.7,\ 0.8,$ and 0.9; (5) longitudinal steel ratio, with four different levels, i.e., $\rho_{sl} = A_{sl} / A_g = 1\%,\ 2\%,\ 4\%,$ and 8%; (6) nominal live to dead load ratio, with five different levels, i.e., $LL_n / DL_n = 0.2,\ 0.5,\ 1,\ 2,$ and 3; and (7) relative steel and FRP confinement coefficient C_s, with six different levels, i.e., $C_s = 0\%,\ 30\%,\ 60\%,\ 90\%,$ 120%, and 200%. The considered design parameters are summarized in Table 5-1 and correspond to a total of 38,400 possible design combinations. It is highlighted here that the parameters' ranges were deliberately chosen to be very wide, in order to include both common and extreme (i.e., allowable although unlikely) design conditions. This selection was performed to ensure that the design equation newly proposed in this study does not produce excessively low reliability index values (i.e., lower than 3.5), even under unlikely design conditions.

Table 5-1. Design parameters considered in the structural reliability analysis

Parameter	Values
f_{yl} / f_c'	5.9, 8.3, 13.8, 20.7
f_{lf} / f_c'	0.08, 0.12, 0.2, 0.3, 0.4
ε_{fu}	0.01, 0.012, 0.018, 0.024
A_c / A_g	0.6, 0.7, 0.8, 0.9
A_{sl} / A_g	0.01, 0.02, 0.04, 0.08
LL_n / DL_n	0.2, 0.5, 1, 2, 3
C_s (%)	0, 30, 60, 90, 120, 200

To facilitate the presentation and comparison of structural reliability analysis results, a reference column is defined hereinafter as a column with $f_{yl} / f_c' = 13.8$, $f_{lf} / f_c' = 0.12$, $\varepsilon_{fu} = 0.012$, $A_c / A_g = 0.8$, $\rho_{sl} = A_{sl} / A_g = 2\%$, and $LL_n / DL_n = 2$.

5.6 Structural reliability analysis and limit state function

The reliability of FRP-confined RC columns can be assessed through a limit state function, *g*, defined in the design space as:

$$g(\mathbf{X}) = R - (DL + LL) \tag{5-7}$$

where $\mathbf{X} = [R \quad DL \quad LL]^{\mathrm{T}}$ denotes the vector or random variables, whose statistical models need to be defined to realistically represent all uncertainties affecting structural performance, and superscript T denotes the matrix transpose operator. Eq. (5-7) corresponds to the difference between the capacity of the structure, *R*, and the demand (expressed as the sum of dead and live load models, *DL* and *LL*, respectively). Failure occurs when $g(\mathbf{X}) \le 0$, i.e., when the values of the random parameters describing the structural response and the loading environment fall in the so-called failure domain. The probability of failure, p_f, corresponds to the probability content of the failure domain, i.e.,

$$p_f = P\left[g(\mathbf{X}) \le 0 \right] \tag{5-8}$$

and can be used to evaluate the generalized reliability index, β, as (Ditlevsen and Madsen 2005):

$$\beta = \Phi^{-1}\left(1 - p_f\right) \tag{5-9}$$

where $\Phi^{-1}(\cdot)$ denotes the inverse of the standard normal cumulative distribution function.

Different structural reliability analysis methods can be employed to estimate the failure probability and the generalized reliability index, e.g., Monte Carlo simulation (MCS), the First-Order Reliability Method (FORM), the Second-Order Reliability Method (SORM), and Importance Sampling (IS) (Ditlevsen and Madsen 2005). MCS generates a large number of samples of the random variables in Eq. (5-7) and uses standard statistics methods to estimate p_f and β. FORM, SORM, and IS use the concept of "design point", which is defined geometrically as the point of minimum distance from the origin in the space of transformed standard normal random variables under the constraint $g(\mathbf{X}) \le 0$. From a structural engineering point of view, the design point represents the most likely failure point in the standard normal space. In this study, the Hasofer and Lind (1974) iterative algorithm as modified by Rackwitz and Fiessler (1978) and improved by Liu and Der Kiureghian (1991) is used to find the design point. The modified Hasofer-Lind Rackwitz-Fiessler algorithm is a specialized version of the steepest gradient descent method for numerical constrained optimization. A detailed description of this algorithm can be found in Nowak and Collins (2000). FORM approximates the failure surface $g(\mathbf{X}) = 0$ with the hyperplane tangent to the failure surface at the design point. In this method, the reliability index β has a geometric interpretation and is given by the distance between the origin and the design point in the standard normal space. SORM approximates the failure surface $g(\mathbf{X}) = 0$ with a paraboloid fitting the surface curvatures at the design point (Der Kiureghian et al. 1987; Breitung 1991). Finally, IS is a

variance reduction technique that uses random sampling based on a joint probability density function centered about the design point to increase the frequency of failure samples and, thus, to reduce the number of samples needed to accurately estimate the failure probability (Melchers 1989).

5.7 Capacity and demand statistical models

Both structural capacity and structural demand in Eq. (5-7) need to be described by appropriate probability distributions, which in general depend on several other random parameters. In this study, the statistical descriptors for each random variable X are given by: (1) bias, λ_X, defined as the ratio between the mean value, μ_X, and its nominal value, X_n; (2) coefficient of variation, V_X, corresponding to the ratio of the standard deviation, σ_X, to the mean value, μ_X; and (3) type of probability distribution. The complete statistical description of all random variables used in this study is found in Table 5-2.

Table 5-2. Statistical description of random parameters

Parameter	Nominal Value	λ	V	Distribution	Reference
Concrete					
f_c' (MPa)	Varies	Eq. (5-10)	0.10	Normal	Nowak and Szerszen (2003)
E_c (MPa)	Eq. (5-11)	1.00	0.086	Normal	Scanlon (1995)
κ_c (-)	0.83	1.00	0.12	Weibull	*
Longitudinal Steel					
f_{yl} (MPa)	414	1.145	0.05	Normal	Nowak and Szerszen (2003)
E_{sl} (GPa)	201	1.00	0.033	Lognormal	Mirza and MacGregor (1982)
b (-)	0.0053	1.00	0.30	Lognormal	*
Transverse Steel					
f_{yt} (MPa)	414	1.145	0.05	Normal	Nowak and Szerszen (2003)
E_{st} (GPa)	201	1.00	0.033	Lognormal	Mirza and MacGregor (1982)
ε_{su} (-)	0.094	1.00	0.149	Normal	Pipa (1995)
FRP					

f_{fu} (MPa)	Varies	1.10	0.083	Weibull	Okeil et al. (2013)
E_f (GPa)	Varies	1.04	0.058	Weibull	Okeil et al. (2013)
κ_c (-)	0.55	1.09	0.33	Weibull	Realfonzo and Napoli (2011)
Dimension and Fabrication Errors					
D (mm)	Varies	1.005	0.04	Normal	Nowak and Szerszen (2003)
c (mm)	50	1.00	0.04	Normal	Nowak et al. (2008)
s (mm)	Varies	1.00	0.04	Normal	Nowak et al. (2012)
A_s (mm^2)	Varies	1.00	0.015	Normal	Nowak and Szerszen (2003)
t_f (mm)	Varies	1.00	0.02	Normal	Okeil et al. (2013)
e/D	0.05/0.10	0.50	0.577	Uniform	Baji et al. (2016)
Modeling Uncertainty					
ξ	1.00	1.01	0.12	Inverse Weibull	*
Load Variability					
DL	DL_n	1.05	0.10	Normal	Ellingwood et al. (1980)
LL	LL_n	1.00	0.25	Extreme Type I	Ellingwood et al. (1980)

* Probability distribution model derived in this study

5.7.1 Probability distributions for the random parameters

The random parameters considered in study represent material variability (concrete, longitudinal steel, transverse steel, and FRP), dimension and fabrication errors, modeling uncertainty, and load variability. Most of the probability distributions for these random parameters were directly obtained from the literature; however, some of these probability distributions were derived for the first time in this study based on data available in the literature.

The concrete strength uncertainty depends on (Bartlett and MacGregor 1996): (1) the aleatory uncertainty of the concrete strength, f'_c, as estimated from concrete cylinder test results; and (2) the aleatory difference between the compressive strength of in-place concrete and the concrete from the same batch used for concrete cylinder tests, which is described by the parameter κ_c. The first source of uncertainty is described using the probabilistic model proposed by Nowak and Szerszen (2003), which was also used to calibrate the ACI 318 design code (ACI 2019). This

model assumes a uniform coefficient of variation $V_{f_c'} = 0.10$ and a bias, $\lambda_{f_c'}$, which is a function of f_c' (in MPa) given by:

$$\lambda_{f_c'} = -2.47 \cdot 10^{-5} f_c'^3 + 3.17 \cdot 10^{-3} f_c'^2 - 0.135 f_c' + 3.0649 \geq 1.15 \text{ (MPa)} \quad (5\text{-}10)$$

This model accounted for the variation from different concrete mix plants, different testing methods, and different mix and ingredients (Nowak and Szerszen 2003).

A statistical model for the coefficient κ_c, which was first introduced in Richart et al. (1929) and Richart and Brown (1934) as a constant value of 0.85, is not readily available in the literature. In this study, a database of 135 points compiled from five different sources (Richart et al. 1929; Slater and Lyse 1931; Richart and Brown 1934; Petersons 1968; Peng et al. 2012) is used to estimate the statistics of κ_c. This database includes core and cylinders data, as well as real-size columns and cylinders data, in which only concentric compression and concrete specimens with no transverse steel were considered to avoid strain gradient and confinement effects, respectively. A mean value of $\mu_{\kappa_c} = 0.83$ and a coefficient of variation $V_{\kappa_c} = 0.12$ are determined, based on the available data. A Weibull distribution with scale parameter $a_W = 0.870$ and shape parameter $b_W = 9.771$ is found to describe well the collected data distribution, with the Kolmogorov-Smirnov test providing a p-value of 0.359, and the Anderson-Darling test yielding a p-value equal to 0.134. Figure 5-2 compares the experimental histogram and experimental data with the probability density function and the cumulative distribution function corresponding to the fitted Weibull distribution.

Statistics for the initial tangent modulus of concrete are taken from Scanlon (1995), in which the mean value is equal to the nominal value and is given by (where f_c' is expressed in MPa):

$$\mu_{E_c} = 5000\sqrt{f_c'} \text{ (MPa)} \quad (5\text{-}11)$$

the bias is $\lambda_{E_c} = 1.0$, and the coefficient of variation is $V_{E_c} = 0.086$. The concrete strain at peak strength of the unconfined concrete, ε_c', is assumed here deterministic and given by model proposed by De Nicolo et al. (1994).

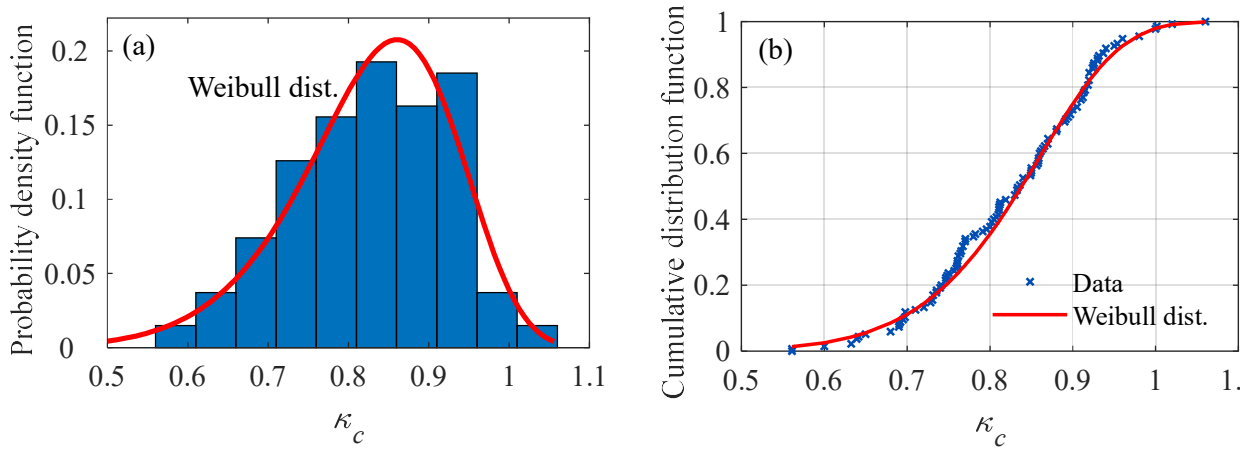

Figure 5-2. Statistical distribution parameters for coefficient κ_c: (a) experimental histogram and fitted Weibull probability density function; and (b) experimental data and fitted Weibull cumulative distribution function.

The statistical descriptions for the yield strength of both longitudinal and transverse reinforcing steel follow the model recommended by Nowak and Szerszen (2003), while the statistical description for the steel modulus of elasticity is taken from Mirza and MacGregor (1982). The statistical distribution for the steel ultimate strain, ε_{su}, is taken from Pipa (1995). The statistical distribution of the strain-hardening ratio, *b*, is not readily available in the literature and is derived here via Monte Carlo simulation using the statistical parameters of ultimate strength, f_{su}, yield strength, f_y, and ultimate strain, ε_{su}, taken from Pipa (1995). A lognormal distribution with a mean value $\mu_b = 0.0053$ and a coefficient of variation $V_b = 0.30$ is found to provide the best fit to the simulated results.

The statistical distributions for the FRP material parameters (f_{fu} and E_f) are taken from Okeil et al. (2013), which also provides a correlation coefficient of $\rho_{f_{fu},E_f} = 0.6945$. The statistical distribution for the efficiency factor, κ_ε, is taken from Realfonzo and Napoli (2011), which recommends a Weibull distribution with a mean value $\mu_{\kappa_\varepsilon} = 0.60$ and a coefficient of variation of $V_{\kappa_\varepsilon} = 0.33$. The nominal value $\kappa_{\varepsilon,n} = 0.55$ used in this study for design purposes is selected in accordance with ACI 440.2R-17 (ACI 2017).

The statistical distributions for the geometric parameters and fabrication errors are taken from the literature. To account for accidental load eccentricity, ACI 318-19 (ACI 2019) reduces the nominal axial strength under pure compression by a factor of 0.80 or 0.85 for columns with closed ties or spirals, respectively. This strength reduction corresponds to an eccentricity-to-diameter ratio, *e*/*D*, of 0.10 and 0.05, respectively. The uncertainty associated to this accidental eccentricity is accounted for in this study by modeling *e*/*D* as a uniformly distributed random variable (Baji et al. 2016) with range going from zero to 0.10 for columns with closed ties, and from zero to 0.05, for columns with spirals. The consideration of accidental load eccentricity in the nonlinear FE model provides a more realistic representation of the actual axial and bending moment interaction taking place in nominally concentrically loaded members. This is particularly relevant because previous studies suggested that load eccentricities are more detrimental to FRP-confined RC members than to conventional RC members (Li and Hadi 2003; Bisby and Ranger 2010).

The statistical distribution for the modeling uncertainty, ξ, corresponding to the Zignago et al. (2018) model, is obtained here for the first time. This quantity is defined as the ratio between experimental estimates and numerical measurements of the peak strength of FRP-confined RC columns. The experimental and numerical values were taken from the tests reported in Zignago et al. (2018) and previously summarized in this paper's section describing the validation of the

adopted confinement model. The coefficient ξ reflects the overall error associated with the nonlinear FE analysis. Based on the results of a Kolmogorov-Smirnov test (p-value = 0.860) and an Anderson-Darling test (p-value = 0.309) performed for the distribution of variable $1/\xi$, an inverse Weibull distribution with $\mu_{\xi} = 1.01$, $\lambda_{\xi} = 1.00$, and $V_{\xi} = 0.12$ was found to provide the best fit to the available data, with the associated Weibull distribution described by a scale parameter a_w = 1.044 and a shape parameter b_w = 13.485.

The statistical models for dead and live loads are obtained from Ellingwood et al. (1980). For a given ratio of live to deal load, the nominal loads are obtained by equating the right- and left-hand sides of Eq. (5-2), as commonly done in the literature (Israel et al. 1987; Diniz and Frangopol 1997).

5.7.2 Structural capacity probabilistic model

In this study, the structural capacity distribution for any specific combination of design parameters is obtained from Monte Carlo simulation based on advanced nonlinear FE analyses. In particular, for each combination of the design variables, 10,000 Monte Carlo simulations are performed to generate the statistics for the structural capacity, *R*. Each realization involves a nonlinear FE analysis of a short column with fiber-discretized cross-sections performed using the general-purpose software Open System for Earthquake Engineering Simulation (OpenSees) (Mazzoni et al. 2006), in which each basic variable is randomly generated based on the probability distributions given in Table 5-2. The structural response of the column is obtained by employing a fiber-discretized zero-length element (Mazzoni et al. 2006), which is subjected to a monotonically increasing combination of axial load and the associated bending moment due to accidental eccentricity. Figure 5-3 shows the zero-length element model and the cross-section fiber discretization. Different uniaxial constitutive models are associated to the different fibers in the

cross-section, as illustrated in Figure 5-3(b). The concrete fibers are modeled by employing the Zignago et al. (2018) confinement model. For the concrete cover fibers, which are confined only by FRP, the FRP-and-steel confined concrete model reduces to the Spoelstra and Monti (1999) model. The longitudinal steel reinforcement fibers are modeled using the Menegotto and Pinto (1973) model, as extended by Filippou et al. (1983) to include isotropic hardening effects. Additional details on the modeling and analysis of FRP-confined RC columns can be found in Hu and Barbato (2014) for the FE model, in Zignago et al. (2018) for the material constitutive model of the FRP-and-steel confined concrete, and in Zignago and Barbato (2021) for the use of a zero-length fiber-section element. The ultimate compressive strength of the column is obtained as the largest axial load achieved until the maximum allowable strain of the concrete, $\varepsilon_{c,\max}$, is attained by any concrete fiber in the FE model. The sample values of $\varepsilon_{c,\max}$ were calculated by using Eq. (5-6) with the randomly sampled values of the input parameters listed in Table 5-2, and assuming a deterministic upper limit value equal to 0.01. The axial load capacity obtained via FE analysis is then multiplied by a randomly generated modeling uncertainty value, ξ, to obtain the sample structural capacity. Figure 5-4 shows a histogram of the Monte Carlo simulation results for the reference column with C_s = 60% and steel ties, in which the simulated capacity is normalized with respect to the nominal axial strength, R_n. It is observed that a lognormal distribution provides a very good fit to the generated resistance model, with the Kolmogorov-Smirnov test providing a p-value = 0.649, and the Anderson-Darling test yielding a p-value = 0.201.

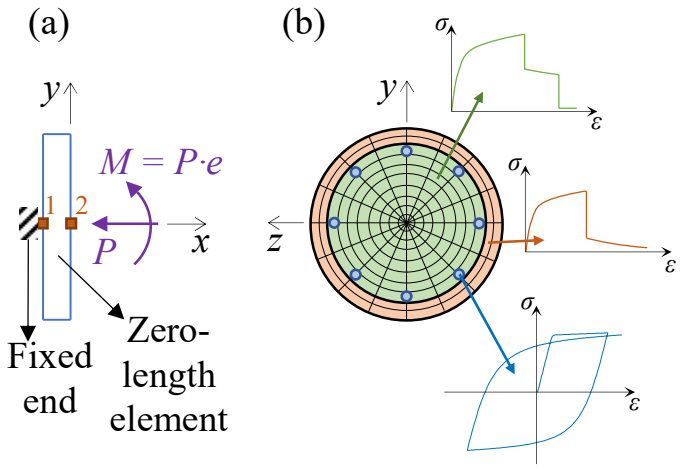

Figure 5-3. FE model description: (a) zero-length element and (b) cross-section fiber discretization

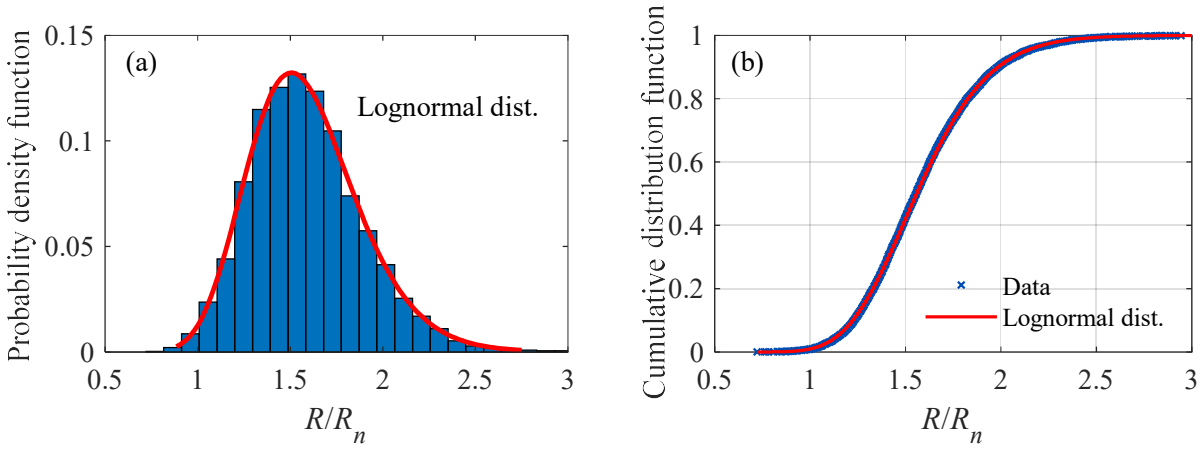

Figure 5-4. Statistical characterization of normalized capacity model for a reference column with C_s = 60% and steel ties: (a) histogram of normalized capacity model and fitted lognormal probability density function; and (b) normalized capacity model data and fitted lognormal cumulative distribution function

5.7.3 Comparison of reliability index estimates obtained using different reliability analysis techniques for the reference column

The different structural reliability techniques considered in this study are employed to estimate the generalized reliability indices corresponding to the reference column with steel ties designed by using the design equation for axially-loaded FRP-confined RC column given in ACI 440.2R-17

(ACI 2017). These reliability indices are reported in Table 5-3 for different levels of C_s. The SORM-based reliability indices are obtained using curvature fitting and the Breitung's asymptotic formula (Breitung 1991). The MCS and IS estimates have a coefficient of variation equal to 5%, corresponding to $1.55 \cdot 10^8$ and $2.03 \cdot 10^3$ samples, respectively, for the reference column with C_s = 60%. The maximum difference among the reliability indices obtained from different methods for any given value of C_s is equal to $\Delta\beta = \max_{C_s}\left\{\max\left[\beta\left(C_s\right)\right] - \min\left[\beta\left(C_s\right)\right]\right\} = 0.017$. This result indicates that the reliability indices obtained from different structural reliability techniques are equivalent for this application. Therefore, FORM is adopted hereinafter to calculate all reliability indices and corresponding failure probabilities, as this method has been historically used to calibrate design equations based on Load and Resistance Factor Design (Ellingwood et al. 1980), and in particular to calibrate the design equations in ACI 318-19 and ACI 440.2R-17 for nominally axially-loaded RC columns without and with FRP confinement, respectively (Szerszen and Nowak 2003; Baji et al. 2016; Baji 2017).

Table 5-3. Reliability indices obtained using different structural reliability analysis methods for reference column with transverse steel ties

C_s (%)	FORM	SORM	MCS	IS
0	4.005	3.993	4.006	3.999
30	4.364	4.356	4.357	4.358
60	4.554	4.550	4.545	4.552
90	4.676	4.673	4.661	4.678
120	4.770	4.769	4.775	4.771
200	4.888	4.887	4.900	4.889

5.8 Proposed design equation and calibration

This study proposes a new design equation that incorporates the steel confinement effect on the axial capacity of FRP-confined RC columns. This new design equation is obtained from the

equation of pure axial compression in ACI 440.2R-17 (ACI 2017) by adding a multiplicative coefficient, $\gamma_f \geq 1$, as follows:

$$P_r = \phi \cdot P_n = \gamma_f \cdot \alpha \cdot \phi \cdot \left[0.85 f'_{cc} \cdot (A_g - A_{sl}) + f_{yl} \cdot A_{sl} \right] \tag{5-12}$$

The strength amplification factor γ_f can be accurately described by a bilinear function of C_s (Zignago and Barbato 2021). In this study, the first branch of the function describing γ_f is assumed to have a cutoff point at C_s = 120%, with the second branch assumed to be flat for the sake of conservativeness. This cutoff value of C_s approximately corresponds to the location in which the bilinear model found in Zignago and Barbato (2021) changes slope, with the second slope being significantly smaller than the first one. It is noteworthy that realistic values of C_s are typically smaller or equal to 120%. The slope of the first branch of γ_f is calibrated based on the structural reliability analysis procedure previously described and applied to the reference column. In particular, the functional form assumed for γ_f is:

$$\gamma_f = \begin{cases} 1 + I \cdot \dfrac{C_s}{1.2} & \text{for} \quad 0 \leq C_s \leq 1.2 \\ 1 + I & \text{for} \quad C_s > 1.2 \end{cases} \tag{5-13}$$

in which I represents the maximum relative increase of a column axial capacity due to the transverse steel confinement effect.

Figure 5-5(a) and Figure 5-5(b) show the reliability indices for the reference column with transverse steel reinforcement given by closed ties and spirals, respectively, for several combinations of I and C_s. It is observed that the design based on the current ACI 440.2R-17 equation (ACI 2017), which corresponds to the results obtained for I = 0.00 (i.e., no confinement effect from transvers steel reinforcement), becomes significantly excessively conservative (even reaching values of $\beta > 4.5$) for increasing values of C_s. Among the considered values of I, I = 0.25

provides the smaller variability of the reliability index with C_s for the columns with closed ties, as it is observed in Figure 5-5(a). For the columns reinforced with spirals, the results presented in Figure 5-5(b) suggest that a maximum increment $I = 0.30$ provides the smaller variability of the reliability index. This fact is attributed to the lower accidental eccentricity assumed in ACI 318-19 (ACI 2019) for this type of transverse reinforcement. However, in order to avoid cases in which the final reliability index is smaller than for a column with $C_s = 0$ and for the sake of simplicity, the value $I = 0.25$ is recommended for all columns, regardless of their transverse steel reinforcement type (i.e., closed ties or spirals). Thus, the proposed new design equation assumes the following calibrated form:

$$\gamma_f = \begin{cases} 1 + 0.25 \cdot \dfrac{C_s}{1.2} & \text{for} \quad 0 \le C_s \le 1.2 \\ 1.25 & \text{for} \quad C_s > 1.2 \end{cases} \tag{5-14}$$

which corresponds to a maximum relative increase in axial strength due to transverse steel confinement equal to 25% of the axial strength obtained neglecting the transverse steel confinement effect.

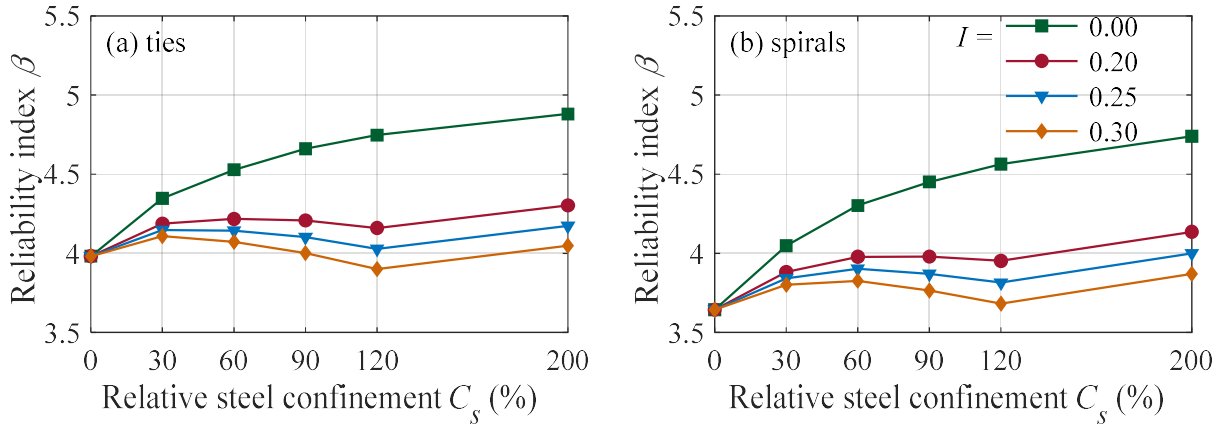

Figure 5-5. Reliability-based calibration of maximum increment I for FRP-confined RC columns with transverse steel reinforcement corresponding to: (a) ties and (b) spirals

5.8.1 Possible alternative design equation expressions

In addition to the design equation proposed in Eq. (5-12), the following two alternative mathematical expressions were also tested to identify the best compromise between accuracy and complexity:

$$\phi \cdot P_n = \phi \cdot \alpha \cdot \left[\gamma_{f1} \cdot 0.85 f'_{cc} \cdot (A_c - A_{sl}) + 0.85 f'_{cc} \cdot (A_g - A_c) + f_{yl} \cdot A_{sl} \right] \quad (5\text{-}15)$$

$$\phi \cdot P_n = \phi \cdot \alpha \cdot \left[\gamma_{f2} \cdot 0.85 f'_{cc} \cdot (A_g - A_{sl}) + f_{yl} \cdot A_{sl} \right] \quad (5\text{-}16)$$

in which the two multiplicative coefficients γ_{f1} and γ_{f2} are described by the same bilinear functional form as γ_f in Eq. (5-13). For each of these coefficients, the maximum increment I was separately calibrated to minimize the variability of the reliability index with C_s, thus obtaining maximum values of $\gamma_{f1} = 1.40$ and $\gamma_{f2} = 1.30$, respectively. The three considered expressions for the design equation correspond to different levels of complexity and accuracy in estimating the strength of the FRP-confined RC column to be designed. In particular, Eq. (5-15) is expected to provide the best estimates of the column's strength, as it rigorously accounts for the effects of FRP-and-steel confinement on the core concrete, effectively providing a modified estimate for the f'_{cc} of the core concrete to account for the additional confinement provided by the internal steel reinforcement. Eq. (5-16) is expected to be less accurate than Eq. (5-15), as the simultaneous FRP-and-steel confinement effect on the core concrete is averaged over the entire concrete area. Finally, Eq. (5-12) is expected to be the least accurate of the three proposed equations, as the simultaneous FRP-and-steel confinement effect on the concrete core is averaged over the entire strength contribution of both concrete and longitudinal steel. However, the complexity of the proposed design equation increases with its accuracy. It is observed here that a design equation based on a more accurate estimate of the column's strength corresponds to a reliability index β closer to the

target reliability index, which here is assumed to be the reliability index corresponding to a column without internal steel confinement, based on the assumption used for the current design equation in ACI 440.2R-17 (ACI 2017).

Figure 5-6 compares the reliability indices obtained by designing an FRP-confined RC column using Eqs. (4-12), (4-15), and (4-16), respectively. As expected, Eq. (5-15) provides the smallest variation of β among the three proposed equations. However, it is also observed that the differences in reliability indices obtained using the three equations are negligible for any engineering purpose, with a maximum difference $\Delta\beta$ equal to 0.038 for columns with steel ties, and equal to 0.040 for columns with steel spirals. These differences are smaller than those produced by rounding the maximum values of the γ_f, γ_{f1}, and γ_{f2} coefficient to the nearest multiple of 0.05, and are significantly smaller than those produced by the discrete variability of the FRP confinement thickness used for real-world design applications. Therefore, the three proposed equations are equivalent for any practical purpose in terms of accuracy, whereas Eq. (5-12) is the simplest in terms of implementation and requires the minimum amount of changes for the existing design equation in ACI 440.2R-17 (ACI 2017).

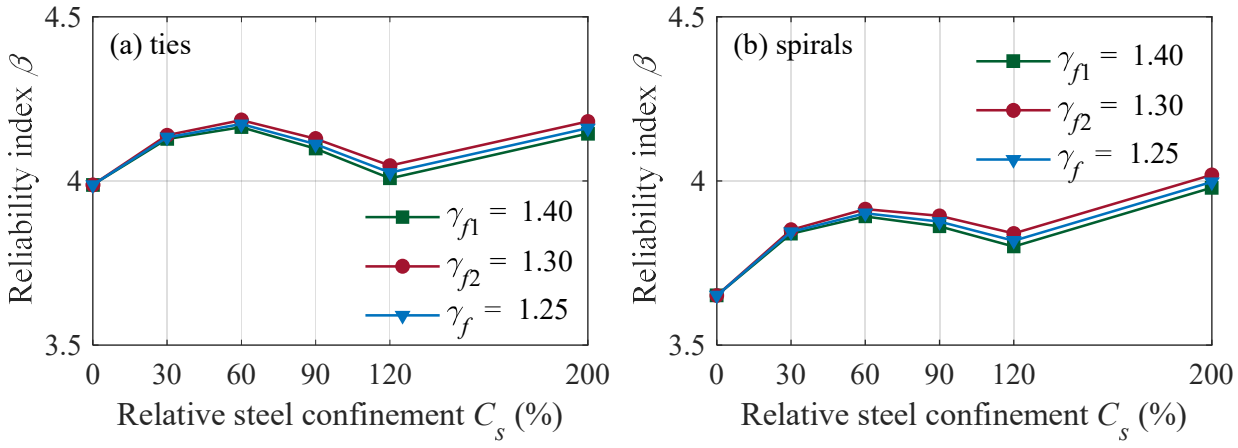

Figure 5-6. Reliability indices of the three possible alternative design equation expressions for FRP confined columns with: (a) steel ties and (b) steel spirals

5.9 Validation of the proposed design equation

After calibration of the proposed design equation for the reference columns, the axial strength obtained using the newly proposed design equation is compared against the experimental data found in the literature and used to validate the Zignago et al. (2018) model. The data points used for this comparison include only 21 columns out of the 46 reported in Figure 5-1, for which the axial strength values of identically-built columns without internal steel reinforcement (i.e., with FRP confinement only) were also available in the literature. In particular, the proposed and calibrated strength amplification factor γ_f is directly compared to the ratio between the axial capacity $\overline{P}_{\max}$ of the specimens with both FRP wraps and internal transverse steel and the axial capacity $\overline{P}_{f0}$ of the specimens reinforced with FRP wraps only. To take into account the design constraint on the maximum allowable concrete strain $\varepsilon_{c,\max}$, the experimentally obtained values of $\overline{P}_{\max}$ and $\overline{P}_{f0}$ correspond to the specimens' axial capacity at the compressive concrete axial strain $\varepsilon_{c,\max}$, as opposed to the ultimate axial capacity. The effect of this design strain limitation is analyzed in Zignago and Barbato (2021). Figure 5-7 plots the strength ratio $\overline{P}_{\max} / \overline{P}_{f0}$ of the experimental data and the amplification factor γ_f as functions of the relative steel confinement coefficient C_s. It is observed that the proposed design equation generally underestimates the actual gain in strength attributed to the confinement produced by the internal transverse steel as measured by the strength ratio $\overline{P}_{\max} / \overline{P}_{f0}$. This is consistent with the fact that the proposed design equation with the calibrated amplification factor γ_f represents a fractile of the strength distribution that is lower than the mean (i.e., approximately a 20% fractile, based on the available experimental data).

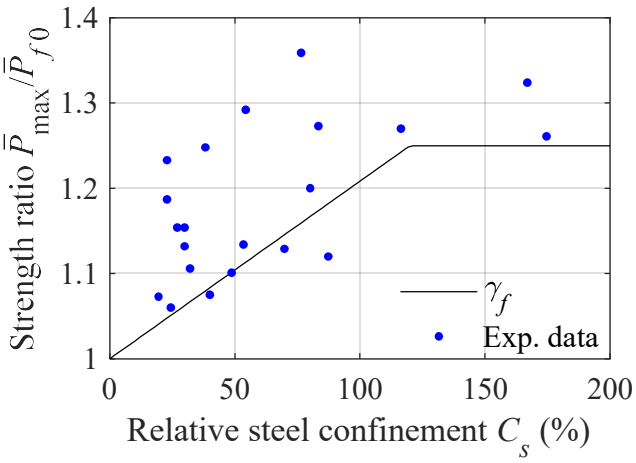

Figure 5-7. Comparison of the experimental data strength ratio $\bar{P}_{max} / \bar{P}_{f0}$ with the calibrated amplification factor γ_f

The proposed design equation is also quantitatively validated by assessing the reliability index variability for all other design conditions corresponding to the parameters' values given in Table 5-1Table 6-1. Due to space limitations, only select results are reported and discussed in detail. The effects on the reliability index of the six design parameters considered in this study (i.e., steel to concrete strength ratio, FRP confining ratio, FRP ultimate strain, cross-section core to gross area ratio, longitudinal steel ratio, and live to dead load ratio) are separately analyzed as a function of C_s by changing one parameter at a time, while keeping all other parameter values constant and equal to their values for the reference column. Figure 5-8(a) through Figure 5-8(f) show the calculated reliability indices obtained by changing each of the design parameters. It is observed that, in all analyzed cases, the reliability indices are always larger than or equal to 3.73 for $C_s = 0$ (i.e., $p_f \leq 1.0 \cdot 10^{-4}$) and larger than or equal to 3.78 for $C_s > 0$ (i.e., $p_f \leq 8 \cdot 10^{-5}$). These results demonstrate that the proposed design equation is consistent with the design philosophy and the target reliability indices described in Section 9.1 of the ACI 440.2R-17 guidelines, in which FRP-related reductions factors are calibrated targeting reliability indices usually above 3.5 (ACI 2017).

In particular, for brittle failures as the one considered in this paper (column failure due to axial compression), reliability index values between 3.5 and 4.5 are typically considered appropriate, as suggested in Table 1.3-1 of ASCE 7-16 (ASCE 2017).

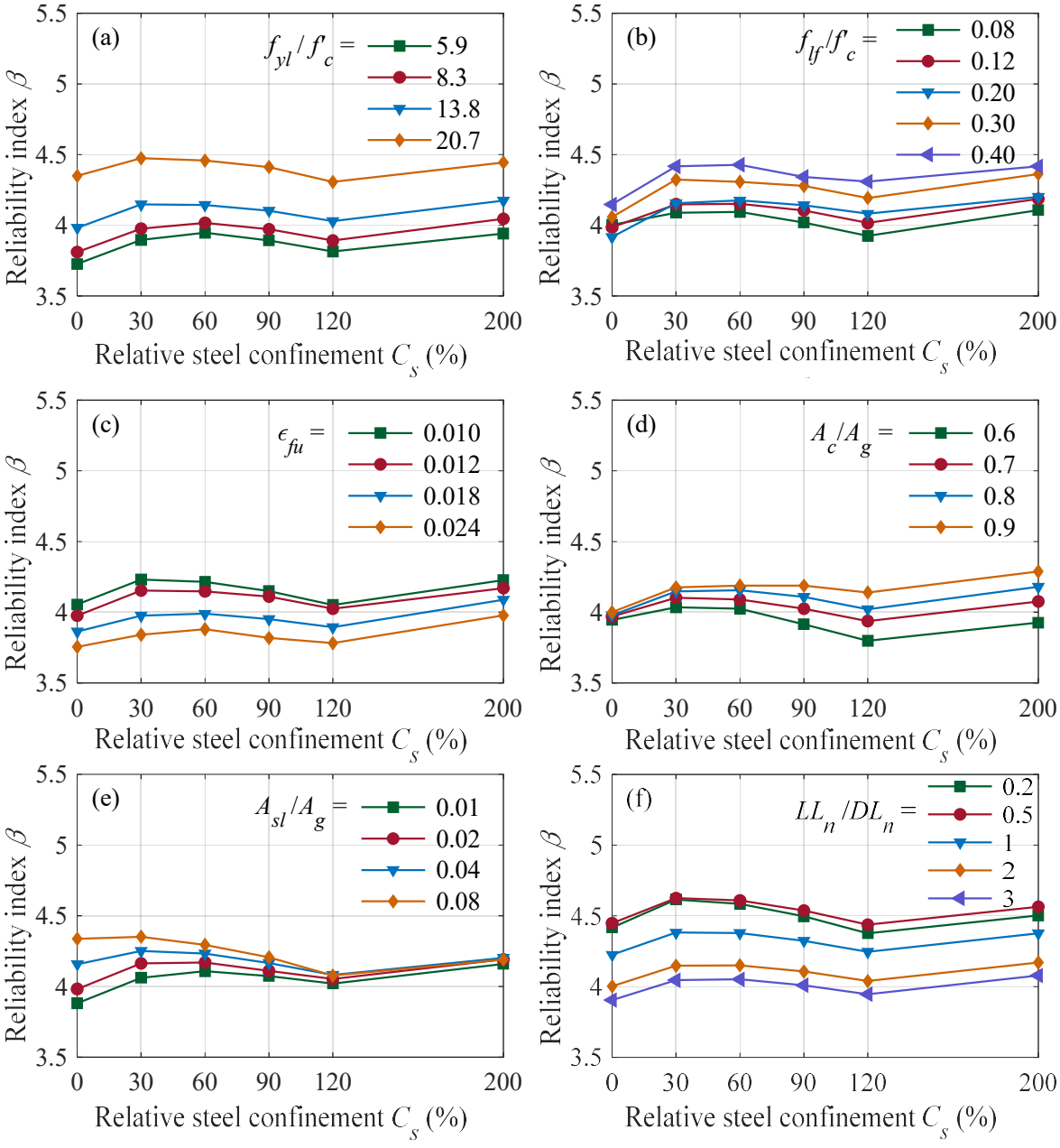

Figure 5-8. Reliability assessment of FRP-confined RC columns for each of the studied paremeters in the design space: (a) steel to concrete strength ratio; (b) FRP confining ratio; (c) FRP ultimate strain; (d) core to gross area ratio; (e) longitudinal reinforcing steel ratio; and (f) nominal live to dead load ratio

Figure 5-8(a) shows that the reliability index of the FRP-wrapped RC columns is highly affected by the longitudinal steel yield strength to unconfined concrete strength ratio, f_{yl} / f_c'. In particular, columns with lower concrete strength present higher reliability indices (e.g., for $f_c' = 20$ MPa, corresponding to $f_{yl} / f_c' = 20.7,\ 4.31 \le \beta \le 4.47$) than those with higher concrete strength (e.g., for $f_c' = 70$ MPa, corresponding to $f_{yl} / f_c' = 5.9,\ 3.73 \le \beta \le 3.95$). These changes in the reliability indices are consistent with the characteristics of the statistical model adopted for f_c' in this study, which describes the bias $\lambda_{f_c'}$ as a decreasing function of f_c'. This model was developed to statistically represent the concrete produced in the U.S. and to calibrate the ACI 318-19 design code (Nowak and Szerszen 2003; Wiśniewski et al. 2012; ACI 2019). It is also observed that the changes in reliability index for $0 \le C_s \le 200\%$ are very small for any given value of f_{yl} / f_c' (i.e., $\Delta\beta = \max_{C_s} \beta - \min_{C_s} \beta \le 0.23$).

Figure 5-8(b) shows that the reliability index is little sensitive to the FRP confining pressure levels for $f_{lf} / f_c' \le 0.20,$ and generally increases for increasing f_{lf} / f_c' when $f_{lf} / f_c' > 0.20.$ This phenomenon is due to the fact that, for $f_{lf} / f_c' \ge 0.20$, the nominal strength of the FRP-confined RC columns is controlled by the design strain limitation of $\varepsilon_{c,\max} = \varepsilon_{ccu} \le 0.01$ and not by the f_{cc}' value calculated using Eq. (5-5). Also in this case, the variability of the reliability index with C_s is very small for all considered f_{lf} / f_c' values (i.e., $\Delta\beta \le 0.30$).

Figure 5-8(c) shows the reliability results for varying FRP ultimate strains, which implicitly represent the effects of different types of fibers. It is observed that the reliability indices decrease as ε_{fu} increases. This phenomenon is explained by the diminished confinement effectiveness for fibers with larger ultimate strains due to the presence of a design strain limit (Zignago and Barbato

2021). Also in this case, the changes in the reliability index with C_s are small and practically independent of ε_{fu} (i.e., $\Delta\beta \le 0.23$).

Figure 5-8(d) shows that the core to gross area ratio, A_c / A_g, has a negligible influence on the reliability index for $C_s = 0\%$; however, its influence increases with the increase of C_s, as the reliability index is higher for higher values of A_c / A_g. This result was expected because the steel confinement effect increases with A_c / A_g, everything else being the same (Zignago and Barbato 2021). It is noteworthy that low values of A_c / A_g generally correspond to columns with small diameters (e.g., assuming a concrete cover of 25 mm, a column with diameter $D = 250$ mm would correspond to $A_c / A_g = 0.64$, whereas a column with $D = 1{,}000$ mm would correspond to $A_c / A_g = 0.90$). It is also observed that, for $A_c / A_g \le 0.7$ and $90\% \le C_s \le 120\%$, the reliability index becomes slightly lower than the value corresponding to $C_s = 0$. Therefore, for the unlikely design cases of small columns with high amounts of transverse steel and low amounts of FRP, the proposed design equation can produce a design that is slightly less safe than the design that would be obtained using the existing ACI 440.2R-17 equation (ACI 2017). However, the maximum reduction in reliability index is very small even for these extreme cases, as $\max\left[\beta\left(C_s = 0\right) - \min_{C_s} \beta\right] \le 0.15$.

Figure 5-8(e) indicates that the reliability index of FRP-confined RC columns is affected by the longitudinal steel reinforcing ratio only for low values of C_s, for which larger amounts of longitudinal reinforcement lead to higher reliability indices. This phenomenon is due to the fact that, when a larger portion of a constant axial load capacity is provided by the longitudinal steel, the lower variability of the steel yield strength when compared to that of concrete produces a higher

reliability index. However, as the confinement effect of transverse steel increases, a higher portion of the axial load capacity is provided by the confined concrete and, thus, the reduction in variability due to the higher amounts of steel becomes negligible. It is observed that $\beta \geq 4.0$ for $C_s > 0$.

Figure 5-8(f) shows that the live to dead load ratio has a significant effect on β, resulting in higher reliability index values for lower LL_n / DL_n ratios, as result of the larger variability of the live loads when compared to the dead loads. However, for very low LL_n / DL_n ratios, the effect of the dead load bias $\lambda_{DL} = 1.05$ becomes significant, resulting in slightly lower reliability indices, as shown by the comparison of the reliability indices obtained for LL_n / DL_n ratios equal to 0.2 and 0.5. It is observed that the reliability indices for $C_s > 0$ are always larger than or equal to those for $C_s = 0$. In addition, the changes in the reliability index with C_s are small (i.e., $\Delta\beta \leq 0.30$).

5.10 Design procedure

The retrofit design of a deficient RC column consists of determining the minimum number of FRP plies, n, required to satisfy a desired increased design demand, $P_{u,\text{new}}$. The design equation proposed in this study requires the computation of a coefficient γ_f by using Eq. (5-14), which implicitly depends on n. Thus, this study proposes an iterative procedure to determine an appropriate (optimal) solution, which is described by the flowchart shown in Figure 5-9.

The proposed design procedure uses as input information the design demand of the original column, $P_{u,\text{old}}$, the desired increased design demand, $P_{u,\text{new}}$, and the FRP material's properties. An initial value $1.00 \leq \gamma_f \leq 1.25$ is assumed to compute a tentative minimum number of plies, n (first trial). The value of γ_f is then updated to obtain the strengthened column axial capacity, P_r, by using Eq. (5-12). A first minimum strength check is performed, i.e., to verify if $P_r \geq P_{u,\text{new}}$. If this

condition is not satisfied, an FRP ply is added, i.e., n is set equal to n +1 (second trial and first iteration). This process is repeated until the design passes the minimum strength check, after which an efficiency check is performed, i.e., to verify if $P_r \le m \cdot P_{u,\text{new}}$, in which the efficiency factor $m > 1.0$ reflects how much overdesign is considered acceptable by the designer. This study recommends to select $1.05 \le m \le 1.10$, and uses hereinafter $m = 1.05$, based on which a 5% overstrength is considered acceptable. However, if efficiency is not a concern, a designer could also decide to skip the efficiency check and terminate the design as soon as the minimum strength check is satisfied, thus greatly simplifying the proposed design procedure.

In case the efficiency check is not satisfied, the proposed design procedure requires an additional iteration to check for more economical design with $n = n$ -1. The iterations associated with both strength and efficiency checks include an additional check to determine if a specific value of n has been already used in a previous trial, in order to avoid a possible infinite loop that could be produced by the selection of an excessively small value of m. It is observed that the optimal solution (i.e., minimum number of plies that satisfies the strength check) is always achieved when the initially assumed value of γ_f is larger than its optimal value, whereas a slightly less efficient design is possible when the initial value assumed for γ_f is lower than the optimal value, and the selected value of m is large.

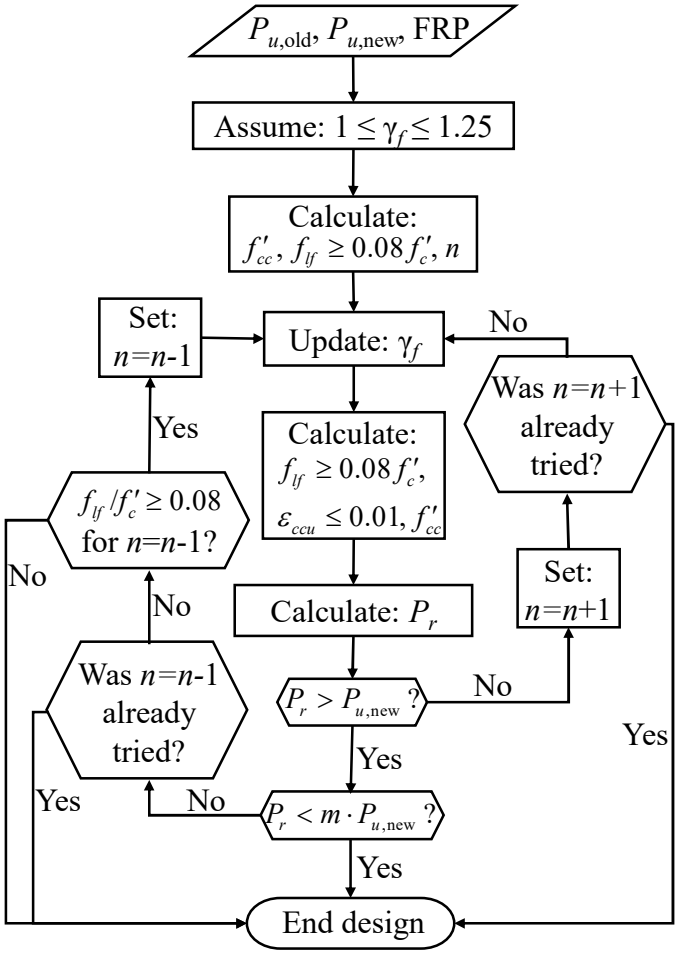

Figure 5-9. Proposed iterative design procedure

5.11 Application Example

The proposed design procedure for the FRP confinement strengthening of RC columns is illustrated here with an application example that is obtained through a slight modification of the design example presented in Wu and Eamon (2017). The considered unretrofitted column has diameter D = 711 mm (28 in.), concrete cover c = 50 mm (2 in), and unconfined concrete compressive strength f_c' = 26.7 MPa (4 ksi). The transverse reinforcement consists of #6 (diameter = 19 mm) Grade 60 steel spiral at a pitch s = 115 mm (4.5 in.), and the longitudinal reinforcement is comprised of 12 #8 (diameter = 25.4 mm) Grade 60 rebars. The design demand

for the unretrofitted RC column is assumed $P_{u,\text{old}} = 7400$ kN. Based on ACI 318-19 (ACI 2019), the unretrofitted column's axial capacity is $P_{r,\text{old}} = 7455$ kN, with a lateral confining pressure exerted by the spirals equal to $f_{ls} = 3.16$ MPa (Mander et al. 1988). The column needs to be strengthened with FRP wraps to reach an increased design demand, e.g., due to a change in use classification of the building where the unretrofitted column is located. Three different strengthening levels are considered, i.e., $P_{u,\text{new}} = 1.25P_{u,\text{old}}$, $1.35P_{u,\text{old}}$, and $1.45P_{u,\text{old}}$. The mechanical properties of the FRP reinforcement are: modulus of elasticity $E_f = 228$ GPa, ultimate strength $f_{fu}^* = 3.8$ GPa, ultimate strain $\varepsilon_{fu}^* = 0.0167$, and ply thickness $t_f = 0.167$ mm. Considering an exterior exposure for carbon FRP (CFRP), an environmental reduction factor $C_E = 0.85$ is applied, which gives an effective ultimate strength $f_{fu} = C_E \cdot f_{fu}^* = 3.23$ GPa, and an effective ultimate strain $\varepsilon_{fe} = C_E \cdot \kappa_\varepsilon \cdot \varepsilon_{fu}^* = 0.00781$. Due to space limitations, the complete calculations are reported in Table 5-4 only for the case $P_{u,\text{new}} = 1.45P_{u,\text{old}} = 10,730$ kN and a starting value $\gamma_f = 1.25$.

Table 5-4. Design calculations for the case $P_{u,\text{new}} = 1.45P_{u,\text{old}}$ and initial $\gamma_f = 1.25$.

Initialization
Assume $\gamma_f = 1.25$
Calculate $f'_{cc} = \dfrac{\left(\dfrac{P_{u,\text{new}}}{\gamma_f \cdot \phi \cdot \alpha} - f_y \cdot A_{sl}\right)}{0.85(A_g - A_{sl})} = \dfrac{\left[\dfrac{10730 \cdot 10^3}{1.25 \cdot 0.75 \cdot 0.85} - 414 \cdot 6080\right]}{0.85 \cdot (3.973 \cdot 10^5 - 6080)} = 32.94 \text{ MPa}$

$$f_{lf} = \frac{f'_{cc} - f'_c}{\psi_f \cdot 3.3\kappa_a} = \frac{32.94 - 27.6}{(0.95)(3.3)(1.0)} = 1.70 \text{ MPa} < 0.08 f'_c = 2.21 \text{ MPa}$$

$$n = \frac{f_{lf} \cdot D}{2E_f \cdot t_f \cdot \varepsilon_{fe}} = \frac{(2.21)(711)}{2(228 \cdot 10^3)(0.167)(0.00781)} = 2.64 \rightarrow n = 3$$

Trial #1

$$K_f = 0.5\rho_f \cdot E_f = \frac{2n \cdot t_f \cdot E_f}{D} = \frac{2(3)(0.167)(228 \cdot 10^3)}{711} = 321.3 \text{ MPa}$$

$$C_s = \frac{100 f_{ls} \cdot A_c}{K_f \cdot A_g} = \frac{100 \cdot 3.16 \cdot 2.934 \cdot 10^5}{321.3 \cdot 3.973 \cdot 10^5} = 0.726 < 1.20$$

$$\gamma_f = \left(1 + 0.25 \cdot \frac{C_s}{1.2}\right) = \left(1 + 0.25 \cdot \frac{0.726}{1.2}\right) = 1.151$$

$$f_{lf} = \frac{2n \cdot E_f \cdot t_f \cdot \varepsilon_{fe}}{D} = \frac{2 \cdot 3 \cdot 228 \cdot 10^3 \cdot 0.167 \cdot 0.00781}{711} = 2.51 \text{ MPa}$$

$$\varepsilon_{ccu} = \varepsilon'_c \cdot \left[1.5 + 12\kappa_b \cdot \frac{f_{lf}}{f'_c} \cdot \left(\frac{\varepsilon_{fe}}{\varepsilon'_c}\right)^{0.45}\right] = 0.0019 \cdot \left[1.5 + 12 \cdot 1.0 \cdot \frac{2.51}{27.6} \cdot \left(\frac{0.00781}{0.0019}\right)^{0.45}\right] = 0.0068 < 0.01$$

$$f'_{cc} = f'_c + \psi_f \cdot 3.3\kappa_a \cdot f_{lf} = 27.6 + 0.95 \cdot 3.3 \cdot 1.0 \cdot 2.51 = 35.47 \text{ MPa}$$

$$P_r = \gamma_f \cdot \phi \cdot \alpha \cdot \left[0.85 f'_{cc} \cdot (A_g - A_{sl}) + f_{yl} \cdot A_{sl}\right]$$

$$= 1.151 \cdot 0.75 \cdot 0.85 \cdot \left[0.85 \cdot 35.47 \cdot (3.973 \cdot 10^5 - 6080) + 414 \cdot 6080\right] = 10498 \text{ kN}$$

$$P_r = 10498 \text{ kN} < P_{u,\text{new}} = 10730 \text{ kN} \rightarrow \text{Set } n = n + 1 = 4$$

Trial #2 (Iteration #1)

$$K_f = \frac{2 \cdot 4 \cdot 0.167 \cdot 228 \cdot 10^3}{711} = 428.4 \text{ MPa}$$

$$C_s = \frac{100 \cdot 3.16 \cdot 2.934 \cdot 10^5}{428.4 \cdot 3.973 \cdot 10^5} = 0.545 < 1.20$$

$$\gamma_f = \left(1 + 0.25 \cdot \frac{0.545}{1.2}\right) = 1.113$$

$$f_{lf} = \frac{2 \cdot 4 \cdot 228 \cdot 10^3 \cdot 0.167 \cdot 0.00781}{711} = 3.35 \text{ MPa}$$

$$\varepsilon_{ccu} = 0.0019 \cdot \left[1.5 + 12 \cdot 1.0 \cdot \frac{3.35}{27.6} \cdot \left(\frac{0.00781}{0.0019}\right)^{0.45}\right] = 0.0081 < 0.01$$

$$f'_{cc} = 27.6 + 0.95 \cdot 3.3 \cdot 1.0 \cdot 3.35 = 38.09 \text{ MPa}$$

$P_r = 1.113 \cdot 0.75 \cdot 0.85 \cdot \left[0.85 \cdot 38.09 \cdot (3.973 \cdot 10^5 - 6080) + 414 \cdot 6080 \right] = 10771$ kN
$P_r = 10771$ kN $> P_{u,\text{new}} = 10730$ kN $\rightarrow$ OK
$P_r = 10771$ kN$<1.05P_{u,\text{new}} = 11267$ kN $\rightarrow$ OK $\rightarrow$ Design is complete with $n = 4$

Table 5-5 summarizes the results of the considered application example by comparing the final designs obtained by using the design equation in ACI 440.2R-17 (ACI 2017) and the one proposed in this work. This table reports three sets of β values: (1) the target β, which corresponds to the reliability index for the retrofitted column designed using the ACI 440.2R-17 equation and assuming no transverse steel reinforcement; (2) the actual β for a column designed according to ACI 440.2R-17, which is calculated by accounting for the effect of the actual transverse steel reinforcement; and (3) the actual β for a column designed according to the newly proposed design equation and calculated by accounting for the effect of the actual transverse steel reinforcement. The target β values correspond to the desired safety levels according to ACI 440.2R-17 guidelines (ACI 2017), but these values are inaccurate reliability index estimates for any columns with internal transverse steel reinforcement, as previously shown in this paper. By contrast, the actual β values reported in Table 5-5 are accurate estimates of the reliability index corresponding to the different designs. It is observed that the newly proposed design equation produces a more efficient and economical design (with FRP savings up to 43%) than the existing design equation, while maintaining adequate reliability index values (i.e., always higher than the corresponding target β values).

Table 5-5. Comparison of application example results using ACI 440.2R-17 design equation (ACI 2017) and proposed design equation for different load increments

$P_{u,\text{new}}$	*n* (ACI 440 equation)	*n* (proposed equation)	FRP saved	Target β (ACI 440 equation)	Actual β (ACI 440 equation)	Actual β (proposed equation)
$1.25P_{u,\text{old}}$	4	3	25%	3.77	4.41	4.28
$1.35P_{u,\text{old}}$	5	3	40%	3.67	4.23	4.02
$1.45P_{u,\text{old}}$	7	4	43%	3.61	4.13	3.90

The effects of using different initial values of γ_f are also investigated. Table 5-6 compares the final designs and the number of trials (and corresponding iterations) needed to achieve convergence of the design corresponding to each of the three considered strengthening levels for three different initial values of γ_f, i.e., $\gamma_f = 1.000, 1.125, 1.250$. It is observed that: (1) in general, the initial value of γ_f has only a small effect, if any, on the final design; (2) the proposed design methodology converges to an acceptable design in a very small number of trials (i.e., 1 to 3 trials in this example, or 0 to 2 iterations); (3) when starting with an initial value of γ_f close or greater than the optimal value, the proposed design procedure converges very quickly to the optimal design; (4) when starting with an initial value of γ_f smaller than the optimal value, if multiple solutions exist in the range $P_{u,\text{new}} \le P_r \le m \cdot P_{u,\text{new}}$, the design procedure converges to the higher strength solution; and (5) if a solution does not exist in the range $P_{u,\text{new}} \le P_r \le m \cdot P_{u,\text{new}}$ (i.e., when the condition $f_{lf} / f_c' \ge 0.08$ controls, or when the selected *m* is too small), the procedure converges to the most efficient design with a strength higher than $m \cdot P_{u,\text{new}}$. As a result, an initial choice of $\gamma_f = 1.250$ ensures that the most efficient design is always found, but at potential cost of a few additional iterations than if a smaller value (e.g., $\gamma_f = 1.125$) were to be used. By contrast, an

initial choice of $\gamma_f = 1.000$ can produce a less efficient but still acceptable design, and it can require additional iterations than selecting a larger initial value for γ_f.

Table 5-6. Effects of initial choice of γ_f for m = 1.05

$P_{u,\text{new}}$	$1.25P_{u,\text{old}}$			$1.35P_{u,\text{old}}$			$1.45P_{u,\text{old}}$		
Starting γ_f	1.000	1.125	1.250	1.000	1.125	1.250	1.000	1.125	1.250
Final γ_f	1.151	1.151	1.151	1.151	1.151	1.151	1.091	1.113	1.113
Final $P_r/P_{u,\text{new}}$	1.135	1.135	1.135	1.051	1.051	1.051	1.040	1.004	1.004
Final n	3	3	3	3	3	3	5	4	4
Number of trials (iterations)	2 (1)	1 (0)	1 (0)	3 (2)	1 (0)	1 (0)	2 (1)	1 (0)	2 (1)

5.12 Conclusion

This paper proposes a new design equation for FRP-confined RC circular columns subject to axial compression, which accounts for the simultaneous confinement effects of transverse steel and FRP. This newly proposed equation depends on an easy-to-compute coefficient γ_f that measures the axial strength ratio for an RC column confined by both transverse steel and FRP when the strength is obtained by considering and by neglecting the transverse steel effects. The coefficient γ_f is calibrated by using a structural reliability analysis approach, which accounts for the uncertainties associated with material, dimension, modeling, and loading variables. Monte Carlo simulation is employed to develop the probability distribution for the axial capacity of the columns by means of advanced nonlinear FE response analysis. The first-order reliability indices for a wide range of design parameters are evaluated via the Hasofer-Lindt Rackwitz–Fiessler iterative algorithm. The newly proposed design equation generally yields a more efficient design with a reliability index that is not lower than that implied by the existing design equation for axial

compression given in ACI 440.2R-17 (ACI 2017). In fact, the proposed equation produces almost uniform reliability indices for varying levels of transverse steel reinforcement, whereas the ACI 440.2R-17 equation becomes excessively conservative for large amounts of transverse steel. A new iterative design procedure is also proposed and demonstrated via a realistic application example. It is shown that the proposed procedure yields an efficient design solution within 1 to 3 trials (i.e., 0 to 2 iterations), thus being very efficient, and is only slightly affected (in terms of final design and of algorithm efficiency) by different initial assumptions of the γ_f value.

The proposed design equation has been calibrated for axially-loaded RC circular columns with preserved structural integrity only. Further research is needed to investigate its application to other shapes (e.g., rectangular cross-sections) or pre-damaged RC columns.

6 New analytical analysis-oriented stress-strain model for FRP-and-steel confined concrete

The performance of eight candidate families of analytical functions in fitting the monotonic envelope of the original iterative formulation of the stress-strain curve of FRP-and-steel confined concrete is evaluated in terms of computational cost, simplicity, and accuracy. A new optimization procedure to obtain an analytical expression for the corresponding monotonic stress-strain envelope is developed. The computational costs associated with both the original iterative model and the analytical model are compared via the nonlinear seismic time-history analysis of (1) a two-column bridge pier; and (2) a five-span bridge structure with FRP-retrofitted RC piers.

6.1 Introduction

External confinement by fiber-reinforced polymer (FRP) composites can enhance both the compressive strength and ductility of reinforced concrete (RC) columns, and can be used as a means to strengthen and/or repair these structural members when structurally deficient or damaged (Parvin and Brighton 2014). The confinement effect produced by the externally bonded FRP acts simultaneously with the confining mechanism of the existing internal reinforcing steel in the concrete core of RC columns, while the concrete cover is solely subject to FRP wrapping confinement (Zignago et al. 2018).

FRP-confined concrete has been extensively studied in the last four decades (Fardis and Khalili 1982; Lam and Teng 2003a; Raza et al. 2019), including (although to a lesser degree) FRP-and steel-confined concrete (Demers and Neale 1999; Wang and Restrepo 2001; Eid et al. 2009; Wang et al. 2012), with several stress-strain models for confined concrete being developed based on these studies (Li et al. 2003; Ilki et al. 2008; Lee et al. 2010; Megalooikonomou et al. 2012; Hu and Seracino 2014; Teng et al. 2015; Zignago et al. 2018). These models can be classified into two

main categories (Lam and Teng 2003a; Teng and Lam 2004): (1) design-oriented models and (2) analysis-oriented models. The first group contains models that are expressed by closed-form equations and are generally obtained by fitting experimental testing results. Because design-oriented models are mainly developed to predict ultimate conditions, they usually cannot be used for analysis purposes or present lower accuracy at intermediate loading stages than analysis-oriented models; however, they are convenient to use for design purposes (Teng and Lam 2004; Ozbakkaloglu et al. 2013). By contrast, analysis-oriented models predict the behavior of FRP-confined concrete by using equilibrium and compatibility conditions between the confined concrete and the confining FRP through an incremental approach (Teng and Lam 2004; Ozbakkaloglu et al. 2013), in which the externally-wrapped FRP composites apply a linearly-increasing confining pressure into the radially-expanding concrete that is loaded in compression. However, these models often use explicit lateral-to-axial strain relationships that are fitted to experimental data via regression analysis (Mimiran and Shahawy 1997; Harries and Kharel 2002; Moran and Pantelides 2002; Albanesi et al. 2007; Jiang and Teng 2007; Teng et al. 2007; Xiao et al. 2010) and, thus, may result in lower accuracy in representing the stress-strain response of FRP-confined concrete for design parameter combinations that are outside the calibration range (Ozbakkaloglu et al. 2013). Some of these models are based on iterative procedures that satisfy equilibrium and compatibility relationships at the material level (Spoelstra and Monti 1999; Fam and Rizkalla 2001; Chun and Park 2002; Marques et al. 2004; Binici 2005; Aire et al. 2010; Zignago et al. 2018), but at a higher computational cost than fitted models through regression analysis.

This paper proposes an efficient procedure for finding a mathematical closed-form expression for a recently-developed analysis-oriented model for FRP-and-steel confined concrete, referred to as

Zignago-Barbato-Hu (ZBH) model hereinafter, which can accurately model the highly nonlinear confining mechanisms from both confining materials, individually and simultaneously (Zignago et al. 2018). The original ZBH model is first modified to remove discontinuities in the monotonic envelope deriving from the FRP and steel ruptures. Different families of mathematical functions are considered as potential fits for the stress-strain curves generated using the ZBH model. A global optimization algorithm is employed to identify the feasible domain of the fitting parameters where the global optimum solution is located. The analytical expression for the stress-strain curve's monotonic envelope is found using a local optimization algorithm. Then, the different function families are compared in terms of accuracy, complexity, and robustness in fitting the stress-strain curves generated using the ZBH model. Finally, the computational costs of the original iterative ZBH model and a select analytical function fitted to the model are compared with the aid of a numerical example consisting in the nonlinear dynamic finite element (FE) analysis of a realistic bridge structure subject to an earthquake ground motion record.

6.2 Novelty and relevance

The proposed procedure to obtain the monotonic envelope of the FRP-and-steel confined concrete's stress-strain constitutive model is innovative, because it does not rely on parameter calibration to fit analytical curves to available experimental data for concrete confined by FRP only or by both FRP and steel. In contrast with existing analysis-oriented models based on explicit lateral-to-axial strain relationships with calibrated fitting parameters, the newly proposed model uses numerical optimization to fit the analytical expression of the monotonic envelope to the ZBH model's stress-strain curve corresponding to any specific set of material and geometric properties under consideration, thus retaining the original model's ability to describe the FRP-and-steel

confined concrete stress-strain curve based on fundamental equilibrium and compatibility properties at the material level.

The newly proposed FRP-and-steel confined concrete model can improve the computational efficiency and robustness of nonlinear FE analysis of FRP-confined RC structures, while accounting in a rigorous manner for the simultaneous confinement of steel and FRP. The properties of computational efficiency and robustness are particularly relevant for applications involving large FE models and/or numerous repetitions of the FE analyses, such as structural reliability analysis, probabilistic response analysis, reliability-based design, parametric studies, and performance-based engineering analysis and design.

6.3 Smoothed Zignago-Barbato-Hu (ZBH) model

The original ZBH model is based on the constitutive model developed by Spoelstra and Monti (1999), which uses the formulation proposed by Mander et al. (1988) as the basic constant pressure-confined model, and iteratively solves the force equilibrium and compatibility between axial strain and lateral deformation of concrete and FRP wrap at each axial strain level. Thus, the ZBH model provides the axial-to-lateral strain relationship only implicitly, and builds the monotonic envelope of the FRP-and-steel confined concrete's stress-strain response for different levels of axial deformation through an iterative procedure (Zignago et al. 2018). This iterative procedure increases the computational cost of FE analyses of fiber-discretized RC members, since the iterative procedure is carried out for every fiber at each time step of the analysis, and can introduce numerical convergence issues in nonlinear dynamic FE analyses of large structures. This effect can be exacerbated in nonlinear dynamic FE analyses of large structures, for which small and/or adaptive time steps may be needed to compute an accurate tangent stiffness matrix, which is needed to achieve global convergence of the solution algorithm. It is noted here that the Spoelstra

and Monti (1999) model suffers from the same numerical limitation. However, the accuracy of the ZBH model in describing the FRP-and-steel confined concrete's stress-strain response derives from simultaneously satisfying force equilibrium and strain compatibility at the material/fiber level. Therefore, the development of an FRP-and-steel confined concrete constitutive model that can overcome this numerical limitation while retaining the accuracy of the original ZBH model is highly relevant and non-trivial.

An additional issue that can create numerical instability in the original ZBH model is the presence of a discontinuity in the monotonic envelope in the event of a rupture of either confining mechanism (i.e., FRP wraps or transverse steel). These discontinuities divide the monotonic envelope into three independent branches. The first branch corresponds to concrete confined by both FRP and steel and is characterized by an implicit relation between stress and strain that needs to be resolved through an iterative procedure (Zignago et al. 2018; Zignago and Barbato 2021). The second branch commonly starts after the confining FRP rupture and corresponds to concrete confined only by steel; thus, it coincides with the Mander model (Mander et al. 1988), which explicitly provides the relation between stress and strain. Finally, the third branch starts after the confining steel breaks, corresponds to unconfined concrete, and coincides with the Popovics-Saenz model (Popovics 1973), which also consists in an explicit relation between stress and strain.

It has been shown for other material constitutive models that this type of discontinuities can create numerical issues, particularly for applications requiring repetitions of FE analyses with different values of the modeling parameters, such as structural reliability analysis (Barbato and Conte 2005, 2006). In order to address this issue, a smoothed ZBH model is introduced in this study by connecting two subsequent branches of the monotonic envelope through linear branches with negative slopes equal in absolute value to the initial concrete stiffness, E_{c0}, as shown in Figure

6-1.

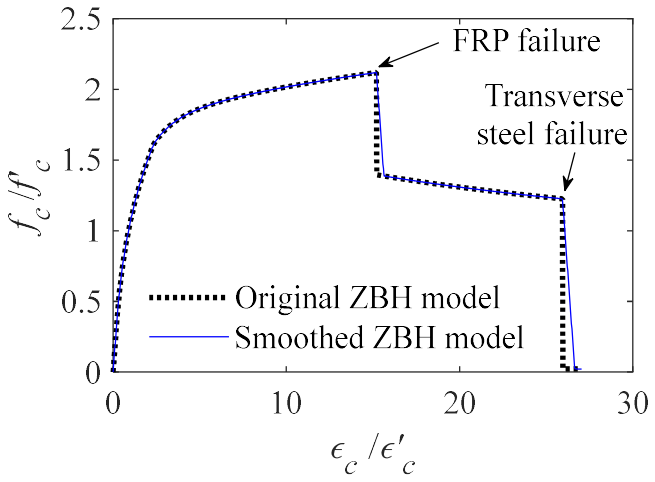

Figure 6-1. Monotonic envelope curves for the original and smoothed ZBH models

This simple modification removes the discontinuities in the monotonic envelope of the original ZBH model with minimal changes in the actual structural response of any FE model adopting this confined concrete model, and without requiring any modifications to the hysteretic portion of the model (Zignago et al. 2018). It is noted here that the obtained stress-strain model is a continuous function with discontinuous derivatives with respect to the modeling parameters (i.e., with discontinuous response sensitivities), which is suboptimal for structural engineering applications requiring response sensitivity calculations, such as structural reliability analysis (Barbato and Conte 2006; Haukaas and Kiureghian 2006). However, further smoothing of the constitutive model can be performed without loss of generality to obtain continuous response sensitivities. This further smoothing of the ZBH constitutive model is outside the scope of the present study. Hereinafter, the smoothed ZBH model with the first branch of the monotonic envelope obtained using the iterative procedure is, in short, referred to as iterative ZBH model.

Figure 6-2 presents the experimental validation of the original ZBH model, conducted in Zignago et al. (2018), with experimental data available in the literature. It demonstrates the capability of

the model to predict the structural behavior of FRP-confined RC columns for different loading conditions, namely: concentric axial loads, eccentric axial loads, and cyclic lateral loads.

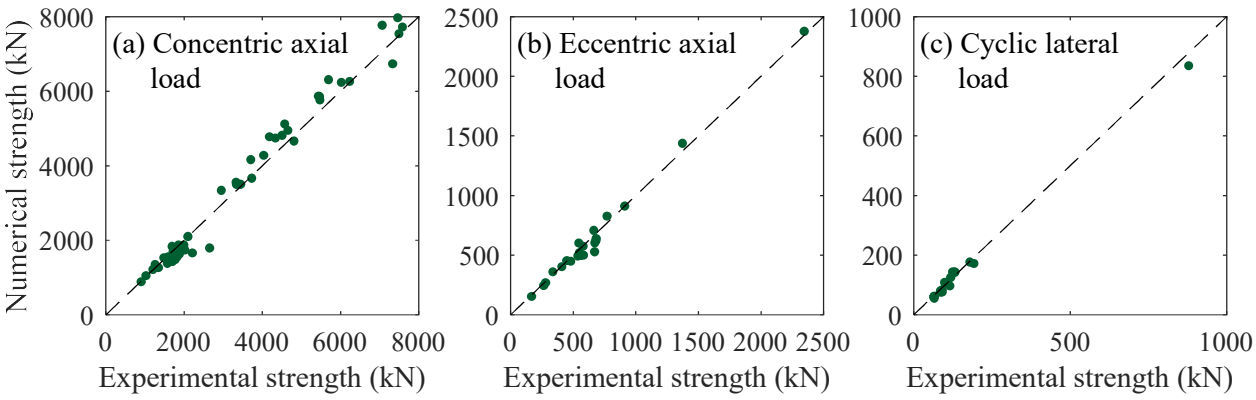

Figure 6-2. Experimental validation of the ZBH model for: (a) concentric axial loads; (b) eccentric axial loads; and (c) cyclic lateral loads

It is also noted here that the current fiber-section FE implementation does not include a transfer of information across different fibers within a cross-section to account for the sudden failure of FRP or steel confinement. However, previous results indicate that this effect is negligible (Hu and Barbato 2014; Zignago et al. 2018; Megalooikonomou and Papavasileiou 2019).

6.4 Dimensional analysis and parameter range of validity

A dimensional analysis is performed here to identify the minimum set of nondimensional variables needed to describe the stress-strain curve of the FRP-and-steel confined concrete model (Zignago et al. 2018). Based on the model developed in Zignago et al. (2018), the concrete stress f_c at a given axial strain ε_c depends on the following seven mechanical properties: unconfined concrete strength, f_c'; concrete initial tangent stiffness, E_{c0}; unconfined concrete strain at peak strength, ε_c'; effective confining pressure applied by the FRP wraps, $f_{lf} = 0.5\rho_f E_f \varepsilon_{fe}$, in which ρ_f is the

FRP volumetric reinforcement ratio, E_f is the FRP Young's modulus, and ε_{fe} is the effective strain of FRP at rupture; confining pressure exerted by the internal steel, $f_{ls} = 0.5k_s\rho_s f_y$, in which k_s is the steel confinement effectiveness coefficient (Mander et al. 1988), ρ_s is the transverse steel volumetric reinforcement ratio, and f_y is the transverse steel yielding strength; yielding strain of transverse steel, ε_y; and effective strain of FRP at failure, $\varepsilon_{fe} = \kappa_\varepsilon \varepsilon_{fu}$, in which κ_ε = FRP strain efficiency factor, and ε_{fu} = ultimate strain of the FRP obtained from flat coupon tensile tests. Therefore, a total of $n_v = 9$ variables are needed to fully describe the stress-strain curve, i.e., $V_V = \{f_c, \varepsilon_c, f_c', E_{c0}, \varepsilon_c', f_{lf}, f_{ls}, \varepsilon_y, \varepsilon_{fe}\}$, among which the $m = 2$ variables $Q_v = \{f_c', \varepsilon_c'\}$ are selected as repeating variables, where m = number of independent primary dimensions and Q_v is the set containing the repeating variables. By using the modified Buckingham's Π-theorem (Butterfield 1999) and by normalizing the results in terms of f_c / f_c' as a function of $\varepsilon_c / \varepsilon_c'$, a valid set of dimensionless groups is given by: $\pi_1 = f_c / f_c'$, $\pi_2 = \varepsilon_c / \varepsilon_c'$, $\pi_3 = f_{lf} / f_c'$, $\pi_4 = f_{ls} / f_c'$, $\pi_5 = E_{c0}\varepsilon_c' / f_c'$, $\pi_6 = \varepsilon_y / \varepsilon_c'$, and $\pi_7 = \varepsilon_{fe} / \varepsilon_c'$. Therefore, π-groups π_3 through π_7 completely define the normalized curve $\pi_1 = f_c / f_c'$ versus $\pi_2 = \varepsilon_c / \varepsilon_c'$. It is pointed out that the dimensional analysis performed here is more general than that presented in Zignago and Barbato (2022) because: (1) it identifies the nondimensional groups needed to describe the entire stress-strain response of the FRP-and-steel confined concrete instead of focusing only on the peak strength, and (2) it considers E_{c0} and ε_c' as independent parameters instead of calculating them from f_c'.

Based on the identified π-groups, realistic parameter ranges are selected as follows: (1) f_{lf} / f_c' = FRP confining ratio ranges from 0.00 to 0.40 with increments equal to 0.01 (41 levels); (2) f_{ls} / f_c' = transverse steel confining ratio ranges from 0.00 to 0.25 with increments equal to 0.01

(26 levels); (3) $E_{c0}\varepsilon_c' / f_c' =$ 1.64, 1.70, 1.79, and 1.86 (4 levels), which correspond to concrete with f_c' = 20 MPa, 30 MPa, 50 MPa, and 70 MPa, respectively, associated with commonly used expressions for E_{c0} and ε_c' (Mander et al. 1988; De Nicolo et al. 1994); (4) $\varepsilon_y / \varepsilon_c'$ = 0.75, 1.05, and 1.25 (3 levels); and (5) $\varepsilon_{fe} / \varepsilon_c'$ = 4, 8, and 12 (3 levels). The upper bound of the FRP confining ratio is selected to be slightly higher than the upper limits recommended by Equation 5.3.2.2-2 of AASHTO (2014) and the limit of 0.33 recommended by the ISIS Canada Manual No. 4 (ISIS Canada 2002). The values of $E_{c0}\varepsilon_c' / f_c'$, $\varepsilon_y / \varepsilon_c'$, and $\varepsilon_{fe} / \varepsilon_c'$ are selected based on mechanical properties of commercially available FRP laminates, U.S. reinforcement steel, and U.S. concrete (De Nicolo et al. 1994). The upper bound of the transverse steel confining ratio is selected to represent a practical limit for real-world applications, based on the shear strength cap in Provision 11.4.3 of ACI 440.2R-17 (2017). This selection of parameter values corresponds to a total 38,376 stress-strain curves, which were evaluated using the original version of the ZBH model. The considered parameters with their corresponding values/ranges are summarized in Table 6-1.

Table 6-1. Parameters considered in this study

Parameter	Values
f_{lf} / f_c'	0.00 – 0.40
f_{ls} / f_c'	0.00 – 0.25
$E_{c0}\varepsilon_c' / f_c'$	1.64, 1.70, 1.79, 1.86
$\varepsilon_y / \varepsilon_c'$	0.75, 1.05, 1.25
$\varepsilon_{fe} / \varepsilon_c'$	4, 8, 12

The following parameter values are assumed as reference values (rv) to help visualize the effects of each parameter on the FRP-and-steel confined concrete stress-strain curve: $f_{lf} / f_c' = 0.16$, $f_{ls} / f_c' = 0.12$, $E_{c0}\varepsilon_c' / f_c' = 1.70$, $\varepsilon_y / \varepsilon_c' = 1.05$, and $\varepsilon_{fe} / \varepsilon_c' = 8$. Figure 6-3 shows how the first

branch of the normalized stress-strain curves of the ZBH model change when only one parameter at a time is changed while the other parameters are kept constant and equal to their respective reference values.

It is observed that the FRP confining ratio, f_{lf} / f_c', the steel confining ratio, f_{ls} / f_c', and the ratio of effective strain of FRP at failure to unconfined concrete strain at peak strength, $\varepsilon_{fe} / \varepsilon_c'$, have a significant effect on the stress-strain curves (Figure 6-3a, b and e), whereas the other two parameters, $E_{c0}\varepsilon_c' / f_c'$ and $\varepsilon_y / \varepsilon_c'$, have a very small influence on the stress-strain curves. In particular, an increasing value of $E_{c0}\varepsilon_c' / f_c'$ results in a small shift upward of the curve (Figure 6-3(c)); whereas an increasing value of $\varepsilon_y / \varepsilon_c'$ has a very small and localized effect corresponding to a curvature decrease at the confining steel's transition point between elastic and plastic behavior (Figure 6-3(d)).

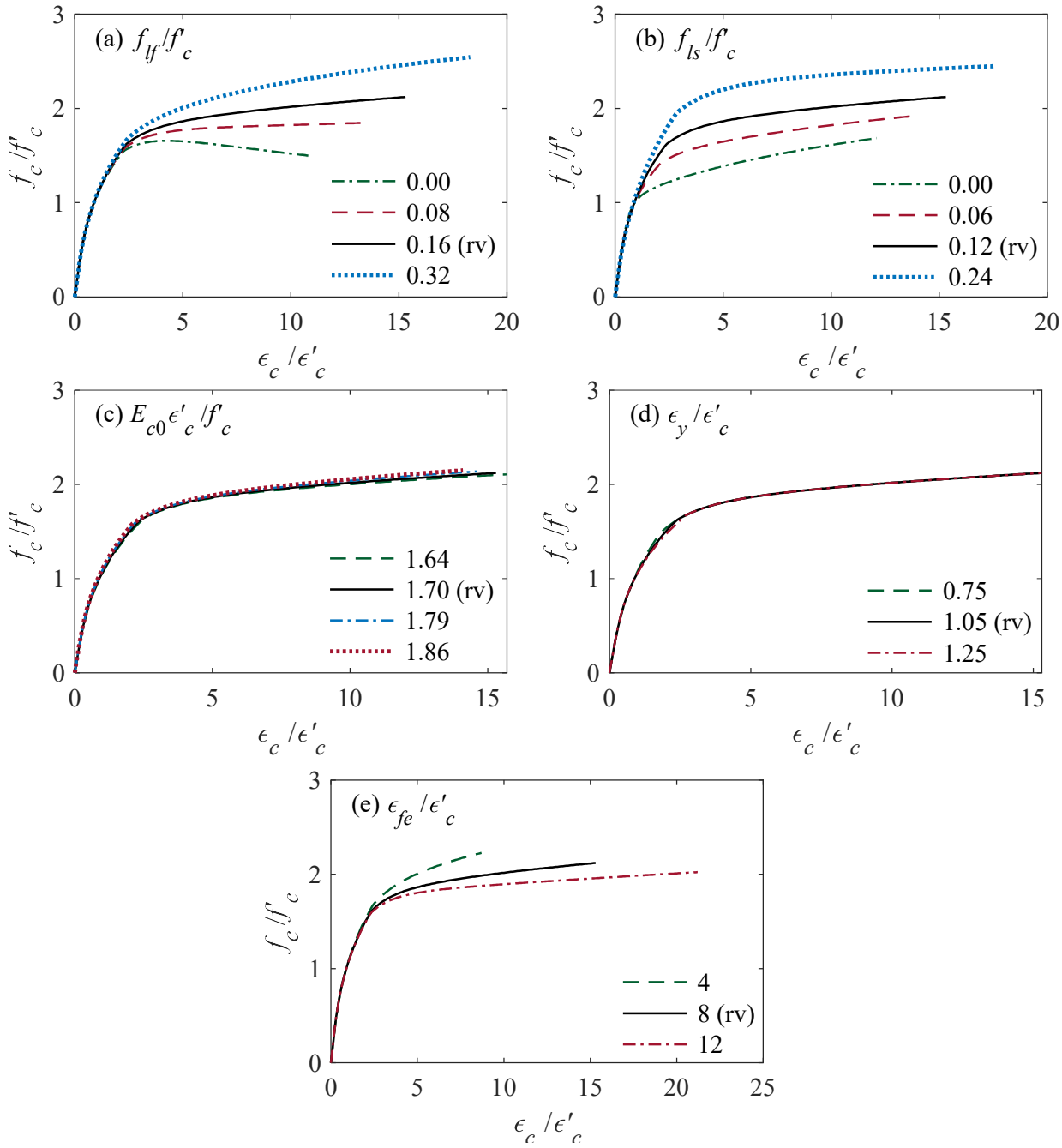

Figure 6-3. Sensitivity of normalized stress-strain curve to different nondimensional parameters.

6.5 Optimization-based analytical monotonic envelope

As previously noted, the monotonic envelope of the original ZBH model (Zignago et al. 2018) consists of three different branches, of which only the first branch is obtained through an iterative procedure. Therefore, an analytical expression needs to be identified only for the first branch of the FRP-and-steel confined concrete model. It is highlighted that the same procedure developed in this paper for the FRP-and-steel confined concrete model is also valid for the Spoelstra and Monti model (Spoelstra and Monti 1999), which represents the special case of the FRP-and-steel confined concrete model when there is no confining steel.

The analytical expression for the first branch of the ZBH model's monotonic envelope is obtained through an optimization procedure that provides a different curve for each specific combination of nondimensional parameters. Preliminary test results indicated that: (1) the fitting parameters are functions of the nondimensional parameters; (2) the functional dependence of the fitting parameters on the nondimensional parameters is extremely complex even for the simplest analytical functions (thus, making any explicit equation unfeasible for practical use); (3) when calculating the fitting parameter values via optimization, multiple local optimum solutions generally exist, sometimes corresponding to physically-unrealizable stress-strain curves; and (4) the computational cost of using global optimization to obtain the analytical curve with the best fit to the ZBH model's monotonic envelope can exceed the computational saving associated with using the analytical curve in the FE analyses. Therefore, the following approach is used to derive the optimization-based analytical expression of the FRP-and-steel confined concrete's stress-strain monotonic envelope: (1) a set of function families is selected, (2) the curve fitting problem is cast as a nonlinear constrained minimization problem, (3) a global optimization algorithm is used to identify the feasible domain of the fitting parameters corresponding to the global optimum and the

starting points for local optimization, (4) an optimization procedure based on local optimization is proposed to find the analytical expression for the ZBH model's stress-strain monotonic envelope, and (5) the proposed methodology is validated and the function family with the best overall performance (in terms of computational cost, simplicity, and accuracy) is identified.

6.5.1 Selected families of analytical functions

Eight families of analytical functions are considered in this study, as described in Table 6-2: two of them (i.e., I and II) are inspired by the equation proposed by Popovics (1973) to describe the stress-strain behavior of unconfined concrete, whereas the other six function families (i.e., III through VIII) are rational functions of polynomials with different orders, inspired by the general expression in the model proposed by Sargin (1971). Among this sub-group, analytical functions V, VII, and VIII consist of two rational function branches intersecting at the axial strain value $\varepsilon_c = \varepsilon_{c,y}$ (i.e., the axial concrete strain corresponding to the yielding of the lateral confining steel). Analytical functions VI through VIII are characterized by an additional constraint imposing that the tangent stiffness at any point of the stress-strain curve, E_c, is smaller than or equal to the unconfined concrete initial stiffness E_{c0}.

Table 6-2. Summary of considered analytical fit functions

#	Fit Function F	Constraints
I	$\frac{f_c}{f'_c} = \frac{c_1\left(\frac{\varepsilon_c}{\varepsilon'_c}\right)}{c_2 - 1 + \left(\frac{\varepsilon_c}{\varepsilon'_c}\right)^{c_3}}$	$c_2 > 1$

II

$$\frac{f_c}{f_c'}=\frac{\left[1+c_1\left(\frac{\varepsilon_c}{\varepsilon_c'}\right)\right]\left(\frac{\varepsilon_c}{\varepsilon_c'}\right)}{c_2-1+c_3\left(\frac{\varepsilon_c}{\varepsilon_c'}\right)^{c_4}} \qquad c_2>1,\ c_3>0$$

III

$$\frac{f_c}{f_c'}=\frac{c_1\left(\frac{\varepsilon_c}{\varepsilon_c'}\right)^3+c_2\left(\frac{\varepsilon_c}{\varepsilon_c'}\right)^2+E_{c0}\left(\frac{\varepsilon_c}{\varepsilon_c'}\right)}{c_3\left(\frac{\varepsilon_c}{\varepsilon_c'}\right)^2+c_4\left(\frac{\varepsilon_c}{\varepsilon_c'}\right)+1} \qquad c_4^2-4c_3<0$$

IV

$$\frac{f_c}{f_c'}=\frac{c_1\left(\frac{\varepsilon_c}{\varepsilon_c'}\right)^4+c_2\left(\frac{\varepsilon_c}{\varepsilon_c'}\right)^3+c_3\left(\frac{\varepsilon_c}{\varepsilon_c'}\right)^2+E_{c0}\left(\frac{\varepsilon_c}{\varepsilon_c'}\right)}{c_4\left(\frac{\varepsilon_c}{\varepsilon_c'}\right)^2+c_5\left(\frac{\varepsilon_c}{\varepsilon_c'}\right)+1} \qquad c_5^2-4c_4<0$$

V

$$\frac{f_c}{f_c'}=\begin{cases}\dfrac{c_1\left(\frac{\varepsilon_c}{\varepsilon_c'}\right)^3+c_2\left(\frac{\varepsilon_c}{\varepsilon_c'}\right)^2+E_{c0}\left(\frac{\varepsilon_c}{\varepsilon_c'}\right)}{c_3\left(\frac{\varepsilon_c}{\varepsilon_c'}\right)^2+c_4\left(\frac{\varepsilon_c}{\varepsilon_c'}\right)+1}, & 0\le\left(\frac{\varepsilon_c}{\varepsilon_c'}\right)\le\left(\frac{\varepsilon_{c,y}}{\varepsilon_c'}\right)\\ \dfrac{c_5\left(\frac{\varepsilon_c}{\varepsilon_c'}\right)^3+c_6\left(\frac{\varepsilon_c}{\varepsilon_c'}\right)^2+c_7\left(\frac{\varepsilon_c}{\varepsilon_c'}\right)}{c_8\left(\frac{\varepsilon_c}{\varepsilon_c'}\right)^2+c_9\left(\frac{\varepsilon_c}{\varepsilon_c'}\right)+1}, & \left(\frac{\varepsilon_c}{\varepsilon_c'}\right)>\left(\frac{\varepsilon_{c,y}}{\varepsilon_c'}\right)\end{cases} \qquad c_4^2-4c_3<0$$

VI

$$\frac{f_c}{f_c'}=\frac{c_1\left(\frac{\varepsilon_c}{\varepsilon_c'}\right)^3+c_2\left(\frac{\varepsilon_c}{\varepsilon_c'}\right)^2+E_{c0}\left(\frac{\varepsilon_c}{\varepsilon_c'}\right)}{c_3\left(\frac{\varepsilon_c}{\varepsilon_c'}\right)^2+c_4\left(\frac{\varepsilon_c}{\varepsilon_c'}\right)+1} \qquad c_4^2-4c_3<0,\ E_c\le E_{c0}$$

VII

$$\frac{f_c}{f_c'}=\begin{cases}\dfrac{c_1\left(\frac{\varepsilon_c}{\varepsilon_c'}\right)^3+c_2\left(\frac{\varepsilon_c}{\varepsilon_c'}\right)^2+E_{c0}\left(\frac{\varepsilon_c}{\varepsilon_c'}\right)}{c_3\left(\frac{\varepsilon_c}{\varepsilon_c'}\right)^2+c_4\left(\frac{\varepsilon_c}{\varepsilon_c'}\right)+1}, & 0\le\left(\frac{\varepsilon_c}{\varepsilon_c'}\right)\le\left(\frac{\varepsilon_{c,y}}{\varepsilon_c'}\right)\\ \dfrac{c_5\left(\frac{\varepsilon_c}{\varepsilon_c'}\right)^3+c_6\left(\frac{\varepsilon_c}{\varepsilon_c'}\right)^2+c_7\left(\frac{\varepsilon_c}{\varepsilon_c'}\right)}{c_8\left(\frac{\varepsilon_c}{\varepsilon_c'}\right)^2+c_9\left(\frac{\varepsilon_c}{\varepsilon_c'}\right)+1}, & \left(\frac{\varepsilon_c}{\varepsilon_c'}\right)>\left(\frac{\varepsilon_{c,y}}{\varepsilon_c'}\right)\end{cases} \qquad c_4^2-4c_3<0,\ E_c\le E_{c0}$$

VIII	$\frac{f_c}{f_c'}=\begin{cases}\dfrac{c_1\left(\frac{\varepsilon_c}{\varepsilon_c'}\right)^3+c_2\left(\frac{\varepsilon_c}{\varepsilon_c'}\right)^2+E_{c0}\left(\frac{\varepsilon_c}{\varepsilon_c'}\right)}{c_3\left(\frac{\varepsilon_c}{\varepsilon_c'}\right)^2+c_4\left(\frac{\varepsilon_c}{\varepsilon_c'}\right)+1}, & 0\le\left(\frac{\varepsilon_c}{\varepsilon_c'}\right)\le\left(\frac{\varepsilon_{c,y}}{\varepsilon_c'}\right) \\ \dfrac{c_5\left(\frac{\varepsilon_c}{\varepsilon_c'}\right)^3+c_6\left(\frac{\varepsilon_c}{\varepsilon_c'}\right)^2+c_7\left(\frac{\varepsilon_c}{\varepsilon_c'}\right)}{c_8\left(\frac{\varepsilon_c}{\varepsilon_c'}\right)+1}, & \left(\frac{\varepsilon_c}{\varepsilon_c'}\right)>\left(\frac{\varepsilon_{c,y}}{\varepsilon_c'}\right)\end{cases}$	$c_4^2-4c_3<0$ $E_c\le E_{c0}$

6.5.2 Definition of curve fitting problem

The curve fitting problem is cast as a nonlinear constrained minimization problem with the objective function corresponding to the sum of the squares of the residuals, and is expressed by:

$$\min_{\mathbf{c}} \sum_{j=1}^{n}\left[F\left(\mathbf{c},x_j\right)-y_j\right]^2 \quad \text{subject to } \mathbf{r}(\mathbf{c})\le 0,\ \mathbf{lb}\le\mathbf{c}\le\mathbf{ub} \tag{6-1}$$

in which the residuals correspond to the difference between the target normalized stress $y_j = f_{c,j}/f_c'$ obtained from the iterative ZBH model and the fitted normalized stress $F\left(\mathbf{c},x_j\right)=f_c\left(\mathbf{c},x_j\right)/f_c'$ corresponding to the considered analytical function, F, calculated at the normalized strain $x_j=\varepsilon_{c,j}/\varepsilon_c'$; n denotes the total number of data points in which the stress-strain curve is discretized; $\mathbf{c}=\left[c_1,\ldots,c_p\right]^T$ denotes the vector of fitting parameters that need to be optimized, with the superscript T = transpose operator and $p=$ number of fitting parameters for a given function family and varying between 3 and 9 (see Table 6-2); $\mathbf{r}(\mathbf{c})\le 0$ denotes the vector of nonlinear constraints listed in Table 6-2; and $\mathbf{lb}$ and $\mathbf{ub}$ correspond to the lower and upper bound values, respectively, of the fitting parameters. The vector inequalities in Eq. (6-1) represent component-wise inequalities. In order to ensure an approximately homogeneous discretization of

all stress-strain curves, the normalized strain increments are assumed constant and equal to $\Delta x_j = x_j - x_{j-1} = 0.1$, with $j = 1,\ldots,n$ and $x_0 = 0$. By assuming zero initial stresses corresponding to zero strain, $F\left(\mathbf{c}, x_0\right) = y_0 = 0$.

6.5.3 Global optimization and identification of parameter bounds

Each mathematical function from Table 6-2 is fitted to the 38,376 stress-strain curves obtained from the ZBH model and corresponding to all possible combinations of nondimensional parameters listed in Table 6-1. This optimization is performed by using the multiple starting point algorithm *GlobalSearch* (Ugray et al. 2007; Mathworks 2021), which is available in the global optimization toolbox of MATLAB, version R2021a (Mathworks 2021). This algorithm generates a set of potential start points (trial points) within the domain bounds, **lb** and **ub**, based on a scatter-search method, i.e., an iterative heuristic search method used to find global optima in optimization problems (Ugray et al. 2007; Mathworks 2021). These trial points are then filtered out to increase efficiency. Finally, the local nonlinear constrained optimization solver *fmincon* is employed to evaluate the local minima associated with each of the remaining trial points (Mathworks 2021). Preliminary results showed that all components c_i of the optimized coefficients $\mathbf{c}^*$ assumed values contained within the interval [-2, 20]. Thus, this interval was used as the feasible domain of the optimization variables in the global optimization procedure. The first global optimization step is used to: (1) identify the lower and upper bounds containing the global optima $\mathbf{c}^*$ corresponding to physically-realizable stress-strain curves, and (2) find appropriate hot starting points for the local optimization algorithm used to obtain the analytical function representing the stress-strain monotonic envelope. The lower and upper lower boundary values identified in this first global optimization step are reported in Table 6-3. They were obtained by

analyzing both local and global minima obtained through the global optimization algorithm and restricting the feasible domain to avoid regions with starting points that produced local minima that diverged from the corresponding global minimum.

Table 6-3. Parameter bounds for local optimization

Fit function		c_1	c_2	c_3	c_4	c_5	c_6	c_7	c_8	c_9
I	**ub**	5.0	4.6	2.6	-	-	-	-	-	-
	lb	1.0	1.1	0.7	-	-	-	-	-	-
II	**ub**	12.0	3.1	10.0	2.6	-	-	-	-	-
	lb	-0.2	1.2	0.0	0.6	-	-	-	-	-
III	**ub**	0.5	12.0	8.0	5.0	-	-	-	-	-
	lb	-0.2	-0.6	0.0	-0.5	-	-	-	-	-
IV	**ub**	0.1	1.2	25.0	7.0	7.0	-	-	-	-
	lb	-0.05	-1.2	-14.0	-0.1	-0.2	-	-	-	-
V	**ub**	2.4	15.0	7.2	5.2	0.5	4.2	0.6	12.0	20.0
	lb	-0.1	-2.0	0.0	-0.7	-0.5	-0.9	-0.6	-0.6	-2.0
VI	**ub**	0.4	12.0	7.0	5.0	-	-	-	-	-
	lb	-0.2	-0.6	0.0	-0.5	-	-	-	-	-
VII	**ub**	2.4	15.0	7.2	5.2	0.5	4.2	0.7	12.0	20.0
	lb	-0.1	-2.0	0.0	-0.7	-0.5	-0.9	-0.6	-0.6	-2.0
VIII	**ub**	2.4	15.0	7.2	5.2	0.5	0.8	12.0	-	-
	lb	-0.1	-2.0	0.0	-0.7	-0.5	-0.4	-0.9	-	-

6.5.4 Constrained local optimization and error measures

The analytical functions that provide the best fits to the 38,376 stress-strain curves corresponding to the iterative ZBH model are obtained using the local nonlinear constrained optimization solver *fmincon* (Mathworks 2021) in conjunction with the feasibility domains provided in Table 6-3. The start point of this local optimization step corresponds to the midpoint of the feasibility domain for each fitting parameter, i.e., $c_{0i} = (lb_i + ub_i)/2$ for $i = 1,\ldots, p.$ For all cases, the local optimization solutions coincided (within the assumed tolerance $tol = 10^{-4}$ for the numerical optimization

algorithm) with the global optimization solutions $\mathbf{c}^*$, thus corresponding to physically-realizable stress-strain curves.

In order to assess the accuracy of the different function families in fitting the target normalized stress-normalized strain curves, the relative area error (ξ_{area}) and the relative local error (ξ_{local}) are introduced as follows:

$$\xi_{area} = \frac{\int_0^{x_f} \left| F(\mathbf{c}, x) - y \right| \cdot dx}{\int_0^{x_f} y \cdot dx} \approx \frac{\sum_{j=1}^{n} \left| \left[F(\mathbf{c}^*, x_j) + F(\mathbf{c}^*, x_{j-1}) \right] - (y_j + y_{j-1}) \right|}{\sum_{j=1}^{n} (y_j + y_{j-1})} \tag{6-2}$$

$$\xi_{local} = \frac{\max_{1 \le j \le n} \left| F(\mathbf{c}^*, x_j) - y_j \right|}{\max_{1 \le j \le n} \left| y_j \right|} \tag{6-3}$$

in which $x_f =$ normalized strain corresponding to the failure of the FRP confinement.

Table 6-4 summarizes the performance of the different function families in fitting the stress-strain curves generated using the ZBH model in terms of mean and maximum values of ξ_{area} and ξ_{local} calculated over the 38,376 cases considered. It is observed that all eight fit functions have a mean ξ_{area} smaller than 1%, maximum ξ_{area} smaller than 6%, mean ξ_{local} smaller than 3%, and maximum ξ_{local} smaller than 15%. The best performance in terms of accuracy is achieved by fit function V, which presents the smallest values for all four error measures used in this study among all of the considered fit functions (mean ξ_{area} = 0.079%, maximum ξ_{area} = 0.902%, mean ξ_{local} = 0.474%, and maximum ξ_{local} = 3.922%), but also requires the largest number of parameters (i.e., nine parameters). As expected, the use of additional constraints, such as the constraint on the tangent stiffness $E_c \le E_{c0}$, produces a small increase in the error measures, as confirmed by the comparison of the results of fit functions III and V with fit function VI and VII, respectively.

The relative runtimes (i.e., the total runtimes normalized by the total runtime of the local optimization step for fit function I, which is equal to 90.59 s) are also reported in Table 6-4 for both global and local optimization. These runtimes are obtained by running a parallelized MATLAB code on a 6-node machine (Intel® Core™ i7-8700 CPU @ 3.20GHz and 16.0 GB RAM) with the following optimization options: step size = function tolerance = 10^{-4}, maximum number of iterations = maximum number of function evaluations = 10^3, local optimization algorithm = sequential quadratic programming (Gill et al. 1981), and all other options equal to the MATLAB default values. It is observed that the computational cost to obtain each analytical function by using the proposed optimization based approach (i.e., by using local optimization in conjunction with the feasibility domains given in Table 6-3 and using the midpoints as starting points) is contained between 0.002 s and 0.010 s, and that these computational times are slightly higher than those that would be obtained by running a serial code instead of a parallel one. These computational costs are negligible when compared to the computational cost of a nonlinear FE analysis of a structural system with more than a few hundreds of degrees of freedom.

Table 6-4. Assessment of fit functions' statistics after second optimization round

Fit function	Mean ξ_{area} (%)	Maximum ξ_{area} (%)	Mean ξ_{local} (%)	Maximum ξ_{local} (%)	Relative runtime (global)	Relative runtime (local)
I	0.878	5.948	2.884	14.935	38.93	1.00
II	0.490	3.809	2.783	11.769	93.14	3.01
III	0.403	1.259	1.745	4.571	44.31	1.42
IV	0.332	1.635	1.516	4.067	27.90	2.73
V	0.079	0.902	0.474	3.922	140.68	4.32
VI	0.412	1.839	1.807	5.639	32.08	1.45
VII	0.082	1.342	0.481	4.532	132.31	4.40
VIII	0.125	2.117	0.531	5.117	97.81	3.33

For further evaluation of the fitted functions and to help visually examine the accuracy of different

family of fit functions, ZBH model curves and their corresponding fitted curves are compared inFigure 6-4 and Figure 6-5. In particular, Figure 6-4 plots the iterative and analytical ZBH models for fit function III, selected as representative of the fit functions defined with a single mathematical expression. Figure 6-4(a) plots a case in which ξ_{area} is close the mean value of ξ_{area} in Table 6-4, whereas Figure 6-4(b) plots the results for the case in which ξ_{area} is maximum. Figure 6-5 plots the iterative and analytical ZBH models for fit function VII, selected as representative of piecewise fit functions. Figure 6-5(a) plots a case in which ξ_{area} is close the mean value of ξ_{area} in Table 6-4, whereas Figure 6-5(b) plots the results for the case in which ξ_{area} is maximum. In all cases, the accuracy of the analytical ZBH model is found to be satisfactory for numerical modeling of real-world structures.

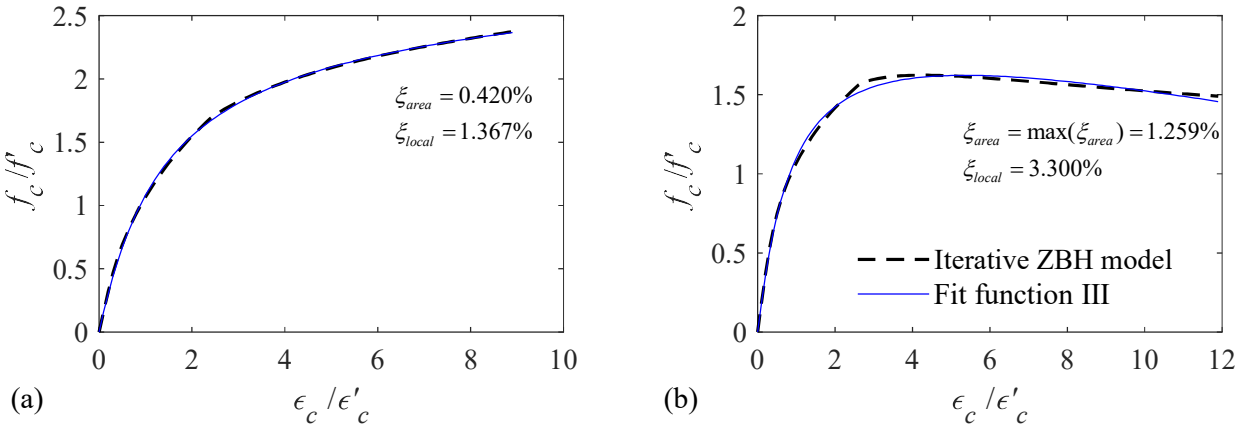

Figure 6-4. Comparison of the iterative and ZBH model and Fit function III for: (a) ξ_{area} close to the mean ξ_{area}; and (b) maximum ξ_{area} in Table 6.4

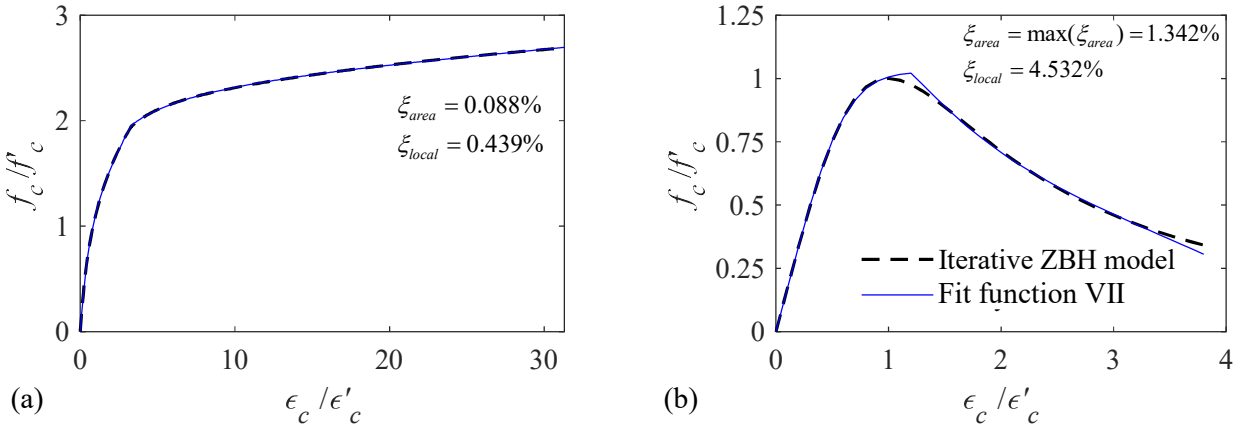

Figure 6-5. Comparison of the iterative and ZBH models using Fit function VII for: (a) ξ_{area} close to the mean ξ_{area}; and (b) maximum ξ_{area} in Table 6.4

6.5.5 Validation, performance comparison, and fitting function selection

The proposed optimization procedure is further validated by: (1) randomly generating (by associating to all π-groups a discrete uniform distribution and considering all design variables as statistically independent) 100,000 samples of FRP-and-steel confined concrete properties, (2) obtaining the corresponding stress-strain curve from the iterative ZBH model, (3) finding the optimum values of the fitting parameters based on the proposed local optimization procedure, and (5) calculating the corresponding error measures and relative runtimes for all eight fit functions considered in this study, as show in Table 6-5. The performance of the candidate fit functions is evaluated taking into account the number of coefficients c_i to be optimized, the relative area error ξ_{area}, the relative local error ξ_{local}, and runtime.

Table 6-5. Validation of performance of fit functions

Fit function	Mean ξ_{area} (%)	Maximum ξ_{area} (%)	Mean ξ_{local} (%)	Maximum ξ_{local} (%)	Relative runtime
I	0.880	5.261	2.811	14.193	2.12
II	0.469	3.266	2.842	12.270	7.13
III	0.374	1.175	1.724	4.381	2.37
IV	0.299	1.405	1.510	4.095	6.51

V	0.077	0.827	0.465	3.246	9.88
VI	0.380	1.570	1.772	4.592	3.19
VII	0.079	1.240	0.464	6.962	10.31
VIII	0.111	1.388	0.489	5.152	8.04

It is observed that fit functions I and II present the largest relative area and local errors among the studied functions, with mean ξ_{area} equal to 0.880% and 0.469%, respectively, and mean ξ_{local} equal to 14.193% and 12.270%, respectively. Although these two fit functions are inspired by the equation proposed by Popovics (1973) for unconfined concrete, they do not provide good curve fitting results for FRP-and-steel confined concrete.

Among the fit functions defined with a single mathematical expression (i.e., fit functions I, II, III, IV and VI), fit function IV contains the largest number of the optimization coefficients c_i (i.e., five) and performs the best in terms of mean ξ_{area} (i.e., 0.299%), mean ξ_{local} (i.e., 1.510%), and maximum ξ_{local} (i.e., 4.095%). Fit function III requires one less coefficient c_i than fit function IV; however, it presents a slightly better performance than fit function IV when considering the maximum ξ_{area} (i.e., 1.175% when compared to 1.405%). Fit function VI, which has the same analytical form of fit function III with the addition of a constraint on the tangent stiffness, presents also a similar performance.

The piecewise fit functions V and VII, which have the same functional form with the latter including a constraint on the tangent stiffness, present the overall best performance among all tested fit functions, with a mean ξ_{area} equal to 0.077% and 0.079%, a maximum ξ_{area} equal to 0.827% and 1.240%, a mean ξ_{local} equal to 0.465% and 0.464%, and a maximum ξ_{local} equal to.3.246% and 6.962%, respectively. For comparison, the best performance among the fit functions with a single mathematical expression (i.e., fit function VI) presents mean ξ_{area} and ξ_{local}

approximately 3.8 and 3.2 times higher than those of fit function VII, respectively. Fit functions V and VII present also the two highest runtimes (i.e., approximately 1.52 and 1.58 times that of fit function IV) and the largest number of optimization coefficients (i.e., nine coefficients). However, these computational cost increases are practically insignificant when compared to the computational cost of the FE analyses in which these material constitutive models would be typically used. In addition, the constraint on the tangent stiffness avoids spurious increases in stiffness that were observed in a few cases when using fit function V. Based on these considerations, it is concluded that fit function VII provides the overall best fit to the original ZBH model's stress-strain curve for FE analysis applications.

6.5.6 Construction of stress-strain curve for FE analysis applications

Based on the previously presented analysis, the following procedure is proposed here to obtain the non-iterative FRP-and-steel confined concrete constitutive model based on the newly-developed optimization-based analytical monotonic envelope (referred to as analytical ZBH model hereinafter) for FE analysis applications:

1) Build the FRP-and-steel confined concrete stress-strain curve using the iterative ZBH model for each representative concrete fiber (i.e., each fiber with different material parameters) in the FE model to be analyzed. Use a maximum axial strain sufficiently large to identify the axial strains corresponding to failure of the FRP and steel confinement.
2) For each of these concrete fibers, find the values of the fitting parameters for fit function VII using a local nonlinear constrained optimization solver (e.g., *fmincon*) and the parameter bounds provided in Table 6.3 to fit the first branch of the corresponding stress-strain curve obtained using the iterative ZBH model.
3) Use the analytical expressions for the Mander and the Popovics-Saenz models to describe

the second and third branches, respectively, of each stress-strain curve.

4) Assign these newly-obtained analytical curves to the corresponding concrete fibers of the FE model to be analyzed.

It is observed here that even large and complex structural FE models contain only a small number of concrete fibers with different material properties (typically, two different fibers for each different cross-section), whereas each column cross-section can contain up to hundreds of individual concrete fibers. Therefore, the computational overhead of obtaining the analytical ZBH model from the original ZBH model is generally small, independent of the FE model discretization, and relatively decreasing for increasing complexity and size of the FE model.

6.6 Application example 1: Experimental validation of seismic analysis for an FRP-confined column

The analytical ZBH model was implemented in OpenSees (Mazzoni et al. 2006) and is tested through a nonlinear seismic response analysis of a concrete filled FRP tube (CFFT) bridge column of a two-column bridge pier subjected to seismic loads, by using the experimental results presented in Zaghi (2009) and Zaghi et al. (2012). The two-column bridge pier consists of two 356-mm (14 in) diameter, 1511-mm (59.5 in) long columns with a center-to-center spacing of 2134 mm (84 in) between them, in addition to a concrete footing and a cap beam. One of the columns is a conventional RC column, while the second column is a CFFT bridge column, consisting of an FRP pipe with a wall thickness $t_f = 7$ mm (0.27 in), and fibers aligned at 55° with respect to the tube longitudinal axis, which contribute to the strength in both the longitudinal and hoop directions of the column. Additional geometric details and the values of the modeling parameters for the material constitutive models are provided in Zaghi (2009) and Zaghi et al. (2012).

The columns are modeled with fiber-discretized cross-sections (Spacone et al. 1996; Barbato 2009;

Hu and Barbato 2014) within nonlinear force-based beam-column elements with nonlinear rotational springs at the bottom to account for bond-slip rotations. At the top, flexural releases and a pipe-pin macro model were added to take into account the effects of slippage in the pipe-pin connections (Zaghi 2009). The cap beam is modeled with an elastic element, with the effective weight of the mass rig equal to 445 kN (100 kip), as shown in Figure 6-6(a). An additional axial load equal to 178 kN (50 kip) is also applied to each column. Figure 6-6(b) illustrates the columns' fiber-discretized cross-sections. The sectional fiber discretization employed in the analysis consists of 20 radial layers for the concrete core, 10 radial layers for the concrete cover, and 20 angular divisions, although Figure 6-6(b) shows only five radial layers for the concrete core and two layers for the concrete cover for the sake of clarity. Both iterative and analytical ZBH models are employed to describe the axial stress-axial strain response of the bridge piers' concrete fibers in order to quantitatively compare their performance. An outer layer is also included to model the longitudinal behavior of the FRP tube. The longitudinal steel rebar fibers are modeled using the extended Menegotto-Pinto model (Menegotto and Pinto 1973; Filippou et al. 1983).

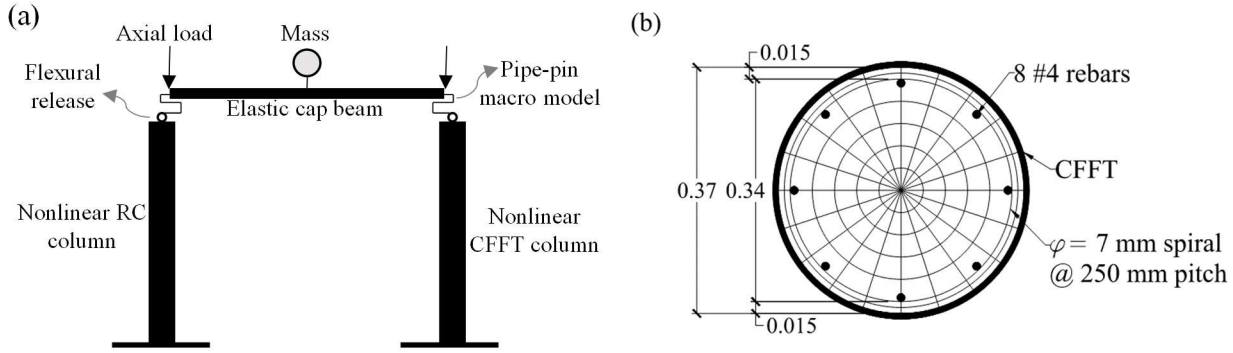

Figure 6-6. Structural model of the two-column bridge pier (units in m): (a) finite element model of the bridge pier; and (b) fiber discretization of the CFFT column cross-section

The two-column pier model is subjected to the 1994 Northridge earthquake ground acceleration

time-history recorded at the Sylmar Converter Station, as shown in Figure 6-7, applied synchronously at the base of both columns. The unscaled ground acceleration time-history is then filtered and compressed to take into account scaling effects, as explained in Zaghi (2009). The model is subjected to six subsequent ground acceleration time-histories of increasing intensity (referred to as runs hereinafter) obtained by applying to the recorded ground acceleration time-history a series of scale factors equal to 0.1, 0.4, 0.7, 1.0, 1.3, and 1.6, respectively. The axial loads are incrementally applied in a quasi-static manner prior to the application of the earthquake ground motion. The Krylov-Newton algorithm is employed, in conjunction with the unconditionally stable Newmark-beta stepping integration scheme (Chopra 2016).

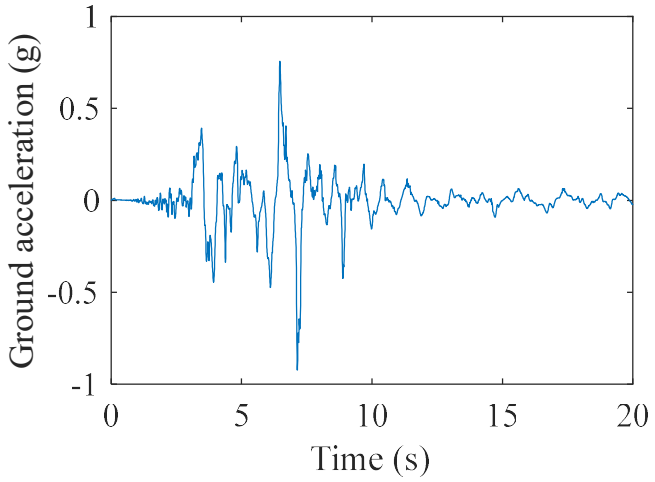

Figure 6-7. Unscaled ground acceleration time-history of the 1994 Northridge earthquake recorded at the Sylmar Converter Station

Figure 6-8(a) plots the displacement time-histories of the CFFT column's top node, simulated using both the iterative and analytical ZBH models, for runs 4, 5, and 6. The simulated responses are in very good agreement with the experimental results, with a maximum absolute difference equal to 21.610 mm (19.511% of the peak displacement) and 21.391 mm (19.313% of the peak displacement) for the iterative and analytical ZBH model, respectively. It is observed that the two

simulated response time-histories are practically identical, with a maximum absolute difference of 0.232 mm during run 6, which corresponds to approximately 0.209% of the peak displacement experimentally recorded during run 6. Similarly, a very good agreement between simulated responses and the base shear versus top displacement experimentally recorded for the CFFT column is observed in Figure 6-8(b).

The total execution times of the FE analyses employing the iterative and analytical ZBH model are also compared, based on a personal computer with Intel® Core™ i7-8700 CPU @ 3.20GHz and 16.0 GB RAM. The corresponding analysis clock time for the iterative ZBH model was 26.723 s, whereas the FE analysis using the analytical ZBH model required 23.147 s for all consecutive runs. This result corresponds to a reduction in computational time of approximately 13%. It is pointed out that this relative improvement in efficiency due to the use of the analytical ZBH model for the confined concrete is obtained for an example in which the difference in runtime stems from only one out of two columns, and a relatively complex and computationally expensive model is employed for the column-cap beam connection.

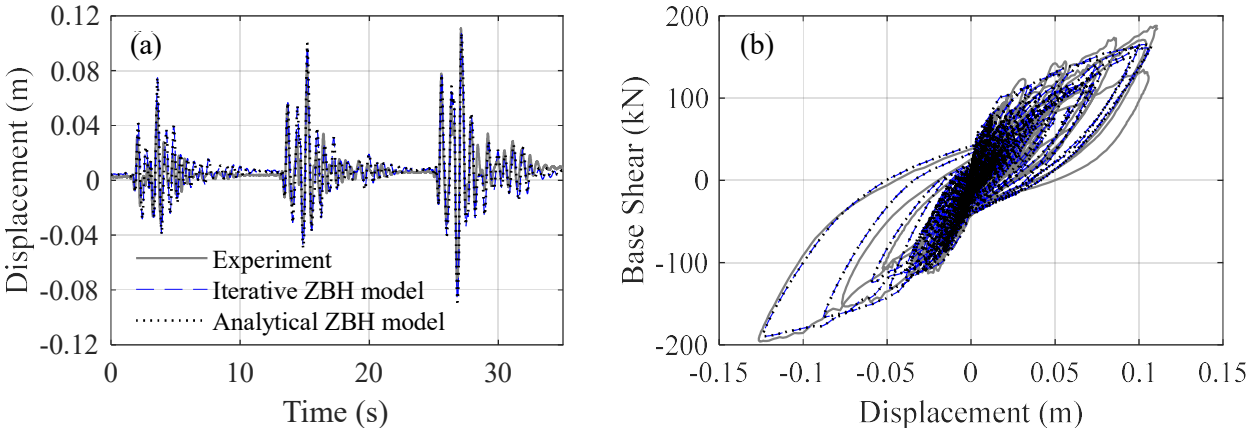

Figure 6-8. Experimental and simulated dynamic responses of the two-column bridge bent tested in Zaghi et al. (2012): (a) displacement time-history of the CFFT column's top node corresponding to runs 4, 5, and 6, with scale factors equal to 1.0, 1.3, and 1.6, respectively; and (b) base shear versus top displacement of the CFFT column

6.7 Application example 2: Nonlinear seismic analysis of a 3-dimensional RC bridge retrofitted with FRP

The analytical ZBH model is also tested through a nonlinear dynamic FE response analysis of a three-dimensional reinforced concrete bridge retrofitted using FRP wraps and subject to a seismic base excitation time-history. The considered bridge corresponds to design example #8 from NCHRP Project 12-49 (ATC/MCEER 2003), which is a five-span bridge with a total length of 152.40 m (500 ft) and five spans of 30.48 m (100 ft) supported by four two-column bents and two abutments, as represented in Figure 6-9(a). Additional geometric details and the values of the modeling parameters for the material constitutive models are provided in ATC/MCEER (2003). For the present application example, all columns of the original structure are retrofitted by using carbon FRP wraps with an elastic modulus $E_f = 137.9$ GPa (20,000 ksi), a tensile strength $\sigma_f =$ 1241 MPa (180 ksi), an FRP strain efficiency factor $\kappa_\varepsilon = 0.679$ (Realfonzo and Napoli 2011), and 10 FRP plies resulting in a total FRP thickness $t_f =$ 1.67 mm (0.06575 in). This FRP amount provides an FRP confinement pressure ratio $f_{lf} / f_c' = 0.082$, which complies with the minimum ratio $f_{lf} / f_c' = 0.08$ recommended by ACI 440.2R-17 guidelines. Figure 6-10 plots the complete stress-strain curve for the iterative and analytical ZBH models employed in the analysis for the concrete core and concrete cover fibers. The monotonic envelopes of the iterative and analytical ZBH models are extremely close, as confirmed by the reported error measurements for the first branch of each curve, with $\xi_{area} = 0.070\%$ and $\xi_{local} = 0.228\%$ for the constitutive model assigned to the concrete cover fibers, and $\xi_{area} = 0.081\%$ and $\xi_{local} = 0.359\%$ for the constitutive model assigned to the concrete core fibers.

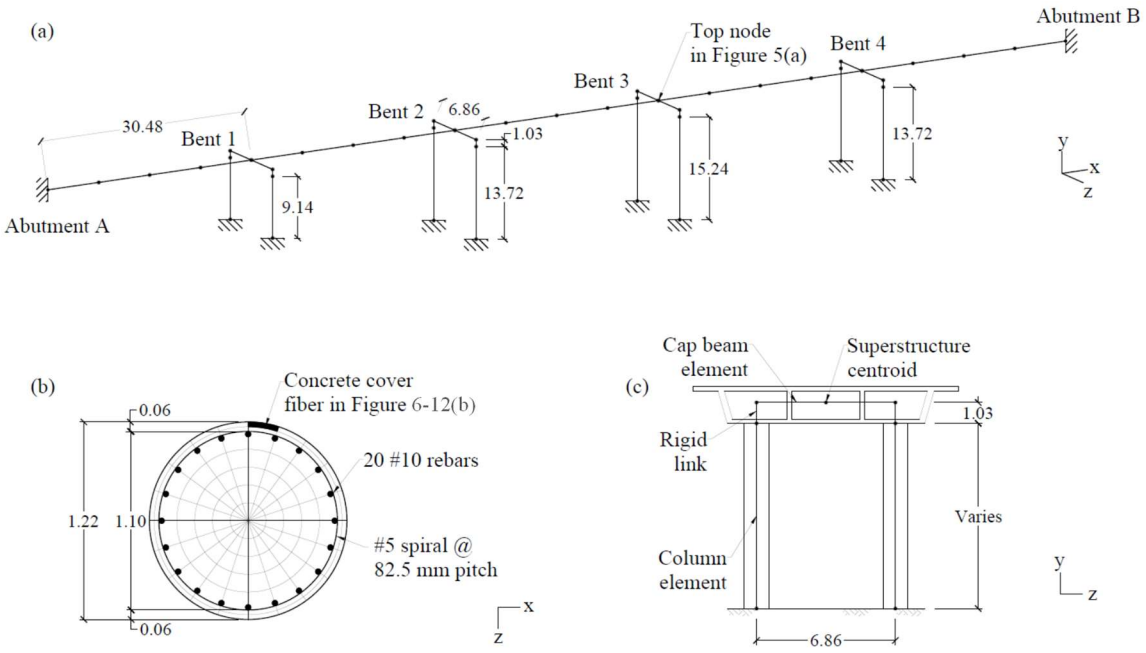

Figure 6-9. Structural model of the bridge (units in m): (a) finite element model of the bridge; (b) fiber discretization of columns cross-section; (c) finite element model of a bent

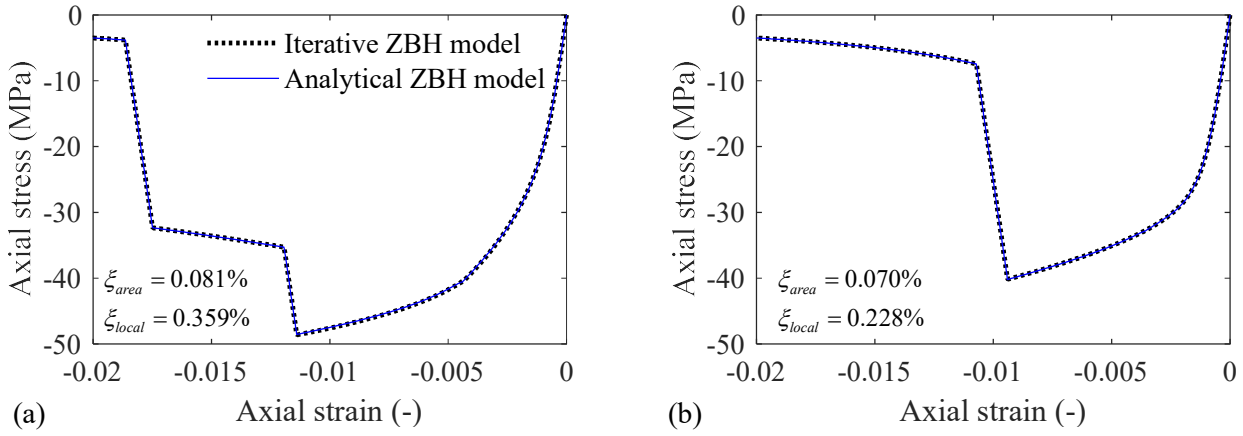

Figure 6-10. Complete stress-strain curve using the iterative and analytical ZBH models for: (a) core concrete fibers; and (b) cover concrete fibers

The columns are modeled with nonlinear force-based beam-column elements with plastic hinges based on the modified Gauss-Radau quadrature (Scott and Fenves 2006) and fiber-discretized cross-sections (Spacone et al. 1996; Barbato 2009; Hu and Barbato 2014), while the superstructure and the cap beams are modeled with elastic elements, as depicted in Figure 6-9(c). For each span,

the superstructure is divided into four 7.62 m (25 ft) elements, with the centerlines of the elements placed along the centroid of the superstructure and passing through the centroid of the cap beams. Figure 6-9(b) shows a representation of the columns' fiber-discretized cross-sections. The sectional fiber discretization employed in the analysis consists of 20 radial layers for the concrete core, 10 radial layers for the concrete cover, and 20 angular divisions, although Figure 6-9(b) shows only five radial layers for the concrete core and two layers for the concrete cover for the sake of clarity. The longitudinal steel fibers are modeled using the extended Menegotto-Pinto model (Menegotto and Pinto 1973; Filippou et al. 1983). For simplicity, all supports for piers and abutments are modeled as fixed restraints. Both iterative and analytical ZBH models are employed to describe the axial stress-axial strain response of the bridge piers' concrete fibers in order to quantitatively compare their performance.

The structural model of this bridge is subjected to the first 20 s of the 1994 Northridge earthquake ground acceleration time history recorded at the Arleta-Nordhoff Fire Station, as shown in Figure 6-11. The base excitation is applied synchronously at all supports in the transverse direction. In order to assess the effects of different levels of nonlinear behavior, three different nonlinear dynamic FE analyses are performed with the earthquake ground acceleration time history scaled by factors equal to 1, 2, and 4, respectively. Before application of the earthquake ground motion, both dead and live loads are incrementally applied in a quasi-static fashion, in which the dead loads are calculated form the geometry of the bridge's components and the unit weight of the materials, and the live-to-dead load ratio is assumed equal to 1. The modified Newton-Raphson algorithm is employed associated with the unconditionally stable Newmark-beta stepping integration scheme and a time discretization $\Delta t = 0.01$ s.

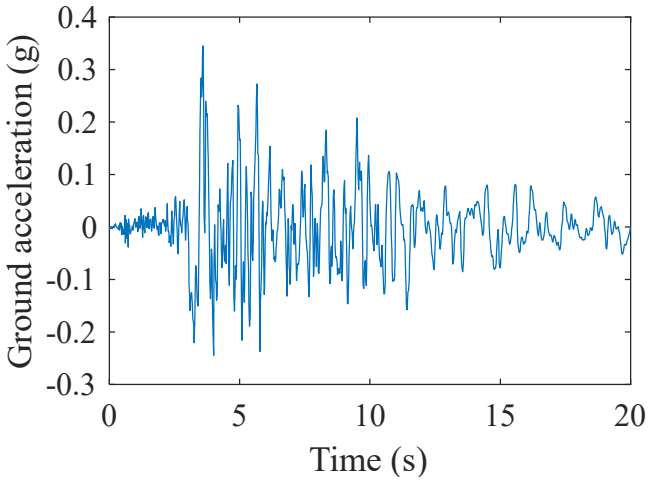

Figure 6-11. Unscaled ground acceleration time history of the 1994 Northridge earthquake recorded at the Arleta-Nordhoff Fire Station

The time histories for the transverse displacement of bent #3's top node, which are obtained using both the iterative and analytical ZBH models, are shown in Figure 6-12(a) for the earthquake ground acceleration time history scaled by a factor of 4. It is observed that the two response time histories are practically identical, with a maximum absolute difference of 0.401 mm over the entire 20 s of the response time histories, which corresponds to approximately 0.066% of the time history peak displacement. However, the FE analysis' total execution times depend on the level of nonlinearity and are significantly different between the FE models based on the iterative and analytical ZBH model. In particular, the nonlinear dynamic FE analyses performed using the iterative ZBH model required 16.617 s, 18.001 s, and 20.582 s for the ground motion records scaled by factors 1, 2, and 4, respectively, when using a personal computer with Intel® Core™ i7-8700 CPU @ 3.20GHz and 16.0 GB RAM. By contrast, the corresponding analysis clock times recorded when using the analytical ZBH model were 10.821 s, 11.486 s, and 12.843 s, respectively, with a reduction in computational time of approximately 35%, 36%, and 38%, respectively. The improved computational efficiency for the analytical ZBH model is obtained by removing the need for iterations at the material level in each of the confined concrete fibers

exhibiting nonlinear behavior, as demonstrated by the fact that the relative improvement in efficiency increases for increasingly nonlinear responses. It is observed that the computational savings are higher than those for the single column application example. This result was expected, as the proposed analytical constitutive model becomes more computationally efficient as the number of fibers included in the FE model increases, because the initial overhead associated with fitting the analytical curves to the corresponding iterative ZBH stress-strain curves becomes relatively smaller when compared to the overall computational cost of the nonlinear FE analysis. It is pointed out that, when the original non-smoothed ZBH model is employed, similar runtimes to those of the smoothed iterative ZBH are observed for the analyses with ground acceleration time-histories scaled by factors equal to 1 and 2. Conversely, when a scale factor equal to 4 is used, the FE analysis fails to achieve convergence at the FRP failure, when the same analysis parameters (i.e., fiber mesh and time step discretization) are used.

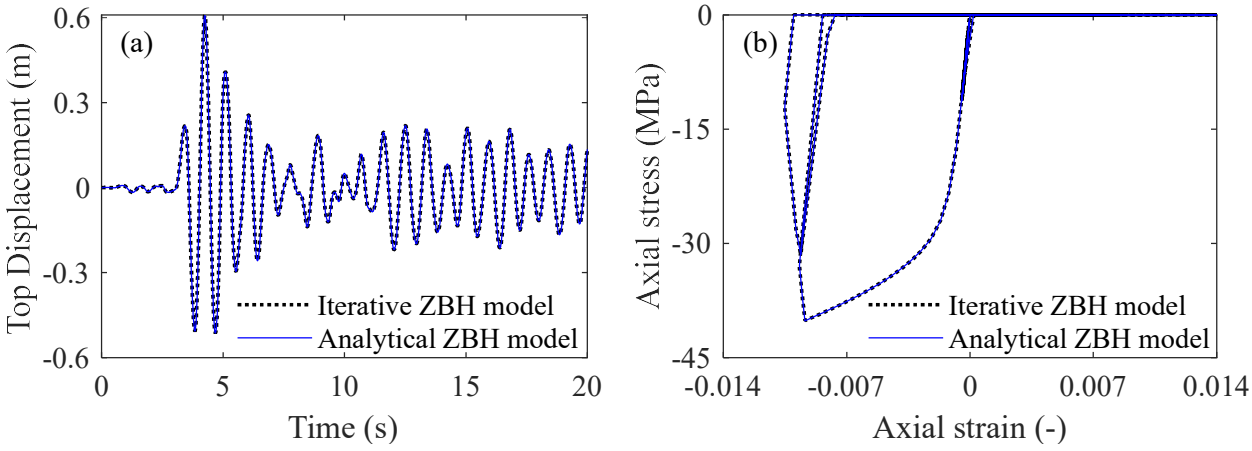

Figure 6-12. Dynamic response of the benchmark bridge subject to the 1994 Northridge earthquake ground acceleration time history scaled by factor equal to 4: (a) transverse displacement of the top node of bent #3; (b) axial stress-strain time-history of the outermost concrete fiber at the bottom plastic hinge of one of the columns in bent #3

Figure 6-12(b) shows the axial stress-axial strain response corresponding to the outermost concrete fiber at the bottom section of the plastic hinge formed at the base of one of the columns in bent #3

when the input ground motion is called by a factor equal to 4. This fiber was selected because it experiences one of the largest axial strains across the entire structure, up to reaching FRP failure. Also in this case, the responses obtained using the iterative and analytical ZBH models are practically identical. This observations demonstrates that: (1) the monotonic envelopes of iterative and analytical ZBH models are extremely close, with ξ_{area} equal to 0.007% and ξ_{local} equal to 0.228% for the constitutive model assigned to the concrete cover fibers, and ξ_{area} equal to 0.008% and ξ_{local} equal to 0.359% for the constitutive model assigned to the concrete core fibers; and (2) the two models produce practically coincident results in terms of both global and local responses when used in nonlinear dynamic FE analyses of structural systems.

6.8 Conclusions

This paper proposes a new analytical expression based on an optimization procedure for a recently developed analysis-oriented iterative FRP-and-steel confinement model for concrete (called hereinafter ZBH model). The monotonic envelope of the original ZBH model is made continuous everywhere by removing the discontinuities at the failure of FRP and transverse steel confinement. Five dimensionless parameters that fully describe the normalized axial stress-strain envelope curve of the ZBH model are identified through a dimensional analysis. The performance of eight candidate families of analytical functions in fitting the iteratively-generated uniaxial stress-strain curve for the monotonic envelope of FRP-and-steel-confined concrete over realistic ranges of the identified dimensionless parameters is evaluated in terms of computational cost, simplicity, and accuracy. The selected family of fitting functions (fit function VII) consists of a piecewise rational function with a total of nine coefficients to be optimized. On average, this method generates

analytical expressions for the ZBH model monotonic envelope with relative area error of 0.079% and relative local error of 0.464% when compared to the original iteratively generated ZBH model. The efficiency and accuracy of the newly proposed analytical expression of the ZBH model are compared with the original iterative formulation through two application examples consisting of nonlinear dynamic FE analyses of: (1) a concrete filled FRP tube (CFFT) bridge column of a two-column bridge pier experimentally subjected to seismic loads, and (2) a three-dimensional five-span bridge structure with FRP-retrofitted RC piers subject to a seismic base excitation time-history. It is found that the newly proposed optimization-based analytical monotonic envelope model produces dynamic responses that are practically coincident to those obtained using the original iterative model for the analyzed bridge at both global and local levels. It is also observed that the analytical model can reduce the computational time associated with the nonlinear dynamic FE analysis by more than 30%, and that its computational efficiency increases with increasing nonlinearity of the analysis. It is concluded that the newly proposed analytical model can be used in place of the original iterative model because it provides the same modeling accuracy at a significantly lower computational cost.

7 Research Summary and Conclusion

Externally-bonded fiber-reinforced polymer (FRP) laminates have been widely used in the retrofitting and rehabilitation of reinforced concrete (RC) columns through a confinement mechanism, in which the axial and bending moment capacities of these compression members can be greatly improved. The confinement produced by FRP laminates acts concurrently with the confining mechanism of the internal transverse steel, although the latter is often neglected in design standards and guidelines. In this dissertation, an analysis-oriented model of concrete that accurately accounts for the simultaneous confinement with FRP and steel is proposed. The complex nonlinear phenomenon of simultaneous confinement is handled at the material level through an iterative-incremental approach, in which force equilibrium and strain compatibility relationships involving the radial deformation of concrete and the confining devices (FRP and steel) are enforced when their respective lateral confining pressures exerted to concrete are superimposed. New hysteresis rules are also proposed based on previously experimental tests results to allow the use of the under cyclic and dynamic loading conditions. The relative confinement coefficient c_f is first introduced to help quantify the importance of the transverse steel confinement to the structural response of FRP-confined RC columns. The model is validated against experimental data available in the literature for three loading conditions: (1) concentric compression, (2) eccentric compression, and (3) combined axial and cyclic lateral loads.

The proposed FRP-and-steel confined concrete model is then employed in parametric studies to quantify the contribution of the often-ignored steel confinement on the load-bearing capacity of FRP-strengthened RC columns. A new design equation for pure compression is proposed and calibrated via structural reliability method. A procedure is also proposed to obtain an analytical expression for the envelope curve of the iteratively-generated original FRP-and-steel confined

concrete model. In the following sections, the major conclusions of this research work are summarized, and future research ideas are listed. The steel-and-FRP confined concrete model developed in this dissertation is suitable for use in finite element (FE) models in conjunction with fiber-section force-based frame and/or zero-length FEs, and can be used for accurate and computationally-efficient FE analysis of real-world large-scale structures (e.g., buildings and bridges) with FRP-confined RC columns, for which more accurate three-dimensional FE models could be computationally prohibitive. Also, the proposed steel-and-FRP confined concrete model can be used to achieve more efficient and economical retrofit design of RC columns through FRP confinement.

7.1 Conclusions

In Chapter 2, an analysis-oriented model of FRP-and-steel confined concrete is proposed. The proposed model is found to provide very good agreement with experimental data. The proposed model is also shown to provide more accurate estimates of the structural behavior of FRP-confined RC column specimens than models that either do not take into account the transverse steel confinement or that linearly superimpose the confinement effects from FRP and internal materials. The confinement effects of transverse steel are found to be significant, particularly for the concentric axial loading conditions. These effects on the columns' strength are comparatively smaller when the columns are subjected to the combined action of axial compression and bending moment, mainly as a result of the reduced average c_f values of the available data for eccentric and cyclic lateral cases. However, these effects are significantly larger for the lateral ductility capacity of columns subject to axial and lateral loads.

In Chapter 3, the proposed FRP-and-steel confined concrete model is employed in a comprehensive parametric study to investigate the steel confinement effects and the relative

importance of key modeling and design parameters on the axial strength of FRP-confined RC columns. The results show that the steel confinement effect can significantly increase the axial strength of FRP-confined RC columns, particularly for large cross-sections, low concrete compressive strengths, and low amounts of confining FRP. The impact of design limits on concrete deformation by design guidelines are also investigated. It is found that the imposition of design strain limits can reduce the gained strength by as much as 66% when compared to columns loaded up to failure. The steel confinement effects induce two distinct behaviors depending on the ratio between the FRP lateral confinement and the unconfined concrete peak axial strength. These two behaviors can be described as functions of two relative confinement coefficients (i.e., c_f, corresponding to the ratio between the steel and FRP confinement forces, and C_s, corresponding to a scaled ratio between the steel confinement force and the FRP confinement stiffness).

In Chapter 4, the parametric study carried out in Chapter 3 for FRP-confined RC columns subject pure compression is extended to the eccentric compression loading condition to investigate the interaction between axial load and bending moment. Design deformation limits as per ACI 440.2R-17 are found to significantly impact the column strength, with a reduction of 90.9% the normalized combined strength (defined as the distance between the origin and the point on the normalized axial-flexural interaction diagram corresponding to the maximum load achieved for a given eccentricity). The effect of steel confinement is affected by the load eccentricity. For this reason, the two relative confinement coefficients proposed in Chapter 3 are modified to quantify the effects of internal steel confinement by taking into account the effects of load eccentricity.

In Chapter 5, the results from the parametric study in Chapter 3 are used to propose a modification the design equation for FRP-confined RC circular columns subject to pure compression to include the transverse steel confinement effects. The new equation is calibrated by means of a structural

reliability analysis approach, taking into account uncertainties related to material, dimension, modeling, and loading variables. The probability distribution for the axial capacity of the columns is developed via Monte Carlo simulation based on advanced nonlinear FE response analysis, in which the FRP-and-steel confined concrete model is used to simulate the structural behavior of confined concrete within the FE model. The Hasofer-Lindt Rackwitz–Fiessler iterative algorithm is used to evaluate the first-order reliability indices for a wide range of design parameters. The newly proposed design equation generally yields a more efficient design than current design guidelines while keeping appropriate reliability indices. In fact, the proposed design equation is shown to produce up to 43% of savings on FRP material based on an application example concerning a retrofit design of a RC column within an adaptive reuse project context. A new iterative design procedure is also proposed and discussed.

In Chapter 6, the performance of eight candidate families of analytical functions in fitting the monotonic envelope of the original iterative formulation of the FRP-and-steel confined concrete curve is evaluated in terms of computational cost, simplicity, and accuracy. The selected family of fitting functions consists of a piecewise rational function with a total of nine coefficients to be optimized. On average, this method generates analytical expressions for the monotonic envelope of the original model with relative area error of 0.079% and relative local error of 0.464% when compared to the original iteratively-generated model. The efficiency and accuracy of the newly-proposed analytical expression of the FRP-and-steel confined concrete model are compared with the original iterative formulation through two application examples consisting in nonlinear seismic time-history analyses of: (1) a two-column bridge pier, and (2) a five-span bridge structure with FRP-retrofitted RC piers. Practically coincident dynamic responses are obtained for both iterative and analytical models, whereas the computational time associated with the nonlinear dynamic FE

analysis can be reduced by more than 30% when the analytical model is employed. It is concluded that the proposed procedure to generate analytical models can be used in place of the original iterative model due to similar modeling accuracy associated with both models, although at a significantly lower computational cost.

7.2 Future research work

Based on the results presented in this dissertation, some ideas for further research are proposed:

1) The FRP-and-steel confined concrete model has been validated for circular cross-sections only. Additional research is needed to extend the proposed model to other shapes (e.g., rectangular). For this purpose, it is crucial to identify the regions within the cross-section that are effectively confined by FRP and steel, by steel only, and by FRP only, and employ the confinement model accordingly.
2) The calibration of the proposed design equation is only valid for circular cross-sections subject to nominal pure compression. A new calibration procedure needs to be conducted for different cross-sections and different loading conditions. For this purpose, a procedure similar to the one adopted in Chapter 4 can be employed. The random variable regarding the modeling error needs to be evaluated for each case.
3) The proposed confinement model has been validated only for specimens presenting preserved structural integrity. Additional research is needed to investigate the behavior of pre-damaged columns. Available data in the literature can be collected to validate the model. In addition, new experimental studies could also be conducted. The results would help develop a database of pre-damaged RC specimens with substantial transverse reinforcement and retrofitted with FRP wraps.
4) The present dissertation focuses on the structural capacity of strengthened columns.

Although the enhanced lateral ductility capacity due to steel confinement is evaluated in Chapter 2, additional research is needed to fully understand and quantify this behavior improvement, especially in light of Provision 13.3 of ACI 440.2R-17 guidelines for seismic rehabilitation. Parametric studies similar to those presented in Chapters 3 and 4 can be carried out to identify important parameters regarding the lateral ductility of FRP-confined RC columns and the effects of internal steel.

References

AASHTO American Association of State Highway and Transportation Officials. 2014. *AASHTO LRFD Bridge Design Specifications*. Washington, D.C.

ACI (American Concrete Institute). 2017. *Guide for the design and construction of externally bonded FRP systems for strengthening concrete structures*. *ACI 440.2R-17*, Farmington Hills, MI: ACI.

ACI (American Concrete Institute). 2019. *Building code requirements for structural concrete*. *ACI 318-19*, Farmington Hills, MI: ACI.

Aire, C., Gettu, R., Casas, J. R., Marques, S., and Marques, D. 2010. "Concrete laterally confined with fibre-reinforced polymers (FRP): experimental study and theoretical model." *Mater. Constr.*, 60(297), 19–31.

Albanesi, T., Nuti, C., and Vanzi, I. 2007. "Closed form constitutive relationship for concrete filled FRP tubes under compression." *Constr. Build. Mater.*, 21, 409–427.

ASCE (American Society of Civil Engineers). 2017. *Minimum design loads for buildings and other structures. ASCE 7-16*.

ATC/MCEER. 2003. *Design Examples - Recommended LRFD guidelines for the seismic design of highway bridges*. NCHRP Project 12-49, FY '98.

Baji, H. 2017. "Calibration of the FRP resistance reduction factor for FRP-confined reinforced concrete building columns." *J. Compos. Constr.*, 21(3), 04016107.

Baji, H., Ronagh, H. R., and Li, C. Q. 2016. "Probabilistic assessment of FRP-confined reinforced concrete columns." *Compos. Struct.*, 153, 851–865.

Bakis, C. E., Bank, L. C., Brown, V. L., Cosenza, E., Davalos, J. F., Lesko, J. J., Machida, A., Rizkalla, S. H., and Triantafillou, T. C. 2002. "Fiber-Reinforced Polymer Composites for ConstructionState-of-the-Art Review." *J. Compos. Constr.*, American Society of Civil Engineers, 6(2), 73–87.

Balan, T. A., Filippou, F. C., and Popov, E. P. 1997. "Constitutive model for 3D cyclic analysis of concrete structures." *J. Eng. Mech.*, 123(2).

Bank, L. C. 2006. *Composites for Construction: Structural Design with FRP Materials*. John Wiley & Sons, Hoboken, NJ.

Barbato, M. 2009. "Efficient finite element modelling of reinforced concrete beams retrofitted with fibre reinforced polymers." *Comput. Struct.*, Elsevier Ltd, 87(3–4), 167–176.

Barbato, M., and Conte, J. P. 2005. "Finite element response sensitivity analysis: A comparison between force-based and displacement-based frame element models." *Comput. Methods Appl. Mech. Eng.*, 194(12–16), 1479–1512.

Barbato, M., and Conte, J. P. 2006. "Finite element structural response sensitivity and reliability analyses using smooth versus non-smooth material constitutive models." *Int. J. Reliab. Saf.*, 1(1–2).

Barbato, M., Monti, G., and Santinelli, F. 2003. "Fiber-section FE of FRP-strengthened RC beam for seismic analysis." *Symp. Concr. Struct. Seism. Reg.*, Technical Chamber of Greece: Athens, Greece.

Bartlett, M., and MacGregor, J. G. 1996. "Statistical analysis of the compressive strength of concrete in structures." *ACI Mater. J.*, 93(2), 158–168.

Basalo, F. J., Matta, F., and Nanni, A. 2012. “Fiber reinforced cement-based composite system for concrete confinement.” *Constr. Build. Mater.*, Elsevier Limited, 32, 55–65.

Bathe, K.-J. 1996. *Finite element procedures*. Prentice Hall, Englewood Cliffs N.J.

Binici, B. 2005. “An analytical model for stress-strain behavior of confined concrete.” *Eng. Struct.*, 27, 1040–1051.

Bisby, L., and Ranger, M. 2010. “Axial-flexural interaction in circular FRP-confined reinforced concrete columns.” *Constr. Build. Mater.*, 24, 1672–1681.

Breitung, K. 1991. “Asymptotic approximations for multidimensional integrals.” *Comput. Mech.*, 691–696.

Butterfield, R. 1999. “Dimensional analysis for geotechnical engineers.” *Geotechnique*, 49(3), 357–366.

Cairns, S. W. 2001. “Circular concrete columns externally reinforced with prefabricated carbon polymer shells.” Master’s thesis, Dept. of Civil Engineering, Univ. of Toronto.

Cao, Y., Wu, Y. F., and Jiang, C. 2018. “Stress-strain relationship of FRP confined concrete columns under combined axial load and bending moment.” *Compos. Part B Eng.*, Elsevier, 134, 207–217.

Carrazedo, R., and Hanai, J. 2006. “Efeitos do confinamento em pilares de concreto armado encamisados com compósito de fibras de carbono.” *[In Port. Cad. Eng. Estruturas, São Carlos*, 8(30), 59–77.

Casas, J. R., and Chambi, J. L. 2014. “Partial safety factors for CFRP-wrapped bridge piers: Model assessment and calibration.” *Compos. Struct.*, 118, 267–283.

Cheng, L., and Karbhari, V. M. 2006. “New bridge systems using FRP composites and concrete: a state-of-the-art review.” *Prog. Struct. Eng. Mater.*, John Wiley & Sons, Ltd, 8(4), 143–154.

Chopra, A. K. 2016. *Dynamics of structures - Theory and applications to earthquake engineering*. 5th ed. Pearson.

Chun, S., and Park, H.-C. 2002. “Load carrying capacity and ductility of RC columns confined by carbon fiber reinforced polymers.” *Proc. of the Inter.Conf. ICCI’02*, 1–12.

Cleveland, W. S. 1985. *The elements of graphing data*. *Wadsworth Publ. Co.*, Belmont, CA.

CNR-DT-200-R1. 2013. *Guide for the design and construction of externally bonded FRP systems for strengthening existing structures.* National Research Council—Advisory Committee on Technical Recommendations for Construction: Rome, Italy.

Coleman, J., and Spacone, E. 2001. “Localization Issues in Force-Based Frame Elements.” *J. Struct. Eng.*, American Society of Civil Engineers, 127(11), 1257–1265.

CSA (Canadian Standards Association). 2017. *Design and construction of building structures with fibre-reinforced polymer*. *CSA S806-17*, Ontario, ON, Canada.

DAfStb. 2012. *DAfStb-RichtIinie: Verstärken von betonbauteilen mit geklebter bewehrung*. Deutscher Ausschuss für Stahlbeton e. V. (DAfStb): Berlin, Germany. (In German).

Demers, M., and Neale, K. W. 1999. “Confinement of reinforced concrete columns with fibre-reinforced composite sheets - an experimental study.” *Can. J. Civ. Eng.*, 26(2), 226–241.

Desprez, C., Mazars, J., Kotronis, P., and Paultre, P. 2013. “Damage model for FRP-confined concrete columns under cyclic loading.” *Eng. Struct.*, Elsevier, 48, 519–531.

Diniz, S. M. C., and Frangopol, D. M. 1997. “Reliability bases for high-strength concrete columns.” *J. Struct. Eng.*, 123(10), 1375–1381.

Ditlevsen, O., and Madsen, H. O. 2005. *Structural Reliability Methods*. John Wiley & Sons Ltd, Chichester, UK.

Eid, R., and Paultre, P. 2008. “Analytical model for FRP-confined circular reinforced concrete columns.” *J. Compos. Constr.*, 12(5), 541–522.

Eid, R., Roy, N., and Paultre, P. 2009. “Normal- and high-strength concrete circular elements wrapped with frp composites.” *J. Compos. Constr.*, 13(2), 113–124.

Ellingwood, B., Galambos, T. V., MacGregor, J. G., and Cornell, C. A. 1980. *Development of a probability based load criterion for American national standard A58*. NBS Special Publication SP577, National Bureau of Standards. Washington, D.C.

Fam, A. Z., and Rizkalla, S. H. 2001. “Confinement model for axially loaded concrete confined by circular fiber-reinforced polymer tubes.” *ACI Struct. J.*, 98(4), 451–461.

Fardis, M. N., Asce, A. M., Alibe, B., and Tassoulas, J. L. 1983. “Monotonic and Cyclic Constitutive Law for Concrete.” *J. Eng. Mech.*, American Society of Civil Engineers, 109(2), 516–536.

Fardis, M. N., and Khalili, H. H. 1982. “FRP-encased concrete as a structural material.” *Mag. Concr. Res.*, 34(121), 191–202.

Fenves, G., and Filippou, F. 2004. “Methods of analysis for earthquake-resistant structures.” *Earthq. Eng. from Eng. Seismol. to performance-based*, Y. Bozorgnia and V. V. Bertero, eds., 366–370.

Filippou, F. C., and Constantinides, M. 2004. *FEDEASLab getting started guide and simulation examples*. *Tech. Rep. NEESgrid-2004-22.*, Berkeley, CA: Univ. of California Berkeley.

Filippou, F. C., Popov, E. P., and Bertero, V. V. 1983. *Effects of bond deterioration on hysteretic behaviour of reinforced concrete joints*. *Earthq. Eng. Res. Cent.*, Report UCB/EERC-83/19, Univ. of California, Berkeley, CA.

Fitzwilliam, J., Bisby, L. A., and Asce, M. 2010. "Slenderness Effects on Circular CFRP Confined Reinforced Concrete Columns." *J. Compos. Constr.*, American Society of Civil Engineers, 14(3), 280–288.

Flaga, K. 2000. "Advances in materials applied in civil engineering." *J. Mater. Process. Technol.*, Elsevier, 106(1–3), 173–183.

GB50608. 2010. *Technical code for infrastructure application of FRP composites*. Ministry of Housing and Urban-Rural Development, General Administration of Quality Supervision, Inspection and Quarantine: Beijing, China. (In Chinese).

Gill, P. E., Murray, W., and Wright, M. H. 1981. *Practical optimization*. Academic Press, New York.

Gu, D.-S., Gang Wu, ;, Wu, Z.-S., and Wu, Y.-F. 2010. "Confinement Effectiveness of FRP in Retrofitting Circular Concrete Columns under Simulated Seismic Load." *J. Compos. Constr.*, American Society of Civil Engineers, 14(5), 531–540.

Hadi, M. N. S. 2006. "Behaviour of FRP wrapped normal strength concrete columns under eccentric loading." *Compos. Struct.*, Elsevier, 72(4), 503–511.

Hadi, M. N. S. 2009. "Behaviour of eccentric loading of FRP confined fibre steel reinforced

concrete columns." *Constr. Build. Mater.*, Elsevier Ltd, 23(2), 1102–1108.

Harries, K. A., and Kharel, G. 2002. "Behavior and modeling of concrete subject to variable confining pressure." *ACI Mater. J.*, 99(2), 180–189.

Hasofer, A. M., and Lind, M. C. 1974. "An exact and invariant first order reliability format." *J. Eng. Mech.*, 100, 111–121.

Haukaas, T., and Kiureghian, A. Der. 2006. "Strategies for finding the design point in non-linear finite element reliability analysis." *Probabilistic Eng. Mech.*, 21(2), 133–147.

Hu, D., and Barbato, M. 2014. "Simple and efficient finite element modeling of reinforced concrete columns confined with fiber-reinforced polymers." *Eng. Struct.*, 72, 113–122.

Hu, H., and Seracino, R. 2014. "Analytical model for FRP-and-steel-confined circular concrete columns in compression." *J. Compos. Constr.*, 18(3), A4013012.

Ilki, A., Peker, O., Karamuk, E., Demir, C., and Kumbasar, N. 2008. "FRP retrofit of low and medium strength circular and rectangular reinforced concrete columns." *J. Mater. Civ. Eng.*, 20(2), 169–188.

Imran, I., and Pantazopoulou, S. J. 1996. "Experimental Study of Plain Concreteunder Triaxial Stress." *Mater. J.*, 93(6), 589–601.

ISIS Canada. 2002. *FRP Rehabilitation of Reinforced Concrete Structures - Manual No 4*.

Ismail, A. M., Fahmy, M. F. M., and Wu, Z. 2017. "Simulating the lateral performance of FRP-confined RC circular columns using a new eccentric-based stress-strain model." *Compos. Struct.*, Elsevier, 180, 88–104.

Israel, M., Ellingwood, B., and Corotis, R. 1987. "Reliability-based code formulations for

reinforced concrete buildings." *J. Struct. Eng.*, 113(10), 2235–2252.

Jaffry, S. A. D. 2001. "Concrete-filled glass fiber reinforced polymer (GFRP) shells under concentric compression." Master's thesis, Dept. of Civil Engineering, Univ. of Toronto.

Jiang, T., and Teng, J. G. 2007. "Analysis-oriented stress-strain models for FRP-confined concrete." *Eng. Struct.*, 29(11), 2968–2986.

Kabir, M. Z., and Shafei, E. 2012. "Plasticity modeling of FRP-confined circular reinforced concrete columns subjected to eccentric axial loading." *Compos. Part B Eng.*, Elsevier, 43(8), 3497–3506.

Kaeseberg, S., Messerer, D., and Holschemacher, K. 2019. "Assessment of standards and codes dedicated to CFRP confinement of RC columns." *Materials (Basel).*, 12(2390), 1–15.

Karbhari, V. M., and Gao, Y. 1997. "Composite jacketed concrete under uniaxial compression - Verification of simple design equations." *J. Mater. Civ. Eng.*, 9(4), 185–193.

Kawashima, K., Hosotani, M., and Yoneda, K. 2000. "Carbon fiber sheet retrofit of reinforced concrete bridge piers." *Int. Work. Annu. Commem. Chi-Chi Earthq. - Vol. 2*, Taipei, Taiwan: National Center for Research on Earthquake Engineering, 124–135.

Der Kiureghian, A., Lin, H., and Hwang, S. 1987. "Second-Order Reliability Approximations." *J. Eng. Mech.*, 113(8), 1208–1225.

Lam, L., and Teng, J. G. 2003a. "Design-oriented stress-strain model for FRP-confined concrete." *Constr. Build. Mater.*, 17(6–7), 471–489.

Lam, L., and Teng, J. G. 2003b. "Design-oriented stress-strain model in rectangular columns." *J. Reinf. Plast. Compos.*, 22(13), 1149–1186.

Lam, L., and Teng, J. G. 2004. “Ultimate Condition of Fiber Reinforced Polymer-Confined Concrete.” *J. Compos. Constr.*, American Society of Civil Engineers, 8(6), 539–548.

Lee, J., Yi, C., Jeong, H., Kim, S. W., and Kim, J. K. 2010. “Compressive response of concrete confined with steel spirals and FRP composites.” *J. Compos. Mater.*, 44(4), 481–504.

Li, J., and Hadi, M. N. S. 2003. “Behaviour of externally confined high-strength concrete columns under eccentric loading.” *Compos. Struct.*, 62, 145–153.

Li, Y.-F., Lin, C.-T., and Sung, Y.-Y. 2003. “A constitutive model for concrete confined with carbon fiber reinforced plastics.” *Mech. Mater.*, 35(3), 603–619.

Li, Y. F., and Sung, Y. Y. 2004. “A study on the shear-failure of circular sectioned bridge column retrofitted by using CFRP jacketing.” *J. Reinf. Plast. Compos.*, SAGE Publications, 23(8), 811–830.

Lin, Y. 2010. “Tension stiffening model for reinforced concrete based on bond stress slip relation.” Master’s thesis, Dept. of Civil and Environment Engineering, Pennsylvania State Univ.

Liu, J., and Sheikh, S. A. 2013. “Fiber-Reinforced Polymer-Confined Circular Columns under Simulated Seismic Loads.” *Struct. J.*, 110(6), 941–952.

Liu, P.-L., and Der Kiureghian, A. 1991. “Optimization algorithms for structural reliability.” *Struct. Saf.*, 9(3), 161–177.

Mander, J. 1983. “Seismic Design of Bridge Piers.” Ph.D. Thesis, Univ. of Canterbury, Christchurch, New Zealand.

Mander, J., Priestley, M., and Park, R. 1988. “Theoretical stress-strain model for confined

concrete.” *J. Struct. Eng.*, 114(8), 1804–1826.

Marques, S. P. C., Marques, D. C. dos S. C., Lins da Silva, J., and Cavalcante, M. A. A. 2004. “Model for analysis of short columns of concrete confined by fiber-reinforced polymer.” *J. Compos. Constr.*, 8(4), 332–340.

Mathworks. 2021. “Global Optimization Toolbox: User’s Guide (r2021a).” <www.mathworks.com/help/pdf_doc/gads/gads_tb.pdf>.

MathWorks. 1997. “MATLAB-high-performance numeric computation and visualization software, user’s guide.” *MathWorks, Inc., Natick, MA*.

Matthys, S., Toutanji, H., and Taerwe, L. 2006. “Stress-strain behavior of large-scale circular columns confined with FRP composites.” *J. Struct. Eng.*, 132(1), 123–133.

Mazzoni, S., McKenna, F., Scott, M. H., and Fenves, G. L. 2006. *OpenSees Command Language Manual*. *Pacific Earthq. Eng. Res. Cent.*, Berkeley, CA.

Megalooikonomou, K. G., Monti, G., and Santini, S. 2012. “Constitutive model for fiber-reinforced polymer- and tie-confined concrete.” *ACI Struct. J.*, 109(4), 569–578.

Megalooikonomou, K. G., and Papavasileiou, G. S. 2019. “Analytical stress-strain model for FRP-confined rectangular RC columns.” *Front. Built Environ.*, 5(April), 1–14.

Melchers, R. E. 1989. “Importance sampling in structural systems.” *Struct. Saf.*, 6(1), 3–10.

Menegotto, M., and Pinto, P. E. 1973. “Method of analysis for cyclically loaded reinforced concrete plane frames including changes in geometry and nonelastic behavior of elements under combined normal force and bending.” *IABSE Symp. Resist. Ultim. Deform. Struct. Acted by Well-Defined Repeated Loads*, International Association for Bridge and Structural

Engineering, Zurich, Switzerland, 15–22.

Mertz, D. R. 2003. *Application of fiber reinforced polymer composites to the highway infrastructure*. NCHRP Rep. No. 503. Washington, DC: Transportation Research Board.

Micelli, F., Mazzotta, R., Leone, M., and Aiello, M. A. 2015. "Review study on the durability of FRP-confined concrete." *J. Compos. Constr.*, 19(3), 04014056.

Mimiran, A., and Shahawy, M. 1997. "Behavior of concrete column confined by fiber composites." *J. Struct. Eng.*, 123(5), 583–590.

Mirmiran, A., and Shahawy, M. 1996. "A new concrete-filled hollow FRP composite column." *Compos. Part B Eng.*, 27B, 263–268.

Mirza, S. A., and MacGregor, J. G. 1982. "Probabilistic study of strength of reinforced concrete members." *Can. J. Civ. Eng.*, 9, 431–448.

Moran, D. A., and Pantelides, C. P. 2002. "Stress-Strain Model for Fiber-Reinforced Polymer-Confined Concrete." *J. Compos. Constr.*, 6(4), 233–240.

Mostofinejad, D., and Moshiri, N. 2014. "Compressive Strength of CFRP Composites Used for Strengthening of RC Columns: Comparative Evaluation of EBR and Grooving Methods." *J. Compos. Constr.*, American Society of Civil Engineers, 19(5), 04014079.

Mostofinejad, D., and Torabian, A. 2016. "Experimental study of circular RC columns strengthened with longitudinal CFRP composites under eccentric loading: Comparative evaluation of EBR and EBROG methods." *J. Compos. Constr.*, 20(2), 04015055.

Motavalli, M., and Czaderski, C. 2007. "FRP composites for retrofitting of existing civil structures in Europe: State-of-the-art review." *Int. Conf. Compos. Polycon*, Arlington, VA:

American Composites Manufacturers Association., 1–10.

Nanni, A., and Bradford, N. M. 1995. “FRP jacketed concrete under uniaxial compression.” *Constr. Build. Mater.*, 9(2), 115–124.

Neuenhofer, A., and Filippou, F. C. 1997. “Evaluation of Nonlinear Frame Finite-Element Models.” *J. Struct. Eng.*, American Society of Civil Engineers, 123(7), 958–966.

De Nicolo, B., Pani, L., and Pozzo, E. 1994. “Strain of concrete at peak compressive stress for a wide range of compressive strengths.” *Mater. Struct.*, 27(4), 206–210.

Nilson, A. H., Darwin, D., and Dolan, C. W. 2010. *Design of Concrete Structures*. McGraw-Hill, New York, NY.

Nowak, A. S., and Collins, K. R. 2000. *Reliability of Structures*. McGraw Hill, New York, NY.

Nowak, A. S., Rakoczy, A. M., and Szeliga, E. K. 2012. “Revised statistical resistance models for RC structural components.” *Spec. Publ.*, 284, 1–16.

Nowak, A. S., and Szerszen, M. M. 2003. “Calibration of design code for buildings (ACI 318): Part 1 - Statistical models for resistance.” *ACI Struct. J.*, 100(3), 377–382.

Nowak, A., Szeliga, E., Szerszen, M., and Podhorecki, P. J. 2008. “Reliability-based calibration for structural concrete, Phase 3.” *Portl. Cem. Assoc.*, 2849, 110.

Okeil, A. M., Belarbi, A., and Kuchma, D. A. 2013. “Reliability assessment of FRP-strengthened concrete bridge girders in shear.” *J. Compos. Constr.*, 17(1), 91–100.

Ozbakkaloglu, T., Lim, J. C., and Vincent, T. 2013. “FRP-confined concrete in circular sections: Review and assessment of stress-strain models.” *Eng. Struct.*, 49, 1068–1088.

Pantelides, C. P., Gergely, J., Reaveley, L. D., and Volnyy, V. A. 2000. “Seismic strengthening of reinforced concrete bridge pier with FRP composites.” *12th World Conf. Earthq. Eng. - Vol 127*, Upper Hutt, NZ: New Zealand Society for Earthquake Engineering., 1–8.

Parretti, R., and Nanni, A. 2002. “Axial testing of concrete columns confined with carbon FRP: Effect of fiber orientation.” *3rd Int. Conf. Compos. Infrastruct. - Vol 8*, Tucson, AZ: Dept. of Civil Engineering and Engineering Mechanics, Univ. of Arizona, 1–10.

Parvin, A., and Brighton, D. 2014. “FRP composites strengthening of concrete columns under various loading conditions.” *Polymers*, 6, 1040–1056.

Paulay, T., and Priestley, M. 1992. *Seismic design of reinforced concrete and masonry buildings*. John Wiley & Sons, New York, NY.

Paultre, P., Boucher-Trudeau, R., Eid, R., and Roy, N. 2015. “Behavior of circular reinforced-concrete columns confined with carbon fiber–reinforced polymers under cyclic flexure and constant axial load.” *J. Compos. Constr.*, American Society of Civil Engineers, 20(3), 04015065.

Pellegrino, C., and Modena, C. 2010. “Analytical Model for FRP Confinement of Concrete Columns with and without Internal Steel Reinforcement.” *J. Compos. Constr.*, American Society of Civil Engineers, 14(6), 693–705.

Peng, J., Ho, J. C. M., Pam, H. J., and Wong, Y. L. 2012. “Equivalent stress block for normal-strength concrete incorporating strain gradient effect.” *Mag. Concr. Res.*, 64(1), 1–19.

Petersons, N. 1968. “Should standard cube test specimens be replaced by test specimens taken from structures?” *Matériaux Constr.*, 1(5), 425–435.

Pipa, M. J. 1995. “Ductilidade de elementos de betão armado sujeitos a ações cíclicas. Influência das características mecânicas das armaduras.” Ph.D. Dissertation, Technical University of Lisbon. Lisbon, Portugal. (In Portuguese).

Piscesa, B., Attard, M. M., and Samani, A. K. 2018. “3D Finite element modeling of circular reinforced concrete columns confined with FRP using a plasticity based formulation.” *Compos. Struct.*, 194, 478–493.

Popovics, S. 1973. “A numerical approach to the complete stress-strain curve of concrete.” *Cem. Concr. Res.*, 3(5), 583–599.

Rackwitz, R., and Fiessler, B. 1978. “Structural reliability under combined random load sequences.” *Comput. Struct.*, 9(5), 484–494.

Raza, S., Khan, M. K. I., Menegon, S. J., Tsang, H. H., and Wilson, J. L. 2019. “Strengthening and repair of reinforced concrete columns by jacketing: State-of-the-art review.” *Sustain.*, 11(11), 3208.

Realfonzo, R., and Napoli, A. 2011. “Concrete confined by FRP systems: Confinement efficiency and design strength models.” *Compos. Part B Eng.*, 42, 736–755.

Richart, F. E., Brandtzaeg, A., and Brown, R. L. 1929. “The failure of plain and spirally bound concrete in compression.” *Bull. no. 190*, Univ. of Illinois, Eng. Experiment Station, Champaing, IL.

Richart, F. E., and Brown, R. L. 1934. “An investigation of reinforced concrete columns.” *Bull. no. 267*, Univ. of Illinois, Eng. Experiment Station, Champaing, IL.

Rocca, S. 2007. “Experimental and analytical evaluation of FRP-confined large size reinforced

concrete columns." Ph.D. Dissertation, Univ. of Missouri. Rolla, MO.

Rocca, S., Galati, N., and Nanni, A. 2006. *Evaluation of FRP strengthening of large-size reinforced concrete columns*. Report No. UTC-142. Univ. of Missouri-Rolla, MO.

Roy, N., Paultre, P., and Proulx, J. 2010. "Performance-based seismic retrofit of a bridge bent: Design and experimental validation." *Can. J. Civ. Eng.*, 37, 367–379.

Saadatmanesh, H., Ehsani, M. R., and Li, M. W. 1994. "Strength and Ductility of Concrete Columns Externally Reinforced With Fiber Composite Straps." *Struct. J.*, Publ by American Concrete Inst, 91(4), 434–447.

Samaan, M., Mirmiran, A., and Shahawy, M. 1998. "Model of concrete confined by fiber composites." *J. Struct. Eng.*, 124(9), 1025–1031.

Sargin, M. 1971. "Stress-strain relationship for concrete and the analysis of structural concrete section." University of Waterloo, Ontario, Canada.

Scanlon, A. 1995. "Applications in concrete structures." *Probabilistc Struct. Mech. Handb. Theory Ind. Appl.*, C. Sundararajan, ed., Chapman & Hall, 663–683.

Scott, M. H., and Fenves, G. L. 2006. "Plastic hinge integration Methods for force-based beam–column elements." *J. Struct. Eng.*, 132(2), 244–252.

Seible, F., Priestley, M. J. N., Hegemier, G. A., and Innamorato, D. 1997. "Seismic Retrofit of RC Columns with Continuous Carbon Fiber Jackets." *J. Compos. Constr.*, American Society of Civil Engineers, 1(2), 52–62.

Shao, Y., Zhu, Z., and Mirmiran, A. 2006. "Cyclic modeling of FRP-confined concrete with improved ductility." *Cem. Concr. Compos.*, 28(10), 959–968.

Sheikh, S. A., and Khoury, S. S. 1993. “Confined Concrete Columns With Stubs.” *ACI Struct. J.*, 90(4), 414–431.

Sheikh, S. A., and Yau, G. 2002. “Seismic Behavior of Concrete Columns Confined with Steel and Fiber-Reinforced Polymers.” *Struct. J.*, 99(1), 72–80.

Shirmohammadi, F., Esmaeily, A., and Kiaeipour, Z. 2015. “Stress–strain model for circular concrete columns confined by FRP and conventional lateral steel.” *Eng. Struct.*, Elsevier, 84, 395–405.

Slater, W. A., and Lyse, I. 1931. “First progress report on column tests at Lehigh University.” *Proc. ACI*, 677(31–1).

Spacone, E., Filippou, F. C., and Taucer, F. F. 1996. “Fibre beam-column model for non-linear analysis of RC frames: Part I. Formulation.” *Earthq. Eng. Struct. Dyn.*, 25(7), 711–725.

Spoelstra, M. R., and Monti, G. 1999. “FRP-confined concrete model.” *J. Compos. Constr.*, 3(3), 143–150.

Szerszen, M. M., and Nowak, A. S. 2003. “Calibration of design code for buildings (ACI 318): Part 2 - Reliability analysis and resistance factors.” *ACI Struct. J.*, 100(3), 383–391.

Tatar, J., Sattar, S., Goodwin, D., Milev, S., Ahmed, S., Dukes, J., and Segura, C. 2021. “Performance of externally bonded fiber-reinforced polymer retrofits in the 2018 Cook Inlet Earthquake in Anchorage, Alaska.” *Earthq. Spectra*, 37(4), 2342–2371.

Teng, J. G., Huang, Y. L., Lam, L., and Ye, L. P. 2007. “Theoretical model for fiber-reinforced polymer-confined concrete.” *J. Compos. Constr.*, 11(2), 201–210.

Teng, J. G., and Lam, L. 2004. “Behavior and modeling of fiber reinforced polymer-confined

concrete." *J. Struct. Eng.*, 130(11), 1713–1723.

Teng, J. G., Lin, G., and Yu, T. 2015. "Analysis-oriented stress-strain model for concrete under combined FRP-steel confinement." *J. Compos. Constr.*, 19(5).

Toutanji, H. A. 1999. "Stress-strain characteristics of concrete columns externally confined with advanced fiber composite sheets." *ACI Mater. J.*, 96(3), 397–404.

Ugray, Z., Lasdon, L., Plummer, J., Glover, F., Kelly, J., and Marti, R. 2007. "Scatter search and local NLP solvers: A multistart framework for global optimization." *INFORMS J. Comput.*, 19(3), 328–340.

Val, D. V. 2003. "Reliability of fiber-reinforced polymer-confined reinforced concrete columns." *J. Struct. Eng.*, 129(8), 1122–1130.

Wang, N., and Ellingwood, B. R. 2015. "Limit state design criteria for FRP strengthening of RC bridge components." *Struct. Saf.*, 56, 1–8.

Wang, Y. C., and Restrepo, J. I. 2001. "Investigation of concentrically loaded reinforced concrete columns confined with glass fiber-reinforced polymer jackets." *ACI Struct. J.*, 98(3), 377–385.

Wang, Z., Wang, D., Smith, S. T., and Lu, D. 2012. "Experimental testing and analytical modeling of CFRP-confined large circular RC columns subjected to cyclic axial compression." *Eng. Struct.*, 40, 64–74.

Wight, J. K., and MacGregor, J. G. 2009. *Reinforced concrete mechanics & design*. Pearson, Upper Saddle River, NJ.

Wiśniewski, D. F., Cruz, P. J. S., Henriques, A. A. R., and Simões, R. A. D. 2012. "Probabilistic

models for mechanical properties of concrete reinforcing steel and pre stressing steel." *Struct. Infrastruct. Eng.*, 8(2), 111–123.

Wu, H. C., and Eamon, C. D. 2017. *Strengthening of concrete structures using fiber reinforced polymers (FRP): Design, construction and practical applications*. Woodhead Publishing.

Xiao, Q. G., Teng, J. G., and Yu, T. 2010. "Behavior and Modeling of Confined High-Strength Concrete." *J. Compos. Constr.*, 14(3), 249–259.

Xiao, Y., and Wu, H. 2000. "Compressive behavior of concrete confined by carbon fiber composite jackets." *J. Mater. Civ. Eng.*, 12(2), 139–146.

Xing, L., Lin, G., and Chen, J. F. 2020. "Behavior of FRP-confined circular RC columns under eccentric compression." *J. Compos. Constr.*, 24(4), 04020030.

Yuan, F., Wu, Y.-F., and Zhao, X.-Y. 2022. "Effect of internal stirrups on the eccentric compression behavior of FRP-confined RC columns based on finite-element analysis." *J. Compos. Constr.*, 26(1), 04021069.

Zaghi, A. E. 2009. "Seismic design of pipe-pin connections in concrete bridges." University of Nevada, Reno.

Zaghi, A. E., Saiidi, M. S., and Mirmiran, A. 2012. "Shake table response and analysis of a concrete-filled FRP tube bridge column." *Compos. Struct.*, Elsevier Ltd, 94(5), 1564–1574.

Zignago, D., and Barbato, M. 2019. "Parametric Study on the Effect of Steel Confinement in Short Bridge Piers Retrofitted with Externally-Wrapped FRP." *MATEC Web Conf.*, 271, 01012.

Zignago, D., and Barbato, M. 2021. "Effects of transverse steel on the axial-compression

strength of FRP-confined reinforced concrete columns based on a numerical parametric study." *J. Compos. Constr.*, 25(4), 04021024.

Zignago, D., and Barbato, M. 2022. "Reliability-Based Calibration of New Design Procedure for Reinforced Concrete Columns under Simultaneous Confinement by Fiber-Reinforced Polymers and Steel." *J. Compos. Constr.*, 26(3), 04022017.

Zignago, D., Barbato, M., and Hu, D. 2018. "Constitutive model of concrete simultaneously confined by FRP and steel for finite-element analysis of FRP-confined RC columns." *J. Compos. Constr.*, 22(6).

Zou, Y., and Hong, H. P. 2011. "Reliability assessment of FRP-confined concrete columns designed for buildings." *Struct. Infrastruct. Eng.*, 7(3), 243–258.

APPENDIX. C++ code for constitutive models

A1 – Original ZBH model

```
#include <elementAPI.h>
#include "ConcreteZBH_original.h"

#include <Vector.h>
#include <Channel.h>
#include <math.h>
#include <float.h>

#ifdef _USRDLL
#define OPS_Export extern "C" _declspec(dllexport)
#elif _MACOSX
#define OPS_Export extern "C" __attribute__((visibility("default")))
#else
#define OPS_Export extern "C"
#endif

static int numConcreteZBH_original = 0;

OPS_Export void *
OPS_ConcreteZBH_original()
{
 // print out some KUDO's
 if (numConcreteZBH_original == 0) {
   opserr << "ConcreteZBH_original uniaxial material - Use at your Own Peril\n";
   numConcreteZBH_original =1;
 }

 // Pointer to a uniaxial material that will be returned
 UniaxialMaterial *theMaterial = 0;

 // parse the input line for the material parameters
 int    iData[1];
 double dData[18];
 int numData;
 numData = 1;
 if (OPS_GetIntInput(&numData, iData) != 0) {
   opserr << "WARNING invalid uniaxialMaterial ConcreteZBH_original tag" << endln;
   return 0;
 }

 numData = 18;
 if (OPS_GetDoubleInput(&numData, dData) != 0) {
   opserr << "WARNING invalid ...\n";
   return 0;
 }

 //
 // create a new material
 //

 theMaterial = new ConcreteZBH_original(iData[0], dData[0], dData[1], dData[2], dData[3], dData[4], dData[5], dData[6], dData[7],
                          dData[8], dData[9], dData[10], dData[11], dData[12], dData[13], dData[14], dData[15],
                          dData[16], dData[17]);

 if (theMaterial == 0) {
   opserr << "WARNING could not create uniaxialMaterial of type ConcreteZBH_original\n";
   return 0;
 }

 // return the material
 return theMaterial;
}
```

```
ConcreteZBH_original::ConcreteZBH_original(int tag, double _fc0, double _ec0, double _Ec,
                                double _Es, double _fy, double _eults, double _s, double _As_t,
                                double _Ef, double _eultf, double _tf, double _D, double _Ds,
                                double _As_l, double _kg_f, double _ks_s, double _ks_f, double _type_reinf)
:UniaxialMaterial(tag, 0),
 fc0(_fc0), ec0(_ec0), Ec(_Ec), Es(_Es), fy(_fy), eults(_eults),
  s(_s), As_t(_As_t), Ef(_Ef), eultf(_eultf), tf(_tf),
  D(_D), Ds(_Ds), As_l(_As_l), kg_f(_kg_f), ks_s(_ks_s),
  ks_f(_ks_f), type_reinf(_type_reinf)
{
  sigp   = 0.0;
  Ep     = Ec;
  elp    = 0.0;
  epsp   = 0.0;
  eminp  = 0.0;
  eunl1p = 0.0;
  eunl2p = 0.0;
  eunl3p = 0.0;
  Eunlp  = fc0/ec0;
  Eunl2p = fc0/ec0;
  Et3p   = fc0/ec0;
  sunlp  = 0.0;
  flp    = 0.0;
  flunlp = 0.0;
  elunlp = 0.0;
  muunlp = 0.0;
  flaggp = 4;

  sig    = 0.0;
  Et     = Ec;
  eps    = 0.0;
  el     = 0.0;
  emin   = 0.0;
  eunl1  = 0.0;
  eunl2  = 0.0;
  eunl3  = 0.0;
  Eunl   = fc0/ec0;
  Eunl2  = fc0/ec0;
  Et3    = fc0/ec0;
  sunl   = 0.0;
  fl     = 0.0;
  flunl  = 0.0;
  elunl  = 0.0;
  muunl  = 0.0;
  flagg  = 4;

  roj_f  = 4 * tf / D;   //reinforcement ratio
  roj_s  = 4 * As_t / (s*Ds);
  roj_sl = As_l / (0.25*3.1416*pow(Ds, 2));
  kg_s = (1 - 0.5*(s - 2 * pow((As_t / 3.1416), 0.5)) / Ds);
  kg_s = (kg_s > 0) ? (pow((1 - 0.5*(s - 2 * pow((As_t / 3.1416), 0.5)) / Ds), type_reinf) / (1 - roj_sl)) : 0;
  kg_s = fmin(kg_s, 1.0);   //effectiveness coefficient by Mander et al. (1988)

  beta = Ec/fabs(fc0)-1/fabs(ec0);

  double fls = 0.5 * ks_s * kg_s * roj_s * fy;
  double fccs = (2.254 * pow((1 + 7.94 * fls / fabs(fc0)), 0.5) - 2 * fls / fabs(fc0) - 1.254) * fc0;
  eccus = -0.004 - 1.4 * roj_s * fy * eults / fabs(fccs);

}

ConcreteZBH_original::ConcreteZBH_original()
:UniaxialMaterial(0, 0),
 fc0(0.0), ec0(0.0), Ec(0.0), Es(0.0), fy(0.0), eults(0.0),
  s(0.0), As_t(0.0), Ef(0.0), eultf(0.0), tf(0.0),
  D(0.0), Ds(0.0), As_l(0.0), kg_f(0.0), ks_s(0.0),
  ks_f(0.0), type_reinf(0.0)
{
sigp   = 0.0;
  Ep     = Ec;
```

```
  elp    = 0.0;
  epsp   = 0.0;
  eminp  = 0.0;
  eunl1p = 0.0;
  eunl2p = 0.0;
  eunl3p = 0.0;
  Eunlp  = fc0/ec0;
  Eunl2p = fc0/ec0;
  Et3p   = fc0/ec0;
  sunlp  = 0.0;
  flp    = 0.0;
  flunlp = 0.0;
  elunlp = 0.0;
  muunlp = 0.0;
  flaggp = 4;

  sig    = 0.0;
  Et     = Ec;
  eps    = 0.0;
  el     = 0.0;
  emin   = 0.0;
  eunl1  = 0.0;
  eunl2  = 0.0;
  eunl3  = 0.0;
  Eunl   = fc0/ec0;
  Eunl2  = fc0/ec0;
  Et3    = fc0/ec0;
  sunl   = 0.0;
  fl     = 0.0;
  flunl  = 0.0;
  elunl  = 0.0;
  muunl  = 0.0;
  flagg  = 4;
}

ConcreteZBH_original::~ConcreteZBH_original()
{
  // does nothing
}

int
ConcreteZBH_original::setTrialStrain(double strain, double strainRate)
{
                // retrieve concrete hitory variables

                //emin = eminp;
                flagg = flaggp;

  sig   = sigp;
  Et    = Ep;
  el    = elp;
  eps   = epsp;
  emin  = eminp;
  eunl1  = eunl1p;
  eunl2 = eunl2p;
  eunl3 = eunl3p;
  Eunl  = Eunlp;
  Eunl2 = Eunl2p;
  Et3   = Et3p;
  sunl  = sunlp;
  fl    = flp;
  flunl = flunlp;
  elunl = elunlp;
  muunl = muunlp;

                // calculate current strain

                eps = strain;
                double deps = eps - epsp;
                emin = fmin(eps, eminp);
```

```
if (fabs(deps) < 10*DBL_EPSILON){
      sig = sigp;
      Et  = Ep;
                                    el  = elp;
}
else if (eps <= 0.) {                  // compression
      if (flagg == 4) {                // monotonic envelope
         if (deps < 0.)  {             // negative strain increment: loading
            this->envelope(eps, deps, fl, sig, Et, el);
           // emin = eps;
         }
         else {                    // deps > 0 - unloading
            elunl = elp;
            Eunl2 = Ec/(1+2*20*elunl);
            sunl  = sigp;
            eunl1 = emin-sigp/Ec;
            eunl2 = emin-sigp/Eunl2;
            muunl = 0.4*elunl*Eunl2/sunl;
            if (eps > eunl2) {       // crack has opened
               flagg = 2;
               sig   = 0.;
               //Et    = 0.;
                                                                  Et    = 1e-10;
               el    = elunl+(Ec/Eunl2)*muunl*(eunl1-emin);
            }
            else if (eps > eunl1) {
               flagg = 1;
               sig   = 0.;
               //Et    = 0.;
                                                                  Et    = 1e-10;
               el    = elunl+(Ec/Eunl2)*muunl*(eunl1-emin);
            }
            else {
               sig   = Ec*(eps-eunl1);
               Et    = Ec;
               flagg = 0;
               el    = elunl+(Ec/Eunl2)*muunl*(eps-emin);
            }
         }
      }
      else if (flagg == 0) {
         if (eps <= emin) {            // the strain increment brings back on the envelope
            flagg = 4;
            this->envelope(eps, deps, fl, sig, Et, el);
           // emin = eps;
         }
         else if (eps > eunl2) {       // crack has opened
            flagg = 2;
            sig   = 0.;
            //Et    = 0.;
                                                            Et    = 1e-10;
            el    = elunl+(Ec/Eunl2)*muunl*(eunl1-emin);
         }
         else if (eps > eunl1) {
            flagg = 1;
            sig   = 0.;
            //Et    = 0.;
                                                            Et    = 1e-10;
            el    = elunl+(Ec/Eunl2)*muunl*(eunl1-emin);
         }
         else {                    // eunl1 > eps > emin
            sig   = Ec*(eps-eunl1);
            Et    = Ec;
            el    = elunl+(Ec/Eunl2)*muunl*(eps-emin);
                                                            flagg = 0;
         }
      }
      else if (flagg == 1) {
         if (eps <= emin) {            // the strain increment brings back on the envelope
```

```
      flagg = 4;
      this->envelope(eps, deps, fl, sig, Et, el);
     // emin = eps;
    }
    else if (eps > eunl2) {       // crack has opened
      flagg = 2;
      sig   = 0.;
      //Et    = 0.;
                                                  Et    = 1e-10;
                                                  el    = elunl+(Ec/Eunl2)*muunl*(eunl1-emin);
    }
    else if (deps < 0.) {          // loading
      flagg = 3;
      eunl3 = epsp;
      Et3   = sunl/(emin-eunl3);
      Et    = Et3;
      sig   = Et*(eps-eunl3);
      el    = elunl+(Et3/Eunl2)*muunl*(eps-emin);
    }
    else {                    // keeps flag = 1
      //Et    = 0.;
      flagg = 1;
                                                  Et    = 1e-10;
      sig  = 0.;
                                                  el   = elunl+(Ec/Eunl2)*muunl*(eunl1-emin);
    }
  }
  else if (flagg == 2) {
    if (eps <= emin) {          // the strain increment brings back on the envelope
      flagg = 4;
      this->envelope(eps, deps, fl, sig, Et, el);
     //  emin = eps;
    }
    else if (eps > eunl2) {       // crack has opened
      flagg = 2;
      sig   = 0.;
      //Et    = 0.;
                                                  Et    = 1e-10;
                                                  el    = elunl+(Ec/Eunl2)*muunl*(eunl1-emin);
    }
    else {                    // eunl2 > eps > emin
      flagg = 2;
      sig   = Eunl2*(eps-eunl2);
      Et    = Eunl2;
      el    = elunl+muunl*(eps-emin);
    }
  }
  else if (flagg == 3) {
    if (eps <= emin) {          // the strain increment brings back on the envelope
      flagg = 4;
      this->envelope(eps, deps, fl, sig, Et, el);
     // emin = eps;
    }
    else if (eps > eunl2) {        // crack has opened
      flagg = 2;
      sig   = 0.;
      //Et    = 0.;
                                                  Et    = 1e-10;
                                                  el    = elunl+(Ec/Eunl2)*muunl*(eunl1-emin);
    }
    else if (eps > eunl3) {
      flagg = 1;
      sig   = 0.;
      //Et    = 0.;
                                                  Et    = 1e-10;
                                                  el    = elunl+(Ec/Eunl2)*muunl*(eunl1-emin);
    }
    else {                     // eunl3 > eps > emin
      flagg = 3;
      Et    = Et3;
```

```
            sig   = (eps - eunl3)*Et;
            el    = elunl+(Et3/Eunl2)*muunl*(eps-emin);
          }
        }
   }
   else {                          //eps > 0
        flagg = 2;
        sig   = 0.;
        //Et    = 0.;
                                    Et    = 1e-10;
                                    el    = elunl+(Ec/Eunl2)*muunl*(eunl1-emin);
   }
 return 0;

}

double
ConcreteZBH_original::getStrain(void)
{
 return eps;
}

double
ConcreteZBH_original::getStress(void)
{
 return sig;
}


double
ConcreteZBH_original::getTangent(void)
{
 return Et;
}

int
ConcreteZBH_original::commitState(void)
{
 sigp   = sig;
 Ep     = Et;
 elp    = el;
 epsp   = eps;
 eminp  = emin;
 eunl1p = eunl1;
 eunl2p = eunl2;
 eunl3p = eunl3;
 Eunlp  = Eunl;
 Eunl2p = Eunl2;
 Et3p   = Et3;
 sunlp  = sunl;
 flp    = fl;
 flunlp = flunl;
 elunlp = elunl;
 muunlp = muunl;
 flaggp = flagg;

 return 0;
}


int
ConcreteZBH_original::revertToLastCommit(void)
{
 sig   = sigp;
 Et    = Ep;
 el    = elp;
 eps   = epsp;
 emin  = eminp;
 eunl1  = eunl1p;
 eunl2 = eunl2p;
```

```
  eunl3 = eunl3p;
  Eunl  = Eunlp;
  Eunl2 = Eunl2p;
  Et3   = Et3p;
  sunl  = sunlp;
  fl    = flp;
  flunl = flunlp;
  elunl = elunlp;
  muunl = muunlp;
  flagg = flaggp;

  return 0;
}


int
ConcreteZBH_original::revertToStart(void)
{
  sigp   = 0.0;
  Ep     = Ec;
  elp    = 0.0;
  epsp   = 0.0;
  eminp  = 0.0;
  eunl1p = 0.0;
  eunl2p = 0.0;
  eunl3p = 0.0;
  Eunlp  = fc0/ec0;
  Eunl2p = fc0/ec0;
  Et3p   = fc0/ec0;
  sunlp  = 0.0;
  flp    = 0.0;
  flunlp = 0.0;
  elunlp = 0.0;
  muunlp = 0.0;
  flaggp = 4;

  sig    = 0.0;
  Et     = Ec;
  eps    = 0.0;
  el     = 0.0;
  emin   = 0.0;
  eunl1  = 0.0;
  eunl2  = 0.0;
  eunl3  = 0.0;
  Eunl   = fc0/ec0;
  Eunl2  = fc0/ec0;
  Et3    = fc0/ec0;
  sunl   = 0.0;
  fl     = 0.0;
  flunl  = 0.0;
  elunl  = 0.0;
  muunl  = 0.0;
  flagg  = 4;
  return 0;
}


UniaxialMaterial *
ConcreteZBH_original::getCopy(void)
{
  ConcreteZBH_original *theCopy =
    new ConcreteZBH_original(this->getTag(), fc0, ec0, Ec, Es, fy, eults,
                                                                                                    s, As_t, Ef, eultf, tf, D, Ds, As_l, kg_f, ks_s,
ks_f, type_reinf);

  return theCopy;
}


int
```

```
ConcreteZBH_original::sendSelf(int cTag, Channel &theChannel)
{
  int res = 0;
  static Vector data(37);

data(0) =fc0;
data(1) =ec0;
data(2) =Ec;
data(3) =Es;
data(4) =fy;
data(5) =eults;
data(6) =s;
data(7) =As_t;
data(8) =Ef;
data(9) =eultf;
data(10) =tf;
data(11) =D;
data(12) =Ds;
data(13) =As_l;
data(14) =kg_f;
data(15) =ks_s;
data(16) =ks_f;
data(17) = type_reinf;
data(18) =sigp;
data(19) =Ep;
data(20) =elp;
data(21) =epsp;
data(22) =eminp;
data(23) =eunl1p;
data(24) =eunl2p;
data(25) =eunl3p;
data(26) =Eunlp;
data(27) =Eunl2p;
data(28) =Et3p;
data(29) =sunlp;
data(30) =flp;
data(31) =flunlp;
data(32) =elunlp;
data(33) =muunlp;
data(34) =flaggp;
data(35) = eccus;
  data(36) = this->getTag();

  res = theChannel.sendVector(this->getDbTag(), cTag, data);
  if (res < 0)
    opserr << "ConcreteZBH_original::sendSelf() - failed to send data\n";

  return res;
}

int
ConcreteZBH_original::recvSelf(int cTag, Channel &theChannel,
                                                FEM_ObjectBroker &theBroker)
{
  int res = 0;
  static Vector data(37);
  res = theChannel.recvVector(this->getDbTag(), cTag, data);
  if (res < 0)
    opserr << "ConcreteZBH_original::recvSelf() - failed to recv data\n";
  else {
                fc0 = data(0);
                ec0 = data(1);
                Ec = data(2);
                Es = data(3);
                fy = data(4);
                eults = data(5);
                s = data(6);
                As_t = data(7);
                Ef = data(8);
                eultf = data(9);
```

```
                tf = data(10);
                D = data(11);
                Ds = data(12);
                As_l = data(13);
                kg_f = data(14);
                ks_s = data(15);
                ks_f = data(16);
                type_reinf = data(17);
                sigp = data(18);
                Ep = data(19);
                elp = data(20);
                epsp = data(21);
                eminp = data(22);
                eunl1p = data(23);
                eunl2p = data(24);
                eunl3p = data(25);
                Eunlp = data(26);
                Eunl2p = data(27);
                Et3p = data(28);
                sunlp = data(29);
                flp = data(30);
                flunlp = data(31);
                elunlp = data(32);
                muunlp = data(33);
                flaggp=      int(data(34));
                eccus = data(35);
                this->setTag(int(data(36)));
 }

 eps = epsp;
 sig = sigp;
 Et  = Ep;
 el  = elp;
 fl  = flp;

 return res;
}

void
ConcreteZBH_original::Print(OPS_Stream &s, int flag)
{
 s << "ConcreteZBH_original tag: " << this->getTag() << endln;

}

void
ConcreteZBH_original::Conf_Pressure (double eps, double flp, double &fc, double &fl, double &el)
{

double fcc   = (2.254*pow((1+7.94*flp/fabs(fc0)),0.5)-2*flp/fabs(fc0)-1.254)*fc0;
double ecc   = ec0*(1+5*(fcc/fc0-1));
double x     = eps/ecc;
double Esecc = fcc/ecc;
double r     = Ec/(Ec-Esecc);
fc    = fcc*x*r/(r-1+pow(x,r));
el    = (Ec*eps-fc)/(2*beta*fc);
double el0   = 0;
double el1   = 0;

if (el >= eultf) {
   el0 = 0;
}
else {
   el0 = fabs(el);
}
if (eps <= eccus) {
                el1 = 0;
}
else {
                el1 = fabs(el);
```

```
}

fl    = 0.5*ks_f*kg_f*roj_f*Ef*el0+0.5*ks_s*kg_s*roj_s*fmin(Es*fabs(el1),fy);

 return;
}

void
ConcreteZBH_original::envelope (double eps, double deps, double &fl, double &sig, double &Et, double &el)
{
        this->Conf_Pressure(eps, flp, sig, fl, el);
        int count = 0;
        while(fabs(fl-flp)>fmax(fl/10000,0.0000001))
        {
                count = count+1;
                flp = fl;
                this->Conf_Pressure(eps, flp, sig, fl, el);
                if (count>20){break;}
        }
        Et  = (sig-sigp)/deps;

        return;
}
```

A2 – Smoothed ZBH model

```
#include <elementAPI.h>
#include "ConcreteZBH_smoothed.h"

#include <Vector.h>
#include <Channel.h>
#include <math.h>
#include <float.h>

#ifdef _USRDLL
#define OPS_Export extern "C" _declspec(dllexport)
#elif _MACOSX
#define OPS_Export extern "C" __attribute__((visibility("default")))
#else
#define OPS_Export extern "C"
#endif

static int numConcreteZBH_smoothed = 0;

OPS_Export void *
OPS_ConcreteZBH_smoothed()
{
  // print out some KUDO's
  if (numConcreteZBH_smoothed == 0) {
    opserr << "ConcreteZBH_smoothed uniaxial material - Use at your Own Peril\n";
    numConcreteZBH_smoothed =1;
  }

  // Pointer to a uniaxial material that will be returned
  UniaxialMaterial *theMaterial = 0;

  //
  // parse the input line for the material parameters
  //
  int    iData[1];
  double dData[18];
  int numData;
  numData = 1;
  if (OPS_GetIntInput(&numData, iData) != 0) {
```

```
  opserr << "WARNING invalid uniaxialMaterial ConcreteZBH_smoothed tag" << endln;
  return 0;
 }

 numData = 18;
 if (OPS_GetDoubleInput(&numData, dData) != 0) {
  opserr << "WARNING invalid ...\n";
  return 0;
 }

 //
 // create a new material
 //

 theMaterial = new ConcreteZBH_smoothed(iData[0], dData[0], dData[1], dData[2], dData[3], dData[4], dData[5], dData[6], dData[7],
                        dData[8], dData[9], dData[10], dData[11], dData[12], dData[13], dData[14], dData[15],
                        dData[16], dData[17]);

 if (theMaterial == 0) {
  opserr << "WARNING could not create uniaxialMaterial of type ConcreteZBH_original\n";
  return 0;
 }

 // return the material
 return theMaterial;
}

ConcreteZBH_smoothed::ConcreteZBH_smoothed(int tag, double _fc0, double _ec0, double _Ec,
                                double _Es, double _fy, double _eults, double _s, double _As_t,
                                double _Ef, double _eultf, double _tf, double _D, double _Ds,
                                double _As_l, double _kg_f, double _ks_s, double _ks_f, double _type_reinf)
:UniaxialMaterial(tag, 0),
 fc0(_fc0), ec0(_ec0), Ec(_Ec), Es(_Es), fy(_fy), eults(_eults),
 s(_s), As_t(_As_t), Ef(_Ef), eultf(_eultf), tf(_tf),
 D(_D), Ds(_Ds), As_l(_As_l), kg_f(_kg_f), ks_s(_ks_s),
 ks_f(_ks_f), type_reinf(_type_reinf)
{
 sigp   = 0.0;
 Ep     = Ec;
 elp    = 0.0;
 epsp   = 0.0;
 eminp  = 0.0;
 eunl1p = 0.0;
 eunl2p = 0.0;
 eunl3p = 0.0;
 Eunlp  = fc0/ec0;
 Eunl2p = fc0/ec0;
 Et3p   = fc0/ec0;
 sunlp  = 0.0;
 flp    = 0.0;
 flunlp = 0.0;
 elunlp = 0.0;
 muunlp = 0.0;
 flaggp = 4;

 sig    = 0.0;
 Et     = Ec;
 eps    = 0.0;
 el     = 0.0;
 emin   = 0.0;
 eunl1  = 0.0;
 eunl2  = 0.0;
 eunl3  = 0.0;
 Eunl   = fc0/ec0;
 Eunl2  = fc0/ec0;
 Et3    = fc0/ec0;
 sunl   = 0.0;
 fl     = 0.0;
 flunl  = 0.0;
 elunl  = 0.0;
```

```
  muunl  = 0.0;
  flagg  = 4;

  roj_f  = 4 * tf / D;
  roj_s  = 4 * As_t / (s*Ds);
  roj_sl = As_l / (0.25*3.1416*pow(Ds, 2));
  kg_s = (1 - 0.5*(s - 2 * pow((As_t / 3.1416), 0.5)) / Ds);
  kg_s = (kg_s > 0) ? (pow((1 - 0.5*(s - 2 * pow((As_t / 3.1416), 0.5)) / Ds), type_reinf) / (1 - roj_sl)) : 0;
  kg_s = fmin(kg_s, 1.0);
  //kg_s = pow((1 - 0.5*(s - 2 * pow((As_t / 3.1416), 0.5)) / Ds), 2) / (1 - roj_sl);

  beta = Ec/fabs(fc0)-1/fabs(ec0);

  fls = 0.5*ks_s*kg_s*roj_s*fy;
  fccs = (2.254 * pow((1 + 7.94 * fls / fabs(fc0)), 0.5) - 2 * fls / fabs(fc0) - 1.254) * fc0;
  eccs = ec0 * (1 + 5 * (fccs / fc0 - 1));
  eps_ccus = -0.004 - 1.4 * roj_s * fy * eults / fabs(fccs);
  double x = eps_ccus / eccs;
  double Esecs = fccs / eccs;
  rs = Ec / (Ec - Esecs);
  sig_ccus = fccs * x * rs / (rs - 1 + pow(x, rs));

  double flf = 0.5 * ks_f * kg_f * roj_f * Ef * eultf + 0.5 * ks_s * kg_s * roj_s * fy;
  double fccf = (2.254 * pow((1 + 7.94 * flf / fabs(fc0)), 0.5) - 2 * flf / fabs(fc0) - 1.254) * fc0;
  double eccf = ec0 * (1 + 5 * (fccf / fc0 - 1));
  double Esecf = fccf / eccf;
  double Esecu = Ec / (1 + 2 * beta * eultf);
  eps_ccuf = eccf * pow(((Esecf * (Ec - Esecu)) / (Esecu * (Ec - Esecf))), 1 - (Esecf / Ec));
  sig_ccuf = Esecu * eps_ccuf;

  r0 = Ec / (Ec - fc0 / ec0);

  if (fabs(eps_ccuf) > fabs(eps_ccus)) {
                eps_ccus = eps_ccuf;
     sig_ccus = sig_ccuf;
  }

}

ConcreteZBH_smoothed::ConcreteZBH_smoothed()
:UniaxialMaterial(0, 0),
 fc0(0.0), ec0(0.0), Ec(0.0), Es(0.0), fy(0.0), eults(0.0),
  s(0.0), As_t(0.0), Ef(0.0), eultf(0.0), tf(0.0),
  D(0.0), Ds(0.0), As_l(0.0), kg_f(0.0), ks_s(0.0),
  ks_f(0.0), type_reinf(0.0)
{
sigp   = 0.0;
  Ep     = Ec;
  elp    = 0.0;
  epsp   = 0.0;
  eminp  = 0.0;
  eunl1p = 0.0;
  eunl2p = 0.0;
  eunl3p = 0.0;
  Eunlp  = fc0/ec0;
  Eunl2p = fc0/ec0;
  Et3p   = fc0/ec0;
  sunlp  = 0.0;
  flp    = 0.0;
  flunlp = 0.0;
  elunlp = 0.0;
  muunlp = 0.0;
  flaggp = 4;

  sig    = 0.0;
  Et     = Ec;
  eps    = 0.0;
  el     = 0.0;
  emin   = 0.0;
  eunl1  = 0.0;
```

```
 eunl2  = 0.0;
 eunl3  = 0.0;
 Eunl   = fc0/ec0;
 Eunl2  = fc0/ec0;
 Et3    = fc0/ec0;
 sunl   = 0.0;
 fl     = 0.0;
 flunl  = 0.0;
 elunl  = 0.0;
 muunl  = 0.0;
 flagg  = 4;
}

ConcreteZBH_smoothed::~ConcreteZBH_smoothed()
{
 // does nothing
}

int
ConcreteZBH_smoothed::setTrialStrain(double strain, double strainRate)
{
              // retrieve concrete hitory variables

              //emin = eminp;
              flagg = flaggp;

 sig   = sigp;
 Et    = Ep;
 el    = elp;
 eps   = epsp;
 emin  = eminp;
 eunl1  = eunl1p;
 eunl2 = eunl2p;
 eunl3 = eunl3p;
 Eunl  = Eunlp;
 Eunl2 = Eunl2p;
 Et3   = Et3p;
 sunl  = sunlp;
 fl    = flp;
 flunl = flunlp;
 elunl = elunlp;
 muunl = muunlp;

              // calculate current strain

              eps = strain;
              double deps = eps - epsp;
              emin = fmin(eps, eminp);

  if (fabs(deps) < 10*DBL_EPSILON){
        sig = sigp;
        Et  = Ep;
                                    el  = elp;
  }
  else if (eps <= 0.) {                 // compression
        if (flagg == 4) {                 // monotonic envelope
           if (deps < 0.)  {              // negative strain increment: loading
              this->envelope(eps, deps, fl, sig, Et, el);
             // emin = eps;
           }
           else {                     // deps > 0 - unloading
              elunl = elp;
              Eunl2 = Ec/(1+2*20*elunl);
              sunl  = sigp;
              eunl1 = emin-sigp/Ec;
              eunl2 = emin-sigp/Eunl2;
              muunl = 0.4*elunl*Eunl2/sunl;
              if (eps > eunl2) {        // crack has opened
                 flagg = 2;
                 sig   = 0.;
```

```
            //Et    = 0.;
                                                                Et    = 1e-10;
            el    = elunl+(Ec/Eunl2)*muunl*(eunl1-emin);
         }
         else if (eps > eunl1) {
            flagg = 1;
            sig   = 0.;
            //Et    = 0.;
                                                                Et    = 1e-10;
            el    = elunl+(Ec/Eunl2)*muunl*(eunl1-emin);
         }
         else {
            sig   = Ec*(eps-eunl1);
            Et    = Ec;
            flagg = 0;
            el    = elunl+(Ec/Eunl2)*muunl*(eps-emin);
         }
      }
   }
   else if (flagg == 0) {
      if (eps <= emin) {            // the strain increment brings back on the envelope
         flagg = 4;
         this->envelope(eps, deps, fl, sig, Et, el);
        // emin = eps;
      }
      else if (eps > eunl2) {       // crack has opened
         flagg = 2;
         sig   = 0.;
         //Et    = 0.;
                                                        Et    = 1e-10;
         el    = elunl+(Ec/Eunl2)*muunl*(eunl1-emin);
      }
      else if (eps > eunl1) {
         flagg = 1;
         sig   = 0.;
         //Et    = 0.;
                                                        Et    = 1e-10;
         el    = elunl+(Ec/Eunl2)*muunl*(eunl1-emin);
      }
      else {                        // eunl1 > eps > emin
         sig   = Ec*(eps-eunl1);
         Et    = Ec;
         el    = elunl+(Ec/Eunl2)*muunl*(eps-emin);
                                                        flagg = 0;
      }
   }
   else if (flagg == 1) {
      if (eps <= emin) {            // the strain increment brings back on the envelope
         flagg = 4;
         this->envelope(eps, deps, fl, sig, Et, el);
        // emin = eps;
      }
      else if (eps > eunl2) {       // crack has opened
         flagg = 2;
         sig   = 0.;
         //Et    = 0.;
                                                        Et    = 1e-10;
                                                        el    = elunl+(Ec/Eunl2)*muunl*(eunl1-emin);
      }
      else if (deps < 0.) {         // loading
         flagg = 3;
         eunl3 = epsp;
         Et3   = sunl/(emin-eunl3);
         Et    = Et3;
         sig   = Et*(eps-eunl3);
         el    = elunl+(Et3/Eunl2)*muunl*(eps-emin);
      }
      else {                        // keeps flag = 1
         //Et    = 0.;
         flagg = 1;
```

```
                                                    Et    = 1e-10;
            sig  = 0.;
                                                    el   = elunl+(Ec/Eunl2)*muunl*(eunl1-emin);
         }
      }
      else if (flagg == 2) {
         if (eps <= emin) {            // the strain increment brings back on the envelope
            flagg = 4;
            this->envelope(eps, deps, fl, sig, Et, el);
          //  emin = eps;
         }
         else if (eps > eunl2) {       // crack has opened
            flagg = 2;
            sig   = 0.;
            //Et    = 0.;
                                                    Et    = 1e-10;
                                                    el    = elunl+(Ec/Eunl2)*muunl*(eunl1-emin);
         }
         else {                        // eunl2 > eps > emin
            flagg = 2;
            sig   = Eunl2*(eps-eunl2);
            Et    = Eunl2;
            el    = elunl+muunl*(eps-emin);
         }
      }
      else if (flagg == 3) {
         if (eps <= emin) {            // the strain increment brings back on the envelope
            flagg = 4;
            this->envelope(eps, deps, fl, sig, Et, el);
           // emin = eps;
         }
         else if (eps > eunl2) {       // crack has opened
            flagg = 2;
            sig   = 0.;
            //Et    = 0.;
                                                    Et    = 1e-10;
                                                    el    = elunl+(Ec/Eunl2)*muunl*(eunl1-emin);
         }
         else if (eps > eunl3) {
            flagg = 1;
            sig   = 0.;
            //Et    = 0.;
                                                    Et    = 1e-10;
                                                    el    = elunl+(Ec/Eunl2)*muunl*(eunl1-emin);
         }
         else {                        // eunl3 > eps > emin
            flagg = 3;
            Et    = Et3;
            sig   = (eps - eunl3)*Et;
            el    = elunl+(Et3/Eunl2)*muunl*(eps-emin);
         }
      }
   }
   else {                           //eps > 0
      flagg = 2;
      sig   = 0.;
      //Et    = 0.;
                                       Et    = 1e-10;
                                       el    = elunl+(Ec/Eunl2)*muunl*(eunl1-emin);
   }
 return 0;

}

double
ConcreteZBH_smoothed::getStrain(void)
{
 return eps;
}
```

```
double
ConcreteZBH_smoothed::getStress(void)
{
 return sig;
}


double
ConcreteZBH_smoothed::getTangent(void)
{
 return Et;
}

int
ConcreteZBH_smoothed::commitState(void)
{
 sigp   = sig;
 Ep     = Et;
 elp    = el;
 epsp   = eps;
 eminp  = emin;
 eunl1p = eunl1;
 eunl2p = eunl2;
 eunl3p = eunl3;
 Eunlp  = Eunl;
 Eunl2p = Eunl2;
 Et3p   = Et3;
 sunlp  = sunl;
 flp    = fl;
 flunlp = flunl;
 elunlp = elunl;
 muunlp = muunl;
 flaggp = flagg;

 return 0;
}


int
ConcreteZBH_smoothed::revertToLastCommit(void)
{
 sig   = sigp;
 Et    = Ep;
 el    = elp;
 eps   = epsp;
 emin  = eminp;
 eunl1  = eunl1p;
 eunl2 = eunl2p;
 eunl3 = eunl3p;
 Eunl  = Eunlp;
 Eunl2 = Eunl2p;
 Et3   = Et3p;
 sunl  = sunlp;
 fl    = flp;
 flunl = flunlp;
 elunl = elunlp;
 muunl = muunlp;
 flagg = flaggp;

 return 0;
}


int
ConcreteZBH_smoothed::revertToStart(void)
{
 sigp   = 0.0;
 Ep     = Ec;
 elp    = 0.0;
 epsp   = 0.0;
```

```
  eminp  = 0.0;
  eunl1p = 0.0;
  eunl2p = 0.0;
  eunl3p = 0.0;
  Eunlp  = fc0/ec0;
  Eunl2p = fc0/ec0;
  Et3p   = fc0/ec0;
  sunlp  = 0.0;
  flp    = 0.0;
  flunlp = 0.0;
  elunlp = 0.0;
  muunlp = 0.0;
  flaggp = 4;

  sig    = 0.0;
  Et     = Ec;
  eps    = 0.0;
  el     = 0.0;
  emin   = 0.0;
  eunl1  = 0.0;
  eunl2  = 0.0;
  eunl3  = 0.0;
  Eunl   = fc0/ec0;
  Eunl2  = fc0/ec0;
  Et3    = fc0/ec0;
  sunl   = 0.0;
  fl     = 0.0;
  flunl  = 0.0;
  elunl  = 0.0;
  muunl  = 0.0;
  flagg  = 4;
  return 0;
}


UniaxialMaterial *
ConcreteZBH_smoothed::getCopy(void)
{
  ConcreteZBH_smoothed *theCopy =
    new ConcreteZBH_smoothed(this->getTag(), fc0, ec0, Ec, Es, fy, eults,
                                                                                                                    s, As_t, Ef, eultf, tf, D, Ds, As_l, kg_f, ks_s,
ks_f, type_reinf);

  return theCopy;
}


int
ConcreteZBH_smoothed::sendSelf(int cTag, Channel &theChannel)
{
  int res = 0;
  static Vector data(46);

  data(0) = fc0;
  data(1) = ec0;
  data(2) = Ec;
  data(3) = Es;
  data(4) = fy;
  data(5) = eults;
  data(6) = s;
  data(7) = As_t;
  data(8) = Ef;
  data(9) = eultf;
  data(10) = tf;
  data(11) = D;
  data(12) = Ds;
  data(13) = As_l;
  data(14) = kg_f;
  data(15) = ks_s;
  data(16) = ks_f;
```

```
  data(17) = type_reinf;
  data(18) = beta;
  data(19) = fls;
  data(20) = eps_ccuf;
  data(21) = eps_ccus;
  data(22) = sig_ccuf;
  data(23) = sig_ccus;
  data(24) = fccs;
  data(25) = eccs;
  data(26) = rs;
  data(27) = r0;
  data(28) = sigp;
  data(29) = Ep;
  data(30) = elp;
  data(31) = epsp;
  data(32) = eminp;
  data(33) = eunl1p;
  data(34) = eunl2p;
  data(35) = eunl3p;
  data(36) = Eunlp;
  data(37) = Eunl2p;
  data(38) = Et3p;
  data(39) = sunlp;
  data(40) = flp;
  data(41) = flunlp;
  data(42) = elunlp;
  data(43) = muunlp;
  data(44) = flaggp;

  data(45) = this->getTag();

  res = theChannel.sendVector(this->getDbTag(), cTag, data);
  if (res < 0)
    opserr << "ConcreteZBH_original::sendSelf() - failed to send data\n";

  return res;
}

int
ConcreteZBH_smoothed::recvSelf(int cTag, Channel &theChannel,
                                                FEM_ObjectBroker &theBroker)
{
  int res = 0;
  static Vector data(46);
  res = theChannel.recvVector(this->getDbTag(), cTag, data);
  if (res < 0)
    opserr << "ConcreteZBH_smoothed::recvSelf() - failed to recv data\n";
  else {
                fc0 = data(0);
                ec0 = data(1);
                Ec = data(2);
                Es = data(3);
                fy = data(4);
                eults = data(5);
                s = data(6);
                As_t = data(7);
                Ef = data(8);
                eultf = data(9);
                tf = data(10);
                D = data(11);
                Ds = data(12);
                As_l = data(13);
                kg_f = data(14);
                ks_s = data(15);
                ks_f = data(16);
                type_reinf = data(17);
                beta = data(18);
                fls = data(19);
                eps_ccuf = data(20);
                eps_ccus = data(21);
```

```
                sig_ccuf = data(22);
                sig_ccus = data(23);
                fccs = data(24);
                eccs = data(25);
                rs = data(26);
                r0 = data(27);
                sigp = data(28);
                Ep = data(29);
                elp = data(30);
                epsp = data(31);
                eminp = data(32);
                eunl1p = data(33);
                eunl2p = data(34);
                eunl3p = data(35);
                Eunlp = data(36);
                Eunl2p = data(37);
                Et3p = data(38);
                sunlp = data(39);
                flp = data(40);
                flunlp = data(41);
                elunlp = data(42);
                muunlp = data(43);
                flaggp = int(data(44));
this->setTag(int(data(45)));
  }

  eps = epsp;
  sig = sigp;
  Et  = Ep;
  el  = elp;
  fl  = flp;

  return res;
}

void
ConcreteZBH_smoothed::Print(OPS_Stream &s, int flag)
{
  s << "ConcreteZBH_smoothed tag: " << this->getTag() << endln;
  /*s << "  E: " << E << endln;
  s << "  ep: " << ep << endln;
  s << "  stress: " << trialStress << " tangent: " << trialTangent << endln;*/
}

void
ConcreteZBH_smoothed::Conf_Pressure (double eps, double flp, double &fc, double &fl, double &el)
{

double fcc   = (2.254*pow((1+7.94*flp/fabs(fc0)),0.5)-2*flp/fabs(fc0)-1.254)*fc0;
double ecc   = ec0*(1+5*(fcc/fc0-1));
double x     = eps/ecc;
double Esecc = fcc/ecc;
double r     = Ec/(Ec-Esecc);
fc    = fcc*x*r/(r-1+pow(x,r));
el    = (Ec*eps-fc)/(2*beta*fc);


fl = 0.5*ks_f*kg_f*roj_f*Ef*el + 0.5*ks_s*kg_s*roj_s*fmin(Es*fabs(el), fy);
  return;
}

void
ConcreteZBH_smoothed::envelope(double eps, double deps, double &fl, double &sig, double &Et, double &el)
{
        if (fls == 0.0) {
                if (eps >= eps_ccuf) {
                        this->Conf_Pressure(eps, flp, sig, fl, el);
                        int count = 0;
                        while (fabs(fl - flp) > fmax(fl / 100000000, 0.00000000001))
                        {
```

```
                        count = count + 1;
                        flp = fl;
                        this->Conf_Pressure(eps, flp, sig, fl, el);
                        if (count > 20) { break; }
                }
                Et = (sig - sigp) / deps;
        }
        else {
                double sig2 = sig_ccuf - (eps - eps_ccuf) * Ec;
                double sig1 = fc0 * r0 * (eps / ec0) / (r0 - 1 + pow((eps / ec0), r0));
                if (sig1 <= sig2) {
                        sig = sig1;
                        Et = (fc0 * r0 / ec0) / (r0 - 1 + pow((eps / ec0), r0)) -
                                (fc0 * pow(r0, 2) * (pow((eps / ec0), r0)) / ec0) / pow((r0 - 1 + pow((eps / ec0), r0)), 2);
                        el = (Ec * eps - sig) / (2 * beta * sig);
                }
                else {
                        sig = sig2;
                        Et = -Ec;
                        el = (Ec * eps - sig) / (2 * beta * sig);
                }
        }
}
else {
        if (eps >= eps_ccuf) {
                this->Conf_Pressure(eps, flp, sig, fl, el);
                int count = 0;
                while (fabs(fl - flp) > fmax(fl / 100000000, 0.00000000001))
                {
                        count = count + 1;
                        flp = fl;
                        this->Conf_Pressure(eps, flp, sig, fl, el);
                        if (count > 20) { break; }
                }
                Et = (sig - sigp) / deps;
        }
        else if (eps >= eps_ccus)
        {
                double sig1 = fccs * (eps / eccs) *rs / (rs - 1 + pow((eps / eccs), rs));
                double sig2 = sig_ccuf - (eps - eps_ccuf) * Ec;
                if (sig1 <= sig2) {
                        sig = sig1;
                        Et = (fccs * rs / eccs) / (rs - 1 + pow((eps / eccs), rs)) -
                                (fccs * pow(rs, 2) * (pow((eps / eccs), rs)) / eccs) / pow((rs - 1 + pow((eps / eccs), rs)), 2);
                        el = (Ec * eps - sig) / (2 * beta * sig);
                }
                else {
                        sig = sig2;
                        Et = -Ec;
                        el = (Ec * eps - sig) / (2 * beta * sig);
                }
        }
        else {
                double sig_p2 = sig_ccuf - (eps_ccus - eps_ccuf) * Ec;
                double sig_p = fmin(sig_ccus, sig_p2);

                double sig2 = sig_p - (eps - eps_ccus) * Ec;
                double sig1 = fc0 * r0 * (eps / ec0) / (r0 - 1 + pow((eps / ec0), r0));
                if (sig1 <= sig2) {
                        sig = sig1;
                        Et = (fc0 * r0 / ec0) / (r0 - 1 + pow((eps / ec0), r0)) -
                                (fc0 * pow(r0, 2) * (pow((eps / ec0), r0)) / ec0) / pow((r0 - 1 + pow((eps / ec0), r0)), 2);
                        el = (Ec * eps - sig) / (2 * beta * sig);
                }
                else {
                        sig = sig2;
                        Et = -Ec;
                        el = (Ec * eps - sig) / (2 * beta * sig);
                }
        }
```

```
        }

        return;
}
```

A3 – Fitted ZBH model

```
#include <elementAPI.h>
#include "ConcreteZBH_fitted.h"

#include <Vector.h>
#include <Channel.h>
#include <math.h>
#include <float.h>


#ifdef _USRDLL
#define OPS_Export extern "C" _declspec(dllexport)
#elif _MACOSX
#define OPS_Export extern "C" __attribute__((visibility("default")))
#else
#define OPS_Export extern "C"
#endif

static int numConcreteZBH_fitted = 0;

OPS_Export void *
OPS_ConcreteZBH_fitted()
{
 // print out some KUDO's
 if (numConcreteZBH_fitted == 0) {
   opserr << "ConcreteZBH_fitted uniaxial material - Use at your Own Peril\n";
   numConcreteZBH_fitted =1;
 }

 // Pointer to a uniaxial material that will be returned
 UniaxialMaterial *theMaterial = 0;

 //
 // parse the input line for the material parameters
 //
 int    iData[1];
 double dData[20];
 int numData;
 numData = 1;
 if (OPS_GetIntInput(&numData, iData) != 0) {
   opserr << "WARNING invalid uniaxialMaterial ConcreteZBH_fitted tag" << endln;
   return 0;
 }

 numData = 20;
 if (OPS_GetDoubleInput(&numData, dData) != 0) {
   opserr << "WARNING invalid ...\n";
   return 0;
 }

 //
 // create a new material
 //

 theMaterial = new ConcreteZBH_fitted(iData[0], dData[0], dData[1], dData[2], dData[3], dData[4], dData[5], dData[6], dData[7],
                        dData[8], dData[9], dData[10], dData[11], dData[12], dData[13], dData[14], dData[15], dData[16], dData[17], dData[18],
dData[19]);
```

```
  if (theMaterial == 0) {
    opserr << "WARNING could not create uniaxialMaterial of type ConcreteZBH_fitted\n";
    return 0;
  }

  // return the material
  return theMaterial;
}

ConcreteZBH_fitted::ConcreteZBH_fitted(int tag, double _fc0, double _ec0, double _Ec, double _fccs, double _eccs, double _rs,
                                       double _e1, double _e2, double _e3, double _e4, double _e5, double _e6, double _e7, double _e8, double _e9,
                       double _eps_cy, double _eps_ccuf, double _sig_ccuf, double _eps_ccus, double _sig_ccus)
:UniaxialMaterial(tag, 0),
  fc0(_fc0), ec0(_ec0), Ec(_Ec), fccs(_fccs), eccs(_eccs), rs(_rs),
  e1(_e1), e2(_e2), e3(_e3), e4(_e4), e5(_e5), e6(_e6), e7(_e7), e8(_e8), e9(_e9),
                eps_cy(_eps_cy), eps_ccuf(_eps_ccuf), sig_ccuf(_sig_ccuf), eps_ccus(_eps_ccus), sig_ccus(_sig_ccus)

{
  sigp   = 0.0;
  Ep     = Ec;
  elp    = 0.0;
  epsp   = 0.0;
  eminp  = 0.0;
  eunl1p = 0.0;
  eunl2p = 0.0;
  eunl3p = 0.0;
  Eunlp  = fc0/ec0;
  Eunl2p = fc0/ec0;
  Et3p   = fc0/ec0;
  sunlp  = 0.0;
  elunlp = 0.0;
  muunlp = 0.0;
  flaggp = 4;

  sig    = 0.0;
  Et     = Ec;
  eps    = 0.0;
  el     = 0.0;
  emin   = 0.0;
  eunl1  = 0.0;
  eunl2  = 0.0;
  eunl3  = 0.0;
  Eunl   = fc0/ec0;
  Eunl2  = fc0/ec0;
  Et3    = fc0/ec0;
  sunl   = 0.0;
  elunl  = 0.0;
  muunl  = 0.0;
  flagg  = 4;

  beta = (Ec / fabs(fc0) - 1 / fabs(ec0));
  r0 = Ec / (Ec - fc0/ ec0);

}

ConcreteZBH_fitted::ConcreteZBH_fitted()
:UniaxialMaterial(0, 0),
fc0(0.0), ec0(0.0), Ec(0.0), fccs(0.0), eccs(0.0), rs(0.0),
e1(0.0), e2(0.0), e3(0.0), e4(0.0), e5(0.0), e6(0.0), e7(0.0), e8(0.0), e9(0.0),
eps_cy(0.0), eps_ccuf(0.0), sig_ccuf(0.0), eps_ccus(0.0), sig_ccus(0.0)
{
sigp   = 0.0;
  Ep     = Ec;
  elp    = 0.0;
  epsp   = 0.0;
  eminp  = 0.0;
  eunl1p = 0.0;
  eunl2p = 0.0;
  eunl3p = 0.0;
```

```
 Eunlp  = fc0/ec0;
 Eunl2p = fc0/ec0;
 Et3p   = fc0/ec0;
 sunlp  = 0.0;
 elunlp = 0.0;
 muunlp = 0.0;
 flaggp = 4;

 sig    = 0.0;
 Et     = Ec;
 eps    = 0.0;
 el     = 0.0;
 emin   = 0.0;
 eunl1  = 0.0;
 eunl2  = 0.0;
 eunl3  = 0.0;
 Eunl   = fc0/ec0;
 Eunl2  = fc0/ec0;
 Et3    = fc0/ec0;
 sunl   = 0.0;
 elunl  = 0.0;
 muunl  = 0.0;
 flagg  = 4;


}

ConcreteZBH_fitted::~ConcreteZBH_fitted()
{
  // does nothing
}

int
ConcreteZBH_fitted::setTrialStrain(double strain, double strainRate)
{
              // retrieve concrete hitory variables

              //emin = eminp;
              flagg = flaggp;

 //sig   = sigp;
 //Et    = Ep;
 //el    = elp;
 //eps   = epsp;
 emin  = eminp;
 eunl1 = eunl1p;
 eunl2 = eunl2p;
 eunl3 = eunl3p;
 Eunl  = Eunlp;
 Eunl2 = Eunl2p;
 Et3   = Et3p;
 sunl  = sunlp;
 elunl = elunlp;
 muunl = muunlp;

              // calculate current strain

              eps = strain;
              double deps = eps - epsp;
              emin = fmin(eps, eminp);
              //emin = eminp;

  if (fabs(deps) < 10*DBL_EPSILON){
        sig = sigp;
        Et  = Ep;
                                  el  = elp;
  }
  else if (eps <= 0.) {               // compression
        if (flagg == 4) {              // monotonic envelope
           if (deps < 0.)  {          // negative strain increment: loading
```

```
        this->envelope(eps, deps, sig, Et, el);
        //emin = eps;
    }
    else {                      // deps > 0 - unloading
        elunl = elp;
                                                    if (elunl < 0) {
                                                            elunl = 0;
                                                    }
                                                    sunl = sigp;
                                                    Eunl = Ec;
                                                    Eunl2 = Ec / (1 + 40 * elunl);
        eunl1 = emin-sunl/Eunl;
                                                    //eunl1 = fmin(eunl1, 0.0);
        eunl2 = emin-sunl/Eunl2;
                                                    if (eunl2 > 0.0) {
                                                            Eunl2 = sunl / emin;
                                                            Eunl = Eunl2 * (1 + 40 * elunl);
                                                            eunl2 = 0.0;
                                                            eunl1 = emin - sunl / Eunl;
                                                    }
                                                    //eunl2 = fmin(eunl2, 0.0);
        muunl = 0.4*elunl*Eunl2/sunl;
        if (eps > eunl2) {      // crack has opened
            flagg = 2;
            sig   = 0.;
            //Et    = 0.;
                                                            Et    = 1e-10;
            el    = elunl+(Ec/Eunl2)*muunl*(eunl1-emin);
        }
        else if (eps > eunl1) {
            flagg = 1;
            sig   = 0.;
            //Et    = 0.;
                                                            Et    = 1e-10;
            el    = elunl+(Ec/Eunl2)*muunl*(eunl1-emin);
        }
        else {
            sig   = Eunl*(eps-eunl1);
            Et    = Eunl;
            flagg = 0;
            el    = elunl+(Eunl/Eunl2)*muunl*(eps-emin);
        }
    }
}
else if (flagg == 0) {
    if (eps <= emin) {          // the strain increment brings back on the envelope
        flagg = 4;
        this->envelope(eps, deps, sig, Et, el);
        //emin = eps;
    }
    else if (eps > eunl2) {     // crack has opened
        flagg = 2;
        sig   = 0.;
        //Et    = 0.;
                                                    Et    = 1e-10;
        el    = elunl+(Ec/Eunl2)*muunl*(eunl1-emin);
    }
    else if (eps > eunl1) {
        flagg = 1;
        sig   = 0.;
        //Et    = 0.;
                                                    Et    = 1e-10;
        el    = elunl+(Ec/Eunl2)*muunl*(eunl1-emin);
    }
    else {                      // eunl1 > eps > emin
        sig   = Eunl*(eps-eunl1);
        Et    = Eunl;
        el    = elunl+(Eunl/Eunl2)*muunl*(eps-emin);
                                                    flagg = 0;
    }
```

```
}
else if (flagg == 1) {
   if (eps <= emin) {            // the strain increment brings back on the envelope
      flagg = 4;
      this->envelope(eps, deps, sig, Et, el);
      //emin = eps;
   }
   else if (eps > eunl2) {       // crack has opened
      flagg = 2;
      sig   = 0.;
      //Et    = 0.;
                                                    Et    = 1e-10;
                                                    el    = elunl+(Ec/Eunl2)*muunl*(eunl1-emin);
   }
   else if (deps < 0.) {         // loading
      flagg = 3;
      eunl3 = epsp;
      Et3   = sunl/(emin-eunl3);
      Et    = Et3;
      sig   = Et*(eps-eunl3);
      el    = elunl+(Et3/Eunl2)*muunl*(eps-emin);
   }
   else {                        // keeps flag = 1
      //Et    = 0.;
      flagg = 1;
                                                    Et    = 1e-10;
      sig  = 0.;
                                                    el   = elunl+(Ec/Eunl2)*muunl*(eunl1-emin);
   }
}
else if (flagg == 2) {
   if (eps <= emin) {            // the strain increment brings back on the envelope
      flagg = 4;
      this->envelope(eps, deps, sig, Et, el);
      //emin = eps;
   }
   else if (eps > eunl2) {       // crack has opened
      flagg = 2;
      sig   = 0.;
      //Et    = 0.;
                                                    Et    = 1e-10;
                                                    el    = elunl+(Ec/Eunl2)*muunl*(eunl1-emin);
   }
   else {                        // eunl2 > eps > emin
      flagg = 2;
      sig   = Eunl2*(eps-eunl2);
      Et    = Eunl2;
      el    = elunl+muunl*(eps-emin);
   }
}
else if (flagg == 3) {
   if (eps <= emin) {            // the strain increment brings back on the envelope
      flagg = 4;
      this->envelope(eps, deps, sig, Et, el);
     // emin = eps;
   }
   else if (eps > eunl2) {        // crack has opened
      flagg = 2;
      sig   = 0.;
      //Et    = 0.;
                                                    Et    = 1e-10;
                                                    el    = elunl+(Ec/Eunl2)*muunl*(eunl1-emin);
   }
   else if (eps > eunl3) {
      flagg = 1;
      sig   = 0.;
      //Et    = 0.;
                                                    Et    = 1e-10;
                                                    el    = elunl+(Ec/Eunl2)*muunl*(eunl1-emin);
   }
```

```
            else {                      // eunl3 > eps > emin
               flagg = 3;
               Et    = Et3;
               sig   = (eps - eunl3)*Et;
               el    = elunl+(Et3/Eunl2)*muunl*(eps-emin);
            }
         }
   }
   else {                           //eps > 0
         flagg = 2;
         sig   = 0.;
         //Et    = 0.;
                                          Et    = 1e-10;
                                          el    = elunl+(Ec/Eunl2)*muunl*(eunl1-emin);
   }
 return 0;

}

double
ConcreteZBH_fitted::getStrain(void)
{
 return eps;
}

double
ConcreteZBH_fitted::getStress(void)
{
 return sig;
}


double
ConcreteZBH_fitted::getTangent(void)
{
 return Et;
}

int
ConcreteZBH_fitted::commitState(void)
{
 sigp   = sig;
 Ep     = Et;
 elp    = el;
 epsp   = eps;
 eminp  = emin;
 eunl1p = eunl1;
 eunl2p = eunl2;
 eunl3p = eunl3;
 Eunlp  = Eunl;
 Eunl2p = Eunl2;
 Et3p   = Et3;
 sunlp  = sunl;
 elunlp = elunl;
 muunlp = muunl;
 flaggp = flagg;

 return 0;
}


int
ConcreteZBH_fitted::revertToLastCommit(void)
{
 sig   = sigp;
 Et    = Ep;
 el    = elp;
 eps   = epsp;
 emin  = eminp;
 eunl1  = eunl1p;
```

```
  eunl2 = eunl2p;
  eunl3 = eunl3p;
  Eunl  = Eunlp;
  Eunl2 = Eunl2p;
  Et3   = Et3p;
  sunl  = sunlp;
  elunl = elunlp;
  muunl = muunlp;
  flagg = flaggp;

  return 0;
}


int
ConcreteZBH_fitted::revertToStart(void)
{
  sigp   = 0.0;
  Ep     = Ec;
  elp    = 0.0;
  epsp   = 0.0;
  eminp  = 0.0;
  eunl1p = 0.0;
  eunl2p = 0.0;
  eunl3p = 0.0;
  Eunlp  = fc0/ec0;
  Eunl2p = fc0/ec0;
  Et3p   = fc0/ec0;
  sunlp  = 0.0;
  elunlp = 0.0;
  muunlp = 0.0;
  flaggp = 4;

  sig    = 0.0;
  Et     = Ec;
  eps    = 0.0;
  el     = 0.0;
  emin   = 0.0;
  eunl1  = 0.0;
  eunl2  = 0.0;
  eunl3  = 0.0;
  Eunl   = fc0/ec0;
  Eunl2  = fc0/ec0;
  Et3    = fc0/ec0;
  sunl   = 0.0;
  elunl  = 0.0;
  muunl  = 0.0;
  flagg  = 4;


  return 0;
}


UniaxialMaterial *
ConcreteZBH_fitted::getCopy(void)
{
  ConcreteZBH_fitted *theCopy =
    new ConcreteZBH_fitted(this->getTag(), fc0, ec0, Ec, fccs, eccs, rs,
                e1, e2, e3, e4, e5, e6, e7, e8, e9,
                                    eps_cy, eps_ccuf, sig_ccuf, eps_ccus, sig_ccus);

  return theCopy;
}


int
ConcreteZBH_fitted::sendSelf(int cTag, Channel &theChannel)
{
                int             res = 0;
```

```
        static      Vector      data(36);
        data(0) = fc0;
        data(1) = ec0;
        data(2) = Ec;
        data(3) = fccs;
        data(4) = eccs;
        data(5) = rs;
        data(6) = e1;
        data(7) = e2;
        data(8) = e3;
        data(9) = e4;
        data(10) = e5;
        data(11) = e6;
        data(12) = e7;
        data(13) = e8;
        data(14) = e9;
        data(15) = eps_cy;
        data(16) = eps_ccuf;
        data(17) = sig_ccuf;
        data(18) = eps_ccus;
        data(19) = sig_ccus;
        data(20) = sigp;
        data(21) = Ep;
        data(22) = elp;
        data(23) = epsp;
        data(24) = eminp;
        data(25) = eunl1p;
        data(26) = eunl2p;
        data(27) = eunl3p;
        data(28) = Eunlp;
        data(29) = Eunl2p;
        data(30) = Et3p;
        data(31) = sunlp;
        data(32) = elunlp;
        data(33) = muunlp;
        data(34) = flaggp;
        data(35) = this->getTag();


  res = theChannel.sendVector(this->getDbTag(), cTag, data);
  if (res < 0)
    opserr << "ConcreteZBH_fitted::sendSelf() - failed to send data\n";

  return res;
}

int
ConcreteZBH_fitted::recvSelf(int cTag, Channel &theChannel,
                                                FEM_ObjectBroker &theBroker)
{
  int res = 0;
  static Vector data(36);
  res = theChannel.recvVector(this->getDbTag(), cTag, data);
  if (res < 0)
    opserr << "ConcreteZBH_fitted::recvSelf() - failed to recv data\n";
  else {
        fc0 = data(0);
        ec0 = data(1);
        Ec = data(2);
        fccs = data(3);
        eccs = data(4);
        rs = data(5);
        e1 = data(6);
        e2 = data(7);
        e3 = data(8);
        e4 = data(9);
        e5 = data(10);
        e6 = data(11);
        e7 = data(12);
```

```
            e8 = data(13);
            e9 = data(14);
            eps_cy = data(15);
            eps_ccuf = data(16);
            sig_ccuf = data(17);
            eps_ccus = data(18);
            sig_ccus = data(19);
            sigp = data(20);
            Ep = data(21);
            elp = data(22);
            epsp = data(23);
            eminp = data(24);
            eunl1p = data(25);
            eunl2p = data(26);
            eunl3p = data(27);
            Eunlp = data(28);
            Eunl2p = data(29);
            Et3p = data(30);
            sunlp = data(31);
            elunlp = data(32);
            muunlp = data(33);
            flaggp = int(data(34));
            this->setTag(int(data(35)));

 }

 eps = epsp;
 sig = sigp;
 Et  = Ep;

 return res;
}

void
ConcreteZBH_fitted::Print(OPS_Stream &s, int flag)
{
 s << "ConcreteZBH_fitted tag: " << this->getTag() << endln;
 /*s << "  E: " << E << endln;
 s << "  ep: " << ep << endln;
 s << "  stress: " << trialStress << " tangent: " << trialTangent << endln;*/
}

void
ConcreteZBH_fitted::envelope (double eps, double deps, double &sig, double &Et, double &el)
{
        if ((eps / ec0) < eps_ccuf) {
                sig = ((eps / ec0) < eps_cy) ? (e1 * pow((eps / ec0), 3) + e2 * pow((eps / ec0), 2) + (Ec * ec0 / fc0) * eps / ec0) / (e3 *
pow((eps / ec0), 2) + e4 * (eps / ec0) + 1.) : ((e1 * pow(eps_cy, 3) + e2 * pow(eps_cy, 2) + (Ec * ec0 / fc0) * eps_cy) / (e3 * pow(eps_cy, 2) + e4
* eps_cy + 1) + (e5 * pow(((eps / ec0) - eps_cy), 3) + e6 * pow(((eps / ec0) - eps_cy), 2) + e7 * ((eps / ec0) - eps_cy)) / (e8 * pow(((eps / ec0) -
eps_cy), 2) + e9 * ((eps / ec0) - eps_cy) + 1.));
                sig = sig * fc0;
                /*Et = (eps / ec0 < eps_cy) ? ((3 * e1 * pow(eps / ec0, 2) + 2 * e2 * eps / ec0 + (Ec * ec0 / fc0)) * (e3 * pow(eps / ec0, 2) +
e4 * eps / ec0 + 1) - (e1 * pow(eps / ec0, 3) + e2 * pow(eps / ec0, 2) + (Ec * ec0 / fc0) * eps / ec0) * (2 * e3 * eps / ec0 + e3)) / pow((e3 *
pow(eps / ec0, 2) + e4 * eps / ec0 + 1), 2)
                        : ((3 * e5 * pow((eps / ec0 - eps_cy), 2) + 2 * e6 * (eps / ec0 - eps_cy) + e7) * (e8 * pow((eps / ec0 - eps_cy), 2)
+ e9 * (eps / ec0 - eps_cy) + 1) - (e5 * pow((eps / ec0 - eps_cy), 3) + e6 * pow((eps / ec0 - eps_cy), 2) + e7 * (eps / ec0 - eps_cy)) * (2 * e8 * (eps
/ ec0 - eps_cy) + e9)) / pow((e8 * pow((eps / ec0 - eps_cy), 2) + e9 * (eps / ec0 - eps_cy) + 1), 2);
                Et = Et * fc0 / ec0;*/
                Et = (sig - sigp) / deps;
                el = (Ec * eps - sig) / (2. * beta * sig);
        }
        else if ((eps / ec0) <= eps_ccus) {
                double sig1 = fccs * (eps / eccs) *rs / (rs - 1. + pow((eps / eccs), rs));
                double sig2 = sig_ccuf*fc0 - (eps - eps_ccuf*ec0) * Ec;
                if (sig1 < sig2) {
                        sig = sig1;
                        Et = (fccs * rs / eccs) / (rs - 1 + pow((eps / eccs), rs)) -
                                (fccs * pow(rs, 2) * (pow((eps / eccs), rs)) / eccs) / pow((rs - 1 + pow((eps / eccs), rs)), 2);
                        el = (Ec * eps - sig) / (2. * beta * sig);
                }
```

```
                else {
                        sig = sig2;
                        Et = -Ec;
                        el = (Ec * eps - sig) / (2 * beta * sig);
                }
        }
        else {
                double sig_p2 = sig_ccuf * fc0 - (eps_ccus - eps_ccuf)*ec0 * Ec;
                double sig_p = fmin(sig_ccus*fc0, sig_p2);

                double sig2 = sig_p  - (eps - eps_ccus*ec0) * Ec;
                double sig1 = fc0 * r0 * (eps / ec0) / (r0 - 1. + pow((eps / ec0), r0));
                if (sig1 < sig2) {
                        sig = sig1;
                        Et = (fc0 * r0 / ec0) / (r0 - 1. + pow((eps / ec0), r0)) -
                                (fc0 * pow(r0, 2) * (pow((eps / ec0), r0)) / ec0) / pow((r0 - 1. + pow((eps / ec0), r0)), 2);
                        el = (Ec * eps - sig) / (2 * beta * sig);
                }
                else {
                        sig = sig2;
                        Et = -Ec;
                        el = (Ec * eps - sig) / (2. * beta * sig);
                }
        }
        return;
}
```

MATLAB code for Analytical ZBH model:

```
clear;
close all;
clc;

fc0 = 4.;
ec0 = 0.002;
Ec0 = 57000*sqrt(fc0*1000)/1000;
D = 48;
cov = 2.3125;
nb = 20;
dsl = 1.27;
Est = 29000;
fy = 60;
s = 3.25*1;
dst = 0.625;
reinf_type = 1; % (2) for 'tie' or (1) for 'spiral'
Ef = 20000;
efe = 0.006;
tf = 0.065748;

ejult_s = 0.102;

format long

v = Get_analytical_function(fc0,ec0,Ec0,D,cov,nb,dsl,Est,fy,s,dst,ejult_s,Ef,efe,tf,reinf_type)



function [varout] =
Get_analytical_function(fc0,ec0,Ec0,D,cov,nb,dsl,Est,fy,s,dst,ejult_s,Ef,efe,tf,reinf_type)
fc0 = -abs(fc0);
ec0 = -abs(ec0);

Ds = D - 2*cov;   %core diam.
```

```
s_p = s - dst;          %s' (Mander)
% e_s = 0.1;             %ultimate strain steel
%reinf_type = 1;
rho_long = nb*dsl^2/D^4;        %long. steel rho

ke = (1-0.5*s_p/Ds);
if ke >=0
    if reinf_type == 2
        ke = (1-0.5*s_p/Ds)^2/(1-rho_long);
    else
        ke = (1-0.5*s_p/Ds)/(1-rho_long);
    end
else
    ke = 0;
end
ke = min(ke,1);

ey = fy/Est;

rho_f = 4*tf/D;
rho_s = 4*(0.25*pi*dst^2)/(s*Ds);

flf = 0.5*rho_f*Ef*efe;
fls = 0.5*ke*rho_s*fy;

fccs   = (2.254*(1+7.94*fls/abs(fc0))^0.5-2*fls/abs(fc0)-1.254)*fc0;
eccs   = ec0*(1+5*(fccs/fc0-1));
Eseccs = fccs/eccs;
rs     = Ec0/(Ec0-Eseccs);



r_f = abs(flf/fc0);
r_s = abs(fls/fc0);
Ec = Ec0*ec0/fc0;
ey = abs(ey/ec0);
ejult_f = abs(efe/ec0);

eff = (2*tf*Ef/D)*(-0.00003)+0.6806;

beta = (Ec/abs(-1)-1/abs(-1));   %beta SM model
% beta1 = (Ec0/abs(fc0)-1/abs(ec0));   %beta SM model

Ej_s = 1/ey;
Ej_f = 1/ejult_f;

n_ec0 = 10;
[epss, stress, ell] = get_curve(-1,-1,Ec,beta,Ej_f,Ej_s,1,ejult_f,r_f,r_s,n_ec0);
% [epss1, stress1, ell] = get_curve(fc0,ec0,Ec0,beta1,Ef,Est,fy,efe,rho_f/2,ke*rho_s/2,n_ec0);
% plot(epss,stress,'b-',epss1,stress1,'r--');
[xx,eps_cy,eps_ccuf,sig_ccuf] = optimizationfun(epss,stress,ell,ey,Ec);


  eps_ccus = -0.004 - 1.4 * rho_s * fy * ejult_s / abs(fccs);
  x = eps_ccus / eccs;
  sig_ccus = fccs * x * rs / (rs - 1 + x^rs);

  eps_ccus=eps_ccus/ec0;
  sig_ccus=sig_ccus/fc0;

if fls == 0 || abs(eps_ccus)<=abs(eps_ccuf)
    eps_ccus = eps_ccuf;
    sig_ccus = sig_ccuf;
end



% if fls == 0
%     eps_ccus = eps_ccuf;
%     sig_ccus = sig_ccuf;
% else
```

```
%     [epss, stress, ell] = get_curve(-1,-1,Ec,beta,Ej_f,Ej_s,1,abs(ejult_s/ec0),0,r_s,n_ec0);
%     % plot(epss,stress,'b-');
%     eps_ccus = epss(end);
%     sig_ccus = stress(end);
% end

varout = [fc0, ec0, Ec0, fccs, eccs, rs, xx, eps_cy, eps_ccuf, sig_ccuf, eps_ccus, sig_ccus];
end

function [c11,eps_cy,eps_ccuf,sig_ccuf] = optimizationfun(epss,stress,ell,ey,Ec)
A = []; % No other constraints
b = [];
Aeq = [];
beq = [];

ub = [2.4  15 7.2 5.2  0.5  4.2  0.7  12  20];
lb = [-0.1 -2  0 -0.7 -0.5 -0.9 -0.6 -0.6 -2];

dd = find(ell>ey,1,'first');
eps_cy = epss(dd)+0.00000001;

c0 = (ub+lb)/2;
model = @(c,x) (x<eps_cy).*(c(1)*x.^3+c(2)*x.^2+Ec*x)./(c(3)*x.^2+c(4)*x+1) +
(~(x<eps_cy)).*((c(1)*eps_cy.^3+c(2)*eps_cy.^2+Ec*eps_cy)./(c(3)*eps_cy.^2+c(4)*eps_cy+1) +
(c(5)*(x-eps_cy).^3+c(6)*(x-eps_cy).^2+c(7)*(x-eps_cy))./(c(8)*(x-eps_cy).^2+c(9)*(x-eps_cy)+1));
fun = @(x)sum((model(x,epss) - stress).^2);
nonlcon = @(x)confuneq(x,epss,stress,Ec);
% options = optimoptions(@fmincon,'Algorithm','sqp','TolX',1e-4,'MaxFunEvals',1e3,'TolFun',1e-
4,'MaxIter',1e3);
% problem =
createOptimProblem('fmincon','objective',fun,'x0',c0,'lb',lb,'ub',ub,'nonlcon',nonlcon,'options',
options);
% gs = GlobalSearch;
% [c11] = run(gs,problem);
options = optimoptions(@fmincon,'Algorithm','sqp','TolX',1e-4,'MaxFunEvals',1e3,'TolFun',1e-
4,'MaxIter',1e3);
c11 = fmincon(fun,c0,A,b,Aeq,beq,lb,ub,nonlcon,options);
f11 = model(c11,epss);
aerr = sum(abs(f11-stress))/sum(abs(stress)); % error area over total area
lerr = max(abs(f11-stress))/max(abs(stress));
% c11(10) = eps_cy;
eps_ccuf = epss(end);
sig_ccuf = f11(end);



plot(epss,stress,'k--','LineWidth',1.3);hold on;
plot(epss,f11,'b-');hold off;
aerr
end

function [c,ceq] = confuneq(x,epss,stress,Ec)
e = epss(2);
% s = stress(2);
c(1) = (3*x(1)*e^2+2*x(2)*e+Ec)/(x(3)*e^2+x(4)*e+1)-
(x(1)*e^3+x(2)*e^2+Ec*e)*(2*x(3)*e+x(4))/(x(3)*e^2+x(4)*e+1)^2-Ec;
c(2) = x(4)^2-4*x(3);
% c(1) = x(4)^2-4*x(3);
ceq = [];
end
%%---------------------------------------------------------------------

function [epss, stress, ell]= get_curve(fc0,ec0,Ec,beta,Ej_f,Ej_s,fy,ejult_f,r_f,r_s,n_ec0)

% flf_max  = kf*abs(fc0);           %max FRP lateral pressure
% fls_max  = ks*abs(fc0);
%
% r_f = flf_max/(Ej_f*ejult_f);
% r_s = fls_max/fy;

eps = 0;                            %concrete axial strain
```

```
el  = 0;                              %concrete lateral strain
flp = 0;                              %lateral pressure - past
fl  = 0;                              %lateral pressure - current
i   = 1;
epss   = 0;
stress = 0;
ell    = 0;


while abs(el) < ejult_f
    i   = i + 1;
    eps = eps + ec0/n_ec0;
    [fc,el,fl]= Conf_Pressure(eps,fc0,flp,ec0,Ec,beta,Ej_f,Ej_s,fy,r_f,r_s);
    cont=0;
    while abs(fl-flp) > max(fl*1e-10,1e-10)
        cont = cont+1;
        flp  = fl;
        [fc,el,fl]= Conf_Pressure(eps,fc0,flp,ec0,Ec,beta,Ej_f,Ej_s,fy,r_f,r_s);
        if cont>40, break, end
    end
    epss(i)    = eps;
    stress(i)  = fc;
    ell(i)     = el;
end
epss = epss/ec0;
stress = stress/fc0;
end

function [fc,el,fl]= Conf_Pressure(eps,fc0,flp,ec0,Ec,beta,Ej_f,Ej_s,fy,r_f,r_s)

fcc   = (2.254*(1+7.94*flp/abs(fc0))^0.5-2*flp/abs(fc0)-1.254)*fc0;
ecc   = ec0*(1+5*(fcc/fc0-1));
x     = eps/ecc;
Esecc = fcc/ecc;
r     = Ec/(Ec-Esecc);
fc    = fcc*x*r/(r-1+x^r);
el    = (Ec*eps-fc)/(2*beta*fc);

fl    = r_f*Ej_f*el + r_s*min(Ej_s*abs(el),fy);
end
```